University
of Cyprus

DEPARTMENT OF PHYSICS

HADRON MASSES FROM FULL QCD+QED$_C$ SIMULATIONS

MADELEINE EVIE BETH DALE

A dissertation submitted to the University of Cyprus in partial fulfillment of the requirements for the degree of Doctor of Philosophy

November 2023

VALIDATION PAGE

Doctoral Candidate: Madeleine Evie Beth Dale
Doctoral Dissertation Title: Hadron masses from full QCD+QED$_C$ simulations

The present Doctoral Dissertation was submitted in partial fulfillment of the requirements for the Degree of Doctor of Philosophy at the Department of Physics and was approved on the ……… by the members of the Examination Committee.

Examination Committee:

Research Supervisor: Prof. Haralambos Panagopoulos, University of Cyprus

Chairperson of evaluation committee: Prof. Constantia Alexandrou, University of Cyprus

Committee Member: Assoc. Professor Nicolaos Toumbas, University of Cyprus

Committee Member: Prof. Nazario Tantalo, University of Rome Tor Vergata

Committee Member: Prof. Karl Jansen, DESY

DECLARATION OF DOCTORAL CANDIDATE

The present doctoral dissertation was submitted in partial fulfilment of the requirements for the degree of Doctor of Philosophy of the University of Cyprus. It is a product of original work of my own, unless otherwise mentioned through references, notes, or any other statements.

Madeleine Evie Beth Dale

ΠΕΡΙΛΗΨΗ

Η διαρκής αύξηση σε ισχύ και διαθεσιμότητα υπολογιστικών πόρων, παράλληλα με την ανάπτυξη όλο και πιο προχωρημένων αλγοριθμικών τεχνικών, έχει επιτρέψει κατά τα τελευταία έτη τον υπολογισμό ορισμένων μεγεθών της Κβαντικής Χρωμοδυναμικής στο πλέγμα (LQCD), όπως σταθερές διάσπασης και μάζες ελαφρών αδρονίων, με στατιστικά σφάλματα τα οποία είναι μικρότερα του 1%, δηλαδή είναι πλέον παρόμοιας τάξης μεγέθους με το συστηματικό σφάλμα που οφείλεται στην παραμέληση συνεισφορών της Κβαντικής Ηλεκτροδυναμικής (QED). Συνεπώς, η αύξηση της ακρίβειας στους υπολογισμούς της LQCD, με ταυτόχρονη διατήρηση της ορθότητας, επιβάλλει τη συμπερίληψη των συνεισφορών QED.

Στην παρούσα διατριβή, που αποτελεί μέρος ενός συνολικού έργου της ομάδας RC*, έχουν μετρηθεί μάζες αδρονίων, συμπεριλαμβανομένων των νουκλεονίων και του βαρυονίου Ω-, στα πλαίσια πλήρως δυναμικών προσομοιώσεων των QCD+QED. Οι μάζες των αδρονίων είναι σημαντικές όχι μόνο αφ'εαυτών, αλλά και για τη δυνατότητα χρήσης τους στη βαθμονόμηση μετρήσεων της QCD. Η συμπερίληψη της QED αφ'ενός αποφεύγει τη συστηματική μετατόπιση της θεμελιώδους ενέργειας που προκύπτει όταν αμελείται η QED, και αφ'ετέρου επιτρέπει την εξερεύνηση των διεγερμένων καταστάσεων που εμπλέκονται εξ αιτίας της συμπερίληψης των φωτονίων. Η διαφορά μάζας μεταξύ πρωτονίου και νετρονίου αποτελεί σημαντικό παράδειγμα μιας ποσότητας η οποία είναι πολύ ευαίσθητη τόσο στην παραβίαση του isospin που οφείλεται στην QED όσο και στη διαφορά μάζας μεταξύ των κουάρκς up-down. Κατά συνέπεια, για τον υπολογισμό αυτής της ποσότητας είναι σημαντική η προσομοίωση με μη-εκφυλισμένες μάζες των κουάρκς.

Για την προσομοίωση των QCD+QED στο πλέγμα μπορούν να χρησιμοποιηθούν διάφορες στρατηγικές/μέθοδοι και καταστρώσεις. Μια ομάδα μεθόδων βασίζεται στην προσομοίωση της αμιγούς QCD, με δυνατές "εκ των υστέρων" τροποποιήσεις για συμπερίληψη της QED σε διαφορετικό βαθμό. Παραδείγματα αυτής της διαδικασίας είναι η ανάκτηση διατάξεων της πλήρους QCD+QED, μέσω ανα-στάθμισης των διατάξεων της QCD, και το διαταρακτικό ανάπτυγμα γύρω από την αμιγή QCD σε δυνάμεις της σταθεράς λεπτής υφής. Η διαδεδομένη μέθοδος RM123 αναπτύσσει το συναρτησιακό ολοκλήρωμα γύρω από τη θεωρία με συμμετρία isospin σε δυνάμεις τόσο της σταθεράς λεπτής υφής όσο και της διαφοράς μάζας των κουάρκς up-down. Μπορεί επίσης να χρησιμοποιηθεί η μέθοδος "electroquenching", η οποία χρησιμοποιεί ηλεκτρικά ουδέτερα κουάρκς στη "θάλασσα Fermi", και δυναμικά κουάρκς που είναι φορτισμένα. Αυτές οι τεχνικές είναι σε αντιδιαστολή με την πλήρως δυναμική και μη-διαταρακτική προσομοίωση των QCD+QED, η οποία αποφεύγει τους θεωρητικούς περιορισμούς της θεωρίας διαταραχών και δεν βασίζεται σε συνδυασμούς διαταρακτικών αποτελεσμάτων διαφορετικής τάξης. Κατά συνέπεια έχουμε επιλέξει την εκτέλεση πλήρως δυναμικής και μη-διαταρακτικής προσομοίωσης των QCD+QED.

Η σημαντικότερη πρόκληση στην ενσωμάτωση της QED στην LQCD προέρχεται από τον νόμο του Gauss, σύμφωνα με τον οποίο, σ'ένα περιοδικό τοροειδές, μόνο καταστάσεις με συνολικά μηδενικό ηλεκτρικό φορτίο μπορούν να αποτελέσουν μέρος του χώρου Hilbert. Διάφορες καταστρώσεις μπορούν να επιλεγούν για να ικανοποιείται ο νόμος του Gauss. Μια συνήθης επιλογή είναι η κατάστρωση QED_L, η οποία χειρίζεται με μη-δυναμικό τρόπο τους χωροειδείς μηδενικούς ιδιορυθμούς του φωτονικού πεδίου, επιβάλλοντας ένα μη-τοπικό περιορισμό. Αυτή η κατάστρωση είναι συνεπώς μη-τοπική, και επομένως δεν πληρούνται αυτομάτως ορισμένες σημαντικές ιδιότητες της θεωρίας κβαντικών πεδίων, όπως η δυνατότητα επανακανονικοποίησης. Αυτές οι ιδιότητες πρέπει κατά συνέπεια να αποδεικνύονται ξεχωριστά για καθεμιά περίπτωση.

Σε αντίθεση, η κατάστρωση QED_C βασίζεται στην προσάρτηση ενός "κατοπτρικού" πλέγματος, με φορτία στις ίδιες θέσεις αλλά αντίθετα πρόσημα από αυτά του φυσικού πλέγματος, εξαναγκάζοντας έτσι το σύστημα να είναι ηλεκτρικά ουδέτερο. Αυτή η κατάστρωση είναι τοπική και επομένως αποφεύγει κάποιες από τις δυσκολίες της κατάστρωσης QED_L που αναφέρθηκαν πιο πάνω. Ως επιπλέον πλεονέκτημα, η κατάστρωση QED_C επηρεάζεται λιγότερο από τον πεπερασμένο όγκο, συγκριτικά με την QED_L. Βαρυονικές μάζες στην δυναμική QCD+QED έχουν μέχρι τώρα υπολογιστεί από την ομάδα BMW, η οποία χρησιμοποιεί την κατάστρωση QED_L. Ο μακροπρόθεσμος στόχος μας είναι η εκτέλεση ενός ανεξάρτητου υπολογισμού του βαρυονικού φάσματος στην δυναμική QCD+QED, στο ίδιο επίπεδο ακρίβειας όπως η ομάδα BMW, με μη-διαταρακτικό τρόπο και με πλήρη εξασφάλιση της συμμετρίας βαθμίδος. Ένα θεμελιώδες βήμα προς τον στόχο αυτόν παρουσιάζεται στην παρούσα διατριβή, όπου μετρούνται βαρυονικές μάζες σε πέντε συλλογές διατάξεων που δημιουργήθηκαν από την ομάδα RC*.

Προσδιορίσαμε βαρυονικές μάζες με ακρίβεια 1-5%, καθώς και διαφορές μαζών που είχαν μεγαλύτερη διακύμανση στην ακρίβεια απ'ότι οι μάζες. Βρήκαμε ότι οι μάζες βαρυονίων Ω- έτειναν να δίνουν ένα ασθενές πλατό. Μέσω μιας προκαταρκτικής διερεύνησης, με χρήση μιας τροποποιημένης μεθόδου Backus-Gilbert, καταλήξαμε ότι το φαινόμενο αυτό οφείλεται πιθανώς στην παρουσία μιας διεγερμένης κατάστασης με ενέργεια παραπλήσια αυτής της θεμελιώδους κατάστασης του Ω- . Μια ανεπιθύμητη παρενέργεια της κατάστρωσης QED_C είναι ένα φαινόμενο μίξης που παραβιάζει τη συμμετρία γεύσης των κουάρκς. Εξερευνήσαμε τον βαθμό στον οποίο αναμένεται να επηρεάζονται τα αποτελέσματά μας από τη μίξη αυτή. Διαπιστώσαμε ότι, μολονότι η αναμενόμενη εκθετική εξασθένιση σε σωματίδια με μάζα τα οποία διασχίζουν το πλέγμα δεν επαρκεί για να καταστεί αμελητέα η μίξη, τα μικρά μεγέθη πλέγματος στις συλλογές μας έχουν ως αποτέλεσμα ότι ορισμένες καταστάσεις, οι οποίες υποχρεωτικά θα εμφανίζονταν στο διάγραμμα μίξης, είναι έντονα κατεσταλμένες για ενεργειακούς λόγους, και κατά συνέπεια η μίξη αναμένεται να είναι ιδιαίτερα υποβαθμισμένη.

ABSTRACT

The continual increase in the power and availability of computing resources, alongside the development of ever more sophisticated algorithmic techniques, has allowed the statistical error of certain measured quantities in Lattice QCD (LQCD), such as decay constants and the masses of light hadrons, to reach subpercent levels in recent years, thus reaching the same order of magnitude as the systematic error due to neglecting QED effects. In order to increase precision while maintaining accuracy, it therefore becomes necessary to include QED effects in the LQCD calculation.

In this work, which forms part of a body of work by the RC* collaboration, hadron masses, including the nucleons and the $\Omega-$ baryon, have been measured in fully dynamical QCD+QED simulations. Hadron masses are not only important by themselves, but may also be used for the calibration of QCD measurements. Including QED allows both evasion of the systematic shift of the ground energy that would result from its exclusion, and exploration of the excited states that enter due to inclusion of photons. The proton-neutron mass difference is an important example of a quantity that is very sensitive to the combination of isospinbreaking effects due to both QED inclusion and the up-down quark mass difference, rendering simulation with non-mass-degenerate up and down quarks important for the calculation of this quantity.

Different strategies and formulations may be used to simulate QCD+QED on the lattice. One group of strategies is based on the simulation of pure QCD, after which varying degrees of QED inclusion may be allowed through 'a posteriori' adjustment. Examples of this are the recovery of full QCD+QED configurations through the reweighting of QCD configurations, and the perturbative expansion around pure QCD with respect to the fine-structure constant. The popular RM123 method expands the path integral around the isospin-symmetric theory in terms of the fine-structure constant and the up-down mass difference. Electroquenching, keeping the sea quarks neutral while using electrically charged dynamical quarks, may also be used. These techniques contrast with the fully dynamical and non-perturbative simulation of QCD+QED, which avoids the theoretical constraints of the validity of perturbation theory and doesn't rely on the combination of results from different orders of perturbation theory. We therefore choose to perform a fully dynamical and non-perturbative simulation of QCD+QED.

The central challenge in incorporating QED into LQCD is that posed by Gauss's Law, which states that, on a periodic torus, only states with net-zero electric charge may form part of the Hilbert space. Different formulations may be chosen in order to satisfy Gauss's Law. The QED_L formulation is a common choice and involves the quenching of spatial zero-modes of the photon field through the enforcement of a non-local constraint. This formulation is therefore non-local, which causes certain important properties of the quantum field theory, such as renormalisability, to not be automatically satisfied; these properties must then be proven on a case-by-case basis.

The QED_C formulation is instead based upon appending a 'mirror lattice' of identically placed but opposite charges to the physical lattice, forcing the system to be electrically net-neutral. This formulation is local and thus escapes the some of the difficulties of the QED_L formulation discussed above. As a bonus, this formulation also profits from smaller finite-volume effects with respect to the QED_L formulation. Baryon masses in dynamical QCD+QED have been calculated so far by the BMW Collaboration which uses the QED_L formulation. Our long-term aim is to provide an independent calculation of the baryon spectrum in dynamical QCD+QED to the same level of precision as the BMW Collaboration using the QED_C formulation, in a non-perturbative manner and ensuring full gauge-invariance. A foundational step towards this goal is presented in this thesis, as baryon masses are measured on five ensembles generated by the RC* collaboration.

We obtained baryon masses with a precision of between 1-5%, and mass differences that had a greater variation in precision that those of the masses. We found that the $\Omega-$ baryon masses tended to give a weak plateau. Through a preliminary investigation using a modified Backus-Gilbert method, we found that this is likely due to the presence of an excited state close in energy to the $\Omega-$ ground state. We also explored the extent to which we expect flavour-violating mixing, which is an unwanted side-effect particular to the QED_C formulation, to affect our results. We found that while the expected exponential suppression from the traversal of the lattice by massive particles is not enough to render the mixing negligible, the small lattice sizes of our ensembles cause certain states that would necessarily appear in the mixing diagram to be strongly suppressed on energetic grounds, and therefore we expect this mixing to be strongly suppressed.

A C K N O W L E D G E M E N T S

Firstly, I would like to thank the reader for taking the time to read my thesis, and to those who will be acting as its reviewers. I would like to express my deepest gratitude to my main supervisor, Prof. Nazario Tantalo, for his abiding patience with me and for his care for my work. I would also like to thank my other supervisors, Prof. Haris Panagopoulos and Prof. Igor Sokolov. I am glad to have had the pleasure of participating in the RC* collaboration alongside supportive and wise colleagues. I would particularly like to thank Prof. Marina Marinković, who has always been very kind and encouraging to me. I also received help and guidance from Dr. Piotr Korcyl and Dr. Martin Hansen at the start of my studies, for which I give many thanks. I am grateful to the organisers and participants in the STIMULATE-EJD programme and training workshops. The experience was both enriching and challenging, and gave me the cherished opportunity to travel around Europe and meet people from all around the world before the start of the pandemic. Finally, I would like to thank both my friends from the UK and my new friends from STIMULATE, Tor Vergata and my language classes, for helping me feel that I was not alone during the stress of my studies, relocation and family bereavement. My family and my boyfriend have all stood by me through this time and I am immensely thankful to have them in my life.

CONTENTS

LIST OF TABLES

INTRODUCTION

In recent years, the increasing power and availability of computing resources, coupled with the development of more sophisticated algorithmic techniques, has lead to the consistent reduction in the statistical error of quantities measured in lattice QCD (LQCD).

The measurements of certain hadronic observables, such as decay constants and the masses of light hadrons, are now associated with statistical errors reaching subpercent levels, therefore arriving at the same order of magnitude as the systematic error due to neglecting QED [1]. It has thus become pertinent to address this systematic error by including QED effects into LQCD measurements, should we desire to further increase precision while maintaining accuracy.

The subject of this work is the measurement of meson and baryon masses in full QCD+QED simulations. Hadron masses are both important by themselves and are also useful for the calibration of LQCD measurements. Alongside the shift in value of hadronic properties of order $\mathcal{O}(\alpha_{\mathrm{EM}})$ due to the electrically-charged quarks coupling with photons, the inclusion of QED also allows one to investigate a wider range of excited states in the spectrum due to the additional presence of photons.

The incorporation of isospin-breaking into a lattice calculation has two possible sources, the first being electromagnetic effects and the second being the difference in mass between the u and d quarks. Taking the neutron-proton mass difference as a particularly relevant example, the two effects are in competition with each other. The inclusion of electromagnetism shifts the proton mass 1 MeV higher with respect to the neutron, while the effect due to the $u - d$ mass difference is to reduce the proton mass by 2.5 MeV [2]. Therefore, accurate calculation of such a sensitive quantity requires non-mass-degenerate u and d quarks as well as the inclusion of QED. In this work, both of these features are simulated in parallel.

While the basic principle of including QED in LQCD is the straightforward generalisation of the SU(3) gauge field to a U(3) gauge field, and the addition of a photon gauge term to the discretised lattice action, Gauss's Law provides an obstacle to the formulation of QED on the lattice, as it states that, on a periodic torus, only states with net-zero electric charge can form part of the Hilbert space. This complication has spurred the development of different strategies and formulations in order to make the measurement of net-charged objects feasible.

Some approaches to the inclusion of QED on the lattice are based on simulating pure QCD and adjusting 'a posteriori' to allow varying degrees of QED inclusion. These include the reweighting of QCD configurations to recover full QCD+QED configurations [3–5], as well as the perturbative expansion with respect to the fine-structure constant α_{EM} around pure QCD. The RM123 method, in short a path-integral expansion in powers of both the renormalised $d - u$ quark mass difference over the QCD scale, $\frac{m_{d,R} - m_{u,R}}{\Lambda_{\mathrm{QCD}}}$, and the renormalised fine-structure constant, α_R [6], is popular [6–8]. Recent examples of works that have used this technique have featured the calculation of hadronic decay rates [9], HVP contributions to the muon magnetic anomaly [10] and baryon masses [11]. It is also common to use 'electro-quenching', in which the dynamical quarks may be electrically charged but the sea quarks are neutral and therefore the configurations take place in pure QCD. Ref. [12], a pioneering work that introduced non-perturbative QED to the lattice, used this technique. These approaches are in contrast to the fully dynamical and non-perturbative simulation of both QCD and QED on the lattice, which allows one to work unconstrained with regard to the validity of perturbation theory in

QED and doesn't require the quantification of contributions from many different orders of perturbation theory. In this thesis, we are using such a dynamical and non-perturbative QCD + QED setup.

Whether perturbative or full QED is included in the calculation, Gauss's Law must be adhered to; in order to comply with Gauss's Law, a formulation of QED must be chosen. A common choice is the QED_L formulation [12] [13], in which the spatial zero-modes of the photon field are quenched at all times by enforcing a non-local constraint. Physically, this is equivalent to introducing a background of uniform electric charge in order to give the system net-zero electric charge. The non-locality of this formulation, however, leads to certain properties of the quantum field theory not being satisfied automatically; these include renormalisability, the independence of renormalisation constants on the lattice volume, and the validity of the Symanzik improvement program and of the operator product expansion. These properties therefore have to be proven for each case; however, it must be noted that these have been proven for the spectrum.

Another formulation that merits attention here is the QED_M formulation [14], in which a mass term is added to the photon. This formulation is local and has a well-understood renormalisation. In finite volume, it allows a consistent QFT that may be defined order-by-order in a perturbative expansion. The mass term, however, introduces a soft breaking of gauge symmetry. Furthermore, both the limits of zero photon mass and infinite volume must be taken, and these limits do not commute, therefore making the extrapolation to the physical point challenging. Results in the calculation of hadron masses have nonetheless been presented in Ref. [15].

Our choice, the QED_C formulation [16–20], is based instead upon appending to the physical lattice a 'mirror lattice' with identically-placed but opposite electric charges, thus making the system electrically net-neutral. An advantage of this formulation is its locality, which means that the above considered properties such as renormalisability are automatic. This formulation also has benefits in terms of smaller finite-volume effects compared to the QED_L formulation.

The reference calculation for baryon masses including dynamical QED is that of the BMW collaboration [2]. This effort was carried out using the QED_L formulation. The isospin-splittings of baryon masses in dynamical QCD+QED have also been measured in Ref. [21]. Our long-term goal in the RC* collaboration is to perform an independent calculation of the baryon spectrum, of the same level of accuracy as [2], by using the QED_C formulation, ensuring full gauge-invariance and without relying on perturbation theory. The work presented in this thesis is a foundational step in this direction, presenting baryon masses in QCD+QED_C measured on 5 ensembles generated by the RC* collaboration. Part of this work is expected to be published soon as part of Ref. [22] by the RC* collaboration.

This thesis starts with a quick overview of the fundamentals of lattice gauge theories that are relevant to this work in Chapter 2, which may be skipped by the experienced reader. This chapter will take the reader from the transformation of the gauge theory from the continuum on to the lattice, to the expression of the fermionic fields as Wick contractions leading to correlation functions, to the systematic improvement of discretisation errors in the lattice action, to the extrapolation of lattice results to the physical point. Some of the important statistical properties of Markov chains that will inform the explanation of analytical techniques used later on will also be introduced in this chapter.

Chapter 3 explains the challenges and peculiarities that are introduced when QCD is combined with QED using the C* formulation, which have been developed in the recent years and which may by now be considered established. Firstly, the construction of the formulation itself is discussed. Then, the symmetries of the system, such as gauge transformations, translations, parity and flavour symmetries, and how they pertain to the degrees of freedom on the lattice, are discussed. Special attention is paid to the definition of electrically-charged interpolating operators that are invariant under the local U(1) gauge transformations, as well

as the possibility of flavour-violating mixing that arises due to the C^* boundary conditions. The complication that the inclusion of QED in the C^* formulation introduces to the usual sign problem is explained, with further implementation-specific details given in Chapter 4. We then explore the finite-size effects that derive from the long-range interactions of QED, and their magnitude in the $\mathrm{QED_C}$ formulation in comparison with the $\mathrm{QED_L}$ formulation. Finally, the details of the C^* formulation on the lattice are explained.

As this work forms part of a combined effort of the RC* Collaboration, of which the hadron masses form a significant part, the context of the RC* renormalisation strategy and the details of the simulation algorithm are explored in Chapter 4. The renormalisation strategy is parametrised by *trajectory observables* that define lines of constant physics, with the quark masses and the value of α being tuned in order to lie on these lines. This strategy is explained alongside the results for the meson masses. Certain algorithmic details of the simulation, including a novel method for the calculation of the sign of the fermionic Pfaffian developed by the RC* Collaboration, are also discussed.

Chapter 5 provides a catalogue of the techniques used for the optimisation of the signal for the calculation of baryon masses, as well as spectral decomposition techniques for the isolation of the ground state energy. The decreased signal-to-noise ratios for baryons when compared to those of mesons are discussed. The base interpolating operators used for the baryon correlators are then presented, with a discussion of the smearing that is applied to these operators following. The effective mass errors are compared for the Jackknife method and the Gamma method, error analysis methods that are presented in App. E, and the integrated autocorrelation time from the Gamma method is confirmed to be consistent with the errors from the Jackknife method. The Generalised Eigenvalue Problem (GEVP), which is used in order to optimise the isolation of the ground state and to explore the baryon spectra, is explained. The different smearing levels are analysed in comparison to the ground state energy from the GEVP, and an example of the spectrum obtained through the GEVP, including excited states, is presented. A modified version of the Backus-Gilbert method [23][24] is also presented. This is used later on to help analyse some of the baryon mass results in a very preliminary way.

The results for the baryon masses, that are the focus of this thesis, are presented in Chapter 6. The effective mass plots and final masses and mass differences are discussed in the context of the renormalisation strategy. The modified Backus-Gilbert method is used in order to shed light on the excited states of the Ω^- baryon. The magnitude of the suppression of the flavour mixing due to the C^* boundaries is then estimated for the ensembles. The trends of some masses and mass differences are then discussed with reference to their physical values.

LATTICE GAUGE THEORIES

The Standard Model of Particle Physics (SM), and its predictions of the properties and phenomenology of sub-atomic physics, may be understood in part by the separate study of the individual gauge theories that are combined in the SM. For instance, the properties of hadrons, subatomic particles that are composed of quarks and gluons, and the group of particles to which nucleons belong, may be understood largely through the study of the SU(3) gauge theory, with U(1) contributions giving a small correction to these properties.

The SU(3) gauge theory, QCD, is particular in that, whilst theories such as U(1) and SU(2) have relatively weak coupling strengths and are therefore appropriate for study using perturbative methods, the SU(3) coupling strength only becomes small at high energies, while at energies that are not large the coupling strength is too large for a perturbative treatment to be appropriate. It is this phenomenon that leads to the confinement of quarks within hadrons, and this also renders necessary non-perturbative methods for the study of QCD.

Lattice gauge theory is a method of studying vector-like gauge field theories, a group to which QCD belongs, in a non-perturbative manner. Firstly, using a Wick rotation, the quantum field theory in Minkowskian space-time is transformed into a statistical mechanical treatment in Euclidean space-time, through which the path integral defining the theory is numerically calculated. The lattice acts to discretise this Euclidean space-time. On the sites of the lattice are placed quark fields, whereas the links between the sites host the gauge fields. In this way, the lattice acts as the ultra-violet regulator that is necessary to make the field theory finite, and the physical results are recovered through taking the continuum limit of vanishing lattice spacing, which, through the renormalisation group, is equivalent to taking the limit of vanishing bare gauge coupling.

Through the use of LQCD, many physical predictions stemming from the SM have been calculated. Of special importance are the values of the electroweak decay constants and form factors necessary for the calculation of the CKM matrix elements, as well as the quark masses, the value of the strong gauge coupling, and those contributions to the anomalous magnetic moment of the muon, $g_\mu - 2$, that come from the hadronic interactions.

2.1 PATH INTEGRAL REPRESENTATION

In Euclidean space-time in the continuum, the QCD action is given by

$$S_{\text{QCD}} = \frac{1}{4g^2} \int d^4x \sum_{a=1}^{8} G^a_{\mu\nu} G^a_{\mu\nu} + \sum_f \int d^4x \overline{\psi}_f(x)(i\gamma_\mu D_\mu - m_f)\psi_f(x), \qquad (2.1)$$

where the covariant derivative is denoted by $D_\mu = \partial_\mu - igB_\mu(x)$, and the field strength is given by

$$G^a_{\mu\nu} = \partial_\mu B^a_\nu - \partial_\nu B^a_\mu - f^{abc} B^b_\mu B^c_\nu, \qquad (2.2)$$

where f^{abc} are the SU(3) group structure constants. The quark fields each have 12 components, formed of 3 colour $\otimes$ 4 spinor components, and the quark flavours are labelled by the index f. The Dirac matrices used above are Euclidean, $\{\gamma_\mu, \gamma_\nu\} = 2\delta_{\mu\nu}$. This is missing a gauge-fixing

term that would be required in the continuum theory, as it is not necessary when moving to the lattice.

According to Feynman's path integral quantisation procedure, one may write the expectation value of a physical observable O as

$$\langle O \rangle = \frac{1}{Z} \int \mathcal{D}B\mathcal{D}\psi\mathcal{D}\overline{\psi} O(\psi, \overline{\psi}, B) \exp(-S_{\mathrm{QCD}}[\psi, \overline{\psi}, B]). \tag{2.3}$$

where the partition function is given by

$$Z = \int \mathcal{D}B\mathcal{D}\psi\mathcal{D}\overline{\psi} \exp(-S_{\mathrm{QCD}}[\psi, \overline{\psi}, B]). \tag{2.4}$$

This has an obviously statistical mechanical form with a probability density given by $\exp(-S_{\mathrm{QCD}}[\psi, \overline{\psi}, B])/Z$.

2.2 MOVING ON TO THE LATTICE

The lattice formulation of QCD is designed in such a way that SU(3) gauge-invariance is preserved. This is advantageous with respect to perturbative calculations, for which gauge fixing is essential, as it significantly simplifies parts of the calculation. For instance, the pool of operators that can mix under renormalisation is thinned due to requirements on their forms.

Upon moving to the lattice, the fermion fields have the same behaviour under gauge transformations as in the continuum case, with the only distinction being that the space-time points x must now take discrete values to lie on the lattice sites, $x = a(n_1, n_2, n_3, n_4)$, with n_i being integer-valued. For a gauge transformation matrix $\Omega \in \mathrm{SU}(3)$,

$$\psi(x) \to \Omega(x)\psi(x), \qquad \overline{\psi}(x) \to \overline{\psi}(x)\Omega(x)^{\dagger}. \tag{2.5}$$

In order to construct quark bilinears, that link together different sites and form the basis of correlation functions, the gluon field that sits on the links between sites must be introduced. It is worth noting here that, unlike in the continuum where the gauge field $B_{\mu}^{\mathrm{cont.}}$ takes Lie-algebra values, the lattice gluon field takes as its values elements of the gauge group SU(3). The quark bilinear is made gauge-invariant if, in conjunction with the transformation given in Eq. (2.5), the gauge field obeys the transformation

$$U_{\mu}(x) \to \Omega(x)U_{\mu}(x)\Omega^{\dagger}(x + \hat{\mu}a). \tag{2.6}$$

Hence, the quark bilinear provides one fundamental gauge-invariant operator from which more complex gauge-invariant operators may be constructed. As an aside, the gluon field on the lattice may be identified in continuum language with a Wilson line $\mathcal{P}\exp(i\int_x^{x=a\hat{\mu}} dx_{\mu}B_{\mu}(x))$ that connects the two points x and $x + \hat{\mu}a$, where $\mathcal{P}$ denotes a path-ordered integral and B is the gauge field.

The trace in a two-dimensional plane of the gauge links that gives the smallest possible area is called the (elementary) plaquette, given by

$$Q_{\mu\nu}(x) = U_{\mu}(x)U_{\nu}(x + \hat{\mu})U_{\mu}^{\dagger}(x + \hat{\nu})U_{\nu}^{\dagger}(x). \tag{2.7}$$

We note that, from here on, $a = 1$ is taken for simplicity. It may be shown easily through Eq. (2.6) that the plaquette is SU(3)-gauge-invariant. The Wilson gauge action is the simplest possible gauge action, and is formed using the sum over all elementary plaquettes,

$$S_G = \beta \sum_{x,\mu>\nu} \left(1 - \frac{1}{N_c}\mathrm{Re\ Tr}Q_{\mu\nu}(x)\right). \tag{2.8}$$

Here, the inverse gauge coupling $\beta = 6/g_{\text{lat}}^2$, where g_{lat} is the bare gauge coupling on the lattice (from here on, we will refer to this simply as g). Identifying $U_\mu(x) = \exp(iaB_\mu(x))$, if the limit $a \to 0$ is taken, and the sum is replaced with an integral, then to leading order we have

$$S_G \to \int \frac{1}{4g_{\text{lat}}^2} d^4x \sum_{a=1}^{8} G_{\mu\nu}^a G_{\mu\nu}^a. \tag{2.9}$$

2.3 FERMIONS ON THE LATTICE

2.3.1 *Grassmann numbers and Wick's theorem*

The primary property of fermions is that they obey Fermi statistics, which may be expressed mathematically through the requirement that the interchange of the quantum numbers characterising two different fermion states is anti-symmetric. If we write the fermionic vacuum expectation value of a product of fermion fields as

$$\left\langle \psi^{f_1}(n_1)_{\underset{a_1}{\alpha_1}} \psi^{f_2}(n_2)_{\underset{a_2}{\alpha_2}} \cdots \psi^{f_k}(n_k)_{\underset{a_k}{\alpha_k}} \overline{\psi}^{g_1}(m_1)_{\underset{b_1}{\beta_1}} \overline{\psi}^{g_2}(m_2)_{\underset{b_2}{\beta_2}} \right\rangle_F \tag{2.10}$$

where

$$\langle O \rangle_F = \frac{1}{Z_F[U]} \int \mathcal{D}\psi \mathcal{D}\overline{\psi} e^{-S_F[\psi,\overline{\psi},U]} O[\psi,\overline{\psi},U] \tag{2.11}$$

and the fermionic partition function is given by

$$Z_F[U] = \int \mathcal{D}\psi \mathcal{D}\overline{\psi} e^{-S_F[\psi,\overline{\psi},U]}, \tag{2.12}$$

then, for two fermions $\psi^{f_1}(n_1)_{\underset{a_1}{\alpha_1}}$ and $\psi^{f_2}(n_2)_{\underset{a_2}{\alpha_2}}$ that carry the quantum numbers labelled f for flavour, n for lattice site, α for Dirac index and a for colour index, Fermi statistics demand that the vacuum expectation value given in Eq. (2.10) change sign under the interchange

$$f_1 \leftrightarrow f_2, \quad n_1 \leftrightarrow n_2, \quad \alpha_1 \leftrightarrow \alpha_2, \quad a_1 \leftrightarrow a_2. \tag{2.13}$$

As the state is fully described by these quantum numbers, this interchange is of course equivalent to the commutation of the specified fermion fields themselves. Therefore, it is required that the fermion fields anti-commute with each other. This is true for both ψ and $\overline{\psi}$, and ψ and $\overline{\psi}$ must also anti-commute with each other. All fermions in the theory must act as anti-commuting numbers regardless of the combination of indices $f, f', n, n', \alpha, \alpha', a, a'$:

$$\psi^f(n)_{\underset{a}{\alpha}} \psi^{f'}(n')_{\underset{a'}{\alpha'}} = -\psi^{f'}(n')_{\underset{a'}{\alpha'}} \psi^f(n)_{\underset{a}{\alpha}} \ ; \tag{2.14a}$$

$$\overline{\psi}^f(n)_{\underset{a}{\alpha}} \overline{\psi}^{f'}(n')_{\underset{a'}{\alpha'}} = -\overline{\psi}^{f'}(n')_{\underset{a'}{\alpha'}} \overline{\psi}^f(n)_{\underset{a}{\alpha}} \ ; \tag{2.14b}$$

$$\psi^f(n)_{\underset{a}{\alpha}} \overline{\psi}^{f'}(n')_{\underset{a'}{\alpha'}} = -\overline{\psi}^{f'}(n')_{\underset{a'}{\alpha'}} \psi^f(n)_{\underset{a}{\alpha}}. \tag{2.14c}$$

These anti-commuting numbers are referred to as Grassmann numbers. These have particular properties with regard to differentiation and integration that will not be discussed here, but that make possible the derivation of some important formulae.

The first formula of particular relevance is the Matthews-Salam formula, which is

$$\int d\eta_N d\overline{\eta}_N \cdots d\eta_1 d\overline{\eta}_1 \exp\left(\sum_{i,j=1}^{N} \overline{\eta}_i M_{ij} \eta_j\right) = \det[M], \tag{2.15}$$

where M is a complex $N \times N$ matrix. When we set $M = -D$, we see that this describes the fermionic partition function Z_F, which takes the value of the determinant of the Dirac operator, called the *fermion determinant.*

Another useful formula is that for the *generating functional for fermions*

$$W[j, \bar{j}] = \int \prod_{i=1}^{N} d\eta_i d\bar{\eta}_i \exp \left(\sum_{k,l=1}^{N} \bar{\eta}_k M_{kl} \eta_l + \sum_{k=1}^{N} \bar{j}_k \eta_k + \sum_{k=1}^{N} \bar{\eta}_k j_k \right) \tag{2.16}$$

$$= \det[M] \exp \left(- \sum_{n,m=1}^{N} \bar{j}_n \left(M^{-1} \right)_{nm} j_m \right). \tag{2.17}$$

In this expression, the $2N$-dimensional Grassman algebra that is generated by $\eta_i, \bar{\eta}_i, i = 1, 2, \cdots, N$ is embedded within a $4N$-dimensional algebra generated by $\eta_i, \bar{\eta}_i, j_i, \bar{j}_i$, where $i = 1, 2, \cdots, N$. The new Grassman numbers $j, \bar{j}$, however, act as source terms and are not integrated over.

Finally, by noting that

$$\langle \eta_{i_1} \bar{\eta}_{k_1} \cdots \eta_{i_N} \bar{\eta}_{k_N} \rangle_F = \frac{1}{Z_F} \left(\frac{-\partial}{\partial j_{k_1}} \right) \frac{\partial}{\partial \bar{j}_{i_1}} \cdots \left(\frac{-\partial}{\partial j_{k_n}} \right) \frac{\partial}{\partial \bar{j}_{i_n}} W[j, \bar{j}] \Big|_{j, \bar{j} = 0}, \tag{2.18}$$

and using the expression for the generating functional given in Eq. (2.16) and the rules for derivatives of Grassmann numbers, Wick's theorem may be derived:

$$\langle \eta_{i_1} \bar{\eta}_{j_1} \cdots \eta_{i_N} \bar{\eta}_{j_N} \rangle_F$$

$$= \frac{1}{Z_F} \int \prod_{k=1}^{N} d\eta_k d\bar{\eta}_k \eta_{i_1} \bar{\eta}_{j_1} \cdots \eta_{i_N} \bar{\eta}_{j_N} \exp \left(\sum_{l,m=1}^{N} \bar{\eta}_l M_{lm} \eta_m \right), \tag{2.19a}$$

$$= (-1)^n \sum_{P(1,2,\cdots,n)} \text{sgn}(P) \left(M^{-1} \right)_{i_1 j_{P_1}} \left(M^{-1} \right)_{i_2 j_{P_2}} \cdots \left(M^{-1} \right)_{i_n j_{P_n}}, \tag{2.19b}$$

where all permutations P of the numbers $1, 2, \cdots, n$ are included in the sum with their associated sign, $\text{sgn}(P)$, resulting from the anti-commutation of the Grassmann numbers in the permutations. We see that the fermionic expectation value may thus be written as the sum of the products of the matrices M^{-1} for all the possible pairings between η and $\bar{\eta}$, multiplied by the associated sign. Again taking $M = -D$, we see that the above formula may be written in terms of the propagator S,

$$\langle \eta_{i_1} \bar{\eta}_{j_1} \cdots \eta_{i_N} \bar{\eta}_{j_N} \rangle_F = \sum_{P(1,2,\cdots,n)} \text{sgn}(P) \left(S \right)_{i_1 j_{P_1}} \left(S \right)_{i_2 j_{P_2}} \cdots \left(S \right)_{i_n j_{P_n}}, \tag{2.20}$$

where $S(y, z)$, the propagator from y to z, may be determined through solving the linear equation

$$\sum_y D(x, y) S(y, z) = \delta(x - z). \tag{2.21}$$

Because D is a very large sparse matrix, it is necessary to use an iterative linear solver to obtain the propagator.

2.3.2 *The fermionic action*

The discretisation of the quark field action is more delicate than that of the gauge field, as numerous problems may arise, and so to fix them, numerous different quark actions are proposed. It is important to note that these are used to reduce the systematic error from various sources, but the methods should all give consistent results in the continuum limit.

A naive way to discretise the fermion action is through a symmetric difference,

$$D_\mu \psi(x) \rightarrow \frac{1}{2a} \left[\gamma_\mu U_\mu(x) \psi(x+\hat{\mu}) - \gamma_\mu U_\mu^\dagger(x-\hat{\mu}) \psi(x-\hat{\mu}) \right]. \tag{2.22}$$

The inclusion of the gauge field allows the object $D_\mu \psi(x)$ to transform in the same way as $\psi(x)$ under a gauge transformation. The above discretisation, however, is problematic as it introduces 2^d equivalent fields when the continuum limit is taken, where d is the number of dimensions in space-time. This is due to the Nielsen-Ninomiya theorem [25], which states that 'doublers' are an unavoidable consequence of the formulation on the lattice of an exact and continuum-like chiral symmetry.

In order to avoid these doublers, the Wilson term may be added,

$$\begin{aligned}
\frac{ra}{2}\overline{\psi}D^2\psi, & \\
&= \frac{r}{2a}\overline{\psi}\left(U_\mu(x)\psi(x+\hat{\mu}) + U_\mu^\dagger(x-\hat{\mu})\psi(x-\hat{\mu}) - 2\psi(x) \right).
\end{aligned} \tag{2.23}$$

Here, the parameter r is called the Wilson parameter. This term acts to force the decoupling of the doublers in the continuum limit by giving them a mass of $\mathcal{O}(1/a)$. While this solves the problem of the doublers, discretisation errors of order $\mathcal{O}(a)$ are introduced, as well as the chiral symmetry being broken, which may make it unsuitable for use in the measurement of certain physical observables.

If the quark field normalisation is redefined to be

$$\psi \rightarrow \sqrt{2\kappa}\psi, \qquad \kappa = \frac{1}{2(m_0 + 4r)}, \tag{2.24}$$

where m_0 is the bare mass of the quark in question, then the quark action may be defined simply as

$$S^W = \sum_{x,y} \overline{\psi}(x) D(x,y) \psi(y), \tag{2.25}$$

where

$$\begin{aligned}
D(x,y) = \delta_{x,y} - \kappa \sum_\mu \Big\{ &(r - \gamma_\mu) U_\mu(x) \delta_{x+\hat{\mu},y} \\
&+ (r + \gamma_\mu) U_\mu^\dagger(x-\hat{\mu}) \delta_{x-\hat{\mu},y} \Big\}.
\end{aligned} \tag{2.26}$$

This representation is known as the hopping representation, with κ being called the hopping parameter. The most popular choice for the value of r is 1, which we shall use from now on. This expansion allows us to visualise fermions as being composed of points connected to each other by paths of link variables in space-time.

2.4 MARKOV CHAIN MONTE CARLO

In order to discuss later on the statistical analysis techniques that are used to quantify as accurately as possible the measurement errors, we must first explore some of the concepts behind Markov Chain Monte Carlo (MCMC) simulations, the statistical properties of the ensembles they generate, and the Hybrid Monte Carlo algorithm that is used in our simulation and indeed in most large-scale LQCD simulations nowadays.

2.4.1 *Importance sampling*

As explained in Section 2.3, the quark fields that appear within the functional integral for QCD obey Fermi statistics and are described mathematically using Grassmann numbers. No method has to this day been invented to directly simulate these Grassmann-valued quark fields in a practicable way on standard computer architectures. For this reason, it is required to integrate out the quark fields, leading to the partition function for the fermions taking the value of a fermion determinant, $Z_F = -\det[D]$ in the case of one flavour, and the fermionic expectation value taking the form of a product of propagators through Wick contractions.

If we consider as an example a lattice QCD setup with Wilson quarks with two different flavours that are mass-degenerate, the partition function can be written as

$$Z = \int \mathcal{D}[U]\{\det D(U)\}^2 e^{-S_G(U)}, \qquad \mathcal{D}[U] = \prod_{x,\mu} dU(x,\mu). \tag{2.27}$$

Here, the gauge action is denoted by $S_G(U)$, $dU(x,\mu)$ is the link variable integration measure that is invariant under SU(3) gauge transformations, and $D[U]$ is the massive Wilson-Dirac operator that depends on the gauge field U. The quark determinant D may be shown to be real through γ_5-Hermiticity, thus $\{\det D(U)\}^2 \geq 0$ and a valid normalised probability density,

$$p(U) = \frac{1}{Z}\{\det D(U)\}^2 e^{-S_g(U)}, \tag{2.28}$$

may be defined on the space on the gauge fields. This allows us to redefine the expectation value for an observable O as that of a classical statistical system,

$$\langle O \rangle = \int \mathcal{D}[U]p(U)O(U). \tag{2.29}$$

Each possible configuration of the gauge-fields may be thought of as a state that has a certain probability, and the observable is some function of the gauge-field configuration. Attention must be paid in the setup of a simulation such that the product of the quark determinants be negative, so that a probabilistic interpretation of the theory can be valid. This is discussed in the context of our simulations in Sec. 4.8 and Apps. C and D.

In this probabilistic interpretation, due to the gauge action being an extensive quantity, the factor of $e^{-S_G(U)}$ for a great portion of the space of gauge fields will be very small, meaning that these states contribute very little to the final value of the integral. It would be inefficient, not to say impracticable, to attempt such an integration over all states for a reasonably-sized system. Instead, the concept of approximation via importance sampling is used, in order to generate an ensemble of fields that is representative of the space of fields. The idea of this is to select samples from the space of fields according to their probability density; in this way, a subspace with high probability density would be sampled more often than a subspace with low probability density.

In order to obtain a representative ensemble $\{U_1, \cdots, U_N\}$, the fields are selected at random with probability $\mathcal{D}[U]p(U)$; the number of fields therefore in an open region $\mathfrak{R}$ of the field space is given by

$$\text{number of fields in } \mathfrak{R} = \int_{\mathfrak{R}} \mathcal{D}[U]p(U) + \mathcal{O}(N^{-1/2}), \tag{2.30}$$

where the term $\mathcal{O}(N^{-1/2})$ accounts for the statistical error stemming from the finite number of samples N that one selects.

Once one has ensured that the fields U form an approximately-representative sample of the field space, the integral in Eq. (2.29) defining the expectation value of the observable O may be approximated by a sum, through

$$\langle O \rangle = \frac{1}{N} \sum_{i=1}^{N} O(U_i) + \mathcal{O}(N^{-1/2}). \tag{2.31}$$

While this approximation method is not valid for obtaining the expectation value of all observables with high statistical precision, those quantities that are sensitive to large-distance correlations being particularly problematic, this approximation method works very well for many quantities.

2.4.2 *Markov chains*

The focus now turns to how a representative ensemble may be generated. This is generally achieved through a Markov process, which refers to the sequential generation of states from some initial state through a stochastic algorithm. Although the system on which this Markov process acts may be rather general, there are some requirements that the system must satisfy:

  a The system must have a finite number n of states s;

  b The equilibrium distribution of such states $P(s)$ must satisfy $P(s) > 0$ for all s and also $\sum_s P(s) = 1$;

  c The observables are functions $O(s)$ of the states s and are real-valued.

The requirements then validate the calculation of the expectation value $\langle O \rangle$ of the observable $O(s)$ through the finite sum over states

$$\langle O \rangle = \sum_s O(s)P(s). \tag{2.32}$$

In a Markov process that creates a Markov chain of states $s_1, s_2, s_3, \cdots, s_N$ from some system, the degrees of freedom in the creation of the chain are the initial state s_1 and the transition probability $T(s \to s_k)$ to take the system from state s to state s_k. One then designs the transition probability such that a representative ensemble may be obtained for large N regardless of the initial state. In this way, the expectation value for an observable $O(s)$ can be calculated through

$$\langle O \rangle = \frac{1}{N} \sum_{k=1}^{N} O(s_k) + \mathcal{O}(N^{-1/2}). \tag{2.33}$$

Here, the error term $\mathcal{O}(N^{-1/2})$ will be dominated at large N by statistical error caused by random fluctuations in the Markov chain.

In order to construct transition probabilities that do indeed lead to the Markov chain becoming a representative ensemble of states, the following requirements must be met:

  1. Valid probabilities: $T(s \to s') \geq 0$ for all s, s' and $\sum_{s'} T(s \to s') = 1$ for all s

  2. Balance: $\sum_s P(s)T(s \to s') = \sum_s P(s')T(s' \to s) = P(s')$ for all s'

  3. Aperiodicity: $T(s \to s) > 0$ for all s

  4. Ergodicity: Two states $s \in S$ and $s' \notin S$, where S is a non-empty proper subset of states, exist such that $T(s \to s') > 0$ is satisfied.

Running through the properties, we see that Property 1 is simply the requirement that $T(s \to s')$ act as a valid probability distribution in s' for a given fixed s. Property 2 is more interesting as it ensures that there are no sources or sinks in probability space when the system is at equilibrium. This ensures that the update process maintains an equilibrium distribution once the equilibrium has been reached. Although not strictly required to ensure that the simulation is correct, the balance condition is conventionally enforced through requiring that it is satisfied on a term-wise basis, a condition called *detailed balance*:

$$P(i)T(i \to j) = P(j)T(j \to i) \text{ for all } i,j. \tag{2.34}$$

Property 3, which precludes the trapping of the Markov process in a cycle, and Property 4, which ensures that the Markov process doesn't get trapped in a subset of states, force the Markov chain to explore the entirety of the state space. Properties 1-4 together are sufficient to ensure the correctness of the simulation through a Markov process.

Two lemmata are now presented that have important consequences but that shall not be proven in this text. The derivations for these lemmata may be found in [26]. Firstly, we must define some mathematical quantities. If we denote as $\mathcal{H}$ the linear space of all functions $f(s)$ on the set of all states s, then the complementary space of non-stationary functions is given by

$$\mathcal{H}_0 = \left\{ f \in \mathcal{H} \,\middle|\, \sum_s f(s) = 0 \right\}. \tag{2.35}$$

It is also necessary to define the action of the transition probability $T(s \to s')$ through the linear operator T in the space $\mathcal{H}$ as

$$(Tf)(s') = \sum_s f(s)T(s \to s'), \tag{2.36}$$

as well as the norms

$$\|f\|_1 = \sum_s |f(s)|, \tag{2.37}$$

and

$$\|f\| = (f,f)^{1/2}, \tag{2.38}$$

where the scalar product is defined as

$$(f,g) = \sum_s f(s)P(s)^{-1}g(s), \tag{2.39}$$

and where $P(s)$ is the equilibrium distribution.

We may now present the lemmata:

LEMMA 1   *The bound $\|Tf\|_1 \leq \|f\|_1$ holds for all $f \in \mathcal{H}$. Furthermore, if $Tf = f$, there exists $c \in \mathbb{R}$ such that, for all states s, $f(s) = cP(s)$.*

LEMMA 2   *There exists $0 \leq \rho < 1$ such that $\|Tf\| \leq \rho\|f\|$ for all $f \in \mathcal{H}_0$.*

We turn now to a discussion of the statistical properties of the Markov chain. This discussion only makes sense when considering the average properties for a large number of independent chains. As the randomness in the choosing (or proposition) of a new state comes from a sequence of pseudo-random numbers, one considers the practical situation where many simulations are run from the same initial state but with different sequences of random numbers to manufacture the independence of the Markov chains.

If we assume that we have an infinite number of simulations of length N that start from the same initial state, have different sequences of random numbers, and have some transition probability that obeys the conditions of Sec. 2.4.2, then the average of an observable O over the generated states $s_1, s_2, \cdots, s_N$ from a given simulation out of these is given by

$$\overline{O} = \frac{1}{N} \sum_{k=1}^{N} O(s_k). \tag{2.40}$$

If we also consider a function $\phi(s_1, s_2, \cdots, s_N)$ of the states in sequence, then the average of the function over an infinite number of parallel simulations is denoted by $\langle\!\langle \phi \rangle\!\rangle$.

PROBABILITY DISTRIBUTION OF THE STATES   If one considers many parallel and independent simulations with an initial state s_1, the state s_k generated after $k-1$ steps in computer time will differ randomly between the simulations. One may show derive easily the form for the probability $P_k(s) = \langle\!\langle \delta_{ss_k} \rangle\!\rangle$ for an identical s_k and s as

$$P_k(s) = \sum_{s_2, s_3, \cdots, s_{k-1}} T(s_1 \to s_2) T(s_2 \to s_3) \cdots T(s_{k-1} \to s)$$
$$= (T^{k-1} P_0)(s), \qquad P_0(s) = \delta_{ss_1}. \tag{2.41}$$

Considering that the initial probability distribution $P_0 = P + f$, $f \in \mathcal{H}_0$ is formed from the equilibrium distribution along with some non-stationary functions, from property 2, which enforces that the equilibrium distribution is maintained by the transition probability T, and Lemma 2, which ensures that the non-stationary functions will decrease in magnitude upon application of T, $\|Tf\| \leq \rho \|f\|$ where $0 \leq \rho < 1$, it is implied that

$$P_k(s) \underset{k \to \infty}{=} P(s) + \mathcal{O}(e^{-k/\tau_{\mathrm{exp}}}). \tag{2.42}$$

The characteristic time of the exponential decay $\tau_{\mathrm{exp}} = -1/\ln\rho > 0$ is known as the exponential autocorrelation time of the Markov process. For a large number of steps $k \gg \tau_{\mathrm{exp}}$, one may assume that the system has reached the equilibrium state, at which point, the system is thermalised, as it may be said to have forgotten the initial state s_1.

CALCULATION OF EXPECTATION VALUES   Because the observable $O(s)$ is a function of the states on which it is measured, as the states fluctuate according to their probability distribution, so the value of O averaged over the sequence of states $\overline{O}$ of one simulation will fluctuate around the mean value calculated over infinitely many parallel simulations

$$\langle\!\langle \overline{O} \rangle\!\rangle = \frac{1}{N} \sum_{k=1}^{N} \langle\!\langle O(s_k) \rangle\!\rangle = \sum_s O(s) \frac{1}{N} \sum_{k=1}^{N} P_k(s). \tag{2.43}$$

If one substitutes Eq. (2.42) into the above equation and discards the thermalisation phase, dropping the first $k \gg \tau_{\mathrm{exp}}$ measurements, to give only the *measurement phase*, then it is easy to show that

$$\langle\!\langle \overline{O} \rangle\!\rangle = \langle O \rangle. \tag{2.44}$$

Therefore, up to statistical fluctuations, the average of the measured values of an observable over the measurement phase will coincide with the expectation value of the observable.

AUTOCORRELATION FUNCTIONS   As the states in a Markov chain are generated sequentially and each depends on the previous state, there is inevitably some statistical dependence between the states in a given chain. This is quantified through the autocorrelation function

$$\Gamma(t) = \langle\!\langle O(s_k)O(s_{k+t})\rangle\!\rangle - \langle\!\langle O(s_k)\rangle\!\rangle\langle\!\langle O(s_{k+t})\rangle\!\rangle, \tag{2.45}$$

which will be non-zero for correlated states. For a non-negative separation in computing time between two states $t > 0$, after the thermalisation phase, the autocorrelation function will not be dependent on the index $k \gg \tau_{\text{exp}}$ of the state and will have the form

$$\Gamma(t) = \sum_{s_k,s_{k+1},\cdots,s_{k+t}} P(s_k)O(s_k)T(s_k \to s_{k+1})\cdots T(s_{k+t-1})O(s_{k+t}) - \langle O\rangle^2. \tag{2.46}$$

If one notes that the value of an observable O for a system in equilibrium is given by the expectation value plus some non-stationary functions, $P(s)O(s) = P(s)\langle O\rangle + f(s), f \in \mathcal{H}_0$, then we expect from the above expression and Lemma 2 that, at large separations in computer time t, $\Gamma(t) \eqsim e^{-t/\tau_{\text{exp}}}$ decays exponentially. One may therefore assume the independent distribution of two measured values $O(s_i)$ and $O(s_j)$ only if $|i - j| \gg \tau_{\text{exp}}$.

STATISTICAL FLUCTUATIONS   The variance of the measured averages of an observable O on the individual Markov chains around the expectation value $\langle O\rangle$ is given by

$$\langle\!\langle (\overline{O} - \langle O\rangle)^2\rangle\!\rangle = \frac{1}{N^2}\sum_{l,j=1}^{N}\Gamma(|l - j|) = \Gamma(0)\frac{2\tau_{\text{int},O}}{N} + \mathcal{O}(N^{-2}), \tag{2.47}$$

where

$$\tau_{\text{int},O} = \frac{1}{2} + \sum_{t=1}^{\infty}\frac{\Gamma(t)}{\Gamma(0)} \tag{2.48}$$

gives the integrated autocorrelation time associated with O. From the variance we obtain the standard deviation of $\overline{O}$ from the expectation value up to terms of order $N^{-3/2}$,

$$\sigma = \sigma_0\left(\frac{2\tau_{\text{int},O}}{N}\right)^{1/2}, \qquad \sigma_0 = \langle (O - \langle O\rangle)^2\rangle^{1/2}. \tag{2.49}$$

Here, σ_0 is the standard deviation for a single state, if one considers the average over infinitely many parallel simulations. We see from these expressions that the statistical error decreases as $N^{-1/2}$ as the length of the Markov chain increases, and that the *integrated autocorrelation time* $\tau_{\text{int},O}$ decreases the efficiency of the simulation as it multiplies the variance by $2\tau_{\text{int},O}$ where $\tau_{\text{int},O} \geq \frac{1}{2}$. This has the same effect as if the number of configurations were reduced by a factor of $\frac{1}{2\tau_{\text{int},O}}$, and indeed, one may either account for the autocorrelation through separating measurements by discarding a regular number of measurements $\delta t \sim 2\tau_{\text{int},O}$ between those that will be the final measurements, or by using all measurements but adjusting the variance by the factor $2\tau_{\text{int},O}$. Methods of measuring the autocorrelation time will be discussed later in Sections E.2 and E.3.

2.4.3 *Hybrid Monte Carlo*

We will now explore the method for the update of the gauge field, in which the gauge fields are proposed new values according to the transition probability. In the case of a theory that only includes the gauge field, this update may be done on the links one-by-one. When fermions are included in the picture, this becomes impractical as there is a non-local dependence of the fermion determinants of the functional integral upon the gauge field. This would mean

that, in order to update the gauge fields through a one-link update algorithm, one would require a computational effort of order $\mathcal{O}(N^2)$. Happily, there exist algorithms such as the Hybrid Monte Carlo (HMC) algorithm, that update the links simultaneously while preserving important qualities of the system. We note that in this section of the text, the action $S(U)$ is assumed to be differentiable and real, and refers to a general action that could be non-local.

The first step of the HMC algorithm is the molecular dynamics evolution. This is initiated by the introduction of an $\mathfrak{su}(3)$-valued field that acts as the *canonical momentum*,

$$\pi(x,\mu) = \pi^a(x,\mu)T^a, \qquad \pi^a(x,\mu) \in \mathbb{R}. \tag{2.50}$$

The Hamiltonian of the theory is then given by

$$H(\pi,U) = \frac{1}{2}(\pi,\pi) + S(U), \qquad (\pi,\pi) = \sum_{x,\mu} \pi^a(x,\mu)\pi^a(x,\mu). \tag{2.51}$$

It is worth noting here that the canonical momenta are drawn at random from a Gaussian probability distribution $e^{-(\pi,\pi)}$. The physics of the theory do not change with this introduction, as the action and observable O still only depend upon the gauge links,

$$\int \mathcal{D}[U]O(U)e^{-S(U)} = \text{constant} \times \int \mathcal{D}[U]\mathcal{D}[\Pi]O(U)e^{-H(\pi,U)}. \tag{2.52}$$

However, this represents a change in the theory from Lagrangian to Hamiltonian mechanics, in which the evolution of the system is determined by Hamilton's equations, which for the above-described system are given by

$$\dot{\pi}(x,\mu) = -F(x,\mu), \qquad F^a(x,\mu) = \left.\frac{\partial S(e^\omega U)}{\partial \omega^a(x,\mu)}\right|_{\omega=0}, \tag{2.53a}$$

$$\dot{U}(x,\mu) = \pi(x,\mu)U(x,\mu). \tag{2.53b}$$

Here, the time-derivative denoted by a dot above the differentiated quantity is specifically a derivative with respect to computer time.

We may systematise the molecular dynamics step of the HMC algorithm by breaking it down into substeps:

- Before each evolution, the conjugate momenta are sampled anew from a Gaussian distribution.

- The evolution is carried out through the numerical integration of these equations from $t = 0$ up to some predefined value of this computer time, τ, not to be confused with the autocorrelation time discussed earlier. This evolution forms a trajectory in field space that is uniquely dependent on the initial values of the fields.

- When the evolution is complete, the final value of the evolution of the gauge-field U_τ is proposed as the new gauge-field value U'.

For a fixed τ, and assuming acceptance of the proposed gauge-field $U' = U_\tau$, this molecular dynamics step corresponds to the transition probability

$$T(U \to U') = \frac{1}{Z_\pi} \int \mathcal{D}[\pi]e^{-(\pi,\pi)/2} \prod_{x,\mu} \delta(U'(x,\mu), U_\tau(x,\mu)). \tag{2.54}$$

Here, the Dirac δ-function is that which corresponds to the integration measure for the gauge fields, and the correct normalisation of the transition probability is ensured by the momentum partition function Z_π.

14

It may be proven, not only that the four conditions on the transition probabilities are satisfied by Eq. (2.54), but that the above transition probability preserves important quantities such as the Hamiltonian and the phase space integration measure. As the molecular dynamics equations are invariant under time reversal, the transformation of the phase space that the molecular dynamics evolution induces is also reversible. This is important for the fulfilment of the detailed balance condition. The introduction of the Gaussian-distributed canonical momenta also increases the rate at which the system may escape any particular subspace of states.

In practice, the only possible integration of the molecular dynamics equations is numerical integration. This is performed by the division of the time interval $[0, \tau]$ into N_0 steps of length ϵ. Some discrete integration rule is then used, provided that it gives the correct result as $\epsilon \to 0$.

The Taylor expansions of the molecular dynamics equations given in Eq. (2.53a) are given by

$$\pi_{t+\epsilon} = \pi_t - \epsilon \, F|_{U=U_t} + \mathcal{O}(\epsilon^2), \tag{2.55}$$

$$U_{t+\epsilon} = U_t + \epsilon \pi_t U_t + \mathcal{O}(\epsilon^2), \tag{2.56}$$

for some small ϵ. These may be used to construct integration schemes

$$\mathcal{I}_0(\epsilon): \quad \pi, U \to \pi - \epsilon F, U; \tag{2.57a}$$

$$\mathcal{I}_U(\epsilon): \quad \pi, U \to \pi, e^{\epsilon \pi} U, \tag{2.57b}$$

that, used in the combination known as the *leapfrog integrator* $\mathcal{I}_0(\frac{1}{2}\epsilon)\mathcal{I}_U(\epsilon)\mathcal{I}_0(\frac{1}{2}\epsilon)$, evolve the system between t and $t + \epsilon$ up to errors of order ϵ^3. From these incremental steps, the full integration from $t = 0$ to $t = \tau$ consists of the application to the initial fields U, π of the product

$$\mathcal{J}_0(\epsilon, N_0) = \left\{ \mathcal{I}_0 \left(\frac{1}{2}\epsilon \right) \mathcal{I}_U(\epsilon) \mathcal{I}_0 \left(\frac{1}{2}\epsilon \right) \right\}^{N_0}, \qquad \epsilon = \frac{\tau}{N_0}. \tag{2.58}$$

It is easy to show that this integrator is invertible

$$\mathcal{J}_0(-\epsilon, N_0)\mathcal{J}_0(\epsilon, N_0) = 1, \tag{2.59}$$

and that it conserves the integration measure $\mathcal{D}[\pi]\mathcal{D}[U]$, therefore preserving important qualities of the HMC method.

This numerical integration, however, does not preserve the Hamiltonian due to the discreteness of the integration path. Generally, for fixed ϵ,

$$\Delta H(\pi, U) = \{H(\pi_\tau, U_\tau) - H(\pi_0, U_0)\}_{\pi_0 = \pi, U_0 = U} \tag{2.60}$$

is non-vanishing. This leads also to the breaking of the balance condition.

In order to rectify these problems, an additional step is added at the end, in order to complete the HMC method. The proposed gauge-field value is accepted with the probability

$$P_{\mathrm{acc}}(\pi, U) = \min \left\{ 1, e^{-\Delta H(\pi, U)} \right\}, \tag{2.61}$$

instead of the unconditional acceptance we had assumed earlier. If not accepted, the previous gauge field is set as the current value in the Markov chain, $U' = U$. This modification gives the resulting transition probability density

$$T(U \rightarrow U') = \frac{1}{Z_\pi} \int \mathcal{D}[\pi] e^{(\pi,\pi)/2} \{ P_{\mathrm{acc}}(\pi, U) \prod_{x,\mu} \delta(U'(x,\mu), U_\tau(x,\mu)) - $$
$$(1 - P_{\mathrm{acc}}(\pi, U) \prod_{x,\mu} \delta(U'(x,\mu), U(x,\mu))) \}. \tag{2.62}$$

As long as the integrator preserves the integration measure and is reversible in time, this transition probability may be shown to possess the properties required of valid transition probabilities. A compromise must be found between the number of steps N_0 used to divide each trajectory, which determines roughly linearly the computing time required for integration, and the acceptance probability, which decreases with increased ϵ as the numerical integration becomes less accurate, in order to improve the computational efficiency of the simulation.

2.5 REDUCTION OF DISCRETISATION EFFECTS THROUGH IMPROVEMENT

A fundamental step in obtaining physically relevant predictions from lattice gauge theory is the extrapolation to the continuum limit. Unfortunately, a limiting factor in the approach to the continuum limit is the increased computational resources required to simulate a lattice with a smaller lattice spacing at a given volume. A large scaling violation arises from the combined use of the Wilson fermion action and plaquette gauge action that can make the accurate and precise determination of, for instance, continuum-limit hadron masses impracticable from reasonably large lattices.

This problem may be alleviated through the addition of terms to the action or other operators, while of course obeying the required symmetries of the action or operator they are being added to, that reduce the scaling violation; this technique is called *improvement*. In particular, the Symanzik improvement procedure follows the steps:

- The quantity that one wishes to improve is expressed as a discretised expression.

- Correction terms obeying the correct symmetries and dimension are selected, and are expressed in continuum language.

- Discretised versions of the correction terms are developed and are added to the original quantity with coefficients chosen such that discretisation errors up to a certain order vanish.

In our project, improvement is used on both the quark action, by adding Sheikholeslami-Wohlert terms, otherwise known as clover terms, which give $\mathcal{O}(a)$ improvement to the Wilson-Dirac operator, as well as on the SU(3) gauge action, where the Luescher-Weisz action is used to give tree-level improvement.

2.5.1 *Gauge actions*

While the improvement of both gauge actions is possible through the construction of the openQ*D code, we will focus here only on the SU(3) gauge action, as we use the standard U(1) plaquette gauge action given in Eq. (3.61b).

The SU(3) gauge action may be written quite generically as

$$S_{G,\mathrm{SU}(3)} = \frac{\omega_{\mathrm{C}^*}}{g^2} \sum_{k=0}^{1} c_k^{\mathrm{SU}(3)} \sum_{\mathcal{C} \in \mathcal{S}_k} \mathrm{tr}[1 - U(\mathcal{C})], \tag{2.63}$$

where the SU(3) parallel transports on a lattice-defined path $\mathcal{C}$ are denoted by $U(\mathcal{C})$. The weight constant ω_{C^*} depends on the spatial boundary conditions, taking the value 1 in the case of no C* boundary conditions and $1/2$ if C* boundary conditions are used, in order to account for the double counting introduced through summing the loops over both the physical and mirror lattice. The set of all oriented plaquettes and the set of all oriented 1×2 planar loops are given respectively by $\mathcal{S}_0$ and $\mathcal{S}_1$. The respective coefficients for these terms must satisfy $c_0 + 8c_1 = 1$. In particular, the tree-level improved Symanzik action, otherwise known as the Luescher-Weisz action, that we use in our simulations corresponds to $c_0 = \frac{5}{3}$, while the unimproved Wilson action corresponds to $c_0 = 1$. Finally, the bare gauge couplings, g in the case of SU(3) and e_0 in the case of U(1), are related to the bare inverse SU(3) gauge coupling β and the bare fine-structure constant α through

$$\beta = \frac{6}{g^2}, \qquad \alpha = \frac{e_0^2}{4\pi}. \tag{2.64}$$

2.5.2 *Wilson-Dirac operator*

The Wilson-Dirac operator in the openQ*D code is formed of the following components,

$$D = m + D_{\mathrm{w}} + \delta D_{\mathrm{sw}} + \delta D_{\mathrm{b}}, \tag{2.65}$$

where m is the bare quark mass, D_{w} is the unimproved Wilson-Dirac operator as defined above, δD_{sw} is the clover term and δD_{b} is an $\mathcal{O}(a)$-improvement term accounting for the temporal boundaries. As we are using periodic temporal boundary conditions, $\delta D_{\mathrm{b}} = 0$ for our simulations.

The Sheikholeslami-Wohlert improvement term for the Wilson-Dirac operator is given by

$$\delta D_{\mathrm{sw}} = c_{\mathrm{sw}}^{\mathrm{SU(3)}} \sum_{\mu,\nu=0}^{3} \frac{i}{4} \sigma_{\mu\nu} \hat{G}_{\mu\nu} + q c_{\mathrm{sw}}^{\mathrm{U(1)}} \sum_{\mu,\nu=0}^{3} \frac{i}{4} \sigma_{\mu\nu} \hat{F}_{\mu\nu}, \tag{2.66}$$

where q is the physical quark electric charge expressed in units of e; with this normalisation, $c_{\mathrm{sw}}^{\mathrm{U(1)}} = 1$ corresponds to tree-level. The U(1) field tensor used is given by

$$\hat{F}_{\mu\nu}(x) = \frac{i}{4q_{\mathrm{el}}} \mathrm{Im}\Big\{ z_{\mu\nu}(x) + z_{\mu\nu}(x - \hat{\mu}) + z_{\mu\nu}(x - \hat{\nu}) \tag{2.67a}$$
$$+ z_{\mu\nu}(x - \hat{\mu} - \hat{\nu}) \Big\},$$
$$z_{\mu\nu}(x) = z(x,\mu) z(x + \hat{\mu}, \nu) z(x + \hat{\nu}, \mu)^{\dagger} z(x, \nu)^{\dagger}, \tag{2.67b}$$

and is normalised such that, in the naive continuum limit, the canonically-normalised field tensor is retrieved through taking $-ie_0 \hat{F}_{\mu\nu}(x)$. Similarly, the SU(3) field tensor used in this context is given by

$$\hat{G}_{\mu\nu}(x) = \frac{1}{8} \big\{ Q_{\mu\nu,\mathrm{cl}}(x) + Q_{\nu\mu,\mathrm{cl}}(x) \big\}, \tag{2.68a}$$
$$Q_{\mu\nu,\mathrm{cl}}(x) = U(x,\mu) U(x + \hat{\mu}, \nu) U(x + \hat{\nu}, \mu)^{-1} U(x,\mu)^{-1} \tag{2.68b}$$
$$+ U(x,\nu) U(x - \hat{\mu} + \hat{\nu}, \mu)^{-1} U(x - \hat{\mu}, \nu)^{-1} U(x - \hat{\mu}, \mu)$$
$$+ U(x - \hat{\mu}, \mu)^{-1} U(x - \hat{\mu} - \hat{\nu}, \nu)^{-1} U(x - \hat{\mu} - \hat{\nu}, \mu) U(x - \hat{\nu}, \nu)$$
$$+ U(x - \hat{\nu}, \nu)^{-1} U(x - \hat{\nu}, \mu) U(x + \hat{\mu} - \hat{\nu}, \nu) U(x,\mu)^{-1}.$$

As such, both field tensors are constructed in terms of the clover plaquette.

Values for the improvement coefficients chosen for our simulations are given in Sec. 4.1.

2.6.1 *The running coupling and the continuum limit*

The quantities that appear in the action integral, such as the gauge coupling g or the quark mass m, are numbers that cannot be measured directly through physical observations. These parameters are referred to as *bare* parameters, and their values in physical units may only be found through the identification of physical observables, such as the hadron masses, in the theory with their experimentally determined values.

Lattice actions may differ in many respects, such as the choice of the discretisation of the derivative or the structure of the lattice. The observables calculated using these different choices for the lattice action must all converge, however, to the physical values of the observable when the physical point is reached, which involves taking the limit of the lattice spacing $a \to 0$, the so-called *continuum limit*. At the physical point, therefore, the observable predicted from theory should be independent of the value of a. This implies that generally the values of the bare parameters will vary as functions of a, as $g(a), m(a)$.

The mathematical formalism for dealing with the *running* of the bare parameters is called the *renormalisation group*. Considering for simplicity the example of a pure gauge theory, which has only one bare parameter, the gauge coupling $g(a)$, the requirement that the physical observable $P(g(a), a)$ reach the constant value P_0 at the physical point in the continuum limit is expressed mathematically as

$$\lim_{a \to 0} P(g(a), a) = P_0. \tag{2.69}$$

This requirement was formulated as a differential equation by Callan and Symanzik, to give the *renormalisation group equation*,

$$\frac{dP(g,a)}{d\ln a} = \left(\frac{\partial}{\partial \ln a} + \frac{\partial g}{\partial \ln a} \frac{\partial}{\partial g} \right) P(g,a) = \mathcal{O}((a/\xi)^2 \ln(a/\xi)). \tag{2.70}$$

Here, the right hand side is an artifact of the lattice system, where ξ is the correlation length. By convention, the coefficient of the second partial derivative term is called the β-function, and is not to be confused with the inverse gauge coupling. It is defined as

$$\beta(g) \equiv -\frac{\partial g}{\partial \ln a}, \tag{2.71}$$

and gives the relationship of g on a up to an integration constant. For the rest of this section, β will refer to the inverse gauge coupling, whereas the above object will be referred to explicitly as the β-function. Using perturbation theory for the determination of the coefficients, an expansion of the β-function may be made in terms of powers of g around $g = 0$, the form of which, given the rather general example of an $SU(N)$ theory with n_f massless quarks, is given by

$$\beta(g) = -\beta_0 g^3 - \beta_1 g^5 + \mathcal{O}(g^7), \tag{2.72}$$

$$\beta_0 = \frac{1}{(4\pi)^2} \left(\frac{11}{3} N - \frac{2}{3} n_f \right), \tag{2.73}$$

$$\beta_1 = \frac{1}{(4\pi)^4} \left(\frac{34}{3} N^2 - \frac{10}{3} N n_f - \frac{N^2 - 1}{N} n_f \right). \tag{2.74}$$

The coefficients of $\beta(g)$ generally depend upon the regularisation scheme, the exception being β_0 and β_1 which are universal. Separation of variables may be used to solve the above β-function differential to give $a(g)$ in terms of g and the β−function coefficients,

$$a(g) = \frac{1}{\Lambda_L}(\beta_0 g^2)^{-\beta_1/2\beta_0} \exp\left(-\frac{1}{2\beta_0 g^2}\right)(1 + \mathcal{O}(g^2)). \tag{2.75}$$

The inversion of this equation gives the *running coupling*, an expression of the gauge coupling in terms of the lattice spacing,

$$g(a)^{-2} = \beta_0 \ln(a^{-2}\Lambda_L^{-2}) + \frac{\beta_1}{\beta_0}\ln(\ln(a^{-2}\Lambda_L^{-2})) + \mathcal{O}(1/\ln(a^2\Lambda_L^2)). \tag{2.76}$$

In order to obtain a constant value of a physical observable at the physical point, implying independence from the procedure of scale-fixing, the value of the bare parameter $g(a)$ must change with respect to a according to the above equation. The choices of regularisation scheme and lattice action affect the value of Λ_L, however, a 1-loop perturbative calculation may be used in order to relate the different Λ_L values exactly through their ratios. In general, Eq. (2.76) gives a gauge coupling that, in the limit of vanishing lattice spacing, also vanishes. This is referred to as *asymptotic freedom*, and is a central characteristic of QCD.

The naive continuum limit involves simply taking $a \to 0$ whilst requiring that, when this limit is taken, objects such as the discretised action on the lattice take on the same values as their continuum equivalent. However, the evaluation of the path integral is necessary for obtaining measurements from a fully quantised theory, and produces observables that vary as functions of a, which complicates or makes impossible this approach. An alternative, and the conventional method, is to drive the system into phase transition by pushing the gauge couplings to their critical values. During this phase transition, the physical scales, including length scales such as the proton size, become large with respect to the lattice units, which effectively leads to ever-increasing lattice resolution.

We see from Eq. (2.76) that taking the limit $a \to 0$ corresponds to taking the limit $g \to 0$. Given the definition of the inverse coupling, $\beta = 6/g^2$, we can therefore define the true continuum limit through taking the inverse coupling to infinity,

$$\beta \to \infty. \tag{2.77}$$

This is easier said than done, though, as this limit shrinks the lattice to a vanishing physical size, unless the numbers of lattice points is increased. This matter will be discussed in the next subsection.

As a quick example, the hadron masses M are known to have corrections that are dependent on the lattice spacing,

$$M(a) = M_{\text{phys}}(1 + \mathcal{O}(a^\alpha)), \tag{2.78}$$

where α is some real number that depends on the particular action used; for example, the contribution from finite lattice spacing can be shown to be quadratic for the Wilson fermionic action [27], whereas the dependence is weaker when improvement of the fermionic action is used [28].

When moving from QCD to QCD+QED, the continuum limit does not strictly exist, at least in the perturbation theory, as QED contains a Landau pole at vanishing length scales that renders the theory trivial. In the perturbative regime of QED, however, which is relevant at typical hadronic energies and is therefore the regime in which we perform our simulations, the continuum limit exists and is universal at every fixed order in the fine-structure constant.

2.6.2 *Thermodynamic limit*

The *thermodynamic limit*, or infinite volume limit, is defined as

$$N_L \to \infty, \quad N_T \to \infty, \tag{2.79}$$

where N_L is the lattice length in terms of number of points in the spatial dimensions, and N_T is the length in terms of the number of points in the temporal dimension. In principle, before taking the continuum limit described above, the above thermodynamic limit should be taken. This is not practical, however, given the increased computational effort associated with taking this limit.

Instead, the physical observables are calculated for a few different values of β, and therefore for a few different values of a, while keeping the physical volume, usually $L_T \times L^3$, constant, where

$$L = aN, \quad L_T = aN_T. \tag{2.80}$$

A scaling analysis is then performed, in which the dependence of the physical observables on a is analysed and the true continuum limit determined through extrapolation. Here, a naive parametrisation may be used, for instance, in terms of $1/L$, or this extrapolation may be theory-based. This procedure is then carried out on different lattice sizes, after which, extrapolation may be used to obtain the infinite physical volume (continuum) limit.

The convention in spectroscopy studies is to use lattices for which the temporal extent is significantly larger than the spatial extent. This allows one to neglect effects due to the finite time extent, so that leading finite size effects come from the limited spatial extent. A source of finite volume effects, relevant in QCD for observables with a single stable hadron in external states, comes from interactions involving particles travelling around the spatial torus. This produces a contribution of magnitude $\mathcal{O}(\exp(-\alpha L))$, where α is some real constant with units of mass. Finite-volume effects will be more severe for excited states with larger spatial extent, and for QCD+QED, as QED is a long-range interaction.

2.6.3 *Physical quark masses*

Often, quark masses are used that are much greater than the physical values, with the physical point being approached through extrapolation to the physical quark masses. This is done in order to make the simulations less expensive and to avoid somewhat the presence of exceptional configurations that can cause the numerical inversion of the Dirac operator to break down. For these reasons, greater than physical quark masses have been used in our simulations.

QCD+QED IN THE C* FORMULATION

3.1 C* CONSTRUCTION: GENERAL PRINCIPLES AND TECHNICAL DETAILS

In the following section, we will be considering a continuum but finite-sized formulation of QED_C that exists on a torus with C* boundary conditions and physical length L in all spatial directions and arbitrary boundary conditions in the temporal direction of dimension T. These may include: open, periodic, Schrodinger Functional (SF), or open-SF.

In Appendix A, two approaches for the C* formulation on the lattice, the C-even construction and the orbifold construction, are explored and related to each other. In our work we have chosen to use the orbifold construction; however, understanding the two constructions allows one to have an alternative way to check the formulation. In particular, when using C* boundary conditions, as the momentum eigenstates are automatically eigenstates of the charge conjugation operator, it is necessary for the projection to zero-momentum that the correlators be C-even. It is in fact sufficient for the calculation of C-even correlators to take the global sum over both the physical and mirror lattice at the sink; C-odd components in the source field then vanish. This is demonstrated in the case of the meson and has been checked for our implementation of the C* formulation in the case of a unit gauge field, however, this logic holds generically. In our calculations, therefore, the sum over sink position in the correlators has been taken to extend over both the physical and the mirror lattice.

In the QED_C formulation, the total action is given by

$$S[A, \psi] = \int_{L^3 T} d^4 x \left\{ \frac{1}{4e^2} F_{\mu\nu} F_{\mu\nu} + \sum_{f=1}^{N_f} \overline{\psi_f} (\gamma_\mu \overset{\leftrightarrow}{D}{}^f_\mu + m_f) \psi_f \right\}, \tag{3.1}$$

where the U(1) field strength tensor denoted by $F_{\mu\nu}$ and the covariant derivative $\overset{\leftrightarrow}{D}{}^f_\mu$ are given by

$$F_{\mu\nu} = \partial_\mu A_\nu(x) - \partial_\nu A_\mu(x), \tag{3.2a}$$

$$\overset{\leftrightarrow}{D}{}^f_\mu = \overset{\leftrightarrow}{\partial}_\mu - iq_f A_\mu. \tag{3.2b}$$

Here the operator $\overset{\leftrightarrow}{\partial}_\mu = \frac{1}{2}(\overset{\rightarrow}{\partial}_\mu - \overset{\leftarrow}{\partial}_\mu)$ where the partial derivative $\overset{\rightarrow}{\partial}$ acts to the right and $\overset{\leftarrow}{\partial}$ acts to the left.

C* boundary conditions are designed such that a translation of a period $\hat{L}_i$ in a direction i that has C* boundary conditions is equivalent to charge conjugation. This is expressed as

$$A_\mu(x + \hat{L}_i) = A_\mu^{\mathcal{C}}(x) = -A_\mu(x), \tag{3.3a}$$

$$\psi_f(x + \hat{L}_i) = \psi_f^{\mathcal{C}}(x) = C^{-1} \overline{\psi}_f^T(x), \tag{3.3b}$$

$$\overline{\psi}_f(x + \hat{L}_i) = \overline{\psi}_f^{\mathcal{C}}(x) = -\psi_f^T(x) C, \tag{3.3c}$$

The charge–conjugation matrix C used here must be invertible, have a determinant of unity, and must obey

$$C^{-1} \gamma_\mu^T C = -\gamma_\mu. \tag{3.4}$$

A four-by-matrix does exist with these properties that also satisfies

$$C^T = -C, C^\dagger = C^{-1}, \tag{3.5}$$

regardless of the particular chosen gamma matrix representation. In this work, we choose the representation $C = i\gamma^0\gamma^2$.

We note that the action density of $\mathrm{QED_C}$ is invariant under charge–conjugation, as its formula given in Eq. (3.1) is identical to that of the infinite volume action density. We also note that this means that it must be periodic in space as the spatial shift by a period is equivalent to charge conjugation in this formulation.

3.2 GAUGE TRANSFORMATIONS

$U(1)$ gauge transformations in $\mathrm{QED_C}$ are defined as

$$A_\mu^{[\alpha]}(x) = A_\mu(x) + \partial_\mu\alpha(x), \tag{3.6a}$$

$$\psi_f^{[\alpha]}(x) = e^{iq_f\alpha(x)}\psi_f(x), \tag{3.6b}$$

$$\overline{\psi}_f^{[\alpha]}(x) = e^{-iq_f\alpha(x)}\overline{\psi}_f(x). \tag{3.6c}$$

By considering how a translation $\hat{L}_i$ along a spatial direction by a period affects the transformed fields, we can determine the form of the gauge transformation that obeys the C^* boundary conditions and is therefore permissible. Starting with the $U(1)$ compact gauge field A_μ, the transformed and translated field has the form

$$
\begin{aligned}
A_\mu^{[\alpha]}(x + \hat{L}_i) &= A_\mu(x + \hat{L}_i) + \delta_\mu\alpha(x + \hat{L}_i) \\
&= -A_\mu(x) + \delta_\mu\alpha(x + \hat{L}_i) = -A_\mu^{[\alpha]}(x) + \delta_\mu[\alpha(x + \hat{L}_i) + \alpha(x)].
\end{aligned}
\tag{3.7}
$$

We require that the $U(1)$ field be anti-periodic; we must therefore impose the condition on the gauge transformation that

$$\delta_\mu\alpha(x + \hat{L}_i) = -\delta_\mu\alpha(x), \tag{3.8}$$

which limits the form of the gauge transformation to $\alpha(x) = \beta(x) + \gamma$, where $\beta(x) = -\beta(x)$ is some anti-symmetric function and γ is a generic constant.

This can be refined further if we consider the translation of a transformed fermion field in the same manner,

$$
\begin{aligned}
\psi_f(x + \hat{L}_i) &= e^{iq_f\alpha(x + \hat{L}_i)}\psi_f(x + \hat{L}_i) \\
&= e^{iq_f\alpha(x + \hat{L}_i)}C^1\overline{\psi}_f^T(x) = e^{iq_f[\alpha(x + \hat{L}_i) + \alpha(x)]}C^1[\overline{\psi}^\alpha]_f^T(x).
\end{aligned}
\tag{3.9}
$$

Requiring that this field satisfy C^* boundary conditions, we find that

$$\alpha(x) = \beta(x) + \frac{n_f\pi}{q_f}. \tag{3.10}$$

As we are concerned with quarks, whose charge can be expressed as integer multiples of the fundamental unit of charge $q_{\mathrm{el}} = e/3$, the boundary conditions for all fields are respected iff there exists an integer n that obeys

$$\alpha(x) = \beta(x) + \frac{n\pi}{q_{\mathrm{el}}}. \tag{3.11}$$

If we define for each space-time point a gauge transformation that has the form of a transformation on the compact U(1) group, $\Lambda(x) = e^{iq_{\mathrm{el}}\alpha(x)}$, then the matter field of flavour f at that point transforms, according to an irreducible representation of the U(1) gauge group, with $\Lambda(x)^{\hat{q}_f}$, where q_f is the charge associated with the matter field and $\hat{q}_f = q_f/q_{\mathrm{el}}$, i.e. expressed in terms of some fundamental unit of charge q_{el}.

We can choose alternatively to view this in terms of operators; defining the operator for the electric charge as Q, the global gauge transformation generator has the form $\hat{Q} = \frac{Q}{q_{\mathrm{el}}}$, with entirely integer-valued eigenvalues. The U(1) group of global gauge transformations is broken by C* boundary conditions into $\mathcal{Z}_2$, as the sole global gauge transformations permitted under the form Eq. (3.11) are $\Lambda = \pm 1$. This implies that, under C* boundary conditions, electric charge Q is violated while the quantum number $(-1)^{\hat{Q}}$ is conserved.

We shall now define what is meant by certain terms in the context of C* boundary conditions in this thesis. As it is evident that the group of gauge transformations is disconnected and split into sectors characterised by the integer n, *local gauge transformations* are meant to signify those transformations that are continuously connected to the identity, i.e. where $n = 0$ and $\alpha(x) = \beta(x)$ is therefore anti-symmetric. *Large gauge transformations* are defined as the combination of a global and a local gauge transformation.

3.3 TRANSLATIONS

Under C* boundary conditions, translational invariance and charge conjugation are preserved. Momentum and charge conjugation are linked through the definition of C* boundary conditions given in Eq. (3.3a), unlike for an infinite volume.

If we consider a generic field, we see that by definition of the C* boundary conditions

$$\phi(x + \hat{L}_i) = C^{-1}\overline{\phi}^T(x) = \phi^{\mathcal{C}}(x), \tag{3.12}$$

i.e. that translation of a field by a period in a spatial direction i is equivalent to its charge conjugation. This allows us to define the C-even and C-odd components of the generic field $\phi(x)$ as

$$\phi_{\pm} = \frac{\phi(x) \pm \phi^{\mathcal{C}}(x)}{\sqrt{2}}. \tag{3.13}$$

Substitution of Eq. (3.12) shows that $\phi(x)_{\pm}$ is (anti-)periodic in space. This means that the components necessarily have different representations in Fourier space. Expanding the fields in the time-momentum Fourier representation allows one the freedom of arbitrary temporal boundary conditions,

$$\phi_{\pm}(x) = \frac{1}{L^3} \sum_{\mathbf{p} \in \Pi_{\pm}} \tilde{\phi}_{\pm}(x_0, \mathbf{p}) e^{i\mathbf{p}\mathbf{x}}, \tag{3.14}$$

where $\Pi_{\pm}$ is the set of (anti-)periodic momenta,

$$\Pi_{+} = \left\{ \frac{2\pi}{L}\mathbf{n} \quad | \quad \mathbf{n} \in \mathbb{Z}^3 \right\}, \tag{3.15a}$$

$$\Pi_{-} = \left\{ \frac{\pi}{L}(2\mathbf{n} + \overline{\mathbf{n}}) \quad | \quad \mathbf{n} \in \mathbb{Z}^3, \quad \overline{\mathbf{n}} = (1,1,1) \right\}. \tag{3.15b}$$

In this manner, the fermion fields $\psi_{f,\pm}(x)$ can be expressed as

$$\psi_{f,\pm}(x) = \frac{1}{L^3} \sum_{\mathbf{p} \in \Pi_{\pm}} \tilde{\psi}_{f,\pm}(x_0, \mathbf{p}) e^{i\mathbf{p}\mathbf{x}}, \tag{3.16}$$

the (anti-) Majorana condition being satisfied by the components $\psi_{f,\pm}$ of the fermion fields,

$$\psi_{f,\pm}(x) = \pm C^{-1}[\overline{\psi}_{f,\pm}](x). \tag{3.17}$$

In contrast, however, the compact U(1) gauge field $A_\mu(x)$ has only the anti-periodic set of momenta, and is therefore C-odd;

$$A_\mu(x) = \frac{1}{L^3} \sum_{\mathbf{p} \in \Pi_-} \tilde{A}_\mu(x_0, \mathbf{p}) e^{i\mathbf{p}\mathbf{x}}. \tag{3.18}$$

3.4 PARITY

With an appropriate choice of parity operator, we have the properties:

$$A_0(x) \rightarrow A_0(x_P), \tag{3.19a}$$

$$A_k(x) \rightarrow -A_k(x_P), \tag{3.19b}$$

$$\phi_f(x) \rightarrow \eta_P \gamma_0 \phi_f(x_P), \tag{3.19c}$$

$$\overline{\phi}_f(x) \rightarrow \eta_P^* \overline{\phi}_f(x_P) \gamma_0, \tag{3.19d}$$

where $x_P = (x_0, -\mathbf{x})$. Here, η_P, a generic complex phase in infinite space, can be chosen freely, and each choice defines a distinct parity operator. We set aside the standard choice of $\eta_P = 1$, as the parity operator $\mathcal{P}$ thus defined doesn't commute with the charge conjugation operator $\mathcal{C}$ with which the C* boundary conditions are defined. The choice of i, however, can be easily seen to give a parity operator that commutes with our charge conjugation operator. Using the fermion field $\psi_f(x)$ as an example,

$$\psi_f(x) \xrightarrow{\mathcal{C}} C^{-1}\overline{\psi}_f^T(x) \xrightarrow{\mathcal{P}} -iC^{-1}\gamma_0^T\overline{\psi}_f^T(x_P), \tag{3.20a}$$

$$\psi_f(x) \xrightarrow{\mathcal{P}} i\gamma_0\psi_f(x_P) \xrightarrow{\mathcal{C}} i\gamma_0 C^{-1}\overline{\psi}_f^T(x_P) = -iC^{-1}\gamma_0^T\overline{\psi}_f^T(x_P), \tag{3.20b}$$

where we have used that $C^{-1}\gamma_0^T C = -\gamma_0$. Similar checks can be carried out for the other fields. This commutation shows that parity is conserved by C* boundary conditions.

One can also show that the action under C* boundary conditions is invariant under $\mathcal{P}$, therefore in finite volume parity represents an exact symmetry. This knowledge facilitates the construction of operators that describe definite-parity states.

3.5 FLAVOUR SYMMETRIES

Flavour, and thus charge conservation, are violated in C* boundary conditions by charged particles that travel once around the torus, changing into their anti-particles. More precisely, flavour is violated if the winding number $\sum_{i=1}^{3} n_i$ is odd, where n_i is the number of times the particle travels around the torus in direction i. Propagators constructed from a source on the physical lattice and a sink on the mirror lattice, or vice versa, are the cause of the charge-violating flavour violation due to their sensitivity to C* boundary conditions. Whilst these terms vanish in infinite volume, they cause a charge violation of $\Delta Q = \pm 2$. This means that the electric charge is not conserved, although the quantum number $(-1)^{\tilde{Q}}$ is. This leads to a mixing with time between all valid states with odd electric charge, and a separate mixing of all valid states with even electric charge.

As the violation is caused by the motion of charged particles around the torus, these violating effects are suppressed exponentially as

$$\langle \psi(x)\psi^T(y) \rangle \sim \langle \overline{\psi}^T(x)\overline{\psi}(y) \rangle \sim \left(\frac{m}{L}\right)^{\frac{3}{2}} e^{-mL} \tag{3.21}$$

for $L \to \infty$. Moving to the case of N_f flavours, the above argument is generalised with

$$Q = \sum_{f=1}^{N_f} q_f F_f, \tag{3.22}$$

where F_f is the generator of the f-th U(1). This implies a flavour violation of $\Delta F_f = 0$ mod 2.

3.6 DEFINING U(1)-GAUGE-INVARIANT INTERPOLATING OPERATORS

This section concerns the construction of electrically charged states that can represent physical observables. For this to be possible, they must be invariant under local gauge transformations. An advantage of using a non-perturbative formulation of U(1) is the complete avoidance of the necessity of gauge-fixing, which would otherwise be required for the intermediate quantities from which physical observables are measured; we do, however, note that gauge-fixing in QED is problem-free.

In order to build states that represent electrically charged physical observables, we must first consider how a naive electrically charged state will transform under a local gauge transformation. For our interpolating operators to be U(1)-gauge-invariant, it is necessary to multiply them by a gauge factor. If we consider the naked matter field to be $\psi(x)$, we can apply a quite generic dressing factor,

$$\Psi_J(x) = e^{iq \int d^4 y A_\mu(y) J_\mu(y-x)} \psi(x), \tag{3.23}$$

where we define J to be some function or distribution that satisfies the condition

$$\partial_\mu J_\mu(x) = \delta^4(x), \qquad J_\mu(x + \hat{L}_i) = -J_\mu(x). \tag{3.24}$$

If we choose the temporal boundary conditions to be periodic, we must require that J_μ be periodic in time also.

If we perform a global transformation on this expression, we find that $\psi(x) \to e^{iq\alpha}\psi(x)$, so that $\Psi_J(x) \to e^{iq\alpha}\Psi_J(x)$. If we were to take the infinite volume limit, this would imply that the electric charge of the operator would be equal to q. However, in finite volume, α is restricted to the values 0 and π/q, implying that the quantum number $\hat{Q}$ of Ψ_J is given by $(-1)^{\hat{Q}} = -1$.

Defining the non-local factor as

$$\Theta(x) = e^{iq \int d^4 y A_\mu(y) J_\mu(y-x)}, \tag{3.25}$$

we can apply a spatially anti-periodic local gauge transformation to give

$$\begin{aligned}
\Theta(x) &\to \Theta(x) e^{iq \int d^4 y \partial_\mu \alpha(y) J_\mu(y-x)} = \Theta(x) e^{iq \int d^4 y \alpha(y) \partial_\mu J_\mu(y-x)}, \\
&= \Theta(x) e^{-iq\alpha(x)}.
\end{aligned} \tag{3.26}$$

One may note that, due to the periodicity of $\alpha(y)J_\mu(y-x)$ with respect to $\mathbf{y}$, and the periodic temporal boundary conditions, integration by parts results in no boundary terms. We therefore see a cancellation of the factors produced between the non-local factor $\Theta(x) \to e^{-iq\alpha(x)}\Theta(x)$

and the naked matter field $\psi(x) \to \psi(x)e^{iq\alpha(x)}$ when a local gauge transformation is applied. Therefore, the multiplication of $\psi(x)$ with a gauge-dressing factor $\Theta(x)$ renders $\Psi_J(x)$ invariant under local gauge transformations.

We thus are able to construct an electrically-charged interpolating operator with quantum number $(-1)^{\hat{Q}} = -1$ that is nonetheless invariant under local gauge transformations. The application of the gauge-dressing factor conserves the boundary conditions, so that one can use the C-even and C-odd Ψ_J components to construct gauge-invariant operators with definite momentum.

It is practical to use a definition of Ψ_J that is proportional to a delta function $\delta(x_0)$ in time centered at time x_0. This locality in time makes the mapping of the operator $\Psi_J(x)$ onto the Hilbert space natural; if we act on this operator onto the vacuum $|0\rangle$ we obtain the state $\Psi_J(x)|0\rangle$, a state which, like the operator $\Psi_J(x)$, is invariant under local gauge-transformations and has the quantum number $(-1)^{\hat{Q}} = -1$. The gauge-invariant Hamiltonian spectrum can then be extracted through the decomposition of the two-point Euclidean correlator $\langle \Psi_J(x)\overline{\Psi}_J(0)\rangle$ in terms of exponential decays. The spectrum depends upon the Hamiltonian of the system described, rather than any temporally-local interpolating operator chosen to probe the system. For this reason, the energy levels are by construction gauge-invariant and independent of the choice of the function J_μ that parametrises the gauge dressing factor. This thesis, when defining the (finite-volume) mass of the charged particle, more specifically refers to the energy of the lightest state that propagates within the Euclidean two-point function. This is taken to become the mass of the charged particle when the infinite-volume limit is taken.

In the case of periodic boundary conditions in all spatial directions, no solutions exist that satisfy the requirements Eq. (3.24), owing to the constraints imposed by Gauss's Law. There are, however, many possible choices of gauge factor that satisfy these requirements in the case of C* boundary conditions. These are represented by different choices of J.

We consider first the Coulomb gauge, which is defined by the conditions

Coulomb gauge:

$$J_0(x) = 0, \tag{3.27a}$$

$$J_k(x) = \delta(x_0)\partial_k\Phi(\mathbf{x}), \tag{3.27b}$$

$$\partial_k\partial_k\Phi(\mathbf{x}) = \delta^3(\mathbf{x}). \tag{3.27c}$$

Here $x = (x_0, \mathbf{x})$ and $\Psi(\mathbf{x})$ is anti-periodic. If we choose to represent $\Phi(\mathbf{x})$ in terms of the heat-kernel, then the operator $\Psi_J = \Psi_{\mathbf{c}}$ has the form

$$\Phi(\mathbf{x}) = -\frac{1}{L^3}\int_0^\infty du \sum_{\mathbf{p}\in\Pi_-} e^{-u\mathbf{p}^2 + i\mathbf{p}\mathbf{x}}; \tag{3.28a}$$

$$\Psi_{\mathbf{c}}(x) = e^{-iq\int d^3y \partial_k A_k(x_0,\mathbf{y})\Phi(\mathbf{y}-\mathbf{x})}\psi(x). \tag{3.28b}$$

We note that, in the Coulomb gauge, $\partial_k A_k = 0$ for $k = 1, 2, 3$, so we have that $\Phi_{\mathbf{c}}(x) = \psi(x)$. This means that, in Coulomb gauge, $\langle \Psi_{\mathbf{c}}(x)\overline{\Psi}_{\mathbf{c}}(y)\rangle = \langle \psi(x)\overline{\psi}(y)\rangle$, and that the gauge-invariance of the mass using an operator defined in the Coulomb gauge is self-evident.

The second choice here presented is the string gauge, which creates a string that wraps around the torus along a direction k with C* boundary conditions. Visualising the lattice with C* boundary conditions as a box, this allows the electric flux to escape the box in a symmetric way that satisfies Gauss's Law through the effective placement of two image charges at $x + \hat{L}_k$ and $x - \hat{L}_k$ on the mirror lattice, both with charges that are half the magnitude and opposite to that of the original charge. A graphical representation of this effect is given in Fig. 3.1.

String gauge:

$$J_\mu(x) = \frac{1}{2}\delta_{\mu,k}\mathrm{sgn}(x_k)\prod_{\nu\neq k}\delta(x_\nu); \qquad (3.29a)$$

$$\Psi_{\mathbf{s}} = e^{-\frac{iq}{2}\int_{-x_k}^{0} ds A_k(x+s\hat{k})}\psi(x)e^{\frac{iq}{2}\int_{0}^{L-x_k} ds A_k(x+s\hat{k})}. \qquad (3.29b)$$
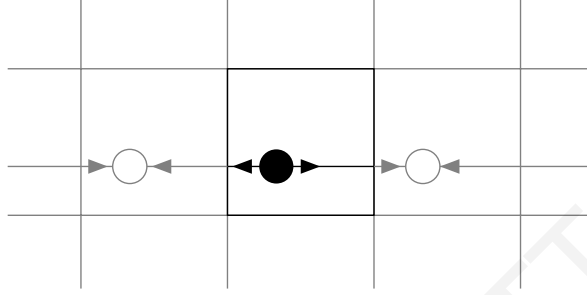
Figure 3.1: Representation of the interpolating operator $\Psi_{\mathbf{s}}$ from Eq. (3.29), constructed such that the electric flux escapes the physical lattice (black) in a symmetric way due to the presence of oppositely and half-charged mirror charges (empty circles).

A third choice is the Landau gauge:

Landau gauge:

$$J_\mu(x) = \partial_\mu\Phi(\mathbf{x}), \qquad (3.30a)$$

$$\partial_\mu\partial_\mu\Phi(\mathbf{x}) = \delta^4(\mathbf{x}), \qquad (3.30b)$$

$$\Psi_\ell(x) = e^{-iq\int d^4y\partial_\rho A_\rho(y)\Phi(y-x)}\psi(x). \qquad (3.30c)$$

$\Phi(\mathbf{x})$ is spatially anti-periodic, as it also is for the Coulomb gauge. Similarly to the case of the Coulomb gauge, when we use the Landau gauge, we find that $\Psi_\ell(x) = \psi(x)$, meaning that in the Landau gauge the only admissible gauge-invariant extension to $\psi(x)$ is $\Phi(\mathbf{x})$.

Despite the usefulnese of the explicitly O(4)-covariant Landau gauge in perturbative calculations, using this gauge factor to define a gauge-invariant operator presents difficulties as it introduces non-localities of the field in time, essentially inducing a time-dependent Hamiltonian. Although it can be shown that this contribution will disappear at large time separations, letting us end up with the same final mass, the convergence to the final mass may be very slow and therefore this choice will not optimally exploit the signal. It is on the whole preferable therefore to use a gauge dressing factor that gives a gauge-invariant operator that is fully local in time, such as either of the Coulomb or string dressing factors.

3.7 QCD + QED$_C$: FLAVOUR SYMMETRY

Considering the coupling of QED with QED, we define the combined action density in the conventional way,

$$S[A,\psi] = \int_{L^3T} d^4x\Big\{\frac{1}{4e^2}F_{\mu\nu}F_{\mu\nu} + \frac{1}{2g^2}\mathrm{tr}G_{\mu\nu}G_{\mu\nu} \\ + \sum_{i=f}^{N_f}\overline{\psi}_f(\gamma_\mu\overset{\leftrightarrow}{D}{}_\mu^f + m_f)\psi_f\Big\}, \qquad (3.31)$$

where $G_{\mu\nu}$ is the SU(3) field strength tensor,

$$G_{\mu\nu} = \partial_\mu B_\nu(x) - \partial_\nu B_\mu(x) - i[B_\mu(x), B_\nu(x)], \tag{3.32}$$

the covariant derivative $\overset{\leftrightarrow}{D}{}^f_\mu$ is defined by

$$\overset{\leftrightarrow}{D}{}^f_\mu = \overset{\leftrightarrow}{\partial}_\mu - iq_f A_\mu - iB_\mu, \tag{3.33}$$

and where $B_\mu(x)$ represents the colour field and is represented by a 3×3 Hermitian traceless matrix. As the fermion fields obey C^* boundary conditions, in order to preserve the periodicity of the action density we must require that the colour field also obey the boundary condition

$$B_\rho(x + \hat{L}_i) = -B_\rho(x)^*. \tag{3.34}$$

Returning now to the question of flavour violation due to the C^* boundary conditions, the situation changes somewhat with the inclusion of QCD. If we express the violation in terms of an elementary unit of charge e_c, we expect from our prior discussion that $\Delta Q = \pm 2e_c$. The elementary unit of charge for quarks is $1/3$; therefore we would expect the charge violation to be quantised as $\Delta Q = 2/3$. This however overlooks that, for a large enough box, the quarks will be confined within hadron objects that are net colourless and cannot transverse the boundaries of the box. We therefore set the elementary unit of charge in this case to be unity, so that charge violation can only occur as $\Delta Q = \pm 2$.

As the traversal of the boundary of the box charge-conjugates a hadron, its baryon number at the same time changes sign. This, in implying that baryon number is thus violated in units of 2, $\Delta B = 0 \bmod 2$, may lead to complications arising due to unintended mixing of a baryon with a lighter state, confounding the measurement of the ground state energy of the baryon, which we want to obtain from analysing the behaviour at long-distance of two-point functions.

Using the nucleons as an example, the proton will not mix with lighter states with a zero baryon number, due to the restraint upon baryon number violation. Due to the constraint on electric charge violation, it will not mix with a neutron state, but may mix with an anti-proton state. There is not, therefore, a lighter state with which it can mix and thus the ground state energy can be calculated without problems. Similarly, the pseudovector mesons can and will mix at the boundary with states that satisfy the above conditions; however, these states are heavier and therefore will not obstruct the calculation of the ground state energy.

Refining further the discussion to express these 'total' quantum numbers in terms of flavour numbers, the quantum numbers of individual quark flavours F_f,

$$Q = \sum_f q_f F_f, \qquad B = \frac{1}{3}\sum_f F_f \tag{3.35}$$

where q_f is the electric charge associated with flavour f in units of the charge of the positron e.

Since the C^* boundary conditions violate flavour-number conservation in the case of each flavour, one might assume that the hadrons with the same charge but different flavour content could mix arbitrarily, taking for example the mixing between a pion and a kaon. This is prevented, however, by the condition that

$$\Delta F_f = 0 \bmod 2. \tag{3.36}$$

Requiring as above that $\Delta B = 0 \bmod 2$ means that the total-flavour number $F = \sum_f F_f$ can only be violated in units of six,

$$\Delta F = 0 \bmod 6. \tag{3.37}$$

Due to the allowed mixing with lighter states, some states, including the Ω^- baryon, are not able to be extracted on a finite lattice from the long-distance behaviour of a two-point function. In these cases, one must take the infinite-volume limit first, and then extract long-distance behaviour.

Flavour-violating effects in QCD+QED$_C$ require the movement of massive particles around the torus, and are therefore exponentially suppressed as $\exp(-\mu L)$, with an exponent proportional to the lattice size and a characteristic mass μ that depends upon the masses of the particles involved in the mixing mechanism. This suppression factor is calculated for the dominant mixing diagrams relevant to our calculations in Sec. 6.2. We show in this section that we expect the effect to be suppressed through the combined effect of both the exponential suppression and due to energetic considerations due to the relatively large minimum photon and kaon energy that comes from using small lattices.

3.8 FINITE-VOLUME EFFECTS

Reference [20] shows that the finite-volume effects on the mass of a stable charged hadron scale far better in QED$_C$ than QED$_L$. This finite-volume calculation has been quantified and may be helpful concerning extrapolation to larger volumes.

For a stable hadron of non-zero electric charge q, the finite-volume corrections can be quantified through the following formula, which is valid to first order in e^2 and up to corrections in the box-size L that fall off faster than any power:

$$\frac{\Delta m(L)}{m} = \frac{e^2}{4\pi} \left\{ \frac{q^2 \xi(1)}{2mL} + \frac{q^2 \xi(2)}{\pi (mL)^2} - \frac{1}{4\pi mL^4} \sum_{\ell=1}^{\infty} \frac{(-1)^\ell (2\ell)!}{\ell! L^{2(\ell-1)}} \mathcal{T}_\ell \xi(2+2\ell) \right\} + \dots \quad (3.38)$$

This therefore allows one to find the mass in infinite volume, m, through the equation $m(L) = m + \Delta m(L)$. In practice, m in Eq. (3.38) can be approximated using $m(L)$ to facilitate the computation of $\Delta m(L)$; we have chosen to use this approximation throughout our work. Stable hadrons for which this formula is valid include the nucleons, and mesons such as the D and B mesons, charged pions and charged kaons.

In this formula, using the notation $\mathcal{T}_\ell$ we denote the ℓ-th derivative with respect to $\mathbf{k}^2$ of the $\mathbf{k} \to 0$ limit of the infinite-volume forward Compton amplitude of a photon of energy $|\mathbf{k}|$, on the charged hadron at rest.

Our boundary conditions are only of relevance in the generalised zeta function $\xi(s)$,

$$\xi(s) = \sum_{\mathbf{n} \neq \mathbf{0}} \frac{(-1)^{\langle \mathbf{n} \rangle}}{|\mathbf{n}|^s} \quad (3.39)$$

where $\mathbf{n}$ is defined as above as a vector of winding numbers. Here, the cases $s > 3$ are real, and analytic continuation is used to obtain the values for $s = 1$ and 2. Equation (B.34) of [20] gives an explicit representation of these coefficients. From this representation, for three C* dimensions the coefficients values are $\xi(1) = -1.7475645946, \xi(2) = -2.5193561521, \xi(4) = -3.8631638072$.

The first two terms of Eq. (3.38), i.e. the terms proportional to $\frac{1}{L}$ and $\frac{1}{L^2}$, depend only upon the electric charge and mass of the hadron; we therefore call these terms 'universal'. In the third term, the coefficients $\mathcal{T}_\ell$ encode dependence upon the spin and internal structure of the hadron. This dependence is suppressed with respect to the first two terms by the greater inverse power of L in the third term.

A similar expression for the finite volume corrections necessary in QED$_L$ has been calculated in Refs. [2, 29, 30]. This expression has a structure close to that of Eq. (3.38), with two universal terms contributing at powers $\frac{1}{L}$ and $\frac{1}{L^2}$ respectively. However, the expression for

$\mathrm{QED_L}$ has spin- and structure-dependent terms starting to contribute at $\frac{1}{L^3}$, as opposed to $\mathrm{QED_C}$ where they contribute at $\frac{1}{L^4}$. We see here one of the benefits of the locality of the $\mathrm{QED_C}$ formulation, which is especially beneficial for smaller lattice sizes, like the lattice sizes that we are using for this exploratory work.

In addition, the universal terms that appear in the expression for $\mathrm{QED_C}$ are significantly smaller than those in the $\mathrm{QED_L}$ expression, as can be seen in the comparison of the magnitude of only these universal terms for both $\mathrm{QED_C}$ and $\mathrm{QED_L}$, as given in Fig. 4 of [20].

3.9 LATTICE FORMULATION

The non-compact formulation of QED on the lattice involves the representation of the U(1) dynamical gauge variable in terms of the field A_μ, rather than the gauge link $e^{iq_f A_\mu(x)}$. To achieve this, either leading order electromagnetic contributions may be extracted as in Ref. [6], or a dynamical simulation of QED may be carried out, as in [2, 4–6, 31, 32]. The choice of the non-compact formulation necessitates however some dampening of the A_μ longitudinal modes, of which gauge fixing is the most common method. Using instead the compact formulation of QED allows us to maintain gauge-invariance.

The formulation of U(1) on the lattice consists of placing the gauge field $U(x, \mu)$, that belongs to the U(1) gauge group, on the links between lattice sites. Using C^* boundary conditions, these links satisfy

$$U(x + \hat{L}_k, \rho) = U(x, \rho)^* \tag{3.40}$$

along spatial direction k, with arbitrary temporal boundary conditions. In this section, we will simplify the argument somewhat by considering a single fermion field with unit electric charge, which will be generalised later on.

A naive formulation of compact U(1) would lead to problems in the discretisation of the interpolating operators that use the string dressing factor. The compact formulation of QED identifies $U(x, \mu) = e^{iA_\mu(x)}$; it is through the expansion of this field in terms of A_μ that a perturbative series can be reached. The string dressing factor would therefore require us to take the square root of the gauge link, an operation which is not gauge-invariant. This issue can be avoided through the use of a somewhat unconventional action that we will describe now.

We consider the following action, which describes a single matter field using compact QED,

$$S = S_\gamma + S_m, \tag{3.41a}$$

$$S_\gamma = \frac{2}{e^2} \sum_x \sum_{\mu\nu} [1 - P(x, \mu, \nu)], \tag{3.41b}$$

$$S_m = \sum_x \overline{\psi}(x) D[U^2] \psi(x). \tag{3.41c}$$

Here, the coupling of the Wilson-Dirac operator to the U(1)-gauge field is particular and described by

$$D[U^2] = m + \frac{1}{2} \sum_{\mu=0}^{3} \left\{ \gamma_\mu (\Delta_\mu^*[U^2] + \Delta_\mu[U^2]) - \Delta_\mu^*[U^2]\Delta_\mu[U^2] \right\}, \tag{3.42a}$$

$$\Delta_\mu[U^2]\psi(x) = U(x, \mu)^2 \psi(x + \hat{\mu}) - \psi(x), \tag{3.42b}$$

$$\Delta_\mu^*[U^2]\psi(x) = \psi(x) U(x - \hat{\mu}, \mu)^{-2} \psi(x - \hat{\mu}). \tag{3.42c}$$

This discretisation of the Dirac operator is not uniquely valid; any other discretisation that preserves charge conjugation may be used in its stead. The plaquette is defined as per convention;

$$P(x, \mu, \nu) = U(x, \mu)U(x + \hat{\mu}, \nu)U(x + \hat{\nu}, \mu)^{-1}U(x, \nu)^{-1}. \tag{3.43}$$

If a local gauge transformation $\Lambda(x) \in \mathrm{U}(1)$ is defined by

$$U(x, \mu) \to \Lambda(x)U(x, \mu)\Lambda(x + \hat{\mu})^{-1}, \tag{3.44a}$$
$$\psi(x) \to \Lambda(x)^2 \psi(x), \tag{3.44b}$$
$$\overline{\psi}(x) \to \overline{\psi}(x)\Lambda(x)^{-2}, \tag{3.44c}$$

the action described in Eq. (3.41a) will be invariant under this transformation, provided that the gauge transformation obeys the boundary conditions

$$\Lambda(x + \hat{L}_k) = \Lambda(x)^*. \tag{3.45}$$

Inspecting the action further, one can observe that the action is invariant when the signs of all those link variables with direction μ that lie on the three-dimensional slice defined by $x_\mu = 0$ are flipped. This is true for all μ, and we can therefore say that the action has a $\mathcal{Z}_2^4$ centre symmetry.

We shall now present a proof that the action is equivalent perturbatively to the conventional QED action when the continuum limit is taken. The first step in expanding the action perturbatively is to find at order $\mathcal{O}(e^0)$ the minima of the action. When we define the direction $\hat{3}$ to have C^* boundary conditions, it is shown in Appendix B that a discrete set of minima exist that are in-equivalent with each other within a local gauge transformation, and that these belong to the set

$$\Omega = \left\{ (z_0, z_1, z_2, 1) \mid z_0^2 = z_1^2 = z_2^2 = 1 \right\}. \tag{3.46}$$

Taking these minima into account, one can always find a vector $z \in \Omega$ so that such a minimum is equivalent within a local gauge transformation to the gauge field

$$\overline{U}_z(x, \mu) = \begin{cases} z_\mu & \text{if } x_\mu = L_\mu - 1, \\ 1 & \text{otherwise} \end{cases}. \tag{3.47}$$

The specification of the direction $\hat{3}$ as a C^* direction in the construction of the problem is the reason that, despite the $\mathcal{Z}_2^4$ centre symmetry, there is not a minimum at $z_3 = -1$, as every minimum with $z_3 = -1$ has an associated minimum with $z_3 = 1$ which is equivalent within a local gauge transformation.

Once the minima have been identified, the expectation values of observables can be perturbatively expanded. We start with the expansion of the gauge field $U(x, \mu)$ about the minimum $\overline{U}_z(x, \mu)$ with a fluctuation A_μ,

$$U(x, \mu) = \overline{U}_z(x, \mu)e^{\frac{i}{2}A_\mu(x)}. \tag{3.48}$$

A gauge-fixing term $S_{\mathrm{gf}} = S_{\mathrm{gf}}(A_\mu)$, that depends only on the fluctuation and not the classical minimum $\overline{U}_z(x, \mu)$, is added to the action. Representing some observable that we wish to measure by a generic functional $\mathcal{F}[U, \psi, \overline{\psi}]$ of the gauge and fermion fields, we obtain an

expression for the expectation value of such an observable, perturbatively expanded to some order $\mathcal{O}(e^n)$,

$$
\begin{aligned}
&\langle \mathcal{F}[U, \psi, \overline{\psi}] \rangle \\
&= \frac{1}{Z} \sum_{z \in \Omega} \int \mathcal{D}A \mathcal{D}\overline{\psi} \mathcal{D}\psi \mathcal{F}[\overline{U}_z e^{\frac{i}{2}A}, \psi, \overline{\psi}] e^{-S[e^{\frac{i}{2}A}, \psi, \overline{\psi}] - S_{\text{gf}}[A]} + \mathcal{O}(e^n).
\end{aligned}
\tag{3.49}
$$

Here, we note that, through its centre symmetry, the action is not dependent on the minima $\overline{U}_z(x, \mu)$ after the substitution in Eq. (3.48) has been made. This expectation value is normalised by the factor

$$
Z = 8 \int \mathcal{D}A \mathcal{D}\overline{\psi} \mathcal{D}\psi e^{-S[e^{\frac{i}{2}A}, \psi, \overline{\psi}] - S_{\text{gf}}[A]} \{1 + \mathcal{O}(e^n)\},
\tag{3.50}
$$

with the coefficient of 8 accounting for the eight gauge-invariant minima.

Similarly to the result of the integration of an odd function over a symmetric window around the origin, we can see that the expectation value will be zero for an observable $\mathcal{F}$ that is charged under center symmetry. Conversely, an observable that is center-invariant simplifies matters in that it is easily mapped onto an adjacent observable in the non-compact formulation. In this case, it is inconsequential which minimum the expansion is taken around; the expression loses its dependence on z and $\overline{U} = 1$ may be substituted,

$$
\begin{aligned}
&\langle \mathcal{F}[U, \psi, \overline{\psi}] \rangle \\
&= \frac{8}{Z} \int \mathcal{D}A \mathcal{D}\overline{\psi} \mathcal{D}\psi \mathcal{F}[e^{\frac{i}{2}A}, \psi, \overline{\psi}] e^{-S[e^{\frac{i}{2}A}, \psi, \overline{\psi}] - S_{\text{gf}}[A]} + \mathcal{O}(e^n).
\end{aligned}
\tag{3.51}
$$

We note that here $S[e^{\frac{i}{2}A}, \psi, \overline{\psi}]$ denotes, up to any arbitrary and irrelevant operators, the standard action in QED.

If one substitutes Eq. (3.48) into the action, it can be expanded perturbatively around the minima in terms of powers of the fields. The unconventional normalisation of the gauge action then accounts for the factor of $\frac{1}{2}$ in the exponent of the definition of the gauge links, restoring the canonical gauge field normalisation:

$$
P(x, \mu, \nu) = 1 + \frac{i}{2} F_{\mu\nu}(x) - \frac{1}{8} F_{\mu\nu}^2(x) + \dots,
\tag{3.52}
$$

$$
S_\gamma = \frac{2}{e^2} \sum_x \sum_{\mu\nu} [1 - P(x, \mu, \nu)] = \frac{1}{4e^2} \sum_x \sum_{\mu\nu} F_{\mu\nu}^2(x)
\tag{3.53}
$$

$$
+ \text{ irrelevant operators.}
$$

This factor of $\frac{1}{2}$ also accounts for the factors of U^2 in the Dirac operator in the matter action such that the electron correctly couples to the U(1) gauge field like

$$
U(x, \mu)^2 = 1 + i A_\mu(x) + \dots,
\tag{3.54}
$$

$$
S_m = \sum_x \overline{\psi}(x) \left\{ \gamma_\mu \left[\frac{\partial_\mu + \partial_\mu^*}{2} + i A_\mu(x) \right] + m \right\} \psi(x)
\tag{3.55}
$$

$$
+ \text{ irrelevant operators,}
$$

where $\partial^* \equiv - \overleftarrow{\partial}$ where $\overleftarrow{\partial}$ is a partial derivative acting to the left. The charge in compact QED being quantised, we see that through the construction of the gauge link, the interaction between the elementary charge and the gauge-field has strength $\frac{1}{2}$. This is accounted for by the electric charge of the dynamical fermion, which is double the elementary charge. This ensures a coupling of strength 1 of the dynamical fermion to the gauge field as required.

These factors of 2 used in the construction of the formulation also appear in the local gauge transformations in Eq. (3.44a).

Returning to the question of the discretisation of the interpolating operator with the string dressing factor, we see that the setup of the gauge link Eq. (3.48) allows one to write the interpolating operator as

$$\Psi_{\mathbf{s}}(x) = \prod_{s=-x_k}^{-1} U(x + s\hat{k}, k)^{-1} \psi(x) \prod_{s=0}^{L-x_k-1} U(x + s\hat{k}, k). \tag{3.56}$$

This evidently avoids the problem of taking the square root of the link that would have arisen had we used the naive formulation. Although $\Psi_{\mathbf{s}}(x)$ is charged under centre symmetry, we note that the product $\Psi_{\mathbf{s}}(x)\overline{\Psi}_{\mathbf{s}}(y)$ is invariant under centre symmetry, and it is only this product that is physically relevant. Due to the C^* boundary conditions, to dress a quark field in this way makes it invariant under local $U(1)$ gauge transformations.

If we take a moment to consider the discretisation of the interpolating operator for the fermion field with the Coulomb dressing factor, it is useful to introduce the field

$$A_{\mu}^{\mathbf{c}}(x) = \Delta^{-1} \partial_k^* \hat{F}_{k\mu}(x) \tag{3.57}$$

where $\Delta = \partial_k \partial_k^*$ denotes the discrete Laplace operator defined for three dimensions with anti-periodic boundary conditions, while $\hat{F}_{\rho\sigma}(x)$ is an arbitrary field tensor discretisation, such as the clover plaquette. This field is equal to the gauge field in the Coulomb gauge when the continuum limit is taken. It can also be shown that the discrete Coulomb gauge constraint $\partial_k^* A_k^{\mathbf{c}}(x) = 0$ is satisfied by the above definition. The interpolating operator, Eq. (3.56), may be discretised through applying the Coulomb dressing factor like

$$\Psi_{\mathbf{c}}(x) = \Psi_{\mathbf{s}}(x) e^{-\frac{i}{2} \sum_{s=0}^{L} A_k^{\mathbf{c}}(x + s\hat{k})}. \tag{3.58}$$

When evaluated in both the continuum theory and the Coulomb gauge, and by taking $A_{\mu}(x) = A_{\mu}^{\mathbf{c}}(x)$ and $\Psi^{\mathbf{c}}(x) = \psi(x)$, one finds that Eq. (3.58) and Eq. (3.56) are equivalent expressions.

We will now discuss how the above formulation of QED$_C$ on the lattice may be extended to include also QCD, and the effect that this has on the quantisation of electric charge. To start with, colour field link variables $V(x, \mu) \in \mathrm{SU}(3)$ are introduced. As above, these obey the C^* boundary conditions

$$V(x + \hat{L}_k, \rho) = V(x, \rho)^*. \tag{3.59}$$

The plaquette is defined as per convention,

$$Q(x, \mu, \nu) = V(x, \mu) V(x + \hat{\mu}, \nu) V(x + \hat{\nu}, \mu)^{-1} V(x, \nu)^{-1}. \tag{3.60}$$

Selecting the Wilson action S_g for the SU(3) gauge field, we add another component to our action, and rescale the photon action S_γ to account for the elementary charge of $\frac{1}{3}$ of the quarks:

$$S = S_g + S_\gamma + S_m, \tag{3.61a}$$

$$S_g = \frac{1}{g^2} \sum_x \sum_{\mu\nu} \mathrm{tr}[1 - Q(x, \mu, \nu)], \tag{3.61b}$$

$$S_\gamma = \frac{18}{e^2} \sum_x \sum_{\mu\nu} [1 - P(x, \mu, \nu)], \tag{3.61c}$$

$$S_m = \sum_f \sum_x \overline{\psi}_f(x) D_f[U, V] \psi_f(x). \tag{3.61d}$$

33

The Dirac equation is adjusted to include the SU(3) gauge field V, and to implement appropriate couplings to the electromagnetic field for the up and down quarks, $q_f = 2/3$ and $1/3$ respectively,

$$
D_f[U, V] = m_f + \frac{1}{2} \sum_{\mu=0}^{3} \left\{ \gamma_\mu (\Delta_\mu^*[U^{6q_f}V] + \Delta_\mu[U^{6q_f}V]) \right.
$$
$$
\left. - \Delta_\mu^*[U^{6q_f}V]\Delta_\mu[U^{6q_f}V] \right\}. \tag{3.62}
$$

As explored in Appendix C, the use of non-degenerate Wilson-Dirac quarks in QCD comes inevitably with a mild sign problem, where the fermionic determinant has the possibility of becoming negative due to lattice artifacts, despite being positive in the continuum limit. This situation persists also when QED is added, however, it may be shown that this problem is not exacerbated by C^* boundary conditions. Section 4.8 presents the results for the sign of the Pfaffian measured on our ensembles, as well as a novel approach that was developed to significantly reduce the computational effort of this measurement.

RC* STRATEGY AND MESON RESULTS

4.1 STRATEGY

The QCD+QED simulations on which we have measured baryon masses take place in a theory that includes the four lightest quark flavours: u, d, s and c. In order to extrapolate to the physical point, six parameters, the four quark hopping parameters κ_f, the SU(3) inverse coupling strength β and the fine-structure constant α, must be matched with their physical values. The strategy of this project is to perform this matching for every chosen value of the inverse coupling β at which a simulation is carried out, and then to perform the extrapolation to the continuum limit $\beta \to \infty$ as for pure QCD. There is flexibility in the choice of parameters, or *renormalisation scheme*, with which to carry this out. Our nonperturbative scheme is defined by six parameters, principally the standard scale $(8t_0)^{1/2}$ obtained through a Wilson gradient flow, the fine-structure constant α_R obtained at the scale t_0 through the same gradient flow, and the dimensionless trajectory observables

$$\phi_0 = 8t_0(M_{K^\pm}^2 - M_{\pi^\pm}^2); \tag{4.1a}$$

$$\phi_1 = 8t_0(M_{\pi^\pm}^2 + M_{K^\pm}^2 + M_{K^0}^2); \tag{4.1b}$$

$$\phi_2 = 8t_0(M_{K^0}^2 - M_{K^\pm}^2)\alpha_R^{-1}; \tag{4.1c}$$

$$\phi_3 = \sqrt{8t_0}(M_{D^s} + M_{D^\pm} + M_{D^0}). \tag{4.1d}$$

These trajectory observables are kept constant while β and α are varied, thus defining *surfaces of constant physics*. Here, M_X is the mass corresponding to the meson labelled X. A relative advantage of the choice of these observables is that they may all be calculated very accurately and precisely on the lattice. In this work, the central value of the CLS determination [33] is used in order to obtain values in physical units,

$$(8t_0)^{1/2} = 0.415 \text{ fm.} \tag{4.2}$$

As t_0 may not be determined experimentally, the scheme described above is not able to locate the physical point at the sub-percent level. The value of t_0 also contains an ambiguity of order $\mathcal{O}(\alpha)$. Although α_R also may not be determined experimentally, we are only aiming up to $\mathcal{O}(\alpha_R^2)$ in the matching to the real hadronic universe. Matching α_R with the PDG value is therefore justified as the value of α_R is independent of the renormalisation scheme at this precision. The aim is eventually to set the scale through the hadronic scheme, meaning a replacement of t_0 with the Ω^- baryon mass.

Maximal sensitivity to the masses of the light quarks is included by design in the definitions of the observables ϕ_0, ϕ_1, ϕ_2. It may be shown in QED-coupled SU(3) chiral perturbation theory [34, 35] that, to leading order,

$$\phi_0 = A(m_{s,R} - m_{d,R}), \tag{4.3a}$$

$$\phi_1 = 2A(m_{u,R} + m_{d,R} + m_{s,R}) + 2B\alpha_R, \tag{4.3b}$$

$$\phi_2 = A\alpha_R^{-1}(m_{d,R} - m_{u,R}) - B. \tag{4.3c}$$

Here, A and B denote low-energy constants. Observable ϕ_0 is directly proportional to the down-strange quark mass difference, and, in fact, $\phi_0 = 0$ if and only if d and s are mass-degenerate, at which point the theory is called U-spin symmetric as it is invariant under an SU(2) flavour symmetry rotating the d and s quarks. The observable ϕ_1, for a fixed α_R value, determines the average value of the u, d and s quarks, and has already been applied in other contexts [36, 37]. Observable ϕ_2 serves to keep constant the ratio between so-called strong isospin-breaking effects of order $\mathcal{O}(m_{d,R} - m_{u,R})$, due to the mass-difference between the u and d quarks, and the effects due to electromagnetic isospin-breaking, which are of order $\mathcal{O}(\alpha_R)$. Lastly, the mass of the c quark is fixed by observable ϕ_3, which has already seen use in, for example, [38].

If one substitutes the above reference value for t_0 along with the physical meson masses in Eq. (4.1a), the values

$$\phi_0^{\text{phys}} \simeq 0.992, \quad \phi_1^{\text{phys}} \simeq 2.26, \quad \phi_2^{\text{phys}} \simeq 2.37, \quad \phi_3^{\text{phys}} \simeq 12.0, \tag{4.4}$$

are obtained. The unphysical surface of constant physics defined by

$$\phi_0 = 0, \quad \phi_1 = 2.13, \quad \phi_2 = 2.37, \quad \phi_3 = 12.1, \tag{4.5}$$

will be targeted in our simulations, with $\phi_0 = 0$ achieved precisely through the use of mass-degenerate d and s quarks, $m_d = m_s$, known as U-spin symmetry. As we are only using a singular fixed value of $\beta = 3.24$ so far, corresponding to an approximate lattice spacing of $a \simeq 0.054$ fm, we will henceforth refer to *lines of constant physics* in the parameter space of α and the quark masses. Interestingly, the line of constant physics meets the $\text{SU}(3)_f$-symmetric point in QCD, where $m_{u,R} = m_{d,R} = m_{s,R} = \frac{1}{3}(m_{u,R} + m_{d,R} + m_{s,R})$ at $\alpha = 0$. At this point, $\phi_1 = 2.174(12)$ and $\phi_3 = 12.059(20)$, as calculated in [38]. The target ϕ_1 has been chosen close to its physical value so that the three mass-degenerate light quarks at the QCD $\text{SU}(3)_F$-symmetric point have masses approximately equal to the average mass of the three physical light quarks. The target values of ϕ_1 and ϕ_3 are close but not equal to the the values given in Eq. (4.1a), as they have been matched to the ones calculated on our gauge configurations with $\alpha_R = 0$. This is not a problem because the physical values of Eq. (4.1a) have an ambiguity that comes from an uncertainty in t_0.

The simulations take place at unphysical values of the parameters, as is usual in LQCD. We expect that direct calculation at physical α_R will not be sufficient on its own to resolve isospin-breaking effects. Isospin-breaking effects are therefore amplified through the use of various different values of α, including the pure QCD case of $\alpha = 0$, after which interpolation may be used to find the values of the observables at the physical fine-structure constant, $\alpha_{\text{phys},R}$. The quark masses used in the simulations are much heavier than their physical values for reasons of computational efficiency, and, as these results are somewhat exploratory, it is advantageous to start at higher masses and be able to assess the setup stability, the efficacy of the tuning strategy, and the trends of the observables, whilst using comparatively fewer computing resources. The approach to physical quark masses will be covered by future studies.

4.2 LATTICE ACTION

The lattice on which all simulations have been performed and measured has the dimensions $L_T \times L^3$, with periodic temporal boundary conditions, and C* boundary conditions in all three spatial dimensions. Whilst the Lüscher-Weisz action is used for the SU(3) gauge action, the U(1) gauge action used is a Wilson action,

$$S_{G,U(1)}(z) = \frac{1}{8\pi q_{\text{el}}^2 \alpha} \sum_x \sum_{\mu \neq \nu} \left[1 - P_{\mu\nu}^{\text{U}(1)}(x) \right]. \tag{4.6}$$

Here, $P_{\mu\nu}^{\mathrm{U}(1)}(x)$ denotes the plaquette constructed by the compact U(1) field $z(x, \mu)$ that starts at site x and extends in the directions μ and ν. The unconventional normalisation of this action is due to the requirement that electric charge be quantised in the compact formulation of QED; the fundamental unit of electric charge q_{el} may be chosen arbitrarily. We are using $q_{\mathrm{el}} = 1/6$. This choice allows the construction of the interpolating operators corresponding to charged hadrons that are invariant under local U(1) gauge transformations.

Four flavours of $O(a)$-improved Wilson fermions are simulated in the unphysical case in which $m_d = m_s$. Therefore, the simulations can be described as $N_f = 1 + 2 + 1$. Two Sheikholeslami-Wohlert (SW) terms are used in the definition of the improved Wilson-Dirac operator in the case of QCD+QED, one each for the two gauge fields. The first term, with coefficient $c_{\mathrm{sw}}^{\mathrm{SU}(3)}$, depends on the field tensor for SU(3), and similarly the second term, with coefficient $c_{\mathrm{sw}}^{\mathrm{U}(1)}$, depends on the U(1) field tensor. In the case of pure QCD, only the first term was used. The value of this was determined in a non-perturbative manner in [39], and is correct up to terms of order $\mathcal{O}(\alpha)$. In the case of the QCD+QED ensembles, the same value of the coefficient $c_{\mathrm{sw}}^{\mathrm{SU}(3)}$ is used for the first SW term, while a tree-level improvement is produced in the U(1) sector through setting $c_{\mathrm{sw}}^{\mathrm{U}(1)} = 1$.

In the case of periodic boundary conditions, a mild sign problem is introduced through the inclusion of Wilson fermions with individual flavours; the determinant inside the path integral is real but not definitely positive after the fermions have been integrated out, the probability of a negative sign of the determinant vanishing in the continuum limit. The situation is similar in the case of C* boundary conditions, as already discussed in Sec. 3.9 and App. C, in which there is a mild sign problem in the fermionic Pfaffian. This sign has been calculated systematically on our ensembles and the results are presented later in Sec. 4.8.

4.3 GAUGE ENSEMBLES

Three different values of α were chosen, $\alpha = 0, \sim \alpha_{\mathrm{phys}}$ and $\alpha = 0.0050 \gg \alpha_{\mathrm{phys}}$ (chosen to over-emphasise isospin-breaking effects), at which seven ensembles in total were generated. Of these, baryon masses were measured on five, due to finite computing resources. The ensembles are labelled first according to the lattice size, i.e. $\mathtt{A} = 64 \times 32^3, \mathtt{B} = 80 \times 48^3, \mathtt{C} = 96 \times 48^3$, then with the approximate charged pion mass, the value of α through the label $\mathtt{a}$ followed by the two digits given by $\mathtt{x}$ in $\alpha = 0.00\mathtt{xx}$, and finally the value of β following the letter $\mathtt{b}$. Table 4.1 gives the parameters of the action for the generated ensembles, whilst a number of observables for the verification of the validity of the ensembles is given in Table 4.2.

For context, the largest integrated autocorrelation time measured over all observables was found to be consistently associated with the t_0/a^2, with a value of approximately 100 MDU on the lattices with 64×32^3 volume. Increasing the lattice size seemed to decrease the integrated autocorrelation time for t_0/a^2, although this phenomenon could be due to an underestimation stemming from a reduction in statistics.

The topological charge Q, an important observable relating to the gauge fields, was also monitored for all ensembles, and topological freezing, a phenomenon in which the topological charge becomes stuck at a certain value, was not observed, as is demonstrated in Fig. 4.1. This absence of topological freezing is a requirement for the ergodicity of the simulation and is not automatically satisfied if periodic boundary conditions in time are used [40].

ensemble	lattice	β	α	κ_u	$\kappa_d = \kappa_s$	κ_c
A400a00b324	64×32^3	3.24	0	0.13440733	0.13440733	0.12784
B400a00b324	80×48^3	3.24	0	0.13440733	0.13440733	0.12784
A450a07b324	64×32^3	3.24	0.007299	0.13454999	0.13441323	0.12798662
A380a07b324	64×32^3	3.24	0.007299	0.13459164	0.13444333	0.12806355
A500a50b324	64×32^3	3.24	0.05	0.135479	0.134524	0.12965
A360a50b324	64×32^3	3.24	0.05	0.135560	0.134617	0.129583
C380a50b324	96×48^3	3.24	0.05	0.1355368	0.134596	0.12959326

Table 4.1: Action parameters for the generated ensembles, which all have periodic temporal boundary conditions and C* boundary conditions in all three spatial dimensions. The SW improvement terms have the coefficients $c_{\mathrm{sw}}^{\mathrm{SU}(3)} = 2.18859$ for the SU(3) term and $c_{\mathrm{sw}}^{\mathrm{U}(1)} = 1$ for the U(1) term.

ensemble	n. cnfg	acc. rate	$\langle e^{-\Delta H} \rangle$	$\tau_{\mathrm{int}}(t_0)$	$\tau_{\mathrm{int}}(Q^2)$	$\tau_{\mathrm{int}}(\alpha_R)$
A400a00b324	2000	95%	0.9979(55)	51(18)	6.4(2.3)	—
B400a00b324	1082	98%	0.9950(25)	31(10)	8.0(2.8)	—
A450a07b324	1000	94%	0.9978(46)	44(19)	6.5(3.0)	2.3(1.6)
A380a07b324	2000	92%	1.0017(46)	46(15)	10.3(3.5)	2.7(1.5)
A500a50b324	1993	97%	0.9961(21)	21.4(5.5)	11.6(2.6)	1.40(55)
A360a50b324	2001	95%	0.9956(45)	47(16)	8.5(2.6)	1.1(1.0)
C380a50b324	600	98%	1.004(12)	12.5(3.9)	10.6(4.1)	3.0(1.2)

Table 4.2: Diagnostic observables for the ensembles. From left to right, these are, for each ensemble: the number of configurations in the ensemble, coinciding with the number of molecular dynamics trajectories where one trajectory is equal to $\tau = 2$ MD units, the Monte Carlo acceptance rate, the diagnostic observable $\langle e^{-\Delta H} \rangle$ with the target of 1, and the integrated autocorrelation times corresponding respectively to the following observables: the scale t_0/a^2, the squared topological charge Q^2, and the renormalised fine-structure constant α_R.
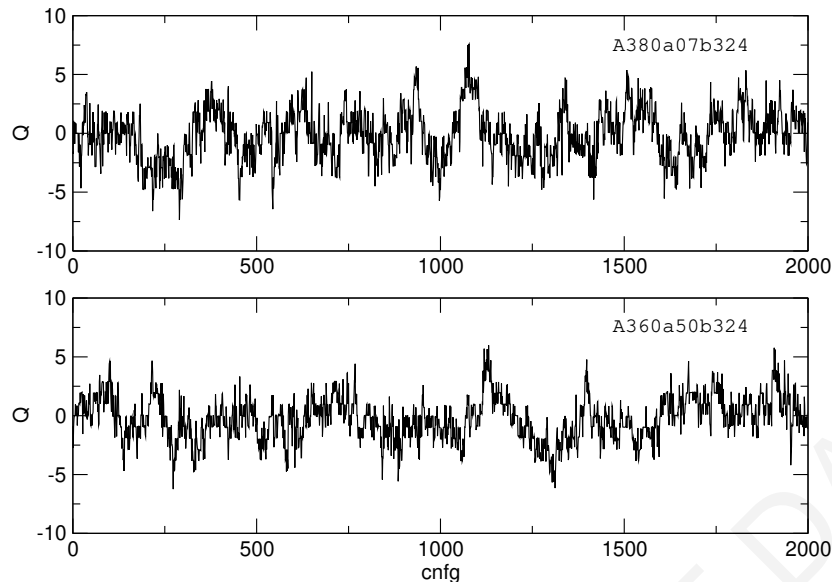
Figure 4.1: Topological charge history for ensembles `A380a07b324` and `A360a50b324`.

reweighting	ensemble	κ_u	$\kappa_d = \kappa_s$	κ_c
RW1	A380a07b324	0.13457969	0.13443525	0.12806355
RW2	A360a50b324	0.1355368	0.134596	0.12959326

Table 4.3: The targeted values of the quark hopping parameters for the mass reweighting factors on the reweighted ensembles.

A complexity arises with the use of compact QED, as it is known to possess two phases in bare parameter space, a weak-coupling Coulomb phase and a strong-coupling confining phase, traversed by a first-order phase transition [41–43]. The value of the average plaquette of U(1) gauge links $P^{U(1)}$ in pure gauge theory jumps between ~ 1 in the Coulomb phase and a small value in the confining phase, and it has been suggested through the use of conventional strong- and weak- coupling analysis that both regimes persist after the introduction of fermions. It is therefore a valid question in which regime we find ourselves, as we are using a compact QED action and values of $\alpha > \alpha_{\text{phys}}$. The largest value of α at which we carry out our simulations, $\alpha = 0.05$, can be expressed as an inverse coupling strength following the conventions in [43], to give the value

$$\beta^{\text{U}(1)} = \frac{1}{4\pi q_{\text{el}}^2 \alpha} \simeq 57, \tag{4.7}$$

a value much greater than the pure gauge theory critical value $\beta_{\text{crit}}^{U(1)} \simeq 1.01$. Measured for example on the ensemble `A360a50b324`, the average U(1) plaquette deviates from one by $1 - P^{\text{U}(1)} = 4.19405(21) \times 10^{-3}$. This clearly shows that this ensemble, and therefore all of our ensembles as this is at the largest value of α used, are situated well into the weak-coupling Coulomb phase.

4.4 TUNING STRATEGY

A combination of different techniques has been used in order to tune the quark masses to lie on the line of constant physics defined in Sec. 4.1, primarily mass reweighting of the quarks, which allows one to correct some small mistunings. The implementation used in this work for the mass reweighting is explained in [44], and has the peculiar feature that the determinant

39

of the rational approximation of some generic power of $D^\dagger D$ must be reweighted. The mass reweighting factors used in this work are labelled by `RWi` where `i` is an integer, and presented in Table 4.3, along with their associated target quark hopping parameters.

As mentioned above, the discretised lattice theory has six dimensionless bare parameters: the quark hopping parameters κ_f, the bare fine-structure constant α and the bare inverse strong coupling β. These parameters are treated in different ways; as it is not important for us to simulate at precise values of α and β, because these will be interpolated or extrapolated towards their physical values or limits, we choose values of α and β to simulate at. As varying β varies the lattice spacing, the continuum limit may be reached through taking $\beta \to \infty$. We therefore choose β in a range that gives a fine yet affordable lattice spacing. Similarly, while the matching of the renormalised α to its physical value would require the tuning of the bare α, it is sufficient to choose α in a reasonable range and then calculate the corresponding α_R. Conversely, we tune the hopping parameters κ_f such that the trajectory parameters ϕ match our targeted values. As we are choosing a U-spin-symmetric trajectory, $\kappa_d = \kappa_s$ is set automatically, and so really only three κ_f need to be tuned.

The following strategy was used in order to realise the tuning of the masses:

1. Some small-statistics ensembles ($\sim$200 thermalised configurations) were generated, and the quark masses $\hat{m}^{(0)} = (m_u^{(0)}, m_{ds}^{(0)}, m_c^{(0)})$ were estimated using these ensembles.

2. An ensemble with larger statistics (> 1000 thermalised configurations) was generated at the determined quark masses $\hat{m}^{(0)}$, and the ϕ observables $\phi^{(0)} = (\phi_1^{(0)}, \phi_2^{(0)}, \phi_3^{(0)})$ were calculated on this ensemble.

3. Three new quark-mass sets $\hat{m}^{(i)}$, where $i = 1, 2, 3$, were chosen to be reasonably close the previous value, $\hat{m}^{(0)}$. Through mass reweighting, the associated $\phi^{(i)}$ observable values were calculated. Linear interpolation, i.e. assuming the linear relation $\phi = A\hat{m} + b$, A being some 3×3 matrix and b some 3-vector, was then used in order to find the tuned quark mass values $\hat{m}^{(t)}$. This was attempted a few times in order to find $\hat{m}^{(i)}$ values that both did not suffer from an overlap problem and from which only interpolation or mild extrapolation was necessary to read the tuned mass values.

4. A full ensemble of $\sim$2000 thermalised configurations was then generated with quark masses equal to the tuned values $\hat{m}^{(t)}$, and the corresponding ϕ observables $\phi^{(t)}$ were measured on this ensemble.

5. Problems in the tuning process were addressed at this point. Using this strategy, two problems may occur: firstly, the extrapolation in step 2 may be too long, causing the target values for the ϕ observables to be missed. In this case, repetition of the entire strategy from step 2 is necessary, while setting $\hat{m}^{(0)} \leftarrow \hat{m}^{(t)}$. The second potential problem is that the linear approximation may create some small residual mistuning. In this case, one can repeat step 2 using $\hat{m}^{(0)} \leftarrow \hat{m}^{(t)}$, after which the correctly-tuned ϕ observables may be calculated using mass reweighting, without the requirement for the generation of a new ensemble.

The results presented in this thesis are those of the ensembles with full statistics; those results associated with the intermediate mass reweighting factors are not presented.

Although in principle the tuning in step 2 may be carried out through alteration of the valence quark masses without the use of a mass reweighting factor, in practice this strategy was found to be impracticable as it led to an overshooting problem. This method may however be a cost-effective way to move closer to the desired region of parameter space provided that one starts at a value of $\hat{m}^{(0)}$ sufficiently far from the target value.

In order to construct U(1)-gauge-invariant interpolating operators, one may dress the interpolating operators with a dressing factor,

$$\Psi_f(x) = \mathcal{D}_f(x)\psi_f(x) , \qquad \overline{\Psi}_f(x) = \overline{\psi}_f(x)\mathcal{D}_f^*(x) , \tag{4.8}$$

and then build the quark bilinears as normal. Expressing the string dressing factor from Eq. (3.56) more precisely in the compact QED formulation gives

$$\mathcal{D}_f(x) = \frac{1}{3} \sum_{k=1}^{3} \prod_{s=0}^{L/a} z^{\hat{q}_f/2}(x + as\hat{k}, k). \tag{4.9}$$

This is, technically speaking, the $(\hat{q}_f/2)$-th power of the spatial U(1) Polyakov loops starting from x, averaged over the three spatial directions, where $\hat{q}_f$ is the charge of the quark field in units of the gauge-action parameter q_{el}, for which we have chosen $q_{el} = 1/6$. For both possible electric charges of the quarks, $(\hat{q}_f/2)$ is an integer. In this way, due to the C* boundary conditions, the dressed quark field will be invariant under local U(1) gauge transformations. This dressing factor is also invariant under $\pi/2$ rotations around x.

Although the above dressing factor makes the hadron interpolating operators non-local in space, they are still local in time and therefore one may extract the Hamiltonian eigenstates from the exponential decay of the spectral representation of the zero-momentum two-point function at large times as per convention.

C-even correlation functions are necessary for the projection to zero momentum, due to the eigenstates of the momentum operator being automatically charge conjugation operator eigenstates under C* boundary conditions. The correlators for mesons with quark content $\overline{f}, g$ where $f \neq g$ are calculated through the C-even two-point functions,

$$C_{fg}(x_0) = \langle P_{fg}(x_0)P_{fg}(0)\rangle, \tag{4.10}$$

where

$$P_{fg}(x_0) = \sum_{\mathbf{x}}\{\overline{\Phi}_f\gamma_5\Phi_g(x_0, \mathbf{x}) + \overline{\Phi}_g\gamma_5\Phi_f(x_0, \mathbf{x})\}, \tag{4.11}$$

which may be derived by applying Eq. (A.3) to the naive interpolating operators

$$O(x_0)_{fg} = \sum_{\mathbf{x}}\{\overline{\Phi}_f\gamma_5\Phi_g(x_0, \mathbf{x})\}, \tag{4.12a}$$

$$\overline{O}(x_0)_{fg} = \sum_{\mathbf{x}}\{\overline{\Phi}_g\gamma_5\Phi_f(x_0, \mathbf{x})\}, \tag{4.12b}$$

and the two-point function

$$C_{fg}(x_0) = \langle \overline{O}_{fg}(x_0)O_{fg}(0)\rangle. \tag{4.13}$$

The meson effective masses $M(x_0)$ are then calculated through solving the following equation numerically,

$$\frac{C(x_0 + a)}{C(x_0)} = \frac{\cosh\left[\left(x_0 + a - \frac{T}{2}\right)M(x_0)\right]}{\cosh\left[\left(x_0 - \frac{T}{2}\right)M(x_0)\right]}. \tag{4.14}$$

Universal finite-volume corrections are then applied to the effective mass curves for mesons with non-zero charge q as detailed in Sec. 3.8,

$$M_c(x_0) = M(x_0) - \alpha_R q^2 \left\{\frac{\zeta(1)}{2L} + \frac{\zeta(2)}{\pi M(x_0)L^2}\right\} , \tag{4.15}$$
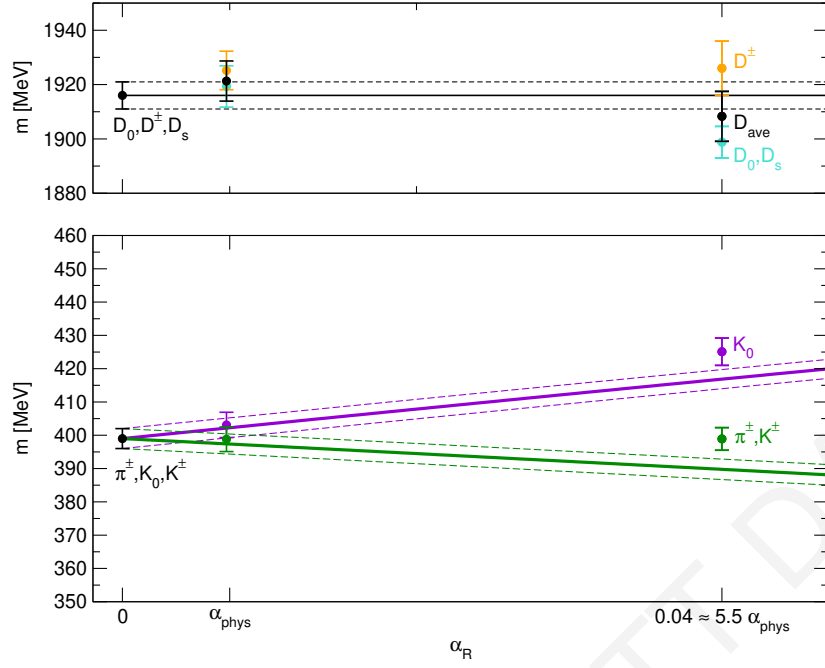
Figure 4.2: Meson masses at different values of α_R compared with their target values. From left to right in the plot, the ensemble `A400a00b324` lies at $\alpha_R = 0$, ensemble `A380a07b324+RW1` at $\alpha_R \simeq 1/137$, and ensemble `A360a50b324+RW2` at $\alpha_R \simeq 0.04$, the latter two ensembles having been reweighted. The target values for the meson masses are presented as functions of α_R, with the purple line giving the target K_0 mass, the green line giving the target $K_\pm$ mass, and the black line giving the average mass of the D mesons, $M_{D_{\mathrm{ave}}} = \frac{1}{3}(M_{D_s^\pm} + M_{D_0} + M_{D^\pm})$, with the reference value $(8t_0)^{1/2} = 0.415$ fm determining the values in MeV.

where $\zeta(1) = -1.7475645946$ and $\zeta(2) = -2.5193561521$. The final mass is then obtained through taking a plateau weighted by the inverse variance of the timepoint and checking the stability of the result with respect to variation of the plateau boundaries.

The effective ϕ observables were calculated using the effective meson masses through Eq. (4.1a), and the plateau was taken as described above for the case of the mesons.

ensemble(+rw)	t_0/a^2	a [fm]	α_R	$\pi\sqrt{3}L^{-1}$ [MeV]
A400a00b324	7.402(66)	0.05393(24)	0	—
B400a00b324	7.383(40)	0.05400(14)	0	—
A450a07b324	7.198(84)	0.05469(32)	0.007076(24)	613.5(3.6)
A380a07b324	7.599(79)	0.05323(28)	0.007081(19)	630.4(3.3)
A380a07b324+RW1	7.525(77)	0.05349(27)	0.007080(22)	627.3(3.2)
A500a50b324	7.789(42)	0.05257(14)	0.040772(85)	638.2(1.7)
A360a50b324	8.427(89)	0.05054(27)	0.040633(80)	663.9(3.5)
A360a50b324+RW2	8.285(79)	0.05098(24)	0.04069(26)	658.2(3.2)
C380a50b324	8.400(26)	0.050625(79)	0.04073(11)	441.86(69)

Table 4.4: Important observables for the different ensembles. From left to right for a given ensemble: reference observable t_0/a^2, lattice spacing a corresponding to the reference value $(8t_0)^{1/2} = 0.415$ fm and the value of the observable t_0/a^2 measured on the given ensemble, the renormalised fine-structure constant α_R, and the energy gap of the photon at tree-level $\pi\sqrt{3}/L$. As above, the reference value $(8t_0)^{1/2} = 0.415$ fm determines the conversion of values to MeV.

43

ensemble(+rw)	$M_{\pi^\pm} = M_{K^\pm}$ [MeV]	M_{K_0} [MeV]	$M_{K_0} - M_{K^\pm}$ [MeV]	$M_{D^\pm} = M_{D_s^\pm}$ [MeV]	M_{D_0} [MeV]	$M_{D^\pm} - M_{D^0}$ [MeV]
A400a00b324	398.5(4.7)	398.5(4.7)	0	1912.7(5.7)	1912.7(5.7)	0
B400a00b324	401.9(1.4)	401.9(1.4)	0	1908.5(4.5)	1908.5(4.5)	0
A450a07b324	451.2(4.3)	451.6(4.7)	0.8(1.1)	1919.8(7.3)	1916.0(8.0)	3.6(1.2)
A380a07b324	383.6(4.4)	390.7(3.7)	7.01(26)	1926.4(7.8)	1921.1(7.6)	5.03(46)
A380a07b324+RW1	398.8(3.7)	403.1(3.8)	4.26(31)	1925.2(7.1)	1919.3(7.6)	5.8(1.1)
A500a50b324	495.0(2.8)	519.1(2.5)	24.0(1.0)	1901.1(4.1)	1870.1(4.4)	31.6(1.6)
A360a50b324	358.6(3.7)	388.8(3.5)	29.5(2.4)	1937.8(6.8)	1912.0(7.7)	26.0(2.8)
A360a50b324+RW2	398.9(3.4)	425.1(4.1)	26.1(1.3)	1926(10)	1898.8(5.8)	26.9(2.2)
C380a50b324	386.5(2.4)	414.5(2.0)	26.89(49)	1932.0(3.9)	1894.3(6.9)	34.5(5.6)

Table 4.5: Meson masses and charged-neutral meson mass differences for each ensemble, including mass reweighted ensembles where applicable. Some meson masses are degenerate due to the $d - s$ mass degeneracy of our simulations. Values are converted to MeV through the use of the reference value $(8t_0)^{1/2} = 0.415$ fm.

ensemble(+rw)	ϕ_1	ϕ_2	ϕ_3
A400a00b324	2.107(50)	—	12.068(36)
B400a00b324	2.143(15)	—	12.042(28)
A450a07b324	2.703(53)	4.4(6.0)	12.097(51)
A380a07b324	1.977(37)	3.39(14)	12.132(48)
A380a07b324+RW1	2.126(39)	2.13(17)	12.122(47)
A500a50b324	3.357(37)	2.60(11)	11.864(28)
A360a50b324	1.806(35)	2.41(19)	12.114(41)
A360a50b324+RW2	2.208(38)	2.348(97)	12.040(58)
C380a50b324	2.088(22)	2.350(44)	12.020(29)
target	2.13	2.37	12.1

Table 4.6: Measured values for the ϕ parameters on each ensemble, including mass-reweighted ensembles where applicable, with the target values that define the lines of constant physics for comparison.

Table 4.4 presents some important observables measured on the different ensembles, such as the lattice spacing a and the renormalised fine-structure constant α_R. The meson masses measured on the generated ensembles, consisting of $\pi^\pm, K_0, K^\pm, D_0, D^\pm$ and $D_s^\pm$, and the associated charged-neutral mass differences, are presented in Table 4.5, where it is encouraging that, even at the physical α_R-value, the $K_0/K^\pm$ is clearly distinguishable from zero. The ϕ observables, which are used in the tuning of the meson masses, are measured on each ensemble, and are given in Table 4.6, with the target values that define the lines of constant physics alongside for reference. Relative precisions of roughly 3%, 5-10% and 0.5% were achieved for ϕ_1, ϕ_2 and ϕ_3 respectively, with the increased relative error of ϕ_2 in comparison being no surprise, due to its definition as a ratio of different isospin-breaking corrections, which is particularly challenging as smaller values of α_R are reached. The meson masses associated with some tuned ensembles are plotted in Figure 4.2.

4.6 FINITE VOLUME EFFECTS

While the majority of ensembles presented in this thesis, and in fact all of the ensembles on which baryon masses were measured, take place on a 64×32^3 lattice, two lattices of larger size, B400a00b324 with $\alpha = 0$ and C380a50b324 with $\alpha = 0.05$, were generated in order to give some indication of the magnitude of finite volume effects in both QCD and QED.

Looking first at the finite volume effects in pure QCD, one may compare the pion mass obtained at different volumes with C* boundary conditions with those calculated at different volumes with periodic boundary conditions at the same values of action parameters. In Fig. 4.3, the pion mass is compared between two of our QCD ensembles with C* boundary conditions, A400a00b324 and B400a00b324, with spatial volumes corresponding to $M_\pi L \approx 3.5$ and $M_\pi L \approx 5.2$ respectively, and the A1 and A2 ensembles of the ALPHA collaboration [38]. We see that, in the case of periodic boundary conditions, the pion mass tends to increase due to finite-volume corrections, whereas for C* boundary conditions it tends to decrease due to finite-volume corrections. Denoting P as corresponding to periodic boundary conditions, and C as corresponding to C* boundary conditions, this is consistent with chiral perturbation theory at leading order:

$$M_{\mathrm{P}}(L) = M + \frac{\xi}{3} \sum_{\mathbf{n} \in \mathbb{Z}^3 \setminus \{0\}} \frac{2}{nL} K_1(nML), \tag{4.16}$$

while

$$M_{\mathrm{C}}(L) = M - \frac{\xi}{3} \sum_{\mathbf{n} \in \mathbb{Z}^3 \setminus \{0\}} \frac{1 - 3(-1)^{\sum_k n_k}}{nL} K_1(nML), \tag{4.17}$$

where K_1 is a modified second-kind Bessel function and $\xi = M^2/(4\pi F)^2$. These predictions are also plotted in Fig. 4.3 as indetermination bands. We find that, for large volumes, finite-volume effects do not seem to exceed 1%, whereas, although higher statistics are required for a definite conclusion on this matter, the finite-volume effects on the pion are reasonably large for the smaller volume.

As $M_\pi L$ is reasonably small for the A400a00b324 ensemble with lattice size 64×32^3, we expect QCD finite-volume effects due to interactions from moving particles moving around the spatial torus to be non-negligible, as discussed in Sec. 2.6.2.

The finite-volume corrections due to QED with C* boundary conditions are given in Eq. (3.38) as a power-law in which the correction terms decrease as inverse powers of the volume. In the following discussion, and indeed the amendment of the masses, we shall consider only the universal structure-independent terms, which are proportional to $1/L$ and $1/L^2$ respectively. The comparative magnitudes of these corrections for the mesons are given for two ensembles in Table. 4.7. We find that, for our largest volume, the structure-independent

	$M_{\pi^\pm} = M_{K^\pm}$ [MeV]			$M_{D^\pm} = M_{D_s^\pm}$ [MeV]		
ensemble(+rw)	no-FV	LO-FV	NLO-FV	no-FV	LO-FV	NLO-FV
A360a50b324+RW2	393.4(3.4)	397.7(3.4)	398.9(3.4)	1922(10)	1926(10)	1926(10)
C380a50b324	383.1(2.4)	386.0(2.4)	386.5(2.4)	1929.0(3.9)	1931.9(3.9)	1932.0(3.9)

Table 4.7: Magnitude of finite-volume corrections for $\pi^\pm$ and $D^\pm$ masses on two different ensembles at $\alpha_R \simeq 0.04$ and with tuned masses. Masses calculated without subtraction of finite-volume corrections are labelled *no-FV*, with subtraction of only the $1/L$ term as *LO-FV*, and with subtraction of both the universal terms $1/L$ and $1/L^2$ as *NLO-FV*. The subtraction of the $1/L^2$ correction term induces a 0.1% shift in the $\pi^\pm$ mass on the larger volume and a 0.3% shift on the smaller volume. The reference value $(8t_0)^{1/2} = 0.415$ fm is used to give masses in MeV.
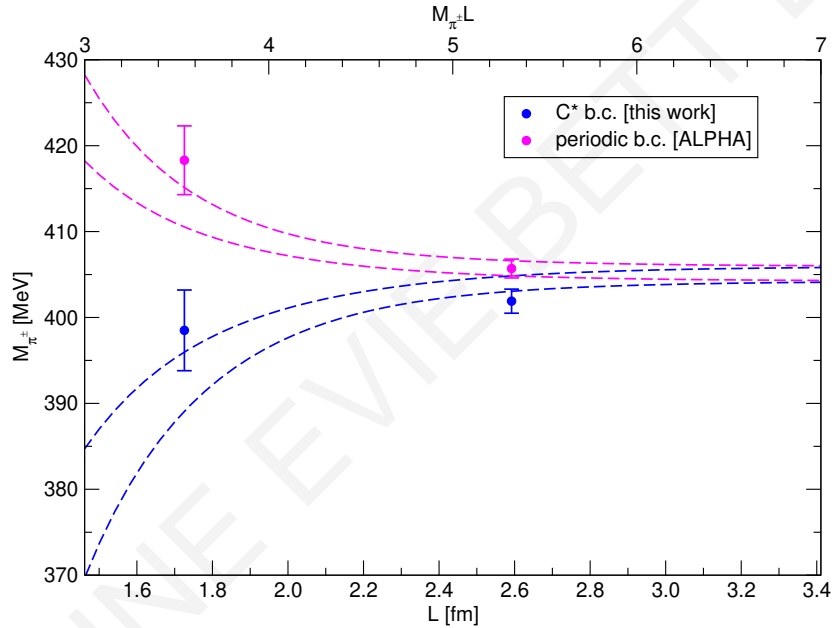
Figure 4.3: Comparison of pion masses in QCD at finite volume, using C*-boundary-condition ensembles `A400a00b324` and `B400a00b324`, and with periodic-boundary-condition ensembles `A1` and `A2` from [38]. The reference value $(8t_0)^{1/2} = 0.415$ fm has been used to give masses in MeV in both cases. A combined fit to the LO χPT formulae gives the curves, given as indetermination bands.

	$M_p = M_{\Sigma^+}$ [MeV]			$M_{\Omega^-} = M_{\Delta^-}$ [MeV]		
ensemble(+rw)	no-FV	LO-FV	NLO-FV	no-FV	LO-FV	NLO-FV
A500a50b324	1275(15)	1279(15)	1280(15)	1609(23)	1613(23)	1614(23)

Table 4.8: Magnitude of finite-volume corrections for p and Ω^- masses on ensemble `A500a50b324` at $\alpha_R \simeq 0.04$. All baryon masses given in this thesis were measured on ensembles with volume $32^3 \times 64 (a^4)$. Masses calculated without subtraction of finite-volume corrections are labelled *no-FV*, with subtraction of only the $1/L$ term as *LO-FV*, and with subtraction of both the universal terms $1/L$ and $1/L^2$ as *NLO-FV*. The subtraction of the $1/L^2$ correction term induces a shift of order 10^{-1}% in both the proton mass and Ω^- mass. The reference value $(8t_0)^{1/2} = 0.415$ fm is used to give masses in MeV.

terms give a shift of magnitude $\sim 0.9\%$ to the $\pi^{\pm}$, and that most of this effect is due to the $1/L$ term. Similarly, the magnitude of finite-volume corrections on the baryons for the ensemble A500a50b324 with $L \sim 1.7$fm are displayed in Tab. 4.8. The baryon masses were only measured on one lattice size and, as we can see, the corrections are not negligible but are small. The structure-independent terms together give a 1.1% correction for the proton and a 0.3% correction for the Ω^-, with most of the contribution coming from the $1/L$ term. One may therefore reason that, at the largest volume, the finite-volume effects due to QED are under control.

4.7 FLOW OBSERVABLES

Both the auxiliary observable t_0, used to set the scale, and the renormalised fine-structure constant α_R, are defined through the Wilson gradient flow, which was also used above on the spatial dimensions in the gauge smearing of the baryon interpolating operators.

The SU(3) gauge field U_t is acted upon by the Wilson-flow discretisation [45] of the SU(3) flow equation at positive flow time,

$$a^2 \partial_t U_t(x,\mu) = -g^2 \left\{ \partial_{x,\mu} S_{\text{SU(3)}}^{\text{W}}(U_t) \right\} U_t(x,\mu). \tag{4.18}$$

Here, $S_{\text{SU(3)}}^{\text{W}}(U)$ denotes the standard Wilson action for SU(3) fields. The above equation may be modified in order to instead give the expression for the Wilson-flow of the compact U(1) gauge field z_t at positive flow time,

$$a^2 \partial_t z_t(x,\mu) = -4\pi\alpha \left\{ \partial_{x,\mu} S_{\text{G,U(1)}}(z_t) \right\} z_t(x,\mu), \tag{4.19}$$

with the U(1) Wilson gauge action $S_{\text{G,U(1)}}(z)$ given by Eq. (4.6). Given the positive-flow-time clover discretisations $\hat{G}_{t,\mu\nu}$ and $\hat{F}_{t,\mu\nu}$ of the SU(3) and U(1) field tensors given respectively by Eq. (2.68) and (2.67), the associated clover action densities may be defined as

$$E_{\text{SU(3)}}(t) = \frac{1}{2} \sum_{\mu\nu} \langle \text{tr} \hat{G}_{t,\mu\nu}^2 \rangle, \qquad E_{\text{U(1)}}(t) = \frac{1}{4q_{\text{el}}^2} \sum_{\mu\nu} \langle \hat{F}_{t,\mu\nu}^2 \rangle. \tag{4.20}$$

These quantities then permit the usual definition of the auxiliary observable t_0,

$$t_0^2 E_{\text{SU(3)}}(t_0) = 0.3, \tag{4.21}$$

as well as the definition of the renormalised fine-structure constant as a function of the scale t_0,

$$\alpha_R = \mathcal{N} t_0^2 E_{\text{U(1)}}(t_0). \tag{4.22}$$

The normalisation $\mathcal{N}$ [46], given by

$$\mathcal{N}^{-1} = \frac{2\pi t_0^2}{TL^3} \sum_p \frac{\sum_{\mu\nu} \mathring{p}_\mu^2 c_\nu^2 - \sum_\mu \mathring{p}_\mu^2 c_\mu^2}{\sum_\mu \hat{p}_\mu^2} e^{-2t_0 \sum_\mu \hat{p}_\mu^2}, \tag{4.23}$$

ensures that the value of α_R is the same as that of α at tree level when a perturbative expansion is carried out. Here, all momenta permitted by the boundary conditions enter into the sum,

$$p_0 \in \frac{2\pi a}{T} \left\{ 0, 1, 2, \ldots, \frac{T}{a} - 1 \right\}, \quad p_k \in \frac{\pi a}{L} \left\{ 1, 3, 5, \ldots, \frac{2L}{a} - 1 \right\}, \tag{4.24}$$

where we have used the following definitions:

$$\hat{p}_\mu = \frac{2}{a}\sin\frac{ap_\mu}{2}\,, \qquad \mathring{p}_\mu = \sin(ap_\mu)\,, \qquad c_\mu = \cos\frac{ap_\mu}{2}\,. \tag{4.25}$$

4.8 SIGN OF THE PFAFFIAN

Choosing the charge-conjugation matrix C to be $i\gamma_0\gamma_2$ in the Euclidean chiral basis, the antiquark field corresponding to a given quark field ϕ may be represented as $\phi^C = C^{-1}\overline{\phi}^T$. The translation of a field by L in a spatial direction $\hat{k}$, by the definition of the C* boundary conditions, performs a charge-conjugation on said field. In the case of the fermion fields, therefore, the C* boundary conditions may be written as

$$\begin{pmatrix} \psi(x+L\hat{k}) \\ \psi^C(x+L\hat{k}) \end{pmatrix} = \begin{pmatrix} \psi^C(x) \\ \psi(x) \end{pmatrix} \equiv K\begin{pmatrix} \psi(x) \\ \psi^C(x) \end{pmatrix}\,. \tag{4.26}$$

Instead of the normal fermion determinant, a Pfaffian $\mathrm{Pf}(CKD)$, CKD being an anti-symmetric matrix as shown in Prop. 1, is produced when the quark fields are integrated out of the path integral. This is due to the non-diagonal nature of the Dirac operator acting on the quark-antiquark doublet under C* boundary conditions, therefore taking the form of a $24V \times 24V$ matrix.

The Pfaffian's absolute value obeys the relation

$$|\mathrm{Pf}(CKD)| = |\det D|^{1/2}\,, \tag{4.27}$$

allowing us to simulate the absolute value following the standard Rational HMC algorithm as for the Dirac operator, and incorporate the sign as a reweighting factor in order to reconstruct the Pfaffian value configuration-by-configuration.

The Hermitian Dirac operator $Q \equiv \gamma_5 D$ is particularly relevant to the calculation of the sign of the Pfaffian. We denote the list of eigenvalues of Q as $\lambda_{n=1,\cdots,12V} \in \mathbb{R}$, with each eigenvalue in the list occurring twice in the spectrum of Q, as Q has a doubly-degenerate spectrum as shown in Prop. 2.

It may be shown through Prop. 3 that the Pfaffian may be expressed using these eigenvalues as

$$\mathrm{Pf}(CKD) = \prod_{n=1}^{12V} \lambda_n\,. \tag{4.28}$$

This gives a simple rule for the sign of the Pfaffian, that an even (odd) number of negative eigenvalues λ_n will give the Pfaffian a positive (negative) sign.

As the eigenvalues of $Q(m)$ may be labelled and treated as continuous functions of the quark mass m, the sign of the Pfaffian may be calculated through observation of the flows of eigenvalues through the variation of m. A change in sign therefore corresponds to the crossing of zero by a degenerate pair of Q eigenvalues. The sign may therefore be expressed as the factorisation of the product into the signs from the composite regions of the mass space. For instance, we see that the sign of the Pfaffian at two masses may be related through the equation

$$\mathrm{sgn}\,\mathrm{Pf}|CKD(m)| = (-1)^{c(m,M)}\,\mathrm{sgn}\,\mathrm{Pf}|CKD(M)|, \tag{4.29}$$

where $c(m,M)$ is the number of times degenerate pairs of $Q(m)$ eigenvalues cross zero through varying the mass from m to M.

Taking M to be very large allows the approximation $Q(M) \approx M\gamma_5$, which gives an even number of negative eigenvalues at $6V$, rendering $\mathrm{Pf}(CKD(M))$ positive. The Pfaffian of

$CKD(m)$ is therefore given by the number of crossings of zero by pairs of eigenvalues of $Q(m)$ up to some large mass M.

We notice that we have different Dirac operators for different electric charges; the Dirac operator can then be labelled by its associated charge and be simply a function of the quark mass m. For example, for the quarks with electric charge $+2/3$, the appropriate Dirac function is the same for both, the $D_{+2/3}(m)$. The Dirac operators for the u and c quarks are then given by this function at the respective quark masses, $D_u = D_{+2/3}(m_u)$ and $D_c = D_{+2/3}(m_c)$. The contribution factor to the sign-reweighting factors from the u and c quarks is then given by

$$\text{sgn Pf}(CKD_u) \ \text{sgn Pf}(CKD_c) = (-1)^{c_{+2/3}(m_u, m_c)}. \tag{4.30}$$

Here, $c_{+2/3}$ denotes the number of level crossings of degenerate eigenvalue pairs of the Hermitian Dirac operator Q for a quark of electric charge $+2/3$. There is also the identification here with the charm quark as the very large mass $m_c = M$.

Likewise, the expression for the contribution from the d and s quarks is

$$\text{sgn Pf}(CKD_d) \ \text{sgn Pf}(CKD_s) = (-1)^{c_{-1/3}(m_d, m_s)}; \tag{4.31}$$

therefore, the reweighting factor due to the sign contributions from all four quarks is given by

$$W_{\text{sgn}} = \prod_{f=u,d,s,c} \text{sgn Pf}(CKD_f) = (-1)^{c_{+2/3}(m_u, m_c)}(-1)^{c_{-1/3}(m_d, m_s)} \tag{4.32}$$

We are simulating at the unphysical U-spin-symmetric point at which $m_d = m_s$, which means that $c_{-1/3}(m_d, m_s) = 0$ trivially, meaning that it is necessary only to count the eigenvalue crossings of the up-type quarks between the masses of the u and c quarks.

In this work, the calculation of $c(m, M)$ is formed of two stages:

1. An interval $I \subset [m, M]$ is found in the specified range of bare masses such that, in the complement of I, no sign flip exists. This is achieved using a fast algorithm that finds I that are typically much smaller than the specified range $[m, M]$ and are empty for the majority of configurations. This method is novel to the calculation of the sign of the Pfaffian and speeds up the calculation considerably. It could also be applied to, for example, the calculation in pure LQCD of the sign of the fermionic determinant, or the fermionic Pfaffian sign calculation in the case of gauge theories containing adjoint fermions.

2. In the case that I is not empty, the flow of those eigenvalues existing inside I that are closest to zero is tracked using the methods outlined in [47, 48], allowing a determination of the factor of the sign that the region I contributes. This requires a reasonably accurate knowledge of the eigenvectors of Q, over the region of masses which itself needs a fine resolution, rendering this stage far more expensive computationally than the previous stage. This is, of course, the motivation for the previous stage, which restricts the necessity for the calculation to a small number of configurations, and then, over small intervals of the masses.

In order to explain the first step, and the restriction of the range considered for the second step in the case that the selected region I is not empty, we must first take into account the theoretical observation, given that $\mu(m)$ is the smallest eigenvalue of $|Q(m)|$,

$$\mu(m) = \min_n |\lambda_n(m)| \ , \tag{4.33}$$

that, for the interval defined by $|m - \overline{m}| < \overline{\mu} \equiv \mu(\overline{m})$, no eigenvalue $\lambda_n(m)$ changes sign as long as $\overline{\mu} > 0$.

Proof. For a normalised vector v, and using the identity $Q(m) = Q(\overline{m}) + \delta m \gamma_5$ where $m = \overline{m} + \delta m$, one may derive the following relation:

$$\|Q(m)v\| \geq \|Q(\overline{m})v\| - |\delta m| \; \|\gamma_5 v\| = \|Q(\overline{m})v\| - |\delta m| \geq \overline{\mu} - |\delta m| \; . \qquad (4.34)$$

Here, the triangle inequality is used to give the first inequality, and the unitarity of γ_5 is used between the second and third expressions. The final expression uses the definition of $\overline{\mu}$ as the smallest eigenvalue of $|Q(\overline{m})|$. Taking the more restrictive case of v being an eigenvector of $Q(m)$, we obtain the inequality

$$|\lambda_n(m)| \geq \overline{\mu} - |\delta m| \; . \qquad (4.35)$$

Provided that $m - \overline{m} = |\delta m| < \overline{\mu}$, $|\lambda_n(m)| > 0$ is satisfied. As a continuous function of m, $\lambda_n(m)$ must therefore be either entirely positive or entirely negative inside the interval defined by $m - \overline{m} < \overline{\mu}$, . $\qquad \square$

The following algorithm restricts the original interval $I = [m, M]$ by considering overlapping subintervals $I' = [m', M]$ passing from smaller to larger masses, applying the above observation to discount the complements of these intervals I' that by definition of the interval must not have sign flips, and stopping either when the considered range is exhausted or if the successive subinterval becomes sufficiently small. Specifically:

1. The variables $m_0 = m$ and $n = 0$ are set.

2. Defining a safe lower bound for $\mu(m_n)$ to be $\mu_n \geq 0$, calculate the lowest eigenvalue of $|Q(m_n)|$, $\overline{\mu}_n$. This may be achieved through the application to $Q(m_n)^{-2}$ of a standard power method.

3. No sign flip happens between $[m_n, m_n + \overline{\mu}_n)$, therefore this region is excluded through setting $m_{n+1} = m_n + (1 - \epsilon)\overline{\mu}_n$. We set the small parameter $\epsilon > 0$ to be 0.1.

4. If the considered region is exhausted, $m_{n+1} > M$, or the selected subinterval is sufficiently small, $m_{n+1} - m_n < \eta m_n$, where $0 < \eta < 1$ is a tunable parameter that we choose as $1/4$, the parameter m' is set to be equal to m_{n+1} and the algorithm is stopped. If this is not the case, the algorithm repeats from step 2.

This method is demonstrated graphically in Fig. 4.4. The above algorithm moves from lower to higher masses, providing a lower bound on the subinterval $I' = [m', M]$ for which the complement is guaranteed to contain no sign flips. The following similar algorithm is applied after the above algorithm if the interval $I' = [m', M]$ is not empty, and acts to restrict the interval from above, to give a new subinterval with a minimised range $I'' = [m', M']$. This is achieved through the following:

1. The variables $M_0 = m$ and $n = 0$ are set.

2. Defining a safe lower bound for $\mu(M_n)$ to be $\mu_n \geq 0$, calculate the lowest eigenvalue of $|Q(M_n)|$, $\overline{\mu}_n$. This may be achieved through the application to $Q(M_n)^{-2}$ of a standard power method.

3. No sign flip happens between $(M_n - \overline{\mu}_n, M_n]$, therefore this region is excluded through setting $M_{n+1} = M_n - (1 - \epsilon)\overline{\mu}_n$. We set the small parameter $\epsilon > 0$ to be 0.1.

4. If the considered region is exhausted, $M_{n+1} < m'$, or the selected subinterval is sufficiently small, $M_n - M_{n+1} < \eta M_n$, where $0 < \eta < 1$ is a tunable parameter that we choose as $1/4$, the parameter M' is set to be equal to M_{n+1} and the algorithm is stopped. If this is not the case, the algorithm repeats from step 2.
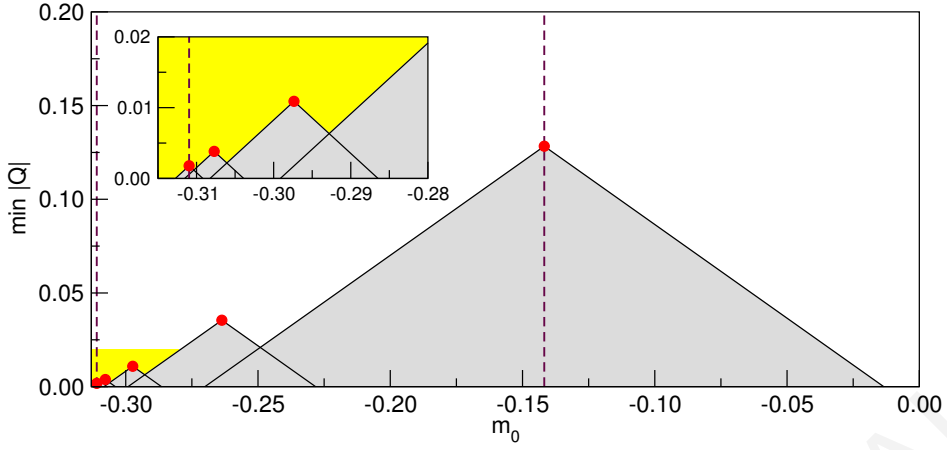
Figure 4.4: Demonstration of the determination of the Pfaffian sign through the exclusion of the possibility of the change of sign for successive ranges of valence quark masses. Minimum $|Q|$ eigenvalue is plotted against valence quark masses, and the grey region indicates that no eigenvalues cross the zero line in that region. We see that the region between the up-quark valence mass (left dashed line) and the charm-quark valence mass (right dashed line), a difference of two orders of magnitude, can be traversed in only five steps using our method.

In the case that the selected small interval $I'' = [m', M']$ is not empty, the eigenvalues and eigenvectors inside the interval are tracked as functions of the quark mass using the somewhat costly methods presented in [47, 48]. Thus the sign of the fermionic Pfaffian may be determined and applied as a reweighting factor to the Pfaffian magnitude determined through RHMC.

4.9 ALGORITHMIC PARAMETERS

This section details some of the algorithmic details and parameters used in the generation of the ensembles presented in this thesis, particularly with regard to the rational approximations, the pseudofermion action and the integration of the HMC molecular dynamics equations.

4.9.1 *Rational approximations*

Due to the peculiarities of the C* boundary conditions, the fermionic determinant is defined as

$$\det(\hat{D}_u^\dagger \hat{D}_u)^{1/4} \det(\hat{D}_{ds}^\dagger \hat{D}_{ds})^{1/2} \det(\hat{D}_c^\dagger \hat{D}_c)^{1/4} \tag{4.36}$$

for the QCD+QED ensembles, where $\alpha \neq 0$ and only the d and s quarks are mass-degenerate, with $\hat{D}$ representing the Dirac operator with even-odd pre-conditioning. More simply, we have

$$\det(\hat{D}_{uds}^\dagger \hat{D}_{uds})^{3/4} \det(\hat{D}_c^\dagger \hat{D}_c)^{1/4}, \tag{4.37}$$

for the QCD ensembles, where $\alpha = 0$ and $m_u = m_d = m_s$. One may approximate the inverse operators $(\hat{D}^\dagger \hat{D})^{-\gamma}$, where $\gamma = 1/4, 1/2, 3/4$, through a rational function in terms of $\hat{D}^\dagger \hat{D}$.

In our work, the rational function $R(x)$ of order (N, N) is constructed such that the relative precision is minimised. This is equivalent to finding the maximum of $|1 - x^\gamma R(x)|$ for some interval $x \in [r_a^2, r_b^2]$ chosen to be inclusive for the majority of the eigenvalues of $\hat{D}^\dagger \hat{D}$.

The rational approximation is, of course, an approximation and therefore has an error associated with it. This has been corrected for in our work through the use of a reweighting factor. This follows the strategy of the openQCD code, but uses the generalisation of the reweighting factor for a generic γ presented in [49]. Table 4.9 presents the parameters involved

51

ensemble	flavours	γ	$[r_a, r_b]$	N [prec.]	N_1	N_2
A400a00b324	uds	3/4	[0.00132,8.0]	18 [4.02e-08]	6	10
	c	1/4	[0.25500,8.0]	8 [7.97e-08]	0	0
B400a00b324	uds	3/4	[0.00132,8.0]	18 [4.02e-08]	6	10
	c	1/4	[0.25500,8.0]	8 [7.97e-08]	0	0
A450a07b324	u	1/4	[0.0004,10.0]	15 [4.73e-06]	5	8
	ds	1/2	[0.0010,10.0]	14 [5.46e-06]	4	7
	c	1/4	[0.2000,10.0]	7 [2.36e-06]	0	0
A380a07b324	u	1/4	[0.0020,10.0]	13 [4.00e-06]	3	6
	ds	1/2	[0.0010,10.0]	13 [1.38e-05]	3	6
	c	1/4	[0.2000,10.0]	7 [2.36e-06]	0	0
A500a50b324	u	1/4	[0.00070,9.0]	15 [2.09e-06]	5	8
	ds	1/2	[0.00132,9.0]	15 [1.25e-06]	5	8
	c	1/4	[0.20000,8.0]	9 [1.84e-08]	0	0
A360a50b324	u	1/4	[0.0004,10.0]	15 [4.73e-06]	5	8
	ds	1/2	[0.0010,10.0]	14 [5.46e-06]	4	7
	c	1/4	[0.2000,10.0]	7 [2.36e-06]	0	0
C380a50b324	u	1/4	[0.0004,10.0]	15 [4.73e-06]	5	8
	ds	1/2	[0.0010,10.0]	14 [5.46e-06]	4	3
	c	1/4	[0.2000,10.0]	7 [2.36e-06]	0	0

Table 4.9: Integration scheme and pseudofermion action parameters. From left to right are presented: 1) the ensemble label, 2) the number of integration steps at the levels (innermost, intermediate, outermost) of the three-level integration scheme, 3) the quark flavours in groups of mass-degeneracy, each group with its own rational approximation of the operator $(\hat{D}^\dagger \hat{D})^{-\gamma}$, 4) the exponent of this operator, 5) the spectral range $[r_a, r_b]$ of said operator, 6) the rational approximation order (N, N) and associated relative uniform precision, 7) the number of factors of the fermion forces integrated in the outermost level, and 8) the number of independent pseudofermion actions chosen.

in the definition of the rational approximations used, which have been chosen such that the errors associated with the considered observables do not show a detectable increase due to the reweighting factor.

The pseudofermion action is used to express the fermion determinant as a Gaussian integral over bosonic variables. When the Dirac operator enters into this action when using the rational approximation, it always exist as part of the combination $\hat{D}^\dagger \hat{D} + \mu^2$, where $\mu > 0$. This, in effect, removes the infinitely-high potential barrier that prevents either the Pfaffian or the fermionic determinant from changing sign [48], in a similar fashion to that of the twisted-mass reweighting in Ref. [50]. This effect can, however, be undermined through a too-large ratio r_b/r_a or a too-precise rational approximation, in which case μ, the smallest twisted mass, becomes too small and the ergodicity and stability of the algorithm may be compromised. In order to avoid this occurring, the precision of the rational approximation used in our work was reduced progressively down to an acceptable compromise at $\mathcal{O}(10^{-6})$.

4.9.2 *Pseudofermion actions and solvers*

Using the above-described rational approximation, the fermionic determinant for a given quark flavour may therefore be approximated as $\det R^{-1}$ through a sum of pseudofermion actions. Assuming the orderings $\nu_1 < \nu_2 < \cdots < \nu_N$ and $\mu_1 < \mu_2 < \cdots < \mu_N$, the rational function is given by

$$R = A \prod_{k=1}^{N} \frac{\hat{D}^\dagger \hat{D} + \nu_k^2}{\hat{D}^\dagger \hat{D} + \mu_k^2} \ . \tag{4.38}$$

For each factor $k = 1, \ldots, N_2$ up to a chosen limit N_2, a pseudofermion action S_k is then introduced, with the remaining factors accounted for by a single pseudofermion action S_{N_2+1},

$$S_k = \phi_k^\dagger \frac{\hat{D}^\dagger \hat{D} + \nu_k^2}{\hat{D}^\dagger \hat{D} + \mu_k^2} \phi_k \ , \qquad \text{for } k = 1, \ldots, N_2 \ , \tag{4.39a}$$

$$S_{N_2+1} = \phi_{N_2+1}^\dagger \left(\prod_{k=N_2+1}^{N} \frac{\hat{D}^\dagger \hat{D} + \nu_k^2}{\hat{D}^\dagger \hat{D} + \mu_k^2} \right) \phi_{N_2+1} \ . \tag{4.39b}$$

The values of N_2 that we have chosen in our work are given in Table 4.9. As outlined in [51], the method of partial fraction decomposition may be used to rewrite these pseudofermion actions. Inversions of different operators are required for the simulation of pseudofermions, the inversion of $(\hat{D} + i\mu_k)$ in the case of pseudofermionic actions and forces, and the inversion of $(\hat{D} + i\nu_k)$ for the generation of pseudofermionic fields. The calculation of the pseudofermionic action S_{N_2+1} uses the multishift conjugate gradient method, whereas for all other pseudofermion actions, the Schwarz-Alternating Procedure-preconditioned deflated generalised conjugate gradient method is used. Residues of 10^{-8}, for the calculation of the source, and 10^{-10} for the pseudofermionic field generation and calculation of the action, were used for all solvers.

QCD+QED simulation are again particular in their requirement that there exist different deflation subspaces for each value of the electric charge, which for the quark may take the values $\hat{q} = 2, 4$. In the simulation, a total of 20 deflation vectors were used, with values of `mu` = 0.001 for the lattice size 64×32^3 and `mu` = 0.005 for the other lattice sizes, and the number of Krylov vectors `nkv` ≥ 24, where we are using the `openQ*D` input file notation [51]. Up to the simulation code constraints and the local lattice size, we have chosen the largest possible size for the deflation blocks.

4.9.3 *HMC parameters and integration of Molecular Dynamics*

Regarding the particular details of the update algorithm, the Hybrid Monte Carlo algorithm is used alongside Fourier acceleration for the U(1) field [52, 53] in order to simulate the sum of the gauge and pseudofermion actions. In order to solve the molecular dynamics equations, a symplectic multilevel integrator [54], using a three-level scheme which is flexible at each level with regards to the number of integration steps, the integrator type, and the forces to be integrated, is used; the trajectory length is set to $\tau = 2$.

Concerning the three-level scheme, the Omelyan-Mryglod-Folk (OMF) second order integrator is used to integrate the fermion forces associated with the pseudofermionic actions S_k where $k = 1, \ldots, N_1$ and where $N_1 \leq N_2$, whereas, in the intermediate level, the OMF fourth-order integrator [55] was used to integrate all other fermionic forces. Lastly, at the innermost level, the OMF fourth-order integrator is used to integrate the gauge forces.

METHOD AND PRELIMINARY RESULTS FOR OPTIMISATION

5.1 SIGNAL-TO-NOISE RATIO: A COMPARISON

The signal-to-noise ratio associated with baryons is known to be much worse than that of mesons. For all hadrons heavier than the pion, the signal-to-noise ratio decreases exponentially with increasing time separation between the source and sink t.

5.1.1 *Pion*

As the interpolating operator for pions is given by $\overline{\psi}\gamma_5\psi$, the pion mass may be extracted from the correlation function

$$\langle C_\pi(t)\rangle = \frac{1}{L^{3/2}}\sum_{\vec{x}}\mathrm{tr}\left[S(x;0)\gamma_5 S^\dagger(0;x)\gamma_5\right], \tag{5.1}$$

by measuring the its exponential decay coefficient

$$\langle C_\pi(t)\rangle \to \mathrm{constant}\times e^{-m_\pi t}. \tag{5.2}$$

The propagator S is computed through inversion of the Dirac operator. Statistical error enters the picture due to the limited number of gauge configurations for which the Dirac operator is inverted. The magnitude of statistical fluctuations on the mean measured correlator $\overline{C_\pi}(t)$ is given by the formula

$$N\sigma_\pi^2(t) \approx \langle\mathrm{tr}\left(S(x;0)\gamma_5 S^\dagger(0;x)\gamma_5\right)^2\rangle - \langle C_\pi(t)\rangle^2, \tag{5.3}$$

where $\sigma_\pi(t)$ is the standard deviation per configuration.

The second term on the right hand side of this expression obviously decreases as $\exp(-2m_\pi t)$. In fact, the first right-hand-side term decreases with the same time dependence, as it involves four quark propagators spanning from time 0 to t. Its behaviour is therefore dependent on the lightest state onto which it may project, which is two pions. The two terms therefore decay with the same behaviour, and the equation

$$\sigma_\pi(t) \sim \frac{\langle C_\pi(t)\rangle}{\sqrt{N}}, \tag{5.4}$$

is satisfied up to some constant factors. This means that for the pion, the signal-to-noise ratio is approximately constant with t at large times:

$$\overline{C(t)}/\sigma_\pi(t) \sim \mathrm{constant}\ \times\sqrt{N}. \tag{5.5}$$

The pion is therefore the easiest hadron to measure in terms of the signal-to-noise ratio.

5.1.2 *Proton*

Simplifying the argument by keeping the colour and Dirac structure implicit, the proton mass may be extracted through a correlation function of the form

$$\langle C_p(t) \rangle = \langle S(t;0)S(t;0)S(t;0) \rangle, \tag{5.6}$$

as the proton is a bound state consisting of three quarks. The statistical error on the mean measured value of the above correlator is then given by

$$N\sigma_p^2(t) \approx \langle S^3 S^{\dagger 3} \rangle - \langle C_p(t) \rangle^2. \tag{5.7}$$

The lowest energy state to which the first term on the right hand side may project consists of three quarks and three anti-quarks, to form a three pion state. The standard deviation per configuration therefore diminishes according to

$$\sigma_p(t) \sim e^{-(3m_\pi/2)t}, \tag{5.8}$$

up to some constants. The signal-to-noise ratio for a correlation function measured on N configurations is therefore given by

$$\overline{C(t)}/\sigma_p(t) \sim \sqrt{N} e^{(m_p - 3m_\pi/2)t}. \tag{5.9}$$

This diminishes rather rapidly as the proton is much heavier than the pion; indeed, baryons tend to have much worse signal-to-noise ratios than mesons. Techniques to enhance the ground state signal such that the effective mass plateau starts before the statistical noise becomes dominant, such as smearing techniques in combination with spectral analysis techniques, are therefore essential for studying the baryon masses.

5.2 INTERPOLATING OPERATORS

In this section, we give the interpolating operators that we have used to select the desired baryon states, disregarding until later any smearing that is applied to the operators to improve the ground state signals. The operators that we have selected are those that not only correspond firstly to the correct quantum numbers of the state that we wish to measure, but that also are known from the literature to give the good signals for the desired physical states.

Firstly, it must be noted that in the following discussion, each quark that appears (in uppercase) in the following operators and indeed throughout the measurements has been made U(1)–gauge–invariant by means of the application of the 'string' dressing factor given in Eq. (3.29). This was performed in practice by the appropriate application of this factor at the source and sink indices. U, D and S are thus defined as the U(1)–gauge–invariant quark operators corresponding to the up, down and strange quarks respectively. The objects formed through the combination of these quark objects and the appropriate dirac matrices will therefore also be U(1)–gauge–invariant. The U(1) gauge invariance of the propagators and the entire meson and baryon objects has been checked for our code.

In our exposition of the different interpolating operators, we must first distinguish between the spin-$\frac{1}{2}$ baryons, which form an octet when only the quarks u, d, s are considered, and the spin-$\frac{3}{2}$ baryons, which form a decuplet when only the u, d, s quarks are considered and which require an additional projection operator to project to the pure spin-$\frac{3}{2}$ state.

5.2.1 *Spin-$\frac{1}{2}$ baryons*

THE PROTON p, NEUTRON n AND THE CASCADE Ξ^- This baryon sink interpolating operator is given by the expression

$$\mathcal{O}_a^\pm(x) = P_{ab}^\pm \epsilon_{ABC} \left[Q_c^A(x)\,(\mathcal{C}\gamma_5)_{cd}\,R_d^B(x) \right] Q_b^C(x), \tag{5.10}$$

where we have denoted Dirac indices with lowercase letters and colour indices with uppercase, and $\mathcal{C}$ denotes the charge-conjugation matrix. The quarks Q and R are placeholders that denote quarks of different flavour; we have, in particular, $Q \equiv U, R \equiv D$ in the case of p, $Q \equiv D, R \equiv U$ for n, and $Q \equiv S, R \equiv D$ for Ξ^-. The operator $P^\pm = \frac{1}{2}(1 \pm \gamma_0)$ acts to project the operator to a definite parity state, of either positive or negative parity. The anti-symmetric tensor, denoted by ϵ, renders the interpolating operator SU(3)–gauge-invariant.

The corresponding operator for this baryon source, which is the formal conjugate of the above baryon sink operator, is given by

$$\overline{\mathcal{O}}_a^\pm(x) = -P_{ab}^\pm \epsilon_{ABC} \left[\overline{Q}_c^A(x)\,(\mathcal{C}\gamma_5)_{cd}\,\overline{R}_d^B(x) \right] \overline{Q}_b^C(x), \tag{5.11}$$

where $\overline{Q} \equiv Q^\dagger \gamma^0$. The time-ordered correlator $T\langle \overline{\mathcal{O}}_a^\pm(0)\mathcal{O}_a^\pm(t)\rangle$, ignoring any smearing for now, forms the primary observable that will be measured on the lattice.

THE Σ^0 BARYON The interpolating operator for the Σ^0 baryon sink is given by

$$\frac{1}{\sqrt{2}} P_{ab}^\pm \epsilon_{ABC} \Big[\left(U_c^A(x)\,(\mathcal{C}\gamma_5)_{cd}\,S_d^B(x) \right) D_b^C(x) \\ + \left(D_c^A(x)\,(\mathcal{C}\gamma_5)_{cd}\,S_d^B(x) \right) U_b^C(x) \Big]. \tag{5.12}$$

The structure of the combination of the different projectors and matrices with the propagators is as described above.

The corresponding source operator, derived through the formal conjugation of the sink operator, is given by

$$-\frac{1}{\sqrt{2}} P_{ab}^\pm \epsilon_{ABC} \Big[\left(\overline{U}_c^A(x)\,(\mathcal{C}\gamma_5)_{cd}\,\overline{S}_d^B(x) \right) \overline{D}_b^C(x) \\ + \left(\overline{D}_c^A(x)\,(\mathcal{C}\gamma_5)_{cd}\,\overline{S}_d^B(x) \right) \overline{U}_b^C(x) \Big]. \tag{5.13}$$

THE Λ^0 BARYON The interpolating operator for the Λ^0 baryon sink is given by

$$\frac{1}{\sqrt{6}} P_{ab}^\pm \epsilon_{ABC} \Big[2\big[U_c^A\,(\mathcal{C}\gamma_5)_{cd}\,D_d^B \big] S_b^C + \big[U_c^A\,(\mathcal{C}\gamma_5)_{cd}\,S_d^B \big] D_b^C \\ - \big[D_c^A\,(\mathcal{C}\gamma_5)_{cd}\,S_d^B \big] U_b^C \Big]. \tag{5.14}$$

The combination with the different projectors and matrices is as described above for the other octet baryons.

The corresponding source operator is given by

$$-\frac{1}{\sqrt{6}} P_{ab}^\pm \epsilon_{ABC} \Big[2\big[\overline{U}_c^A\,(\mathcal{C}\gamma_5)_{cd}\,\overline{D}_d^B \big] \overline{S}_b^C + \big[\overline{U}_c^A\,(\mathcal{C}\gamma_5)_{cd}\,\overline{S}_d^B \big] \overline{D}_b^C \\ - \big[\overline{D}_c^A\,(\mathcal{C}\gamma_5)_{cd}\,\overline{S}_d^B \big] \overline{U}_b^C \Big]. \tag{5.15}$$

5.2.2 Ω^- *baryon*

In order to measure the Ω^- baryon, we use the interpolating operator for the baryon sink

$$\mathcal{O}_a^i(x) = \epsilon_{ABC} \left[S_b^A(x) \left(\mathcal{C}\gamma^i \right)_{bc} S_c^B(x) \right] S_a^C(x), \tag{5.16}$$

where $i = 1, 2, 3$ is a spatial Lorentz index.

The corresponding interpolating operator for the baryon source, derived by formally conjugating the sink operator, is given by

$$\overline{\mathcal{O}}_a^i(x) = \epsilon_{ABC} \left[\overline{S}_b^A(x) \left(\gamma^i \mathcal{C} \right)_{bc} \overline{S}_c^B(x) \right] \overline{S}_a^C(x). \tag{5.17}$$

The combination of these operators, neglecting for now any smearing we may wish to apply, gives the correlator $C_{ab}^{ij}(t) = T \langle 0 | \mathcal{O}_a^i(t) \overline{\mathcal{O}}_b^j(0) | 0 \rangle$, which must then be projected onto a definite spin state. Taking as the more relevant choice the spin-$\frac{3}{2}$ state, one applies the projection

$$C_{ab}^{\frac{3}{2}} = \sum_{i,j=1}^{3} \left(C^{ij} \mathcal{P}_{\frac{3}{2}}^{ji} \right)_{ab}; \qquad \mathcal{P}_{\frac{3}{2}}^{ij} = \delta^{ij} - \frac{1}{3}\gamma^i\gamma^j. \tag{5.18}$$

Here, both i and j are spatial Lorentz indices. The correlator is then projected onto a definite parity state as for the octet baryons,

$$C^{\frac{3}{2},\pm} = \text{Tr}[C^{\frac{3}{2}} P^{\pm}]. \tag{5.19}$$

Lastly, all baryons, octet and decuplet, have been folded according to $C(t) = C^+(t) - C^-(T - t)$ in order to reduce statistical fluctuations on a given time-slice. The above interpolating operators are given, without any smearing, spin-projection or folding for simplicity, in Tab. 5.1.

Due to the renormalisation strategy of the set of ensembles from the RC* collaboration, for all ensembles one may exploit a mass-degeneracy between the down and strange quarks. This renders some of the hadron masses degenerate. In the baryon sector of our results, we have that Ξ^- is degenerate with Σ^-, n is degenerate with Ξ^0, p is degenerate with Σ^+ and Ω^- is degenerate with Δ^-. It must be noted, however, that this degeneracy should be used, and has been in the case of our calculations, only once the necessary Wick contractions have been performed, in order to not confuse fermions of different flavours and to use the Grassman algebra correctly.

As a preliminary check performed with small statistics, the correlators corresponding to the interpolating operators for the Δ^+ and Δ^0 baryons, whose quark contents are *uud* and *udd* respectively, were calculated and then projected to spin-$\frac{1}{2}$ using the projector $\mathbb{I} - \mathcal{P}_{\frac{3}{2}}$. The masses were found to be consistent with the proton and neutron masses as required.

5.2.3 *C-even interpolating operators*

As explained in Sec. 3.1 and App. A, the requirement that the correlation functions be C-even comes from the conditions for projecting to zero-momentum when using C* boundary conditions. Through taking the sum over both the physical and mirror lattice using the interpolating operators given above, we obtain a correlator equivalent to the C-even correlator

Spin	Strange	Symbol	Quarks	Interpolating field (sink above, source below)	I	I_z	Q
$\frac{1}{2}$	$s=0$	p	uud	$P^\pm_{ab}\epsilon_{ABC}\left[U^A_c\left(C\gamma_5\right)_{cd}D^B_d\right]U^C_b$ $-P^\pm_{ab}\epsilon_{ABC}\left[\overline{U}^A_c\left(C\gamma_5\right)_{cd}\overline{D}^B_d\right]\overline{U}^C_b$	$1/2$	$+1/2$	$+1$
		n	udd	$P^\pm_{ab}\epsilon_{ABC}\left[D^A_c\left(C\gamma_5\right)_{cd}U^B_d\right]D^C_b$ $-P^\pm_{ab}\epsilon_{ABC}\left[\overline{D}^A_c\left(C\gamma_5\right)_{cd}\overline{U}^B_d\right]\overline{D}^C_b$	$1/2$	$-1/2$	0
		Λ^0	uds	$\frac{1}{\sqrt{6}}P^\pm_{ab}\epsilon_{ABC}\left[2\left[U^A_c\left(C\gamma_5\right)_{cd}D^B_d\right]S^C_b+\left[U^A_c\left(C\gamma_5\right)_{cd}S^B_d\right]D^C_b-\left[D^A_c\left(C\gamma_5\right)_{cd}S^B_d\right]U^C_b\right]$ $-\frac{1}{\sqrt{6}}P^\pm_{ab}\epsilon_{ABC}\left[2\left[\overline{U}^A_c\left(C\gamma_5\right)_{cd}\overline{D}^B_d\right]\overline{S}^C_b+\left[\overline{U}^A_c\left(C\gamma_5\right)_{cd}\overline{S}^B_d\right]\overline{D}^C_b-\left[\overline{D}^A_c\left(C\gamma_5\right)_{cd}\overline{S}^B_d\right]\overline{U}^C_b\right]$	0	0	0
	$s=1$	Σ^+	uus	$P^\pm_{ab}\epsilon_{ABC}\left[U^A_c\left(C\gamma_5\right)_{cd}S^B_d\right]U^C_b$ $-P^\pm_{ab}\epsilon_{ABC}\left[\overline{U}^A_c\left(C\gamma_5\right)_{cd}\overline{S}^B_d\right]\overline{U}^C_b$	1	$+1$	$+1$
		Σ^0	uds	$\frac{1}{\sqrt{2}}P^\pm_{ab}\epsilon_{ABC}\left[\left[U^A_c\left(C\gamma_5\right)_{cd}S^B_d\right]D^C_b+\left[D^A_c\left(C\gamma_5\right)_{cd}S^B_d\right]U^C_b\right]$ $-\frac{1}{\sqrt{2}}P^\pm_{ab}\epsilon_{ABC}\left[\left[\overline{U}^A_c\left(C\gamma_5\right)_{cd}\overline{S}^B_d\right]\overline{D}^C_b+\left[\overline{D}^A_c\left(C\gamma_5\right)_{cd}\overline{S}^B_d\right]\overline{U}^C_b\right]$	1	0	0
		Σ^-	dds	$P^\pm_{ab}\epsilon_{ABC}\left[D^A_c\left(C\gamma_5\right)_{cd}S^B_d\right]D^C_b$ $-P^\pm_{ab}\epsilon_{ABC}\left[\overline{D}^A_c\left(C\gamma_5\right)_{cd}\overline{S}^B_d\right]\overline{D}^C_b$	1	-1	-1
	$s=2$	Ξ^0	uss	$P^\pm_{ab}\epsilon_{ABC}\left[S^A_c\left(C\gamma_5\right)_{cd}U^B_d\right]S^C_b$ $-P^\pm_{ab}\epsilon_{ABC}\left[\overline{S}^A_c\left(C\gamma_5\right)_{cd}\overline{U}^B_d\right]\overline{S}^C_b$	$1/2$	$+1/2$	0
		Ξ^-	dss	$P^\pm_{ab}\epsilon_{ABC}\left[S^A_c\left(C\gamma_5\right)_{cd}D^B_d\right]S^C_b$ $-P^\pm_{ab}\epsilon_{ABC}\left[\overline{S}^A_c\left(C\gamma_5\right)_{cd}\overline{D}^B_d\right]\overline{S}^C_b$	$1/2$	$-1/2$	-1
$\frac{3}{2}$	$s=3$	Ω^-	sss	$P^\pm_{ab}\epsilon_{ABC}\left[S^A_c\left(C\gamma_i\right)_{cd}S^B_d\right]S^C_b$ $P^\pm_{ab}\epsilon_{ABC}\left[\overline{S}^A_c\left(\gamma^iC\right)_{bc}\overline{S}^B_d\right]\overline{S}^C_b$	0	0	-1

Table 5.1: Baryon interpolating operators in absence of smearing, spin-projection or folding. Colour indices are written in uppercase and Dirac indices are written in lowercase. The charge–conjugation matrix is denoted by C, and the operator $P^\pm = \frac{1}{2}(1\pm\gamma_0)$ projects the state to a definite parity.

$(1/2)^+$ Baryon	Non-zero components of F_{fgh}
p	$F_{uud} = 1$
n	$F_{ddu} = 1$
Λ_0	$F_{sud} = 2$, $F_{dus} = 1$, $F_{uds} = -1$
Σ^+	$F_{uus} = 1$
Σ^-	$F_{dds} = 1$
Ξ_0	$F_{ssu} = 1$
Ξ^-	$F_{ssd} = 1$

Table 5.2: Flavour tensor F_{fgh} defining the interpolating operators for spin-$1/2$ baryons. Flavour indices may take the values u, d, s.

on the physical lattice. The interpolating operators for the octet sink and source that are given above may be written more succinctly as respectively

$$O(x_0) = \sum_{\mathbf{x}} \sum_{ABC} \sum_{fgh} \epsilon_{ABC} \Psi^A_{(s)f} (\Psi^B)^T_{(s)g} C\gamma^5 \Psi^A_{(s)f}(x_0, \mathbf{x}), \qquad (5.20a)$$

$$\overline{O}(x_0) = -\sum_{\mathbf{x}} \sum_{ABC} \sum_{fgh} \epsilon_{ABC} (\overline{\Psi}^A_{(s)f})^T \overline{\Psi}^B_{(s)g} C\gamma^5 (\overline{\Psi}^A_{(s)f})^T (x_0, \mathbf{x}), \qquad (5.20b)$$

where the spin-indices (s) are implicit or contracted, and where the particular baryon is defined through the flavour tensor F_{fgh} for flavour indices f, g, h with non-zero elements given in Table 5.2. The two-point function is then given by

$$C(x_0) = \left\langle \overline{O}(0) \frac{1+\gamma_0}{2} O(x_0) \right\rangle. \qquad (5.21)$$

Using Eq. (A.3), the corresponding C-even interpolating operators for the octet baryons are given by,

$$B(x_0) = \sum_{\vec{x}} \sum_{ABC} \sum_{fgh} \epsilon_{ABC} F_{fgh} \big\{ \Psi^A_{(s)f} (\Psi^B_{(s)g})^T C\gamma_5 \Psi^C_{(s)h}(x_0, \vec{x}) $$
$$- C(\overline{\Psi}^A)^T_{(s)f} \overline{\Psi}^B_{(s)g} C\gamma_5 (\overline{\Psi}^C)^T_{(s)h}(x_0, \vec{x}) \big\}, \qquad (5.22)$$

along with the two-point function

$$C(x_0) = \left\langle B^t(0) C \frac{1+\gamma_0}{2} B(x_0) \right\rangle. \qquad (5.23)$$

Similarly, the C-even interpolating operators for the Ω^- may be written as

$$\Omega_j(x_0) = \sum_{\vec{x}} \sum_{ABC} \sum_{k} \epsilon_{ABC} \left(\delta_{jk} - \frac{1}{3}\gamma_j\gamma_k \right) \big\{ S_{(s)^A} (S^B_{(s)})^T C\gamma_k S^C_{(s)}(x_0, \vec{x}) $$
$$- C(\overline{S}^A)^T_{(s)} \overline{S}^B_{(s)} \gamma_k C(\overline{S}^C)^T_{(s)}(x_0, \vec{x}) \big\}, \qquad (5.24)$$

with the corresponding two-point function having the value

$$C(x_0) = \sum_j \left\langle \Omega^t_j(0) C \frac{1+\gamma_0}{2} \Omega_j(x_0) \right\rangle. \qquad (5.25)$$

As discussed above, these C-even baryon correlators are calculated automatically through the double sum over the sink using the naive interpolating operators and projection described in Secs. 5.2.1 and 5.2.2.

5.3 SMEARING OF INTERPOLATING OPERATORS

Whilst any interpolating operators with the correct quantum numbers will contribute by some amount to the physical state, certain operators contribute more than others. If we wish to isolate the ground state, we may wish to optimise the interpolating operator through smearing the fermions, either with pure fermion smearing or first smearing the gauge fields as an input to the fermion smearing. This should provide a more realistic wave function than a point source would, thereby hopefully increasing the overlap of the operator with the desired ground state. During analysis, this should show up as a mass-curve plateau that starts earlier, as a consequence of reduced contamination from excited states. Fermion smearing is known however to increase statistical noise, and so an optimisation must be performed in order to settle upon smearing parameters that extend the plateau whilst keeping the statistical noise at acceptable levels. In this vein, the combination of gauge smearing with fermion smearing can be useful, as gauge smearing can act to reduce gauge field fluctuations in a gauge-invariant way, counteracting the tendency of fermion smearing to enhance the statistical noise. The measurement of different interpolating operators, using either different levels of smearing or indeed different interpolating Dirac matrices, or both, may also be used to form the Generalised Eigenvalue Problem, which allows one to optimise the ground state overlap and to explore excited states. This is particularly valuable in the context of QCD+QED, as possible coupling with photons may be explored in the spectrum through this method, and indeed we have explored this in this work, as we shall discuss later.

5.3.1 *Gauge smearing*

As alluded to above, gauge smearing allows one to extend the source in another fashion in order to better approximate the spatial wavefunction of the state we wish to replicate, as well as having the effect of reducing statistical noise between configurations in a gauge-invariant way. We have chosen to use the gradient-flow smearing in this endeavour, in place of more conventional techniques such as APE smearing [56], for reasons of practicality; the gradient-flow gauge smearing procedure has the technical advantage of gauge-link unitarity being exactly preserved at all stages, whilst it is roughly equivalent to APE smearing when the plaquette is matched, as has been checked for our code through computation of the plaquette in terms of smeared gauge links and matching for the different procedures. At this point, it is important to note that, as the smearing is applied only in spatial directions, and as the gauge smearing is used only as an input for the fermion smearing and does not affect the Dirac operator, the renormalisation is not affected by this procedure. The gradient-flow smearing procedure [45] is defined by the application of the gradient-flow specified as

$$\dot{V}_t(x,k) = -g^2\{\delta_{x,k} S^{\text{W, spatial}}(V)\} V_t(x,k); \qquad V_0(x,k) = V(x,k);$$

$$\delta_{x,k} f(V) = T^a \delta^a_{x,k} f(V); \qquad \delta^a_{x,k} f(V) = \frac{d}{ds} f(e^{sX} V)|_{s=0};$$

$$X(y,i) = \begin{cases} T^a & \text{if } (y,i) = (x,k) \\ 0 & \text{otherwise} \end{cases};$$

(5.26)

to the SU(3) gauge fields $V(x,\mu)$, in order to produce the smeared gauge links $V_t(x,k)$ for $k = 1, 2, 3$. The SU(3) Lie algebra generators are denoted by T^a, while $S^{\text{W, spatial}}(V)$ denotes

the spatial part of the Wilson gauge action $S_W(V)$, meaning the spatial plaquette sum in the absence of a prefactor.

5.3.2 *Fermion smearing*

The above gauge-smeared links V_t are used as input for the Gaussian fermion smearing [57], through the course of which the U(1)–gauge–invariant fermion operator Ψ is transformed into the smeared operator Ψ_{smeared}, through

$$\Psi_{\text{smeared}}(x) = \left(\frac{1 + \kappa_g H(x,y)}{1 + 6\kappa} \right)^N \Psi(y); \tag{5.27}$$

$$H_t(x,y) = \sum_{j=1}^{3} \left\{ V_t(x,j)\delta(x+\hat{j},y) + V_t(x-\hat{j},j)^\dagger \delta(x-\hat{j},y) \right\} . \tag{5.28}$$

.

In our results, we used for the gauge-smearing an evolution time of $t = 180\epsilon$ where the resolution $\epsilon = 0.02$. For the fermion smearing, we used a strength of $\kappa_g = 0.5$ and a collection of different smearing levels of 0, 200 and 400 smearing steps, applied on the source, the sink, or both the source and the sink. We found that results were optimised, in terms of plateau length and statistical error per time-slice, when 400 smearing steps on the source, and no smearing steps on the sink, were used. That the correlator that is smeared on the source and local on the sink should be optimal is also supported by the literature, as smearing on the sink is known to be more vulnerable to statistical noise.

5.4 QUANTIFYING $\Sigma^0 - \Lambda^0$ MIXING

Another complication to the calculation of the masses with isospin breaking is the possibility of mixing between the Σ^0 and Λ^0 octet baryons. While the two baryons share the same quark flavour content, uds, Σ^0 is a triplet under the SU(2)$_I$ isospin symmetry, whereas Λ^0 is a singlet under the isospin symmetry. As both SU(2)$_I$ and SU(3)$_F$ are not exact symmetries, mixing between the two states is possible. The result of this mixing of isospin singlet and triplet states is the physical baryon states, while the ratio of the energy scales of SU(2)$_I$- and SU(3)$_F$-breaking gives an estimate of the mixing angle.

We therefore give an important note regarding the interpretation of what we call the *naive masses* that we calculate in the same way as the other baryons that do not experience isospin mixing, from the interpolating operators as defined in Sec. 5.2. While in the case of unbroken isospin symmetry, the interpolating operator given in this section would be appropriate for the calculation of the Σ^0 mass, in our case it is not, due to the mixing described above. This mixing causes the lowest energy state projected by the Σ^0 interpolating operator to be the Λ^0 state.

Denoting the interpolating operators for Λ^0 and Σ^0 as $\hat{\Lambda}$ and $\hat{\Sigma}$ respectively, and where the baryon states are physical, we may write the correlators using the given interpolating operators as

$$C_{\Lambda\Lambda} = |\langle 0|\hat{\Lambda}|\Lambda^0\rangle|^2 e^{-m_{\Lambda^0} t} + |\langle 0|\hat{\Lambda}|\Sigma^0\rangle|^2 e^{-m_{\Sigma^0} t} \tag{5.29}$$

$$C_{\Sigma\Sigma} = |\langle 0|\hat{\Sigma}|\Lambda^0\rangle|^2 e^{-m_{\Lambda^0} t} + |\langle 0|\hat{\Sigma}|\Sigma^0\rangle|^2 e^{-m_{\Sigma^0} t} \tag{5.30}$$

where C_{XX} denotes that the interpolating operators used for the source and sink are those corresponding to the same baryon. As the Λ^0 baryon is the lighter of the two baryons, we expect the effective mass curves for both of the correlators above to be dominated by the Λ^0 state at large times, unless the contribution from $\langle 0|\hat{\Sigma}|\Lambda^0\rangle$ is extremely small. The mass of

the Σ^0 baryon is only recoverable in the case of isospin-breaking through spectral analysis techniques, and we do not attempt this in this thesis. This may also require increased statistics and an enlarged set of interpolating operators.

Through the derivation of some standard mass formulae, however, we can give an estimation of the values of the 'unmixed' masses. Denoting the unmixed state of the baryon B as B', the matrix representations of the octet baryons may be written in terms of $SU(3)_F$ as

$$(\mathbf{B}_n)^i_j = \begin{pmatrix} \frac{1}{\sqrt{6}}\Lambda^{0'} + \frac{1}{\sqrt{2}}\Sigma^{0'} & \Sigma^+ & p \\ \Sigma^- & \frac{1}{\sqrt{6}}\Lambda^{0'} - \frac{1}{\sqrt{2}}\Sigma^{0'} & n \\ \Xi^- & \Xi^0 & -\sqrt{\frac{2}{3}}\Lambda^{0'} \end{pmatrix}. \tag{5.31}$$

Thus, a proton would then have the matrix representation $(p)^i_j = \delta^{i1}\delta_{j3}$ and the state $(p)^i_j|^j_i\rangle = |^3_1\rangle$. According to the Standard Model, both quark masses and the electromagnetic interaction break the $SU(3)_F$ symmetry. These may be represented through the matrices M for the quark masses and Q for the quark electric charges, which belong to the $SU(3)_F$ octet and have the forms

$$M = \begin{pmatrix} m_u & 0 & 0 \\ 0 & m_d & 0 \\ 0 & 0 & m_s \end{pmatrix} - \frac{1}{3}(m_u + m_d + m_s); \tag{5.32a}$$

$$Q = \frac{1}{3}\begin{pmatrix} 2 & 0 & 0 \\ 0 & -1 & 0 \\ 0 & 0 & -1 \end{pmatrix}. \tag{5.32b}$$

The baryon mass operator H must therefore be a function of M and Q, so that the mass of octet baryon B with state $|B\rangle$ is given by

$$M_B = \langle B|H(M,Q)|B\rangle. \tag{5.33}$$

This mass operator may be expanded in terms of nth-order approximations, where $n = 0, 1, 2$, and where m and q label the $SU(3)_F$-breaking terms by the sources of said breaking:

$$H(M,Q) = H^0 + H^1_m(M) + H^1_q(Q) + \mathcal{O}(H^2). \tag{5.34}$$

Such an expansion, however, does not provide an intuitive hierarchy due to the possibility that the large s quark mass renders the second-order quark mass correction to be of a similar magnitude as the first-order correction from the u and d quark masses.

An expansion may instead performed with respect to symmetry properties of the $SU(3)_F$-breaking effects as opposed to the sources of these breaking effects. This requires the decomposition of matrices M and Q in terms of matrices T_8 and T_3, where T_8 is isospin-invariant while T_3 is not:

$$M = m_{\bar{s}}T_8 + m_{\bar{q}}T_3 \quad \text{and} \quad Q = \frac{1}{6}T_8 + \frac{1}{2}T_3, \tag{5.35}$$

where $m_{\bar{s}} = -(2m_s - m_u - m_d)/6$ and $m_{\bar{q}} = (m_u - m_d)/2$, and where

$$T_8 = \begin{pmatrix} 1 & 0 & 0 \\ 0 & 1 & 0 \\ 0 & 0 & -2 \end{pmatrix}, \quad T_3 = \begin{pmatrix} 1 & 0 & 0 \\ 0 & -1 & 0 \\ 0 & 0 & 0 \end{pmatrix}. \tag{5.36}$$

Mass differences	SU(3)$_F$ parameters
$M_{\Sigma^-} - M_{\Sigma^+}$	$2I_1 - 2I_2$
$M_{\Sigma^-} - M_{\Sigma^0}$	$I_1 - I_2$
$M_n - M_p$	$-2I_2$
$M_{\Xi^-} - M_{\Xi^0}$	$2I_1$

Table 5.3: SU(3)$_F$ parametrisations of different octet mass differences

Using the linearity of the matrix representation, the baryon mass operator H may therefore be rewritten as

$$H(M,Q) = H^0 + H_m^1(m_{\bar{s}}T_8 + m_{\bar{q}}T_3) \tag{5.37a}$$
$$+ H_q^1\left(\frac{1}{6}T_8 + \frac{1}{2}T_3\right) + \mathcal{O}(H^2),$$
$$= H^0 + \left(H_m^1(m_{\bar{s}}T_8) + H_q^1\left(\frac{1}{6}T_8\right)\right) \tag{5.37b}$$
$$+ \left(H_m^1(m_{\bar{q}}T_3) + H_q^1\left(\frac{1}{2}T_3\right)\right) + \mathcal{O}(H^2),$$
$$\equiv H^0 + H_S^1(T_8) + H_I^1(T_3) + \mathcal{O}(H^2), \tag{5.37c}$$

where the same representation is shared by operators in the same set of outer parentheses. The hierarchy of terms is given by

$$H^0 \gg H_S^1 \gg H_I^1 \sim \mathcal{O}(H^2), \tag{5.38}$$

as H_S^1 contains the first-order correction from m_s and $\mathcal{O}(H^2)$ contains the second-order correction from m_s. Care must therefore be taken to consider only those physical quantities that are not affected by the m_s correction when discarding $\mathcal{O}(H^2)$ in the calculation of H_I^1.

While the eigenstates of $H^0 + H_S^1$ define the baryon wave functions of Eq. (5.31) with the properties

$$\langle B'|H^0 + H_s^1|B\rangle = \langle B'|B\rangle = 0 \quad \text{if } B' \neq B, \tag{5.39}$$

the physical baryon states B_P are the eigenstates of the entire baryon mass operator H, having the property

$$\langle B'_P|H|B_P\rangle = 0 \quad \text{if } B'_P \neq B_P. \tag{5.40}$$

Applying the Wigner-Eckart theorem in order to parametrise the matrix element from Eq. (5.33) in terms of the SU(3)$_F$ parameters M_0, S_i and I_i gives

$$\langle B'|H^0 + H_S^1|B\rangle = M_0 + S_1\text{Tr}(\overline{\mathbf{B}}'_n T_8 \mathbf{B}_n) + S_2\text{Tr}(\overline{\mathbf{B}}'_n \mathbf{B}_n T_8), \tag{5.41a}$$
$$\langle B'|H_I^1 + \mathcal{O}(H^2)|B\rangle = I_1\text{Tr}(\overline{\mathbf{B}}'_n T_3 \mathbf{B}_n) + I_2\text{Tr}(\overline{\mathbf{B}}'_n \mathbf{B}_n T_3) + \mathcal{O}(H^2), \tag{5.41b}$$

where $\overline{\mathbf{B}}_n \equiv \mathbf{B}_n^\dagger$. The above SU(3)$_F$ parameters should be related to physics through experiment. The famous GMO and CG mass formulae may be derived from Eqs. (5.41a) and (5.41b) respectively. Consistency of the equations requires that M_0, S_1 and S_2 be determined through the mean masses of isospin subgroups, while I_1 and I_2 should be determined through differences in mass between baryons that are isospin-related.

From Table 5.3, as well as the famous CG mass formula, which is satisfied trivially under U-spin symmetry due to mass degeneracies, we obtain the formula

$$M_{\Sigma^{0'}} = \frac{1}{2}(M_{\Sigma^+} + M_{\Sigma^-}). \qquad (5.42)$$

from which we may predict the unmixed Σ^0 mass. Through instead taking the average masses of the isospin subgroups and using Eq. (5.41a), the famous GMO formula may be derived:

$$M_{\Lambda^0} \approx M_{\Lambda^{0'}} = \frac{1}{3}[(M_{\Xi^-} + M_{\Xi^0}) + (M_p + M_n) - (M_{\Sigma^+ + \Sigma^-})/2], \qquad (5.43)$$

through which the unmixed Λ^0 may be predicted. It should be noted, however, that the above derivation relies on a linear expansion around the $SU(3)_F$-symmetric theory that may not be entirely appropriate for our ensembles, particularly those that have larger than physical α.

Given that the Σ^0 and Λ^0 states mix according to

$$|\Lambda^0\rangle = \cos\theta_{\Sigma^0-\Lambda^0}|\Lambda^{0'}\rangle - \sin\theta_{\Sigma^0-\Lambda^0}|\Sigma^{0'}\rangle, \qquad (5.44a)$$

$$|\Sigma^0\rangle = \cos\theta_{\Sigma^0-\Lambda^0}|\Sigma^{0'}\rangle - \sin\theta_{\Sigma^0-\Lambda^0}|\Lambda^{0'}\rangle, \qquad (5.44b)$$

the $\Sigma^0 - \Lambda^0$ mixing angle is known to be given by [58][59]

$$\tan\theta_{\Sigma^0-\Lambda^0} = \langle\Sigma^{0'}|H_I^1|\Lambda^{0'}\rangle/(M_{\Sigma^0} - M_{\Lambda^0}), \qquad (5.45)$$

where the mixing mass matrix element is given in terms of the isospin-breaking mass differences for the octet baryons,

$$\langle\Sigma^{0'}|H_I^1|\Lambda^{0'}\rangle = \frac{1}{\sqrt{3}}(I_1 + I_2), \qquad (5.46)$$

where we would use $I_1 + I_2 = (M_{\Sigma^0} - M_{\Sigma^+}) - (M_n - M_p)$, given the knowledge of the necessary baryon masses.

5.5 COMPARISON OF ERROR ESTIMATION BETWEEN JACKKNIFE AND GAMMA METHODS

Figure 5.1 shows a comparison between the error on the effective mass curve carried out using the Jackknife method of error analysis vs. the Gamma method, which takes into account the autocorrelation of the data series. These methods are described in App. E. Later, we show GEVP results that were produced using the Jackknife method; the final baryon mass results presented are, however, produced using the Gamma method. We see that the values of the effective mass at each timepoint are identical, while there is a difference in the error per timepoint calculated with the two methods. As expected, the Gamma method gives a larger error. Keeping in mind Eq. (2.49), we can perform an approximate check of the consistency of the difference in errors with the value of $\tau_{\text{int}} = 1.72 \pm 0.59$. This value was measured on the effective mass curve for the plateau between $[22, 28]$ which is weighted by the inverse variance of the timepoints, using the Gamma method. If we therefore take for each timepoint

$$\tau_{\text{int}} = \frac{1}{2}\left(\frac{\sigma_\Gamma}{\sigma_{\text{JK}}}\right)^2, \qquad (5.47)$$

and take a naive mean over the range $[22, 28]$, we obtain the rough estimate $\tau_{\text{int}} = 1.3 \pm 0.3$, where the error is estimated through simply taking the standard deviation of the timepoints. We see that this rough estimate of τ_{int} is consistent within error with the value calculated
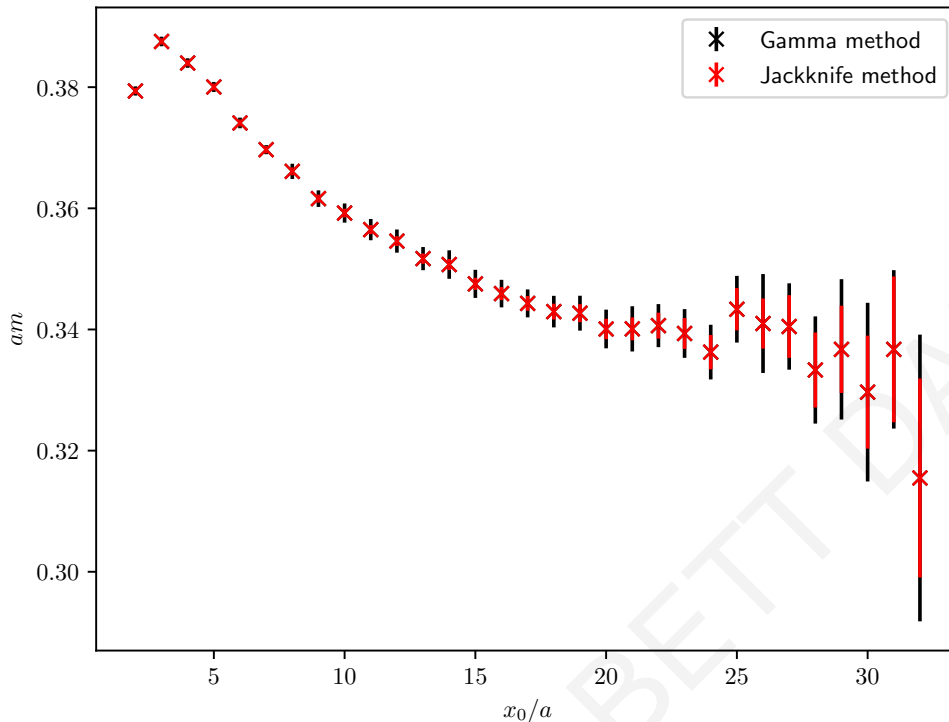
Figure 5.1: Comparison of error on individual timepoints of p effective mass plot (without reweighting or finite-volume corrections and in lattice units) using both the Jackknife method and the Gamma method.

through the Gamma method, and therefore that the magnitude of errors calculated through the Jackknife method and through the Gamma method is consistent with our expectations.

5.6 GEVP

5.6.1 *Method*

We will here outline a method of spectral decomposition, the Generalised Eigenvalue Problem (GEVP). In this method, we consider a matrix formed of correlators, where the two axes represent operators along the source and sink respectively. These operators may include different levels of smearing applied on either the source or sink, or indeed different choices of unsmeared interpolating operator. For simplicity, we will be considering the case in which the matrix of correlators is square, meaning that there are the same number of operators considered at the source and the sink, and in which the operators for the source and the sink are the same. A discussion of the case in which either of these conditions is not true can be found in [60].

At large Euclidean times t, and by neglecting finite-temperature effects, we find that a hadronic correlation function behaves like

$$C(t) = Ze^{-mt} + \cdots . \tag{5.48}$$

Here, the hadronic ground state mass is given by m. Excited energy states, which are suppressed at large times, are given by the additional terms hinted at above. In fact, the energy gap between the ground state and the first excited state determines to what extent

66

the excited states are suppressed. This suppression allows one to extract the ground state mass through taking the logarithm and finding the plateau at large times. This is made more difficult, however, by the exponential decay of the signal-to-noise ratio with increasing t. One is therefore motivated to try another strategy that provides a separation of the contributions from the ground state and the excited states, and thus an extension of the ground state plateau to smaller times, as well as some quantification of the excited states of the hadron's spectrum.

Although the following analysis is valid for non-Hermitian correlator matrices, in our analysis we enforced Hermiticity by redefining $C \to C + C^\dagger$ in order to remove any non-Hermiticity introduced in the calculation and to guarantee real eigenvalues.

Constructing the non-symmetric matrix C_{ij} of correlator functions from correlators using the operators $O_i(t)$ on the sink and $\tilde{O}_j(t)$ on the source, we can write

$$C_{ij}(t) = \langle O_i(t)\tilde{O}_j^\dagger(0)\rangle = \langle 0|O_i e^{-\hat{H}t}\tilde{O}_j^\dagger|0\rangle, \tag{5.49}$$

where the Hamiltonian is given by $\hat{H}$. Defining the eigenstates $|n\rangle$ of the Hamiltonian to satisfy

$$\hat{H}|n\rangle = E_n|n\rangle, \qquad Z_i^n = \langle 0|O_i|n\rangle, \qquad \tilde{Z}_j^{n*} = \langle n|\tilde{O}_j^\dagger|0\rangle, \tag{5.50}$$

we can decompose the correlator matrix in terms of energy eigenstates;

$$C_{ij}(t) = \sum_{n=1}^{\infty} Z_i^n \tilde{Z}_j^{n*} e^{-E_n t}. \tag{5.51}$$

This may also be written in matrix form as

$$C(t) = Z\Lambda\tilde{Z}^\dagger, \tag{5.52}$$

where

$$\Lambda = \mathrm{diag}(e^{-E_1 t}, e^{-E_2 t}, \dots) \equiv \mathrm{diag}(\lambda_1(t), \lambda_2(t), \dots);$$
$$\lambda_i(t) \equiv e^{-E_i t}.$$

Assuming that the system has N non-degenerate energy levels that are ordered as

$$E_1 < E_2 < E_3 \cdots, \tag{5.53}$$

and that we have a set of N source interpolating operators $\tilde{O}_A$ and N sink interpolating operators O_A, the energy levels may be determined through the correlator matrix C_{AB}. We may start by constructing the matrices

$$Q^\dagger = (Z)^{-1}, \qquad \tilde{Q} = (\tilde{Z}^\dagger)^{-1}, \tag{5.54}$$

which, as Z and $\tilde{Z}$ are square matrices and $\det(Z) \neq 0$, $\det(\tilde{Z}) \neq 0$, is always possible. The non-vanishing determinants are guaranteed by the linear independence of the operators O_A and $\tilde{O}_A$. Expressing the correlator thereby as

$$Q^\dagger C(t)\tilde{Q} = \Lambda(t) \tag{5.55}$$

allows one to extract the energies. This expression may be rewritten using the factorisation $\Lambda(t) = \Lambda(t_0)\Lambda(t - t_0)$ as

$$\begin{aligned} C(t)\tilde{Q} &= Q^\dagger\Lambda(t) = Z\Lambda(t_0)\Lambda(t - t_0) \\ &= Z\Lambda(t_0)\tilde{Z}^\dagger\tilde{Q}\Lambda(t - t_0) = C(t_0)\tilde{Q}\Lambda(t - t_0), \end{aligned} \tag{5.56}$$

through which we see that $\tilde{Q}$ is a solution to the generalised eigenvalue problem; this may be written equivalently for each column $\tilde{q}_i$ of matrix $\tilde{Q}$, with $\tilde{q}_i$ being a generalised right eigenvector satisfying the equation

$$C(t)\tilde{q}_i = C(t_0)\tilde{q}_i\lambda_i(t - t_0). \tag{5.57}$$

A similar equation may be used to obtain the solution Q to the left generalised eigenvalue problem. The eigenvalues Λ obtained through this method may then be used to obtain the energy levels in the usual way

$$E_i = \frac{1}{a}\log\left(\frac{\lambda_i(t - t_0)}{\lambda_i(t + a - t_0)}\right). \tag{5.58}$$

One may show that the GEVP behaves similarly to the case of a symmetric correlator matrix when there is the non-ideal case in which the basis of interpolating fields has a different dimension to that of the space on which the Hamiltonian acts. This allows one to choose a somewhat arbitrary number of interpolating operators as the basis of the correlator matrix.

5.6.2 *Results*

The N^2 different smearing levels at which we measured the correlators can be represented as an $N \times N$ matrix that enters the GEVP, with rows corresponding to the source smearing level and columns corresponding to the sink smearing level as described in Sec. 5.3, and the elements may accordingly be labelled from 0 to $N^2 - 1$ with the sink smearing level varying the fastest. For clarity, the results presented in this section are not calculated using reweighting factors, unlike the final mass results given in Sec. 6.1 using the Gamma method. The errors on the masses are calculated using the Jackknife method throughout.

Taking the proton as an example, results from the different smearing levels for the proton mass for ensemble `A500a50b324` are given in Table 5.4. These have been calculated each with an individually chosen plateau range. We see that the different levels of smearing agree with each other within error, and with the ground state energy found through the GEVP. We found that results with a consistently small error in comparison with the other smearing levels, and similar to the error found using the GEVP, were found for the state that was most smeared at the source and local at the sink, in line with the literature. As this was seen to be the case for ensembles `A500a50b324` and `A360a50b324+RW2`, which were measured using three different levels each on the source and the sink, we restricted the measurements on the ensembles measured afterwards to skip the intermediate level of smearing and measure only for both 0 and 400 smearing steps on the source and the sink, which still allows a two-state GEVP analysis. This was done in order to most efficiently exploit computing resources, as the computing time saved in computing four smearing levels instead of nine could then be used to double the number of random hits per configuration for the ensembles with close-to-physical α.

The GEVP and the comparison of it with the individual smearing levels then informed our choice to analyse a single smearing level, with 400 steps at the source and 0 at the sink, using the Gamma method, as there was little difference in the errors between the GEVP ground state and the results from this smearing level.

As an example, the GEVP spectrum for the proton is given by Fig. 5.2. The three energy levels that may be distinguished through the GEVP method are given in Fig. 5.2a, where the plateau of the ground state is shown by the horizontal line. The plateau error is not shown here. If we take a weighted plateau between [11,13] for the second lowest energy level, we find an energy of 2137 ± 52 MeV, using the final measured value of the lattice spacing for the ensemble `A500a50b324` and neglecting its comparatively small error in the error propagation.
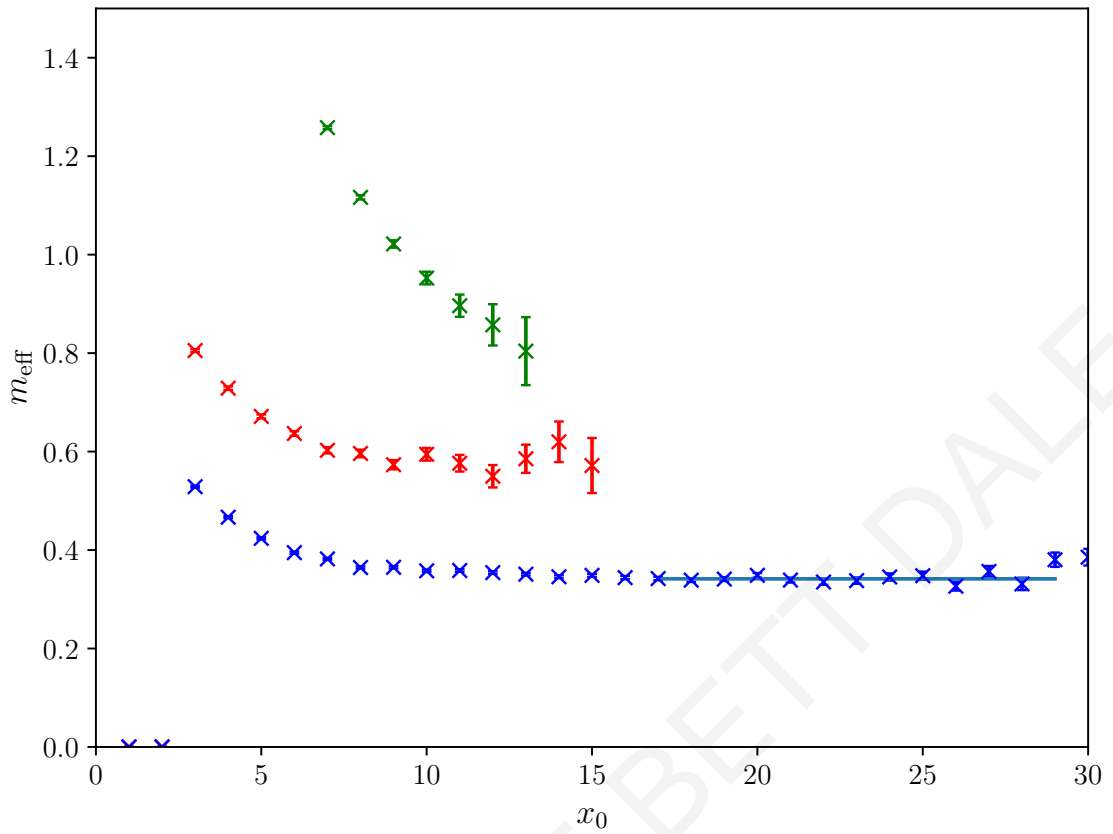
(a) GEVP spectrum. The plateau value and range is given by the horizontal line, whereas the plateau error is not shown.
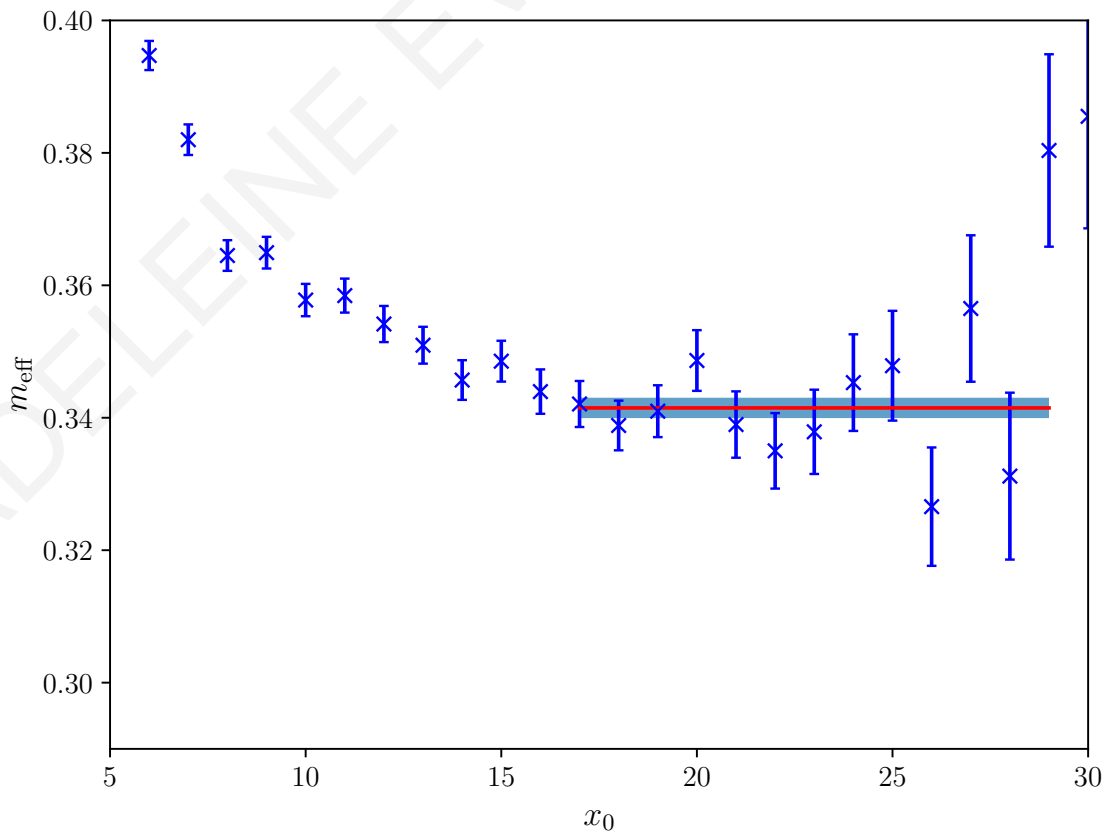
(b) GEVP ground state with plateau value and error.

Figure 5.2: GEVP for proton from ensemble `A500a50b324` using Jackknife error analysis. Effective masses given in lattice units.

0)	0.3465 ± 0.0085	1)	0.3431 ± 0.0045	2)	0.3457 ± 0.0032
3)	0.3417 ± 0.0022	4)	0.3421 ± 0.0028	5)	0.3392 ± 0.0025
6)	0.3408 ± 0.0023	7)	0.3401 ± 0.0022	8)	0.3384 ± 0.0030

Table 5.4: Proton mass results from different smearing levels labelled $0 \dots 8$ on ensemble `A500a50b324`, using Jackknife analysis program and given in lattice units. Smearing levels take values of 0,200,400 steps, increasing on the sink from left to right and increasing on the source from top to bottom. The unsmeared level is therefore labelled 0. The plateaux were chosen individually for each smearing level, and the GEVP gave a ground state energy of 0.3415 ± 0.0015 in lattice units.

Compared with the energy of a combined (proton + photon) state in ensemble `A500a50b324`, $\sqrt{M_p^2 + (\frac{\pi\sqrt{3}}{L})^2} + \frac{\pi\sqrt{3}}{L} = 2068(13)$, we see that the two results have slightly more than a 1σ difference between them. This state may still be a combined (proton + photon) state, as it seems that the second excited state may not have reached its plateau before statistical noise takes over the signal.

We note as an aside that the consistency of the lowest energy levels of the GEVP spectrum has been checked for different numbers of smearing levels and for different normalisation times (t_0 in Eq. (5.56)).

The GEVP ground state of the proton from ensemble `A500a50b324` is shown in Fig. 5.2b, with the plateau average and range shown by the horizontal red line and the plateau error shown in blue. We see a plateau that starts rather early at $t = 15$ and starts to diminish in quality around $t \sim 20$.

5.7 EXTRACTION OF SPECTRAL DENSITIES

An alternative approach to the exploration of the spectrum is the extraction of spectral densities from correlators. In our work, this is used in a very preliminary way to give a more complete picture of the spectrum, particularly for hadrons for which a well-defined plateau may be less obvious.

While, in this work the spectral densities extracted are used to explore the baryon spectrum, this technique may also be used to investigate, for example, the differential cross section of the process $e^+e^- \to$ hadrons, as well as the non-leptonic flavour-changing decay rates of both kaons and heavy flavoured mesons, thermodynamic quantities that arise through the study of the quark-gluon plasma and in finite-temperature QCD, and the deep inelastic scattering cross-section.

The problem of predicting theoretically the hadronic spectral densities in a non-perturbative and model-independent setup, while being in theory approachable from first-principles in lattice QCD, is made significantly more difficult due to the non-trivial theoretical and numerical problems that arise when trying to extract spectral densities from results calculated on the lattice. This is due to the systematic and statistical errors that inevitably affect lattice results, specifically the Euclidean time-ordered correlators calculated on a finite volume with spatial linear extent L and spatial volume $V = L^3$ and at discrete space-time coordinates x, which can be represented as

$$C(t) = \frac{1}{L^3} \sum_{\mathbf{x}} T\langle 0|O(x)\overline{O}(0)|0\rangle_L, \tag{5.59}$$

where O and $\overline{O}$ are generic hadronic operators. These correlators make up the primary observables that result from the lattice calculation. The following explanation does not attempt to make discussion of any cutoff effects that lead to a dependence upon the lattice

spacing for different quantities, but only considers that we know the correlator values only at discrete values of space-time.

Assuming for simplicity an infinite temporal extent of the lattice, one may write the above correlator as

$$C(t) = \int_0^\infty dE \rho_L(E) e^{-tE}, \tag{5.60}$$

for positive Euclidean times $t > 0$. Here, the associated spectral density $\rho_L(E)$ is given by

$$\rho_L(E) = \frac{1}{L^3} \sum_{\mathbf{x}} \langle 0|O(0,\mathbf{x})\delta(E - H_L)\overline{O}(\mathbf{0})|0\rangle_L. \tag{5.61}$$

The above expressions set the stage for a discussion on some of the problems that occur when trying to extract spectral densities from lattice results.

The first problem we encounter is caused by the ever-present statistical fluctuations that affect the correlator, which, apart from some very specific cases, increase exponentially with time relative to the signal and are therefore particularly problematic at large time separations. If we were to try to extract $\rho_L(E)$ numerically from the measured correlator $C(t)$, an inverse Laplace-transform would be required, which becomes an ill-posed problem when statistical fluctuations are included.

We find another problem caused by the discreteness of the Hamiltonian spectrum of a finite-volume system. In this case, the finite-volume spectral density has support only at the eigenvalues $E_n(L)$ of H_L, and is therefore represented as a sum of delta functions rather than an integral,

$$\rho_L(E) = \sum_n w_n(L)\delta(E - E_n(L)). \tag{5.62}$$

The consequence of this is that we cannot directly associate the finite-volume spectral density with any physical observable, even if it were computed exactly.

A solution to these problems has been found [61, 62] in which the spectral densities are smeared in order to increase the information that can be extracted from correlators with statistical noise. This idea forms the basis of the Backus-Gilbert method. The smeared spectral density is defined as

$$\hat{\rho}_L(\sigma, E_*) = \int_0^\infty dE \Delta_\sigma(E_*, E)\rho_L(E), \tag{5.63}$$

where $\Delta_\sigma(E_*, E)$ are smearing functions with support coming from a region centred around E_* with width σ. Naturally, a condition on these smearing functions is that they become Dirac delta functions when the limit $\sigma \to 0$ is taken. The advantage of using the smeared spectral densities is that, at fixed smearing function, the study of their infinite-volume limit is well-posed, and that they are smooth functions of the energy. This simultaneously alleviates both of the problems discussed above. The infinite-volume spectral density may therefore be obtained through taking the strictly-ordered double limit

$$\rho(E_*) = \lim_{\sigma \to 0} \lim_{L \to \infty} \hat{\rho}_L(\sigma, E_*), \tag{5.64}$$

provided that over different volumes, the smearing function used is kept constant. However, it should be kept in mind that for the purpose of comparing experimental results with theoretical expectations, it may not be necessary to take fully the limit of vanishing σ.

The Backus-Gilbert method, despite managing to efficiently control the effect of statistical fluctuation on the estimation of smeared spectral densities, has a particular problem that complicates its use in Lattice QCD. In this method, the shape of the smearing function is the procedure's output, and is optimised in order to best represent the data, taking into account the number of observations, which for us means the temporal extent of $C(t)$, and

71

the statistical errors embedded within $C(t)$. In lattice QCD, these values change between calculations carried out at different lattice volumes. This means that, using the Backus-Gilbert method, we would obtain different smearing functions at different volumes, rendering taking the infinite-volume limit either impossible or at least extremely complicated.

The method presented below [23] is based on the Backus-Gilbert approach [61] (see also [63]), in that statistical errors are controlled through the same smearing mechanism. However, as the smearing function is here an input of the procedure, it is designed with the ease of taking the infinite-volume and continuum limits in mind. An expense of this modification is that the target smearing function is open to distortion from the finite number of observables and from the statistical errors present in the correlator. This method nonetheless provides a quantification of the systematic error this creates. Of course, when the magnitude of the statistical error is taken to be vanishing, and when the number of temporal points in $C(t)$ is taken to infinity, any distortion vanishes and an exact reconstruction of the smeared spectral density, using the smearing functions provided as input, is recovered.

5.7.1 *Method*

The philosophy of the method presented here is to input a target smearing function, an optimal approximation of which is then aimed for through a summation over basis functions. The accuracy that can be attained, as described above, is limited by the number of temporal lattice points in the correlator and by the inevitable statistical fluctuations present in the measured correlators.

An obvious choice for a smearing function that tends to a Dirac delta function in the limit of vanishing width is a Gaussian function. The smearing function

$$\Delta_\sigma(E_*, E) = \frac{e^{-\frac{(E-E_*)^2}{2\sigma^2}}}{\sqrt{2\pi}\sigma} \tag{5.65}$$

is a Gaussian function centred around E_* with width σ.

An optimal approximation of the above smearing function in terms of basis functions b_T is given by

$$\overline{\Delta}_\sigma(E_*, E) = \sum_{t=0}^{t_{\max}} g_t(\lambda, E_*) b_T(t+1, E). \tag{5.66}$$

Here $t_{\max} < T/2$. For baryons measured with periodic boundary conditions in time, we use the basis functions given by

$$b_T(t, E) = e^{-tE}. \tag{5.67}$$

The smeared spectral densities may be computed using the correlator and the coefficients g_t for discrete values of E_*,

$$\hat{\rho}_L(\sigma, E_*) = \sum_{t=0}^{t_{\max}} g_t(E_*) C(t+1). \tag{5.68}$$

The coefficients g_t in the above approximation are determined through the minimisation of a functional $W[\lambda, g]$ consisting of a deterministic part that contains the functional $A[g]$, and a functional representing the error, that contains the functional $B[g]$,

$$W[\lambda, g] = (1-\lambda)A[g] + \lambda \frac{B[g]}{C(0)^2}. \tag{5.69}$$

In this method, the deterministic functional quantifies the discrepancy between the target smearing function and its approximation,

$$A[g] = \int_{E_0}^{\infty} dE\, e^{\alpha E} |\overline{\Delta}_{\sigma}(E_*, E) - \Delta_{\sigma}(E_*, E)|^2, \tag{5.70}$$

where $\alpha < 2$ is some real constant that we have chosen to be $\alpha = 1.99$. One must chose the lower integration limit E_0 such that the finite volume spectral density $\rho_L(E_0) = 0$. As a mass gap appears in both the case of connected correlators in QCD and of the charged sectors of QCD+QED, this is always possible.

The minisation procedure is solved through

$$\mathbf{g}(\lambda, E_*) = \mathtt{W}^{-1}(\lambda)\mathbf{f}(\lambda, E_*) \tag{5.71}$$

where vector $\mathbf{f}(E_*)$ has the entries

$$f_t(\lambda, E_*) = (1 - \lambda) \int_{E_0}^{\infty} dE\, b_T(t+1, E)\Delta_{\sigma}(E_*, E)e^{\alpha E}. \tag{5.72}$$

The elements of the matrix $\mathtt{W}$ are given by

$$\mathtt{W}_{tr}(\lambda) = (1 - \lambda)\mathtt{A}_{tr} + \lambda\frac{\mathtt{Cov}_{tr}}{C(0)^2}, \tag{5.73}$$

where

$$\mathtt{A}_{tr} = \int_{E_0}^{\infty} dE\, b_T(t+1, E)b_T(r+1, E)e^{\alpha E}. \tag{5.74}$$

The optimisation of the choice of $\lambda = \lambda^*$, at which the minimisation is carried out, uses the method discussed in Sec. V.A. of [24], which selects the value of λ for which the systematic error is comparatively small such that the system is in the statistics-limited regime.

Simplifying for now our discussion by ignoring statistical errors, in essence the aim is to approximate best the smeared target function using the basis functions $b(t, E)$, constrained by the functional $A[g]$ defining the norm. Under the assumptions that the target function is analytic within the limits $[E_0, \infty)$ and that it is faster to decay than any power of E approaching infinity, one can see that, by enlarging the space that the basis functions span, i.e. by increasing $t_{\max}$, the error of the approximation can be reduced to an arbitrary size. This is made more evident when the deterministic functional is rewritten using the basis functions $b_T(t) = e^{-Et}$, and using the change of integration variables $x = e^{-E}$:

$$A[g] = \int_0^{e^{-E_0}} dx\, x^{1-\alpha} \left| \sum^{t_{\max,t=0}} g_t x^t - \frac{\Delta_{\sigma}(E_*, -\log(x))}{x} \right|^2. \tag{5.75}$$

BARYON RESULTS

6.1 BARYON MASS RESULTS

In the following, we will refer to the number of point sources placed at random time-slices of the lattice as hits. We shall refer to the region over which the average is calculated, weighted by the inverse variance of the individual time-points, as the plateau. Though some plateaux may have the same chosen range in t, the selection of plateau range was decided for each object individually.

The baryon interpolating operators that we used are described in Sec. 5.2. These are made U(1)-gauge-invariant through the dressing factors described in Sec. 4.5. The baryon effective masses $M(x_0)$ were calculated using the formula

$$M(x_0) = \frac{1}{a}\log\frac{C(x_0)}{C(x_0 + a)}. \tag{6.1}$$

The plateau was chosen as described for the mesons in Sec. 4.5, with the plateau range chosen through a visual inspection of the variation of the value of the plateau with respect to its starting timepoint.

The baryon mass values calculated on different ensembles are given in Table 6.1, whilst the mass differences for the baryons can be found in Table 6.2. Plots of the baryon effective mass curves for each ensemble are found in Figs. 6.1-6.5, whereas the plots for the effective mass curves for the mass differences may be found in Figs. 6.6-6.10.

We obtained baryon masses with a precision between 1-5%, with a higher precision on those ensembles with heavier pions, while the precision on the mass differences varied more between ensembles. While we may expect to get close to the physical values for some of the mass differences, as we have some ensembles with α_R and $m_u - m_d$ close to their physical values, we do not expect to be able to approach in this work the physical values for the baryon masses, as we simulating in a U-spin-symmetric setup and at large pion masses. The approach to the physical point is left for future work.

6.1.0.1 *A450a07b324*

The ensemble A450a07b324 has a large pion mass $M_{\pi^\pm} = 451.2(4.3)$ with respect to all ensembles apart from A500a50b324 and an $\alpha_R = 0.007076(24)$ value close to the physical value and the other ensembles with the same bare α. This ensemble consists of only 1000 configurations as opposed to $\sim$2000 for all of the other ensembles on which the baryons were measured. Eight hits were used for the measurement of this ensemble.

With these values and run parameters in mind, if we inspect the effective mass plots for ensemble A450a07b324, shown in Fig. 6.1, we see that they are generally well-behaved in the case of the spin-$\frac{1}{2}$ baryons, with a level portion of the curve suggesting clearly the plateau region, and with relatively low statistical noise until the region of $t \sim 28$ to the middle of the lattice. Even so, in this end region the errors are still reasonably small. The plateau was chosen to be $t \in [21, 28]$ for all masses. For this ensemble, there is little variation between the results for the spin-$\frac{1}{2}$ baryons: their values, errors and indeed their plots. The Ω^- baryon has a weaker signal-to-noise ratio than the other objects and deteriorates into fluctuations at
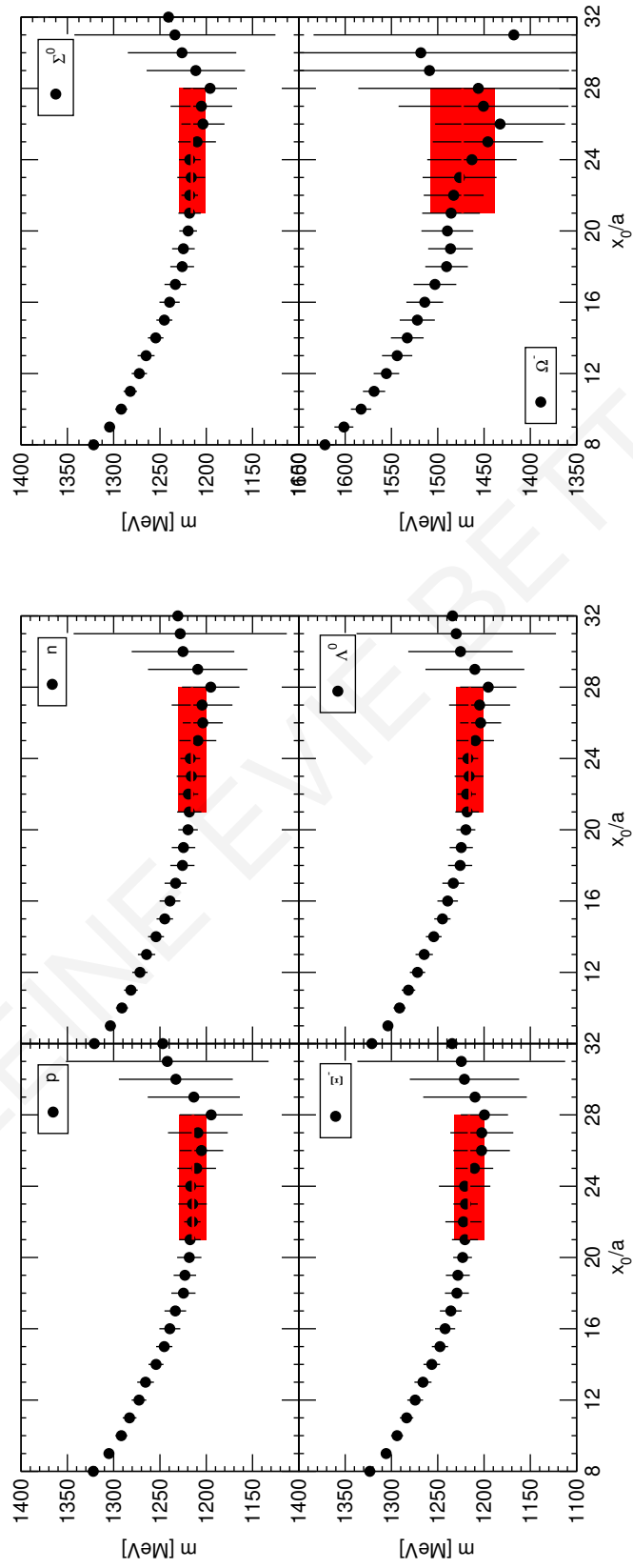
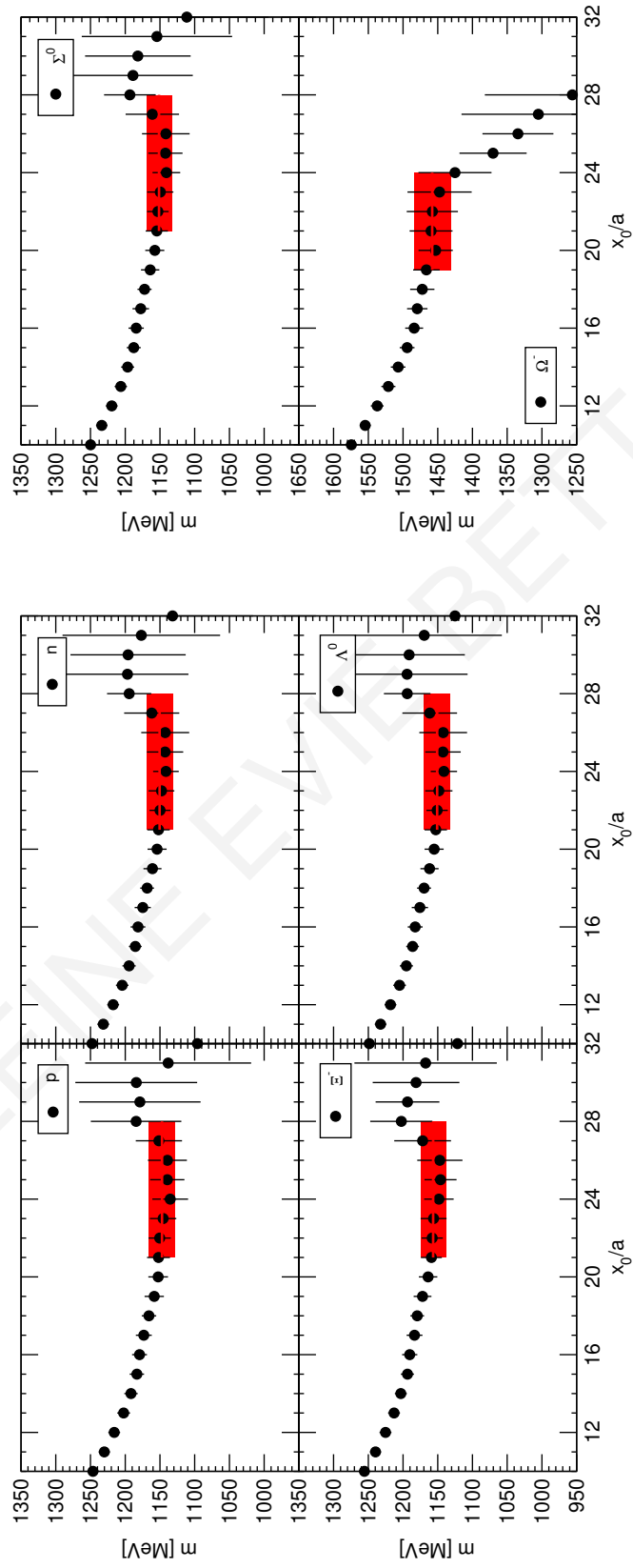Figure 6.1: Baryon masses measured on ensemble A450a07b324.

Figure 6.2: Baryon masses measured on ensemble A380a07b324.
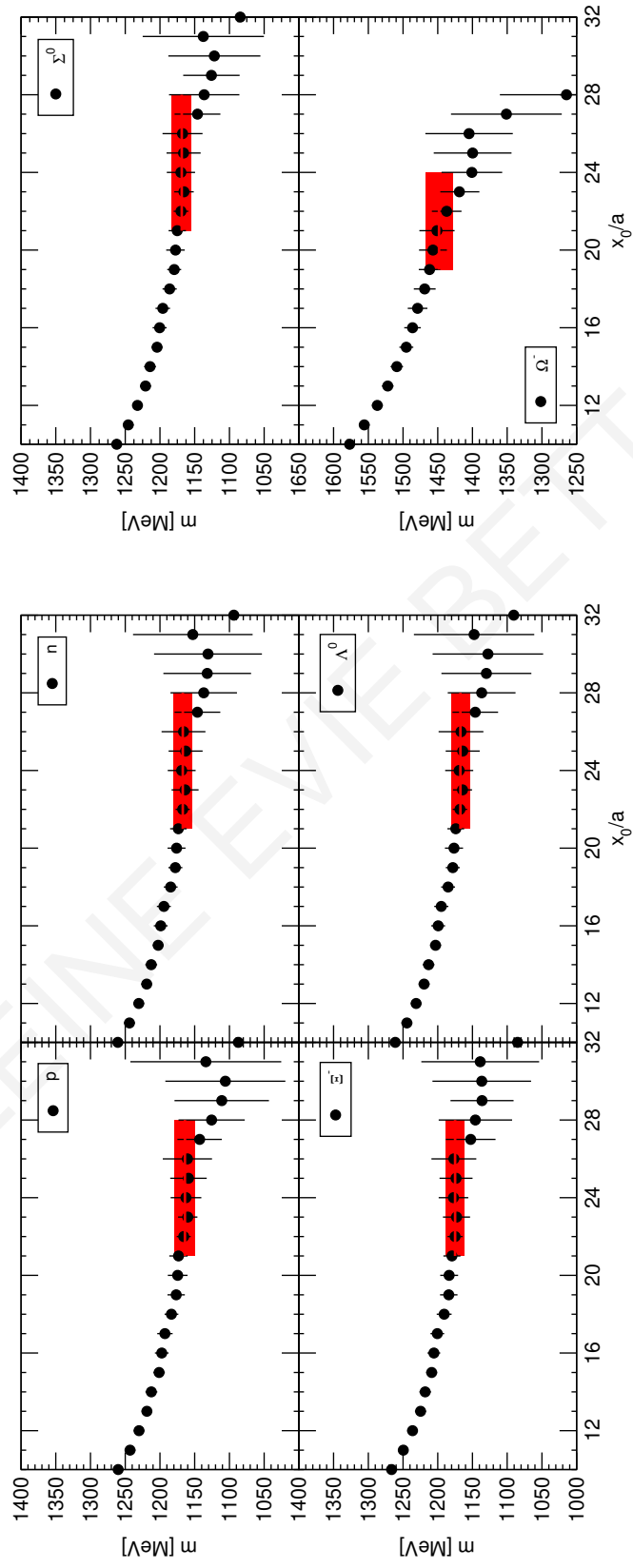
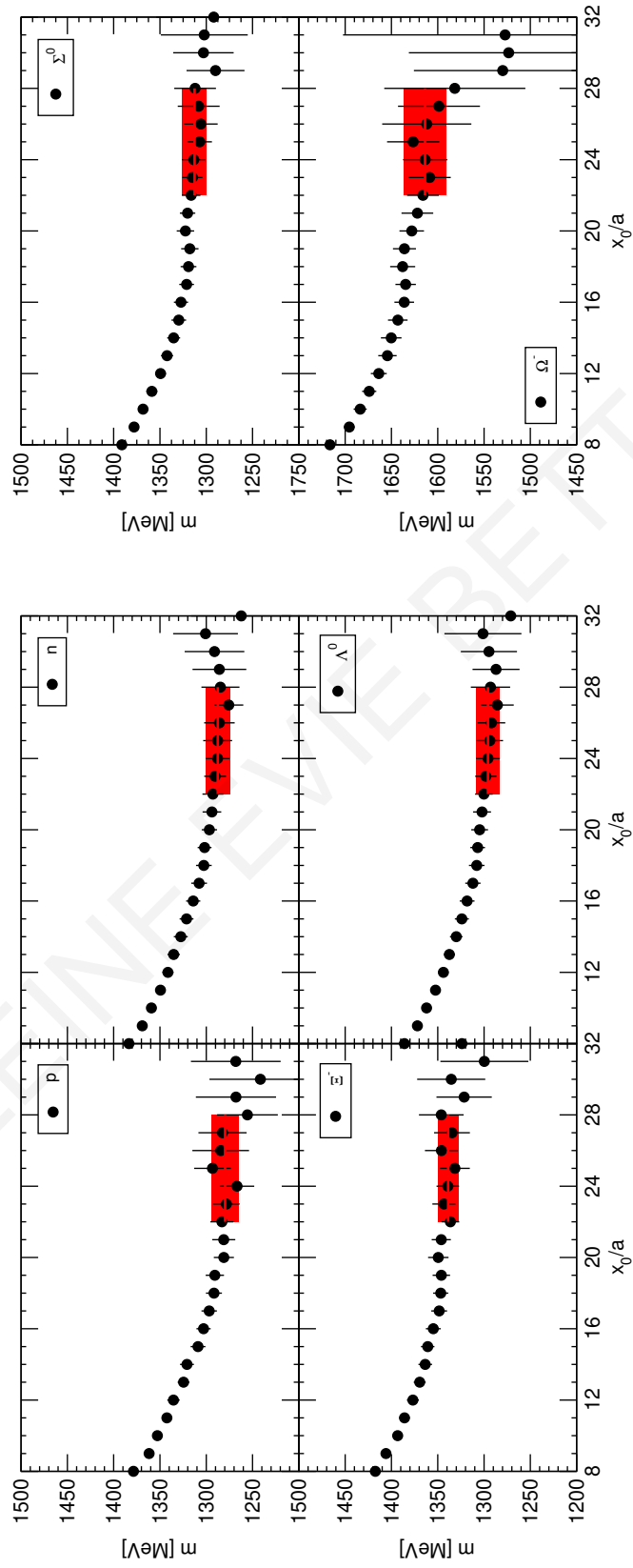Figure 6.3: Baryon masses measured on ensemble A380a07b324+RW1.

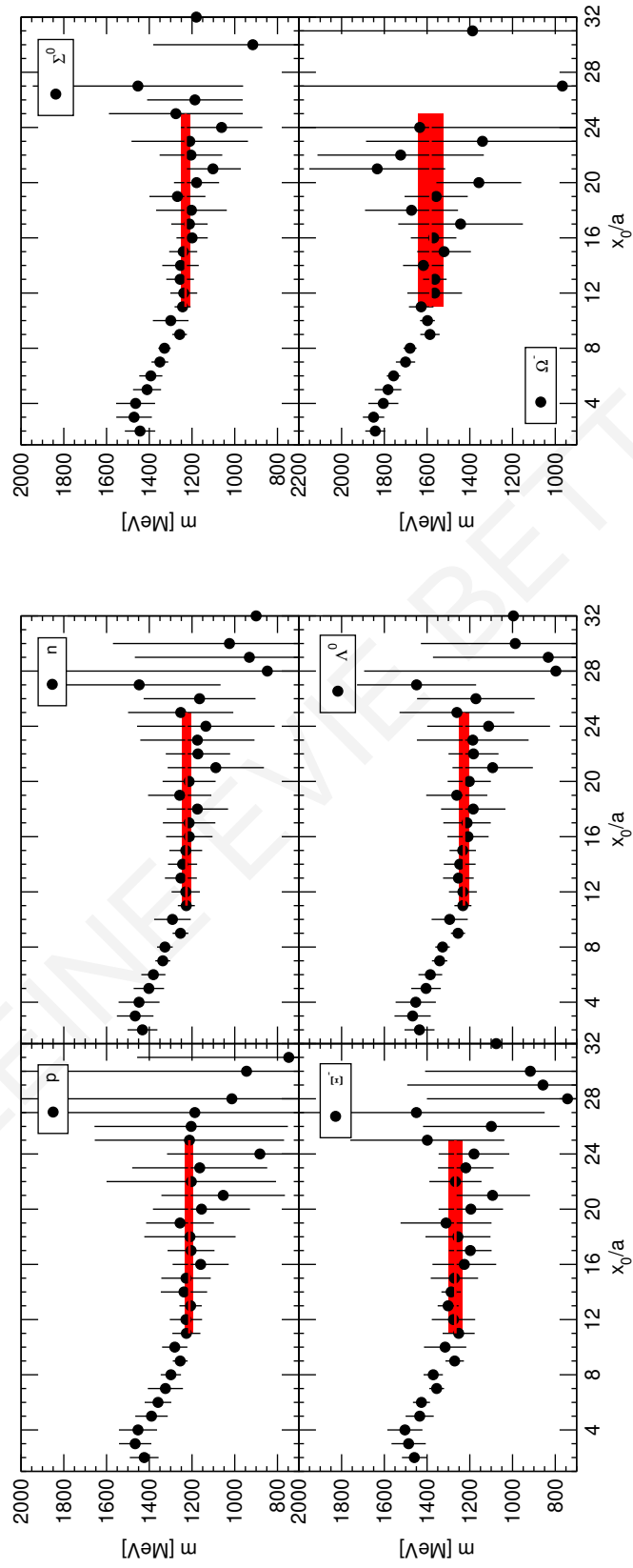Figure 6.4: Baryon masses measured on ensemble A500a50b324.

Figure 6.5: Baryon masses measured on ensemble A360a50b324+RW2.
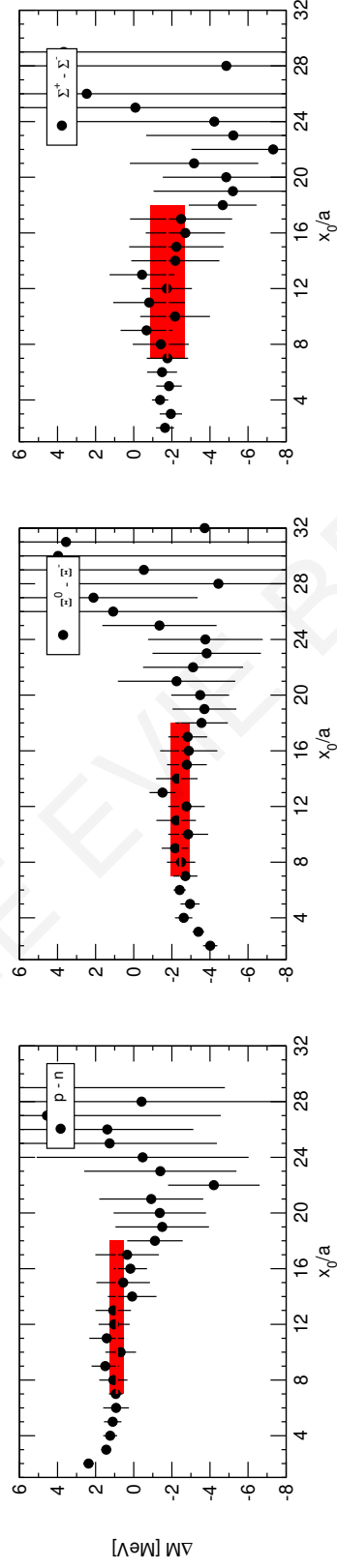
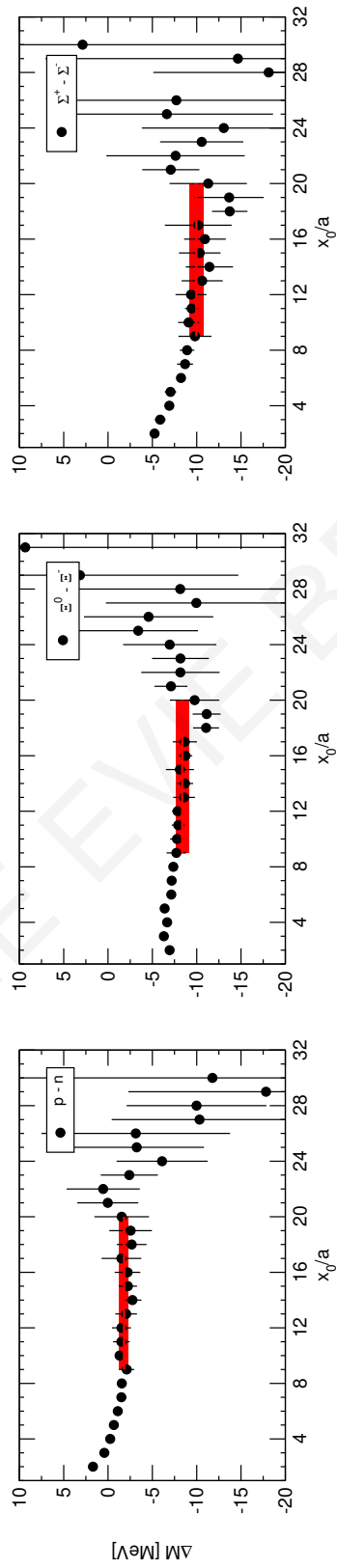Figure 6.6: Baryon mass differences measured on ensemble A450a07b324.

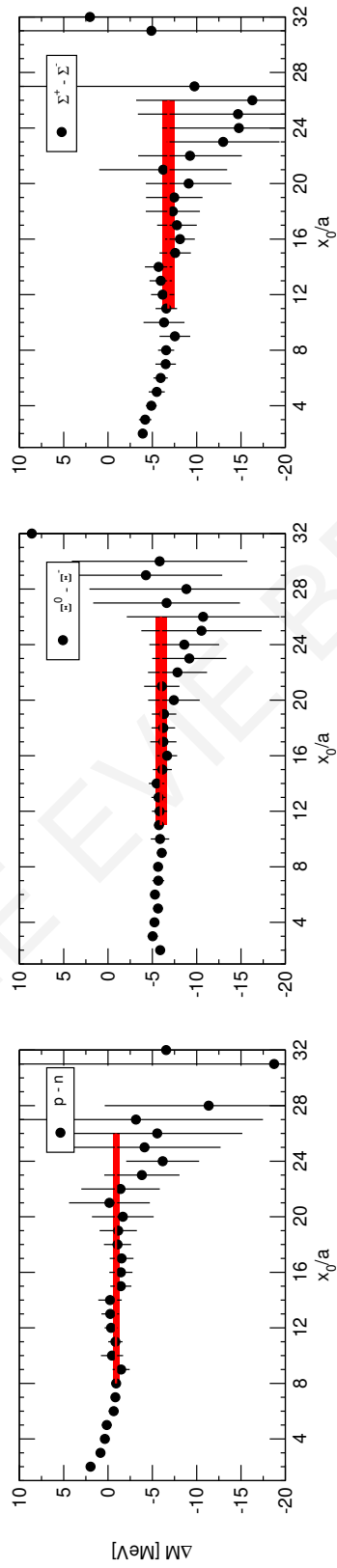Figure 6.7: Baryon mass differences measured on ensemble A380a07b324.

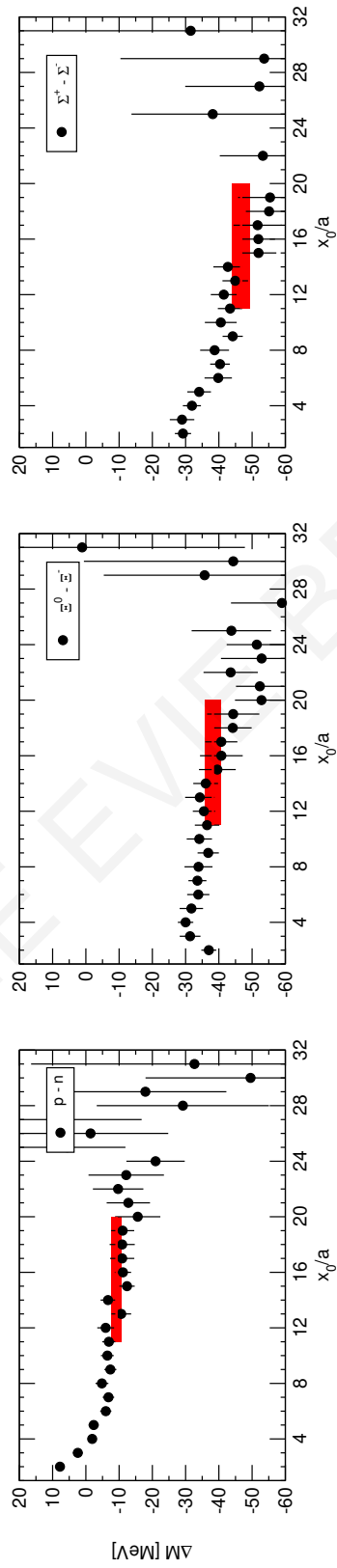Figure 6.8: Baryon mass differences measured on ensemble A380a07b324+RW1.

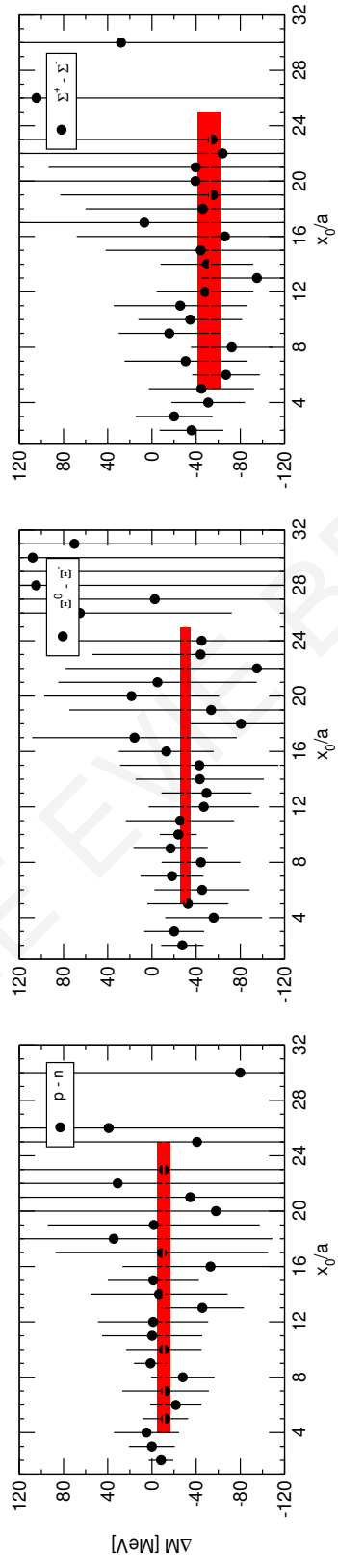Figure 6.9: Baryon mass differences measured on ensemble A500a50b324.

Figure 6.10: Baryon mass differences measured on ensemble A360a50b324+RW2.

ensemble(+rw)	$M_p = M_{\Sigma^+}$	$M_n = M_{\Xi^0}$	$M_{\Xi^-} = M_{\Sigma^-}$	M_{Λ^0}	M_{Σ^0}	$M_{\Omega^-} = M_{\Delta^-}$
A450a07b324	1214(14)	1215(15)	1216(16)	1215(15)	1215(14)	1473(35)
A380a07b324	1147(19)	1151(19)	1157(18)	1151(19)	1151(18)	1458(26)
A380a07b324+RW1	1164(15)	1167(13)	1175(14)	1167(13)	1169(14)	1448(20)
A500a50b324	1280(15)	1288(13)	1339(11)	1296(13)	1313(13)	1614(23)
A360a50b324+Rw2	1212(20)	1226(22)	1268(32)	1227(24)	1230(22)	1584(59)

Table 6.1: Baryon masses in MeV measured on the different ensembles (with or without mass reweighting). Values in MeV are obtained using the reference value $(8t_0)^{\frac{1}{2}} = 0.415$ fm.

ensemble(+rw)	$M_n - M_p$	$M_{\Xi^0} - M_{\Xi^-}$	$M_{\Sigma^+} - M_{\Sigma^-}$
A450a07b324	-0.89(0.38)	-2.44(0.49)	-1.77(0.89)
A380a07b324	1.80(0.52)	-8.37(0.75)	-9.96(0.79)
A380a07b324+RW1	0.90(0.37)	-5.97(0.63)	-6.81(0.68)
A500a50b324	9.2(1.5)	-38.2(2.4)	-46.7(2.7)
A360a50b324+Rw2	10.5(6.0)	-30.2(4.7)	-52(11)

Table 6.2: Baryon mass differences in MeV measured on the different ensembles(with or without mass reweighting). Values in MeV are obtained using the reference value $(8t_0)^{\frac{1}{2}} = 0.415$ fm.

$t \sim 24$ with an increasing error on each time-point. This leads to a relatively large error on the Ω^- mass for this ensemble.

We see from the mass difference plots for ensemble A450a07b324 in Fig. 6.6 that the signals for the mass differences are comparatively very well-behaved, with a long level region, inside which the plateau range $t \in [7, 18]$ has been chosen for all mass differences. At $t \sim 20$, the noise per time-point increases, while fluctuations start to appear in the signal. Nonetheless, the errors on the mass differences for this ensemble are among the smallest for the ensembles measured. Although we obtain the correct sign for the $M_{\Xi^0} - M_{\Xi^-}$ and $M_{\Sigma^+} - M_{\Sigma^-}$ mass differences, we get an incorrect sign for the proton-neutron mass difference. This mass difference is known to be highly sensitive to both the pion mass and the α_R value, so is expected to fluctuate somewhat between different ensembles as these parameters change. We also note that the ϕ_2 observable associated with this ensemble is far from the target values, as discussed later on.

6.1.0.2 *A380a07b324*

In comparison with the other ensembles on which baryon masses were measured, the ensemble A380a07b324 has the smallest pion mass at $M_{\pi^\pm} = 383.6(4.4)$ and a close-to-physical value of α_R. This ensemble is formed of 2000 configurations and eight hits were used per configuration to measure the baryon masses on this ensemble.

When we inspect the effective mass curves, shown in Fig. 6.2, for the ensemble A380a07b324, we find that the spin-$\frac{1}{2}$ baryons are reasonably well-behaving. The forms of the effective mass curves for the different spin-$\frac{1}{2}$ baryons are very similar to each other, and indeed all of the spin-$\frac{1}{2}$ baryons have been given the same plateau range, $t \in [21, 28]$. For all spin-$\frac{1}{2}$ baryons, we see a sharp increase in the statistical noise at around $t = 28$. The associated errors on the spin-$\frac{1}{2}$ baryons are reasonably large compared to other ensembles apart from A360a50b324+RW2. This is perhaps to be expected as the pion mass is relatively small.

The form of the effective mass plot for the Ω^- baryon is different from those of the spin-$\frac{1}{2}$ baryons, as it has a shorter and slightly earlier plateau given by $t \in [19, 24]$, before it descends into statistical noise from $t = 24$ onwards (see the discussion on spectral decomposition below). This shorter plateau gives the Ω^- baryon mass a larger error than for the other baryon masses.

Regarding the effective mass plots for the mass differences on the A380a07b324 ensemble, shown in Fig. 6.7, we see that the signal is reasonably stable for a long period in time. We have chosen the quite long plateau range $t \in [9, 20]$ for all mass differences of this ensemble. Around $t = 22$, we see the statistical noise start to take over as the centre of the lattice is approached. Regarding the values, we find that all the mass differences measured have the correct sign and are reasonably close to their physical values, and we also find that the neutron-proton mass difference is consistent with the physical value within error, which is encouraging. The errors on these values are larger than those of the ensemble A450a07b324, which is to be expected as the pion mass here is smaller.

6.1.0.3 *A380a07b324+RW1*

This ensemble is the above ensemble (A380a07b324) with mass reweighting. Therefore, the number of configurations is the same, at 2000. Again, eight hits were used per configuration. This reweighted ensemble has an almost unchanged α_R value of $0.007080(22)$, but has a significant shift in pion mass, at $M_{\pi^\pm} = 398.8(3.7)$, which is still small compared to that of A450a07b324.

The effective mass plots for the baryon masses calculated on the A380a07b324+RW1 ensemble, shown in Fig. 6.3, show a long quasi-linear region, with the exception of the Ω^- baryon. The region over which the average is taken is chosen to be $t \in [21, 28]$ for all spin-$\frac{1}{2}$ mass baryon masses, while the Ω^- baryon plateau is chosen to be $t \in [19, 24]$, which is relatively

short. For the spin-$\frac{1}{2}$ baryons, we see that the signal-to-noise ratio diminishes noticeably from $t = 26$ onwards, whereas the diminution starts earlier for the Ω^- baryon, at around $t = 24$, after which we see a large fluctuation towards the middle of the lattice. The effect of the mass reweighting of the ensemble `A380a07b324` is to make the pion mass heavier, which is reflected in the increase in masses for the spin-$\frac{1}{2}$ baryons for the `A380a07b324+RW1` ensemble with respect to the `A380a07b324` ensemble. This ensemble has, however, the smallest Ω^- baryon mass of all of the ensembles on which the baryons were measured. Despite the shorter plateaux in the case of the spin-$\frac{1}{2}$ baryons, we see that the errors on the baryons masses for this ensemble are smaller than for the `A380a07b324` ensemble. This is a reflection of the flatter spin-$\frac{1}{2}$ effective mass curves over the plateau region and the reduced statistical error per time-point in the plateau region in the case of the Ω^- baryon.

Looking at the effective mass plots for the baryon mass differences, shown in Fig. 6.8, they have reduced fluctuations and statistical error per time-point with respect to ensemble `A380a07b324`. In light of this, the plateau range has been chosen to encompass $t \in [11, 26]$, a comparatively long plateau, for all mass differences. We see that the signals seem to be very flat for the first half of the plots, with the signal-to-noise ratio diminishing at around $t = 24$. After this point we see significant fluctuations in $M_p - M_n$ and $M_{\Sigma^+} - M_{\Sigma^-}$. The resulting errors for the mass differences are smaller than those for `A380a07b324` and among the smallest for the ensembles on which baryon masses were measured. The value of the proton-neutron mass difference agrees within error with the physical value, and the values of the other mass differences agree within two standard deviations.

6.1.0.4 *A500a50b324*

The ensemble `A500a50b324` has both the largest pion mass of the ensembles, at $M_{\pi^\pm} = 495.0(2.8)$, and, alongside ensemble `A360a50b324+RW2`, a relatively large α_R with respect to the other ensembles, at $\alpha_R = 0.040772(85)$. This ensemble was measured using four hits per configuration, and consits of 1993 configurations.

With these facts in mind, we find that the baryon masses we measure are larger than those measured on the other ensembles. This is to be expected due to the large pion mass associated with `A500a50b324`. The errors on the baryon masses are reasonably small compared to those measured on other ensembles. The plateaux for the baryon masses are each taken according to the interval $t = [22, 28]$, and, in fact, all of the plateaux chosen seem to select well regions of the effective mass curves that are reasonably level apart from some statistical noise between points, as shown in Fig. 6.4. Furthermore, the effective mass curves for the spin-$\frac{1}{2}$ baryons show strong signals and are well-behaved in terms of their forms.

In terms of the final results, we found that, of the spin-$\frac{1}{2}$ baryons, the Ξ^- baryon mass has the smallest error, whilst the proton has the largest error, which seems to be caused by an increased statistical noise time-point-to-time-point inside the plateau region and a diminishing signal-to-noise ratio near the middle of the lattice. In the case of the Ω^- baryon, the error on each time-point grows dramatically as the centre of the lattice is approached. The increased error associated with this object with respect to the other objects seems to be due both to the less stable values of the time-points in the plateau region, and also to the increasing noise towards the end of the plateau region that effectively reduces the length of the plateau, weighted as it is by the inverse variance of the time-points, compared to the other objects. In fact, we found that for all of the ensembles, the error on the Ω^- baryon was greater than that for other objects.

The baryon mass differences we measured on the `A500a50b324` ensemble were large compared with their physical values. We expect the charged-neutral mass differences for this ensemble to be large due to the value of α_R associated with this ensemble which is much greater than the physical value, and, in fact, we see that the results are close to those calculated on the

other ensemble at this α_R value, `A360a50b324+RW2`, although with smaller associated errors. This may be due to the larger pion mass associated with this ensemble when compared to `A360a50b324+RW2`. Looking at the baryon mass difference plots, shown in Fig. 6.9, we see that all of the plots seem to suffer from some sloping up to $t \sim 20$, before the signal-to-noise ratio diminishes to varying degrees depending on the mass difference in question, which makes it more difficult to select a plateau range. The plateaux for these plots were taken using the range $t \in [11-20]$. The increased error in the mass difference values of the objects $M_{\Sigma^+} - M_{\Sigma^-}$ and $M_{\Xi^0} - M_{\Xi^-}$ seems to be due to a greater slope in the region in which the plateaux are taken compared with that of $M_p - M_n$. All mass differences calculated on this ensemble have the correct sign when compared with their physical values.

6.1.0.5 `A360a50b324+RW2`

Ensemble `A360a50b324+RW2` is formed of 2001 configurations. In the measurement of baryon masses on this ensemble, four hits were used per configuration. The pion mass, at $M_{\pi^\pm} = 398.9(3.4)$, is the smallest of the ensembles with larger α_R on which we measured baryon masses. The value of α_R associated with this ensemble is close to that of `A500a50b324`, at $0.04069(26)$.

In comparison with the results from the other ensembles, we see that the mass curves for the `A360a50b324+RW2` ensemble, shown in Fig. 6.5, have a much larger error per time-point than for the other ensembles. The magnitudes of errors per time-point are similar between the curves for the different spin-$\frac{1}{2}$ objects. We can, however, observe a slight increase in the fluctuations of the signal in the M_{Ξ^-} curve. Around $t = 18$, the signal-to-noise ratio worsens for all the objects in the approach to the centre of the lattice. Of the mass curves, the signals of the M_{Σ^0} and M_{Λ^0} curves seem marginally better than for the other objects. As for the Ω^-, the signal-to-noise ratio starts to deteriorate earlier than for the other objects, at around $t = 15$, after which the deterioration is rapid. This leads to M_{Ω^-} on this ensemble having the largest error of all of the baryon mass measurements.

The significantly increased error on the individual time-points for this ensemble may be due to a number of factors, such as only using four hits per configuration, and the pion mass being significantly lighter than the other ensemble we have measured on with higher α_R value, `A500a05b324`. It could also be due to a large effect from the reweighting factors. As we have seen, the length of the plateaux has not changed significantly between ensembles up to now, with most plateaux used being $\sim$7 points long. However, ensemble `A360a50b324+RW2` has longer plateaux than the other ensembles, at $t \in [11, 25]$ for all masses, which may be a result of the increased uncertainty on each time-point making it difficult to ascertain with precision the underlying form of the effective mass function. In the end, the increased plateau length, along with the presence of some time-points with smaller errors that dominate when the plateau value is calculated through an average weighted by the inverse variance, compensates for the increased error on each time-point to give errors on the baryon masses that are on the larger side for the ensembles on which we measured baryon masses, but not significantly larger apart from the Ω^- baryon. The plots for the mass differences for the `A360a50b324+RW2` ensemble, shown in Fig. 6.10, are much more chaotic than for the other ensembles, owing to the increased error per time-point. This error has already been discussed above for the individual masses; the effect of this is magnified by taking the difference between the masses. We see that at $t \sim 16$, the noise increases significantly for all mass differences. The values seem roughly constant within error until to signal-to-noise ratio diminishes at $t \sim 16$. The resulting errors for the mass differences calculated on this ensemble are large in comparison with the other ensembles. However, the values calculated are similar as expected to those given by the other ensemble at this value of α_R, `A500a05b324`, and the signs of the mass differences are the same as those of the physical values.

6.1.1 *Spectral decomposition*

In the results above, we see a consistently weak plateau for the Ω^- baryon, which makes it difficult to select an appropriate plateau range. In order to ascertain whether the plateau we have chosen for Ω^- is suitable, we carried out a spectral analysis using the modified Backus-Gilbert method. We demonstrate this for one of the ensembles with the worst plateau for the Ω^- effective mass curve, A500a50b324. The method described in Sec. 5.7 is applied to the Ω^- correlator, the effective mass plot of which is given in Fig. 6.11a. The plateau value calculated from this effective mass plot is given by denoted E_p.

The selection of the value of λ_* is shown for the point $E_*/E_p = 1$ in Fig. 6.11b, with the selected value corresponding to the value of $\hat{\rho}_L(E_*)$ at $A[g]/A[0] \approx 0.03$. For $A[g]/A[0]$ values below this value, there is no significant change of $\hat{\rho}_L(E_*)$ within error, so we may infer that the systematic errors are negligible with respect to the statistical errors. More details on this procedure may be found in [24]. We then obtain the coefficients g_t using Eq. (5.71), which may then be combined with the correlators as in Eq. (5.68) to give the smeared spectral density at energy E_*. The procedure detailed in this paragraph is then repeated for different E_*, with errors calculated through jackknife bootstrapping over all of the configurations of the ensemble. This gives the discrete points with error bars that are shown in Fig. 6.11c.

A fit of these discrete points is then carried out using the convolution of two different Gaussians of pre-set width $\sigma = 0.2E_p$, for which the coefficients of each Gaussian and the energies at which they are centered are the degrees of freedom. The x-axis of this plot is E/E_p; we therefore see that there is no detectable contribution from states with energies less than the already-calculated plateau, which justifies our choice of plateau. We also see that there is a nearby excited state at $E/E_p = 1.35$, which would not have been resolved at this level of statistics without a two-Gaussian fit. This method is especially advantageous in this application because the error is smallest at low energies, which is the opposite situation to an effective mass plot where low energy states are isolated in the noisy large-t region. The two methods therefore act to complement each other.

6.2 THE EXTENT OF EXPECTED FLAVOUR-VIOLATING MIXING

As explained in Ref. [20], C^* boundary conditions open the possibility for flavour mixing due to disconnected diagrams. These describe colourless particles that travel around the torus, changing flavour content in the process. This mixing causes a change the baryon number of the state by $\Delta B = 0 \mod 2$. This effect is therefore harmless in the cases of pseudo-scalar mesons as presented above, as they do not mix with lighter states, and of nucleons, which are the lightest $B = 1$ states and cannot mix with $B = 0$. This means that, in reality, the only objects that we are interested in, and for which this occurs, are the Ω^- and Ξ baryons.

This section regards the extent to which we expect flavour-violating baryon mixing to be significant for our measurements of baryon masses on C^* ensembles. Examples of the mechanisms by which these mixings may occur for the relevant baryons are given in Fig. 6.12; these are, however, not exhaustive and other diagrams will be possible, including contributions from photons and kaons, and decays of included spin-$\frac{3}{2}$ particles into spin-$\frac{1}{2}$, provided that these diagrams preserve energy, momentum, and the quantum numbers of the initial baryon state. Whilst the objects that we measure that may experience mixing are Ω^- and Ξ^-, there is also the possibility for the Ξ^0 to mix with the n; however, as in our setup in which d and s are mass-degenerate, these two baryons have exactly the same mass in our calculations. The intermediate baryon Λ^0 in this diagram is also of equal mass or heavier than the Ξ^0 for all of our ensembles, so we do not need to quantify the expected suppression of this mixing effect.

ensemble(+rw)	$\exp(-2\mu_{\Xi^-}L)$	$\exp(-2\mu_{\Omega^-}L)$
A450a07b324	0.00038	0.0027
A380a07b324	0.0015	0.030
A380a07b324+RW1	0.0011	0.012
A500a50b324	0.00030	0.0036
A360a50b324+RW2	0.0017	0.077

Table 6.3: Mixing-magnitude factors $\exp(-2\mu L)$ using masses and L from each ensemble.

6.2.1 *Mixing-magnitude factors*

Following the logic of [20], the factor by which we can expect these disconnected contributions, that are due to the effect of massive particles travelling around the torus, to contribute, may be calculated using the hadron masses. The characteristic decay factor μ of the suppression of the flavour-violating mixing for the Ξ^- baryon is given by

$$\mu(M_{\Xi^-}) = \begin{cases} M_{K^\pm} & \text{if } 0 < M_{\Xi^-} \leq M_p; \\ \left(M_{K^\pm}^2 - \left(\frac{M_{\Xi^-}-M_p}{2}\right)^2\right)^{1/2} & \text{if } M_p \leq M_{\Xi^-} \leq \frac{M_{\Lambda^0}^2-M_{K^\pm}^2}{M_p}; \\ \left(M_{K^\pm}^2 - \left(\frac{M_{\Xi^-}^2-M_{\Lambda^0}^2+M_{K^\pm}^2}{2M_{\Xi^-}}\right)^2\right)^{1/2} & \text{if } \frac{M_{\Lambda^0}^2-M_{K^\pm}^2}{M_p} \leq M_{\Xi^-}. \end{cases} \qquad (6.2)$$

Through substitution of the relevant baryons, the corresponding factor may also be calculated for the Ω^- baryon,

$$\mu(M_{\Omega^-}) = \begin{cases} M_{K^\pm} & \text{if } 0 < M_{\Omega^-} \leq M_{\Sigma^+}; \\ \left(M_{K^\pm}^2 - \left(\frac{M_{\Omega^-}-M_{\Sigma^+}}{2}\right)^2\right)^{1/2} & \text{if } M_{\Sigma^+} \leq M_{\Omega^-} \leq \frac{M_{\Xi^0}^2-M_{K^\pm}^2}{M_{\Sigma^+}}; \\ \left(M_{K^\pm}^2 - \left(\frac{M_{\Omega^-}^2-M_{\Xi^0}^2+M_{K^\pm}^2}{2M_{\Omega^-}}\right)^2\right)^{1/2} & \text{if } \frac{M_{\Xi^0}^2-M_{K^\pm}^2}{M_{\Sigma^+}} \leq M_{\Omega^-}. \end{cases} \qquad (6.3)$$

Whilst we have calculated the baryon masses required for the calculation of the mixing-magnitude factor of the Ξ^- baryon, we lack the Σ^{*+} baryon mass that would appear in the formula above for the calculation of the mixing-magnitude factor for the Ω^- baryon. However, when we take into account the possible decays of the Σ^{*+} baryon, we see that the lightest final baryon state is given by the Σ^+ baryon that features in the decay $\Sigma^{*+} \to \Sigma^+ + \gamma$, as this is, out of a few possible decay paths, the decay that gives the lowest energy state for our particular ensembles whilst preserving Q. We therefore use Σ^+ as the lowest final baryon state both for the calculation of the mixing-magnitude factor and for the validation of energetic conditions. For the two relevant mixing diagrams, the mixing-magnitude factor is calculated using the baryon masses we have calculated on each ensemble. The μ are then multiplied by the spatial extent of the lattice L of each of our ensembles in the calculation of the mixing-magnitude factor $\exp(-2\mu L)$.

Table 6.3 gives the estimated mixing-magnitude factors for flavour-violating mixing of the Ξ^- and Ω^- baryons calculated for each ensemble. As we are only using this as a guide for the order of magnitude of the effect, the error is omitted. We see that, while the mixing-magnitude factors are small, they are not negligible.

6.2.2 *Energetic conditions*

A particular energetic condition that we can look at is whether it is energetically possible for a photon to be produced as a intermediate state or final product of the mixing. In the continuum limit, there would exist a continuum of possible states between the lighter (undesired) state and the heavier (desired) state, due to the possible presence in the mixing diagram of any number of photons of any energy up to the maximum energy with regards to energy conservation. Due to the quantisation of space-time imposed by the lattice, the photon is constrained to have a minimum momentum which has the value $\sqrt{3}\pi/L$ due to the anti-symmetry of the photon field in all spatial dimensions. For small lattice sizes, the minimum momentum may therefore become large with respect to the energy gap between baryon states, leading to a vanishing number of allowed states within the gap.

We therefore assess whether either the minimum allowed energy for the photon, combined with the lightest possible final baryon state in the mixing, is less than or equal to the original state i.e. Ξ^- or Ω^-. In the case of Ξ^-, we know that the proton is the lightest baryon, so this is the state we use for the comparison. As discussed above, the lightest possible final state in the case of the Ω^- is Σ^+.

We may also compare whether the combined energy in the middle of the diagram is larger than the energy of the initial baryon object. While it is entirely possible for a kaon to have zero-momentum on the lattice, the mixing $B_1 \leftrightarrow B_2 + P$ of an initial stationary baryon B_1 with a combined baryon and pseudoscalar meson state ($B_2 + P$) is forbidden on the grounds of violation of parity if the products are both stationary, as the baryon states have positive intrinsic parity and the pseudoscalar mesons have negative intrinsic parity. This may be resolved by B_2 and P having equal and opposite momenta. The minimum momentum for a hadron on the lattice is given by π/L, therefore the minimum combined energy of the state is given by $E_{B_2,P} = \sqrt{M_{B_2}^2 + (\pi/L)^2} + \sqrt{M_P^2 + (\pi/L)^2}$.

The adherence to these conditions is shown in Table 6.4. Errors are calculated from error propagation starting from the final mass values and errors. We see that for both objects, the conditions are broken very strongly for all ensembles, as a consequence of the small physical size of the lattices associated with the ensembles. Although the exponential mixing-magnitude factors calculated for the different ensembles are not negligibly small, the energetic unfavourability of the mixing with respect to the existence of intermediate states and additional photons should therefore preclude flavour mixing that would otherwise arise due to the C* boundary conditions for our measurements.

6.3 $\Sigma^0 - \Lambda^0$ mixing results

In the following discussion and results, we call the masses calculated naively from the interpolating operators given in Sec. 5.2 the *naive masses*, which are denoted in the same way as for the baryons that do not experience any isospin mixing.

The expected values of the unmixed baryons can be calculated through formulae that may be derived through the $\mathrm{SU}(3)_F$ parameters of the octet baryon mass differences [64], and we denote these baryons through $B^{'}$. We expect the corrections to the baryon masses due to this isospin-mixing to be small. We calculate the expected values of the unmixed masses of Σ^0 and Λ^0 through the Eqs. (5.42) and (5.43), and label them $\Sigma^{0'}$ and $\Lambda^{0'}$ respectively. The effective mass curves for the required baryons were combined according to these equations to give the effective mass curves in Figs. 6.13a and 6.13b respectively.

In comparison with the naive effective masses given in Figs.6.1-6.5, the effective mass plot for $\Lambda^{0'}$ has an almost identical form to that of the both the naive Λ^0 and naive Σ^0 effective mass curves, as expected. The form of the $\Sigma^{0'}$ plot is distinct from that of the naive Σ^0 plot.

ensemble(+rw)	M_{Ξ^-}	$\sqrt{M_p^2 + (\frac{\pi\sqrt{3}}{L})^2} + \frac{\pi\sqrt{3}}{L}$	$\sqrt{M_p^2 + (\frac{\pi\sqrt{3}}{L})^2} + \frac{\pi\sqrt{3}}{L} \leq M_{\Xi^-}$?	$E_{\Lambda^0,K^\pm}$	$E_{\Lambda^0,K^\pm} \leq M_{\Xi^-}$?
A450a07b324	1216(16)	1974(13)	NO	1840(15)	NO
A380a07b324	1157(18)	1939(17)	NO	1736(19)	NO
A380a07b324+RW1	1175(14)	1950(13)	NO	1761(13)	NO
A500a50b324	1339(11)	2068(13)	NO	1964(12)	NO
A360a50b324+RW2	1268(32)	2038(18)	NO	1836(23)	NO

ensemble(+rw)	M_{Ω^-}	$\sqrt{M_{\Sigma^0}^2 + (\frac{\pi\sqrt{3}}{L})^2} + \frac{\pi\sqrt{3}}{L}$	$\sqrt{M_{\Sigma^0}^2 + (\frac{\pi\sqrt{3}}{L})^2} + \frac{\pi\sqrt{3}}{L} \leq M_{\Omega^-}$?	$E_{\Xi^0,K^\pm}$	$E_{\Xi^0,K^\pm} \leq M_{\Omega^-}$?
A450a07b324	1473(35)	1975(13)	NO	1840(15)	NO
A380a07b324	1458(26)	1943(16)	NO	1736(18)	NO
A380a07b324+RW1	1448(20)	1954(13)	NO	1761(13)	NO
A500a50b324	1614(23)	2098(12)	NO	1956(13)	NO
A360a50b324+RW2	1584(59)	2053(20)	NO	1835(21)	NO

Table 6.4: Addressing whether mixing is energetically possible, considering whether conditions 1) ((total energy of lightest possible final baryon state in diagram plus photon with momentum $\frac{\pi\sqrt{3}}{L}$) $\leq$ (initial baryon state in mixing diagram), and 2) ($E_{B_2,P} \equiv \sqrt{M_{B_2}^2 + (\pi/L)^2} + \sqrt{M_P^2 + (\pi/L)^2}$, the minimum combined energy of the baryon state B_2 and the pseudoscalar meson state P in the middle of the mixing diagrams) $\leq$ (initial baryon state in mixing diagram), are satisfied, through evaluation using masses obtained for our ensembles. Here 'YES' signifies 'possibly satisfied within 1σ', while 'NO' means 'not possibly satisfied within 1σ'.

ensemble(+rw)	M_{Λ^0}	M_{Σ^0}	$M_{\Lambda^{0\prime}}$	$M_{\Sigma^{0\prime}}$
A450a07b324	1215(15)	1215(14)	1216(15)	1217(14)
A380a07b324	1151(19)	1151(18)	1152(19)	1153(19)
A380a07b324+RW1	1167(13)	1169(14)	1168(14)	1169(14)
A500a50b324	1296(13)	1313(13)	1295(13)	1309(12)
A360a50b324+RW2	1227(24)	1230(22)	1229(24)	1233(25)

Table 6.5: Naive and unmixed Σ^0 and Λ^0 baryon masses calculated on the different ensembles. Here the naive 'Σ^0 mass' means the mass calculated using the Σ^0 interpolating operator given in Sec. 5.2. In fact, we expect this object to give the same final mass as the naive Λ^0 interpolating operator.

We find in Table 6.5 that the naive Σ^0 and Λ^0 masses are always consistent within error with each other as expected, even at physical α. From this table, we also see that the expected unmixed mass of the Λ^0 agrees with the naive masses within error.

We therefore conclude that there is expected to be a negligible effect on the masses of Λ^0 due to mixing induced by isospin-breaking for ensembles, but that one must remember that the naive mass that we have labelled as Σ^0 is really another measurement of the Λ^0 mass due to Λ^0 being the lower energy state that is allowed to mix with the Σ^0 baryon through isospin-breaking.

The mixing matrix parametrised by $\theta_{\Sigma^0-\Lambda^0}$ rotates the unmixed baryon states as given in Eq. (5.44). A spectral analysis, using for example the GEVP, could seperate the contributions to the mixed states from the physical Λ^0 and Σ^0 states in order to obtain the unmixed masses, from which it would be possible to determine the mixing angle. This could be the basis of future work.

6.4 TRENDS TOWARDS THE PHYSICAL POINT

In this section, we explore the relation of our results to our expectations and to the physical point. It is worth emphasising that our renormalisation trajectories are unphysical as we are always in the unphysical U-spin-symmetric regime where $m_d = m_s$, which makes it harder to compare with the experimental results at the physical point. Another facet of this is the subsequent mass degeneracy of the baryons due to simulation in the U-spin-symmetric setup. There will be therefore multiple physical masses that will correspond to a single measured baryon mass, which complicates further the discussion of reaching the physical point. Another complication is the fact that we have only simulated at one value of β. We have not, therefore, performed an extrapolation to the continuum limit, nor have we taken into account finite volume effects apart from those due to QED effects. We may therefore check, for instance, that the hierarchy of masses is roughly upheld by our measurements, and that the values of our masses and mass-differences are reasonable given our trajectories, but a detailed and systematic study of our masses with reference to the physical values is not attempted here.

For reference, our simulations were carried out at SU(3) inverse coupling value $\beta = 3.24$, with the target trajectory parameters ($\phi_0 = 0, \phi_1 = 2.13, \phi_2 = 2.37, \phi_3 = 12.1$). In particular, the target value of parameter ϕ_2 is approximately its physical value. As this parameter keeps the ratio between isospin-breaking effects due to the $u - d$ mass difference and isospin-breaking effects due to nonzero α constant, and its scale is set by the reference value $(8t_0)^{1/2} = 0.415$ fm, the central value of the CLS determination [33], the ratio of effects should be close to its physical value. The value $\alpha = 0$ corresponds to the QCD SU(3)-symmetric point for our chosen line of constant physics. Therefore, for our simulations that are at physical α, the

$u - d$ mass difference should be close to its physical value. As we expect isospin-breaking effects to be small at these values, and we are operating in U-spin-symmetric trajectories, we expect that, for our ensembles that have a value of α close to the physical value, we are operating close to the QCD SU(3)-symmetric point.

As the trajectory parameter ϕ_3 fixes the charm quark mass, which does not appear in any of the baryons whose masses we have measured, and the ϕ_2 parameter simply serves to keep the ratio of isospin-breaking effects from the $u - d$ mass difference to the isospin-breaking effects from QED contributions constant between ensembles, provided that the ϕ_2 target value is hit, it is not worthwhile to consider the trends in the masses and mass-differences with respect to these parameters. In the following section, we therefore focus on the trends in masses and mass differences with respect to ϕ_1, which is approximately proportional to the combined renormalised mass of the light quarks, and also with respect to the fine-structure constant α. We expect the value of ϕ_1 to have a greater effect on the masses, whereas we expect the α-value, and the proportional $u - d$ mass difference, to have a greater effect on the mass-differences. It is worth emphasising again that ϕ_0 is set to an unphysical zero-value which we expect to drastically affect the values of the masses. We exclude the ensemble `A380a07b324`, as the same ensemble with mass reweighting, `A380a07b324+RW1`, is given.

We first inspect the degenerate mass $M_p = M_{\Sigma^+}$ for different ensembles, given in Fig. 6.14. We see that the results of all ensembles are closer to the physical mass of Σ^+ than to the physical proton mass. From Figs. 6.14a and 6.14b, we see that both the difference in average quark mass (ϕ_1) and in α have effects of a similar magnitude.

Concerning the values of the degenerate mass $M_{\Omega^-} = M_{\Delta^-}$ for the different ensembles given in Fig. 6.15a, we obtain a mass approximately halfway between the physical masses of Ω^- and Δ^-. Comparing Figs. 6.15a and 6.15b, we see that the value of α has a large effect on the masses in comparison with the effect from varying ϕ_1.

For those ensembles at physical α, `A380a07b324+RW1` and `A450a07b324`, we expect the mass differences to be small, as we are close to the QED SU(3)-symmetric point at which all octet baryons have an equal mass; the same is true for all decuplet baryons at this point. Therefore, we expect to observe that the mass difference is small at physical α, and increases for an increased α, with the $u - d$ mass difference increasing directly proportionally to it. If the parameters ϕ_0 and ϕ_1 were then varied along trajectories to their physical values for a few values of β at physical α, and the finite volume and continuum limit taken, we would then expect the mass differences to increase and the masses to 'fan out' into the hierarchies of physical masses given in Figs. 6.14c and 6.15c.

The measured values of the proton-neutron mass difference for different ensembles are plotted against the α value associated with the ensemble. As expected, we observe that the above expectation is met, with smaller mass differences at physical α and larger mass differences at larger than physical α. At first, the positive value measured on the ensemble `A450a07b324` is puzzling; we expect the primary factors in the mass difference to be α and the $u - d$ mass difference. The ratio of these parameters is supposed to be held constant by a constant ϕ_2 value. In Fig. 6.16, we see that the ensemble `A450a07b324` has a value of ϕ_2 far away from the target value and considerably smaller. This corresponds to the value of α being proportionally larger than the $u - d$ mass difference compared to the target value of ϕ_2. As, for the proton-neutron mass difference there is known to be a positive effect from the QED contribution and a negative effect from the $u - d$ mass difference, the positive value for the ensemble `A450a07b324` makes sense, although it should probably be discounted in any future extrapolation for the proton-neutron mass difference.

The existence of mass degeneracies mixes up the hierarchy of measured masses somewhat. In general, we found that the hierarchies of baryon masses shown in Figs. 6.14c and 6.15c are preserved by the measured mass differences given in Table 6.2. While the mass degeneracies of the U-spin-symmetric setup mean that, for example, what we have labelled $M_n - M_p$ can

equally be labelled as the difference between either M_p or M_{Σ^+} on one side and either M_n or M_{Ξ^0}, in practice we find that our mass differences are small, especially at the close-to-physical value of α, and are therefore closest in value to the differences of masses that are nearby in the hierarchy at the physical point.
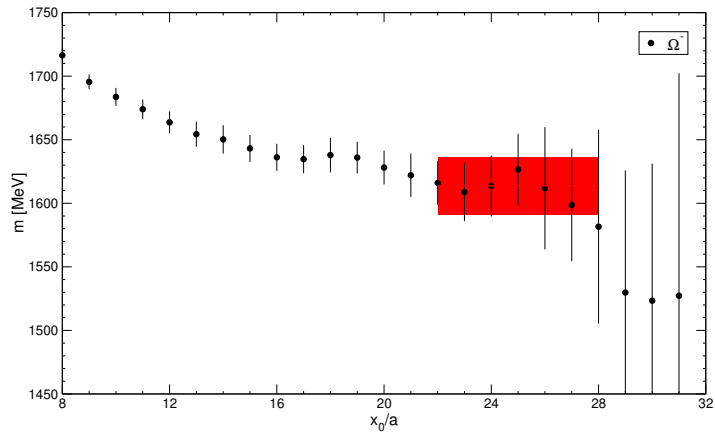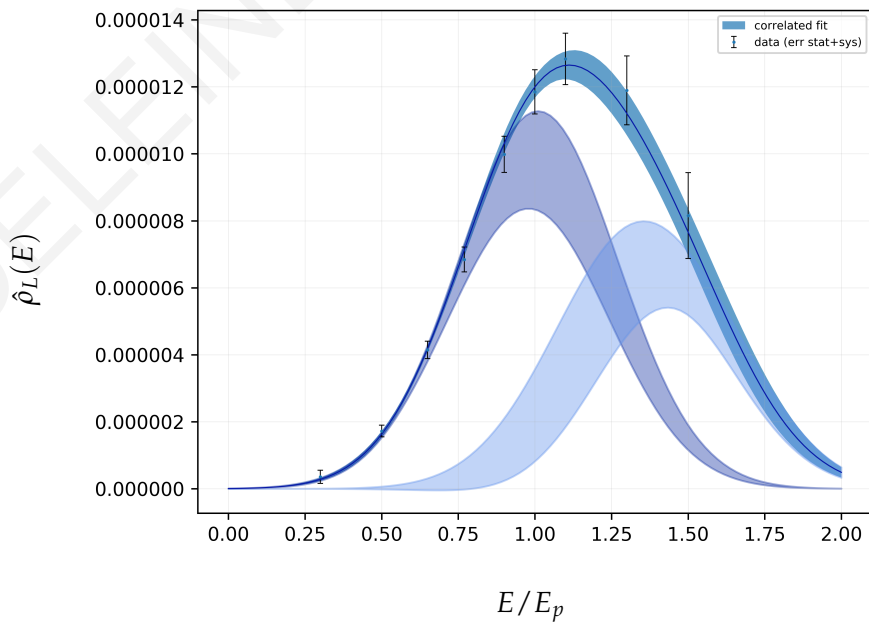
(a) Effective mass curve
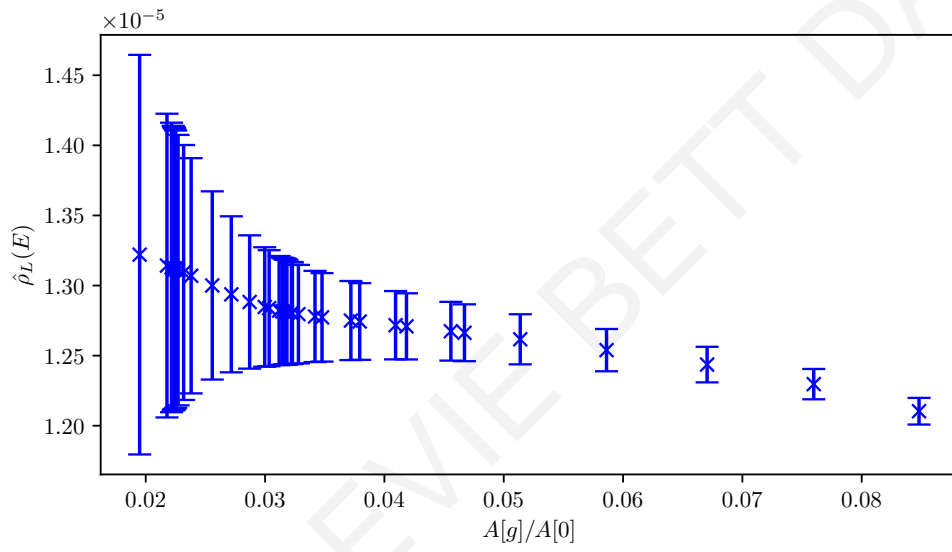
(b) λ_* optimisation

(c) Spectral decomposition

Figure 6.11: Ω^- spectral decomposition process using modified Backus-Gilbert method for ensemble `A500a50b324`
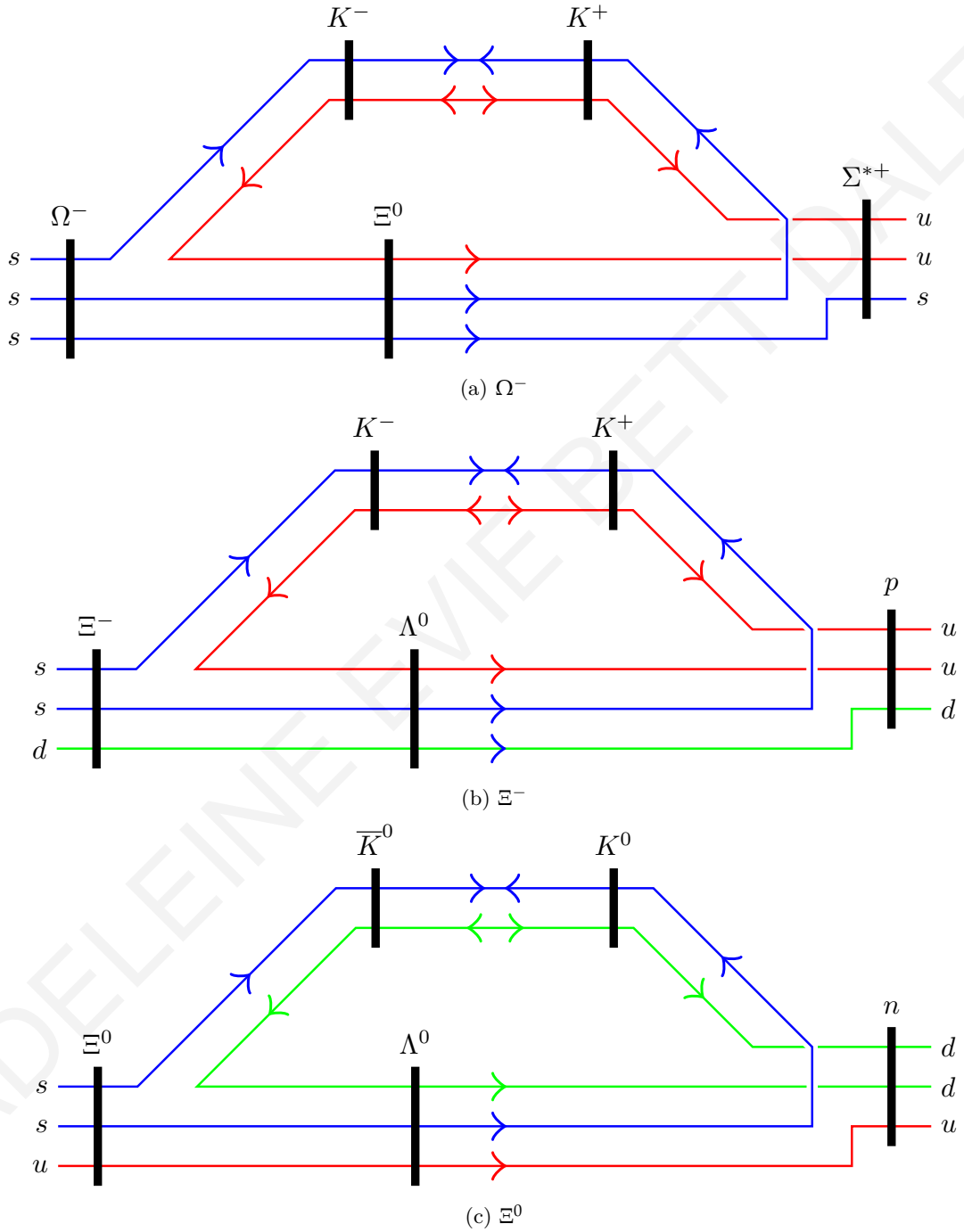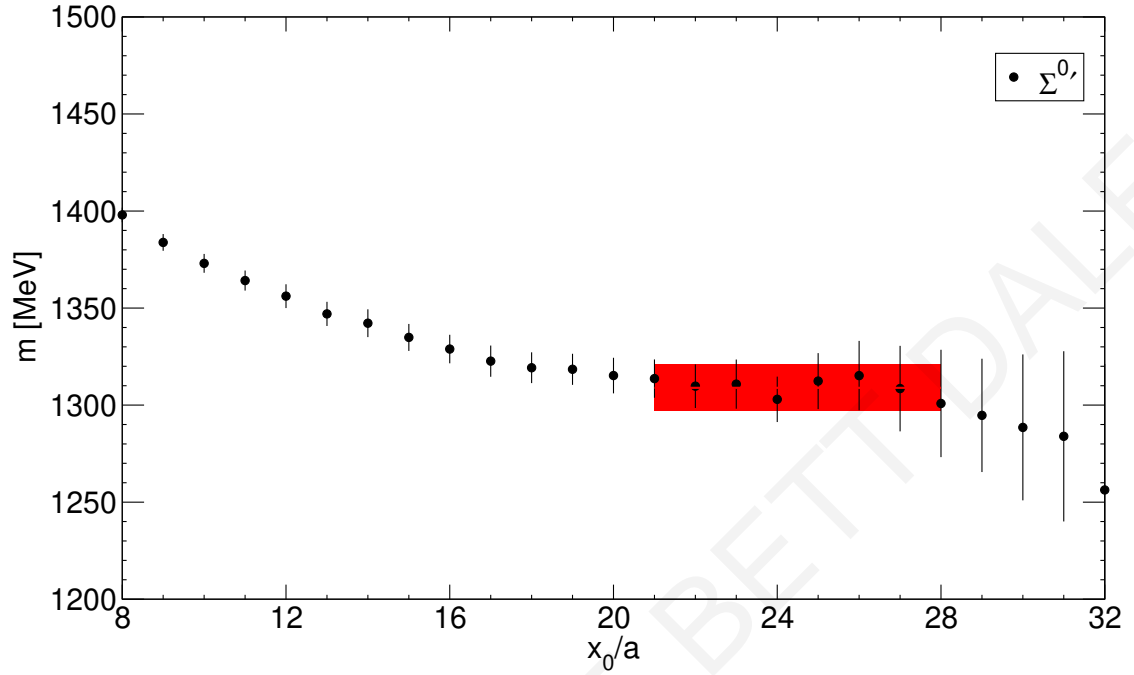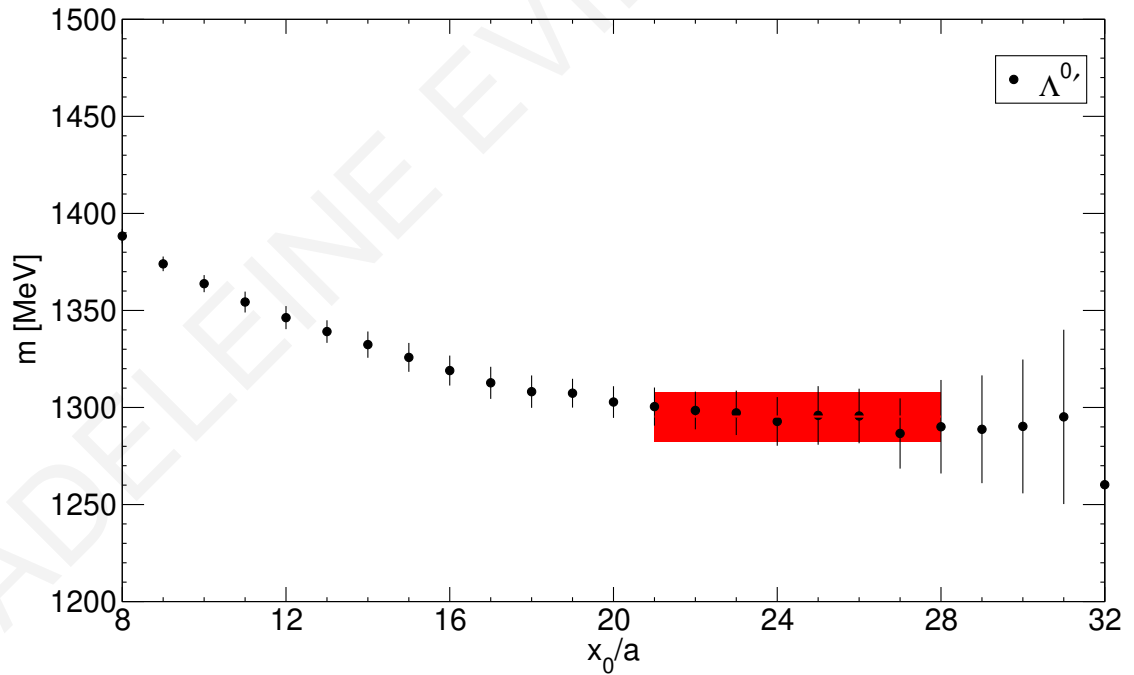
(a) Ω^-

(b) Ξ^-

(c) Ξ^0

Figure 6.12: Examples of mechanisms of flavour-violating mixing due to C* boundary conditions
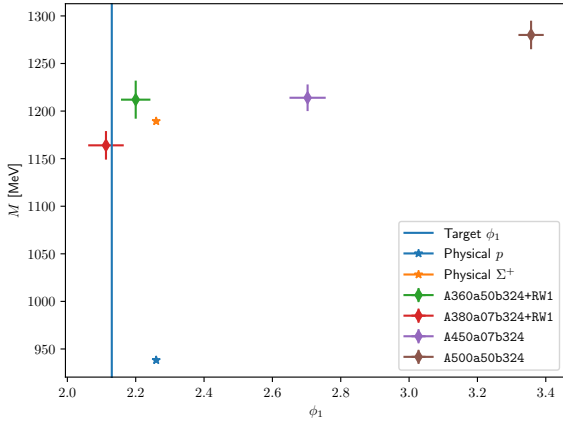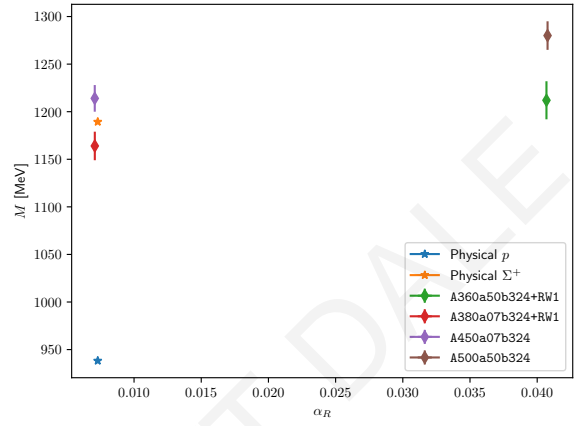
(a) $\Sigma^{0\prime}$

(b) $\Lambda^{0\prime}$

Figure 6.13: Plots related to $\Sigma^0 - \Lambda^0$ mixing for the ensemble `A500a50b324`. Effective mass plots for the unmixed Λ^0 and Σ^0 baryons, calculated through Eq. (5.42) for $\Sigma^{0\prime}$ and through Eq. (5.43) for $\Lambda^{0\prime}$.

(a) Mass of $M_p = M_{\Sigma^+}$ calculated on different ensembles, alongside physical masses of p and M_{Σ^+}, plotted against ensemble ϕ_1-value. The targeted value of ϕ_1 is given by the vertical line.
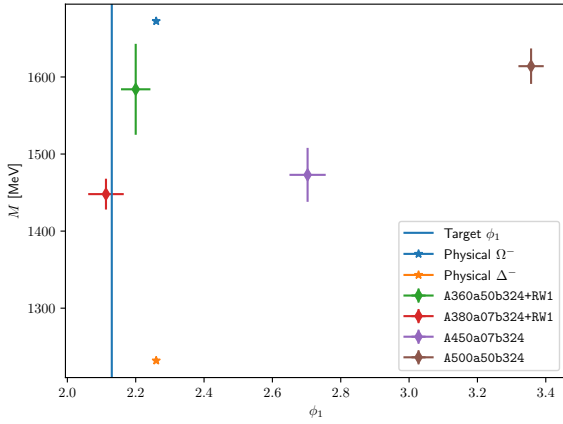
(b) Mass of $M_p = M_{\Sigma^+}$ calculated on different ensembles, alongside physical masses of p and M_{Σ^+}, plotted against ensemble α-value.
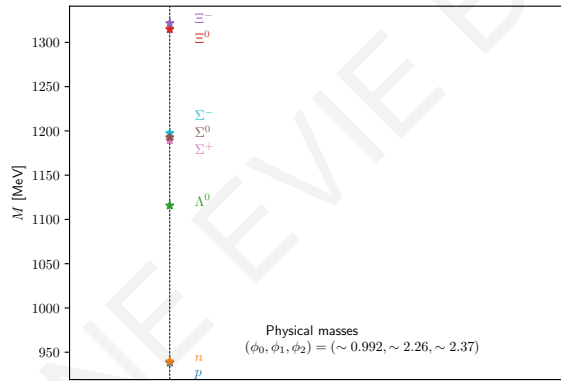
(c) Schematic of octet masses at physical (experimental) values, annotated with relevant trajectory parameters ϕ at the physical point.

Figure 6.14: Trends for masses of octet baryons p and Σ^+.

(a) Mass of $M_{\Omega^-} = M_{\Delta^-}$ calculated on different ensembles, alongside physical masses of Ω^- and Δ^-, plotted against ensemble ϕ_1-value. The targeted value of ϕ_1 is given by the vertical line.
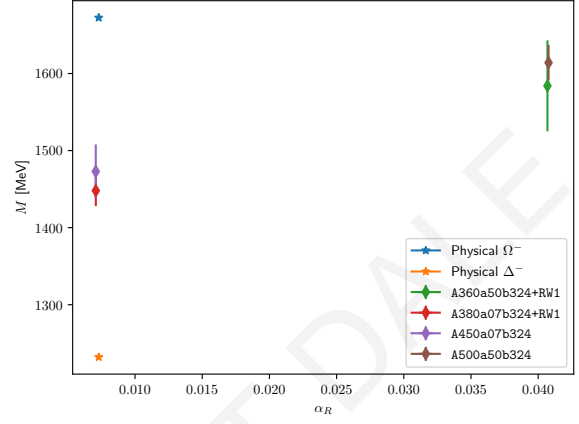
(b) Mass of $M_{\Omega^-} = M_{\Delta^-}$ calculated on different ensembles, alongside physical masses of Ω^- and Δ^-, plotted against ensemble α-value.
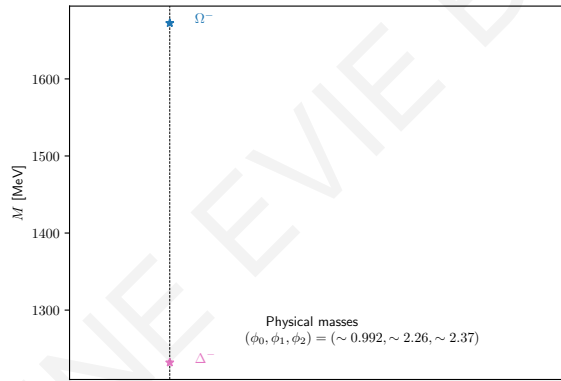
(c) Schematic of decuplet masses at physical (experimental) values, annotated with relevant trajectory parameters ϕ at the physical point.

Figure 6.15: Trends for masses of decuplet baryons Ω^- and Δ^-.
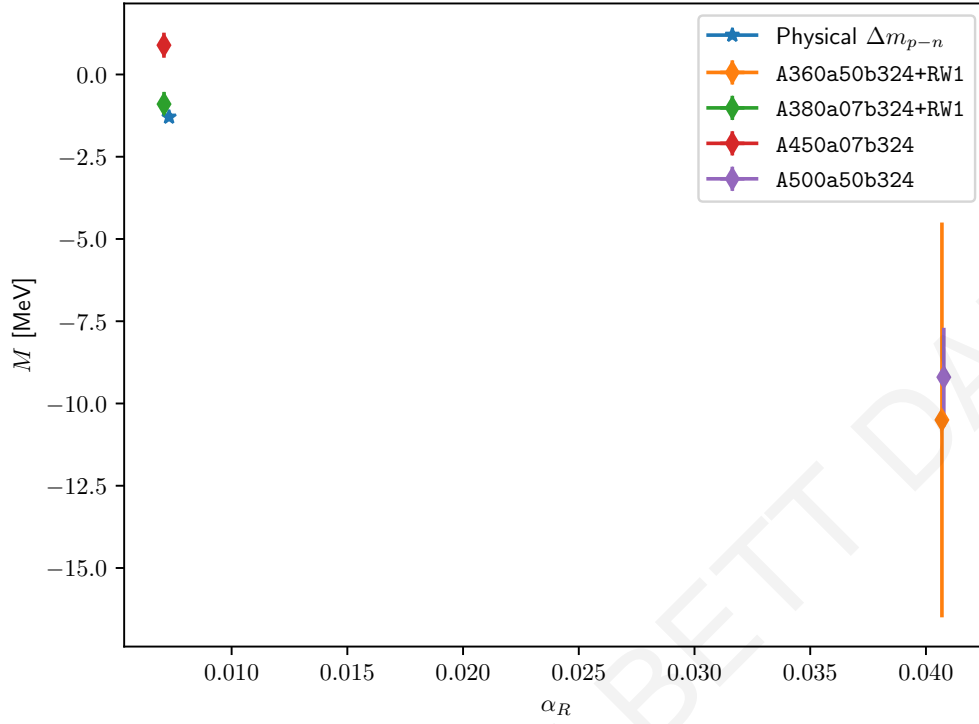
(a) Proton-neutron mass difference for different ensembles plotted against ensemble α-value.
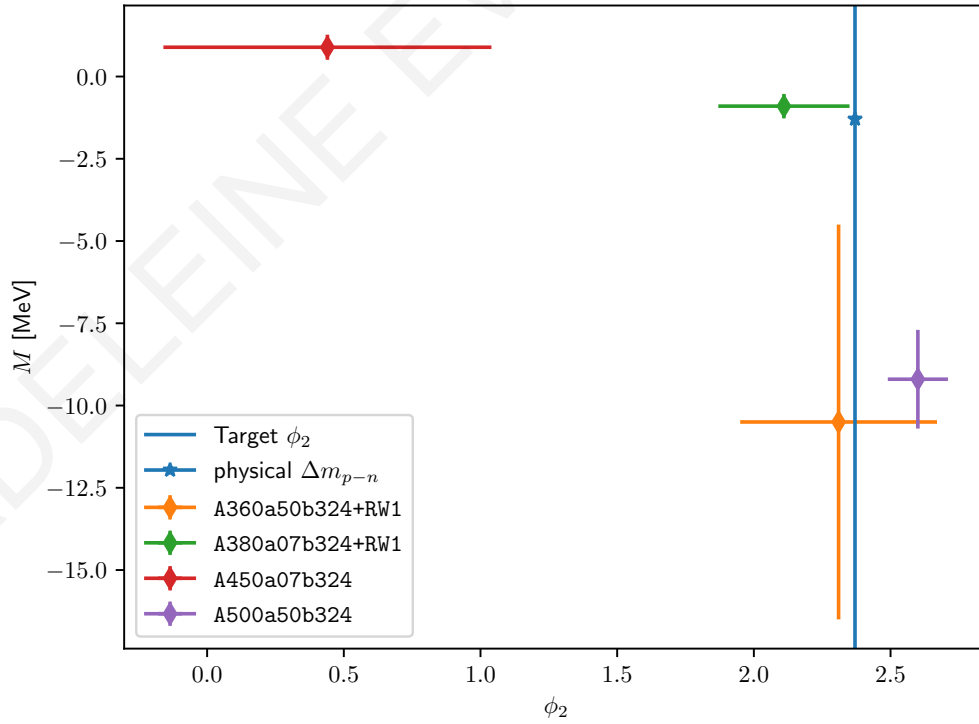
(b) Proton-neutron mass difference for different ensembles plotted against ensemble ϕ_2-value.

Figure 6.16: Trend for proton-neutron mass difference

7

CONCLUSION

In order to further reduce the error associated with quantities such as baryon masses, for which the statistical error of simulations has reduced to the same order of magnitude as the systematic error that arises from the neglect of QED in LQCD calculations, it is now more necessary than ever to include isospin-breaking effects in LQCD simulations. This is usually acheived through either a perturbative QED expansion around pure QCD, the reweighting of QED configurations, or, in the case of full QCD+QED simulations, the QED_L formulation, in which a non-local constraint enforces the quenching of photon zero-modes at all times; the non-locality of this formulation causes complications for the automatic satisfaction of certain properties of the quantum field theory such as renormalisability, which must then be proven on a case-by-case basis. We use instead the QED_C formulation, which is local meaning that these properties are satisfied automatically, and that also tends to have smaller finite-volume effects. Our QCD+QED_C formulation does not rely on perturbation theory and is fully gauge-invariant, and as such it does not depend upon gauge-fixing. This work is novel in the application of the QED_C formulation to the problem of baryon masses.

In Chapter 2, some fundamental theory of the implementation of gauge theories on the lattice was presented, including the simulation of fermions. The statistical properties of the Markov chain were then briefly explored, and the extrapolation of lattice results to the physical point was discussed.

The implementation of QCD+QED in the QED_C formulation was explained in detail in Chapter 3. The equivalence of the C-even symmetry of interpolating operators with the sum of the sink over both the physical and mirror lattice was briefly mentioned in Sec. 3.1 and in more detail in App. A. The symmetries of the formulation under transformations such as translation and parity were described. The details of flavour mixing that were introduced through the C* boundary conditions, as well as the suppression of the effect from the mass of particles that wrap around the torus. We then presented a number of dressing factors that allow electrically-charged fermion interpolating operators to be invariant under local U(1) gauge transformations. In Sec. 3.8, the QED finite-volume corrections that were necessarily applied to our measurements of electrically-charged hadrons were given. Lastly, the details of the implementation of QED_C on the lattice, and its combination with QCD, were presented in Sec. 3.9.

The details of the simulations carried out were given in Chapter 4, including a discussion on the U-spin-symmetric renormalisation strategy, the lattice action, and the particularities of the gauge ensembles. The strategy for tuning the meson masses in order to give the desired trajectory parameters was described, along with the method of calculation of the meson masses and trajectory parameters. A discussion of the magnitude of finite-volume effects on meson masses measured on the different ensembles was given, and the theory of the Wilson gradient flow that defines the energy scale and renormalised α value was presented. Finally, we have discussed the calculation of the sign of the pfaffian, presenting a novel method developed by the RC* collaboration for the optimisation of the calculation of the sign of the Pfaffian, that has then been used as a reweighting factor for the ultimate calculation of the fermionic Pfaffian, and we have also given some technical details of the HMC method and other algorithmic features such as the rational approximation of the fermionic determinant.

The method for the optimised measurement of the baryon correlators and their analysis was given in Chapter 5. Firstly, we explained the typically poor signal-to-noise ratio for the baryon masses in comparison with meson masses, and the interpolating operators were presented along with their smearing, which can help to optimise the correlation signal. A rough check was performed of the relative magnitude of the errors from the two methods of error analysis that we used, the Jackknife bootstrapping method and the Gamma method, that are both explained in App. E, compared with the value of the integrated autocorrelation time measured using the Gamma method. The Generalised Eigenvalue Problem was explained and results using this method were used in the optimisation of our baryon correlators. The mass plateau value and error for the different smearing levels were compared, using the example of the proton in this thesis, with the value and error calculated from the GEVP, and this was used to inform the optimal choice of smearing level that was used later in the Gamma method of error analysis. The energy of the proton first excited state was calculated from the GEVP and found to have a value slightly higher than that of the (proton + photon) excited state, although it seems likely that this is due to us not being able to reach the plateau before the excited state signal quality diminishes. A modified version of the Backus-Gilbert method was then presented.

Our results for the baryon masses and mass differences were given in Chapter 6. We obtained baryon masses with a precision of between 1-5%, with the ensembles with heavier pions tending to give a higher precision, as expected. The precision associated with the mass differences tended to vary more between ensembles than the masses did. We found that the greatest error for both the masses and mass differences was associated with the ensemble `A360a50b324+RW2`, which may be due to a few different factors, such as the pion mass, the smaller number of stochastic sources, and possibly the reweighting factors. The Ω^- baryon masses were then investigated through the modified version of the Backus-Gilbert method. This baryon was chosen in particular because of the weak definition of the plateau that we found for multiple ensembles. We found that this is most probably due to at least one excited state that is close in energy to the ground state. The ground state energy recovered from this method was consistent with that obtained through our choice of plateau.

Comparison at this stage of the measured values of the baryon masses and their mass differences with their physical values is difficult, not least due to the unphysical U-spin-symmetric setup that renders some of the baryons mass-degenerate with each other, even those that have very different masses at the physical point. We have reasoned that those ensembles at physical α lie close to the QCD SU(3)-symmetric point, at which all octet baryons take on the same mass, as do the decuplet baryons. We therefore expect the mass differences at this point to be small, as we observe. We see that the mass-differences calculated on the ensemble with the physical α_R and with the smallest pion mass of all the ensembles on which we measured baryon masses, `A380a07b324+RW1`, are close to the physical values of the mass differences labelled as in Table 6.2. Apart from on ensemble `A450a07b324`, for which the measured trajectory parameter ϕ_2, that controls the ratio between the $u - d$ mass difference and the value of α_R, was far away from its target value, all mass differences had signs in agreement with their physical values.

We also gave an estimate of the magnitude of the exponential suppression of flavour mixing for the two baryons for which we expect this mixing to occur, Ξ^- and Ω^-, as we are in fact only calculating fermion-connected contributions in our baryon mass measurements. The estimated contribution due to flavour mixing was small but not negligible, which seems to be a consequence of the small lattice sizes for which we are performing our simulations. We expect, however, that these small lattice sizes also act to suppress the flavour mixing through the quantisation of the momenta of the intermediate photons and kaons.

The inclusion of isospin-breaking also allows mixing between the Σ^0 and Λ^0 baryons, which means that through using interpolating operators that in isospin-symmetric QCD would select

the Σ^0 and Λ^0 baryons respectively, it is not possible to measure both masses in QCD+QED through only studying the ground state. Therefore, although we have used two different interpolating operators, we have measured the mass of only the lightest of the two baryons, the Λ^0. We found that the masses from the correlators using the two different interpolating operators were consistent within error as expected. It is known in the literature that the aforementioned mixing has a negligible effect on the Λ^0 mass. In order to estimate the corresponding unmixed masses we would expect for these ensembles, two formulae known in the literature [64][59][58], including the famous GMO formula, are used to calculate the expected values of the unmixed Σ^0 and Λ^0 baryon masses in terms of the other baryon masses. The unmixed Λ^0 mass calculated was consistent with the masses calculated naively from their interpolating operators.

In future work, we expect to complete the calculation of the hadron masses through moving to the physical point, which would involve simulations on larger lattices, simulations at different values of the inverse coupling β, and smaller pion masses. In order to reach the physical point, a new trajectory that is not U-spin-symmetric may be necessary. It would also be interesting to try to obtain the Σ^0 baryon mass through the GEVP, although this may require increased statistics. A quantification of the separate effects due to QCD and QED for our QCD+QED results and the comparison of our results with a parallel RM123 method would also be rewarding, especially in the case of observables such as the neutron-proton mass difference for which the QCD and QED isospin-breaking effects work against each other. In order to measure accurately the contribution from flavour-mixing, that is represented by a fermion-disconnected diagram, it is necessary for reasons of computational practicality to use stochastic sources. Some progress on this front has already been made, such as the construction of gauge-invariant propagators with a source in the physical lattice and a sink in the mirror lattice, as well as a study of the convergence of calculations using stochastic sources with various methods of dilution, but has not been included in this thesis.

[1]   Y. Aoki et al. "FLAG Review 2021." In: (Nov. 2021). arXiv: 2111.09849 [hep-lat].

[2]   Sz. Borsanyi et al. "Ab initio calculation of the neutron-proton mass difference." In: *Science* 347 (2015), pp. 1452–1455. DOI: 10.1126/science.1257050. arXiv: 1406.4088 [hep-lat].

[3]   Sinya Aoki, Takumi Doi, Tetsuo Hatsuda, Yoichi Ikeda, Takashi Inoue, Noriyoshi Ishii, Keiko Murano, Hidekatsu Nemura, and Kenji Sasaki. "Lattice QCD approach to Nuclear Physics." In: *PTEP* 2012 (2012), 01A105. DOI: 10.1093/ptep/pts010. arXiv: 1206.5088 [hep-lat].

[4]   S. Aoki et al. "1+1+1 flavor QCD + QED simulation at the physical point." In: *Phys. Rev. D* 86 (2012), p. 034507. DOI: 10.1103/PhysRevD.86.034507. arXiv: 1205.2961 [hep-lat].

[5]   Tomomi Ishikawa, Thomas Blum, Masashi Hayakawa, Taku Izubuchi, Chulwoo Jung, and Ran Zhou. "Full QED+QCD low-energy constants through reweighting." In: *Phys. Rev. Lett.* 109 (2012), p. 072002. DOI: 10.1103/PhysRevLett.109.072002. arXiv: 1202.6018 [hep-lat].

[6]   G. M. de Divitiis, R. Frezzotti, V. Lubicz, G. Martinelli, R. Petronzio, G. C. Rossi, F. Sanfilippo, S. Simula, and N. Tantalo. "Leading isospin breaking effects on the lattice." In: *Phys. Rev. D* 87.11 (2013), p. 114505. DOI: 10.1103/PhysRevD.87.114505. arXiv: 1303.4896 [hep-lat].

[7]   G. M. de Divitiis et al. "Isospin breaking effects due to the up-down mass difference in Lattice QCD." In: *JHEP* 04 (2012), p. 124. DOI: 10.1007/JHEP04(2012)124. arXiv: 1110.6294 [hep-lat].

[8]   N. Carrasco et al. "Up, down, strange and charm quark masses with $N_f = 2+1+1$ twisted mass lattice QCD." In: *Nucl. Phys. B* 887 (2014), pp. 19–68. DOI: 10.1016/j.nuclphysb.2014.07.025. arXiv: 1403.4504 [hep-lat].

[9]   D. Giusti. "QCD+QED lattice calculation of hadronic decay rates." In: *Nuovo Cim. C* 42.4 (2019), p. 149. DOI: 10.1393/ncc/i2019-19149-y. arXiv: 1807.11681 [hep-lat].

[10]   Davide Giusti, Vittorio Lubicz, Guido Martinelli, Francesco Sanfilippo, and Silvano Simula. "Isospin-breaking corrections to the muon magnetic anomaly in Lattice QCD." In: *PoS* CD2018 (2019), p. 063. DOI: 10.22323/1.317.0063. arXiv: 1909.01962 [hep-lat].

[11]   Simone Romiti. "Leading isospin breaking effects in nucleon and   masses." In: *Suplemento de la Revista Mexicana de Física* (2022).

[12]   A. Duncan, E. Eichten, and H. Thacker. "Electromagnetic splittings and light quark masses in lattice QCD." In: *Phys. Rev. Lett.* 76 (1996), pp. 3894–3897. DOI: 10.1103/PhysRevLett.76.3894. arXiv: hep-lat/9602005.

[13]   Masashi Hayakawa and Shunpei Uno. "QED in finite volume and finite size scaling effect on electromagnetic properties of hadrons." In: *Prog. Theor. Phys.* 120 (2008), pp. 413–441. DOI: 10.1143/PTP.120.413. arXiv: 0804.2044 [hep-ph].

[14]   Michael G. Endres, Andrea Shindler, Brian C. Tiburzi, and André Walker-Loud. "Massive Photons: An Infrared Regularization Scheme for Lattice QCD + QED." In: *Phys. Rev. Lett.* 117 (7 Aug. 2016), p. 072002. DOI: 10.1103/PhysRevLett.117.072002. URL: https://link.aps.org/doi/10.1103/PhysRevLett.117.072002.

[15] M. A. Clark, Michele Della Morte, Zack Hall, Ben Hörz, Amy Nicholson, Andrea Shindler, Justus Tobias Tsang, André Walker-Loud, and Haobo Yan. "QED with massive photons for precision physics: zero modes and first result for the hadron spectrum." In: *PoS* LATTICE2021 (2022), p. 281. DOI: 10.22323/1.396.0281. arXiv: 2201.03251 [hep-lat].

[16] L. Polley. "Boundaries for SU(3)(C) x U(1)-el lattice gauge theory with a chemical potential." In: *Z. Phys. C* 59 (1993), pp. 105–108. DOI: 10.1007/BF01555844.

[17] U. J. Wiese. "C periodic and G periodic QCD at finite temperature." In: *Nucl. Phys. B* 375 (1992), pp. 45–66. DOI: 10.1016/0550-3213(92)90333-7.

[18] Andreas S. Kronfeld and U. J. Wiese. "SU(N) gauge theories with C periodic boundary conditions. 1. Topological structure." In: *Nucl. Phys. B* 357 (1991), pp. 521–533. DOI: 10.1016/0550-3213(91)90479-H.

[19] A.S. Kronfeld and U.-J. Wiese. "SU suN) gauge theories with C-periodic boundary conditions (II). Small-volume dynamics." In: *Nuclear Physics B* 401.1 (1993), pp. 190–205. ISSN: 0550-3213. DOI: https://doi.org/10.1016/0550-3213(93)90302-6. URL: https://www.sciencedirect.com/science/article/pii/0550321393903026.

[20] Biagio Lucini, Agostino Patella, Alberto Ramos, and Nazario Tantalo. "Charged hadrons in local finite-volume QED+QCD with C* boundary conditions." In: *JHEP* 02 (2016), p. 076. DOI: 10.1007/JHEP02(2016)076. arXiv: 1509.01636 [hep-th].

[21] R. Horsley et al. "Isospin splittings in the decuplet baryon spectrum from dynamical QCD+QED." In: *J. Phys. G* 46 (2019), p. 115004. DOI: 10.1088/1361-6471/ab32c1. arXiv: 1904.02304 [hep-lat].

[22] Lucius et al. Bushnaq. *First results on QCD+QED with C* boundary conditions.* arXiv: 2209.xxx [hep-lat].

[23] Martin Hansen, Alessandro Lupo, and Nazario Tantalo. "Extraction of spectral densities from lattice correlators." In: *Phys. Rev. D* 99.9 (2019), p. 094508. DOI: 10.1103/PhysRevD.99.094508. arXiv: 1903.06476 [hep-lat].

[24] John Bulava, Maxwell T. Hansen, Michael W. Hansen, Agostino Patella, and Nazario Tantalo. "Inclusive rates from smeared spectral densities in the two-dimensional O(3) non-linear σ-model." In: *JHEP* 07 (2022), p. 034. DOI: 10.1007/JHEP07(2022)034. arXiv: 2111.12774 [hep-lat].

[25] H.B. Nielsen and M. Ninomiya. "A no-go theorem for regularizing chiral fermions." In: *Physics Letters B* 105.2 (1981), pp. 219–223. ISSN: 0370-2693. DOI: https://doi.org/10.1016/0370-2693(81)91026-1. URL: https://www.sciencedirect.com/science/article/pii/0370269381910261.

[26] Martin Luscher. "Computational Strategies in Lattice QCD." In: *Les Houches Summer School: Session 93: Modern perspectives in lattice QCD: Quantum field theory and high performance computing.* Feb. 2010, pp. 331–399. arXiv: 1002.4232 [hep-lat].

[27] S. Aoki et al. "Light hadron spectrum and quark masses from quenched lattice QCD." In: *Phys. Rev. D* 67 (3 Feb. 2003), p. 034503. DOI: 10.1103/PhysRevD.67.034503. URL: https://link.aps.org/doi/10.1103/PhysRevD.67.034503.

[28] Christof Gattringer et al. "Quenched spectroscopy with fixed-point and chirally improved fermions." In: *Nuclear Physics B* 677.1 (2004), pp. 3–51. ISSN: 0550-3213. DOI: https://doi.org/10.1016/j.nuclphysb.2003.10.044. URL: https://www.sciencedirect.com/science/article/pii/S0550321303009453.

[29] Zohreh Davoudi and Martin J. Savage. "Finite-Volume Electromagnetic Corrections to the Masses of Mesons, Baryons and Nuclei." In: *Phys. Rev. D* 90.5 (2014), p. 054503. DOI: 10.1103/PhysRevD.90.054503. arXiv: 1402.6741 [hep-lat].

[30] Z. Fodor, C. Hoelbling, S. D. Katz, L. Lellouch, A. Portelli, K. K. Szabo, and B. C. Toth. "Quantum electrodynamics in finite volume and nonrelativistic effective field theories." In: *Phys. Lett. B* 755 (2016), pp. 245–248. DOI: 10.1016/j.physletb.2016.01.047. arXiv: 1502.06921 [hep-lat].

[31] Subhasish Basak et al. "Finite-volume effects and the electromagnetic contributions to kaon and pion masses." In: *PoS* LATTICE2014 (2014), p. 116. DOI: 10.22323/1.214. 0116. arXiv: 1409.7139 [hep-lat].

[32] T. Blum, R. Zhou, T. Doi, M. Hayakawa, T. Izubuchi, S. Uno, and N. Yamada. "Electromagnetic mass splittings of the low lying hadrons and quark masses from 2+1 flavor lattice QCD+QED." In: *Phys. Rev. D* 82 (2010), p. 094508. DOI: 10.1103/PhysRevD.82.094508. arXiv: 1006.1311 [hep-lat].

[33] Mattia Bruno, Tomasz Korzec, and Stefan Schaefer. "Setting the scale for the CLS $2+1$ flavor ensembles." In: *Phys. Rev. D* 95.7 (2017), p. 074504. DOI: 10.1103/PhysRevD.95.074504. arXiv: 1608.08900 [hep-lat].

[34] H. Neufeld and H. Rupertsberger. "The Electromagnetic interaction in chiral perturbation theory." In: *Z. Phys. C* 71 (1996), pp. 131–138. DOI: 10.1007/s002880050156. arXiv: hep-ph/9506448.

[35] Oliver Bar and Maarten Golterman. "Chiral perturbation theory for gradient flow observables." In: *Phys. Rev. D* 89.3 (2014). [Erratum: Phys.Rev.D 89, 099905 (2014)], p. 034505. DOI: 10.1103/PhysRevD.89.034505. arXiv: 1312.4999 [hep-lat].

[36] W. Bietenholz et al. "Tuning the strange quark mass in lattice simulations." In: *Phys. Lett. B* 690 (2010), pp. 436–441. DOI: 10.1016/j.physletb.2010.05.067. arXiv: 1003.1114 [hep-lat].

[37] Mattia Bruno et al. "Simulation of QCD with $N_f = 2 + 1$ flavors of non-perturbatively improved Wilson fermions." In: *JHEP* 02 (2015), p. 043. DOI: 10.1007/JHEP02(2015)043. arXiv: 1411.3982 [hep-lat].

[38] Roman Höllwieser, Francesco Knechtli, and Tomasz Korzec. "Scale setting for $N_f = 3 + 1$ QCD." In: *Eur. Phys. J. C* 80.4 (2020), p. 349. DOI: 10.1140/epjc/s10052-020-7889-7. arXiv: 2002.02866 [hep-lat].

[39] Patrick Fritzsch, Rainer Sommer, Felix Stollenwerk, and Ulli Wolff. "Symanzik improvement with dynamical charm: a 3+1 scheme for Wilson quarks." In: *JHEP* 06 (2018). [Erratum: JHEP 10, 165 (2020)], p. 025. DOI: 10.1007/JHEP06(2018)025. arXiv: 1805.01661 [hep-lat].

[40] B. Alles, G. Boyd, Massimo D'Elia, A. Di Giacomo, and E. Vicari. "Hybrid Monte Carlo and topological modes of full QCD." In: *Phys. Lett. B* 389 (1996), pp. 107–111. DOI: 10.1016/S0370-2693(96)01247-6. arXiv: hep-lat/9607049.

[41] V. Azcoiti, G. Di Carlo, and A. F. Grillo. "Approaching a first order phase transition in compact pure gauge QED." In: *Phys. Lett. B* 268 (1991), pp. 101–105. DOI: 10.1016/0370-2693(91)90930-0.

[42] Isabel Campos, Andres Cruz, and Alfonso Tarancon. "A Study of the phase transition in 4-D pure compact U(1) LGT on toroidal and spherical lattices." In: *Nucl. Phys. B* 528 (1998), pp. 325–354. DOI: 10.1016/S0550-3213(98)00452-0. arXiv: hep-lat/9803007.

[43] G. Arnold, B. Bunk, T. Lippert, and K. Schilling. "Compact QED under scrutiny: It's first order." In: *Nucl. Phys. B Proc. Suppl.* 119 (2003). Ed. by R. Edwards, John W. Negele, and D. Richards, pp. 864–866. DOI: 10.1016/S0920-5632(03)01704-3. arXiv: hep-lat/0210010.

[44] Jens Luecke, Lucius Bushnaq, Isabel Campos, Marco Catillo, Alessandro Cotellucci, Madeleine Evie Beth Dale, Patrick Fritzsch, Marina Krstić Marinković, Agostino Patella, and Nazario Tantalo. "An update on QCD+QED simulations with C* boundary conditions." In: *PoS* LATTICE2021 (2022), p. 293. DOI: 10.22323/1.396.0293. arXiv: 2108.11989 [hep-lat].

[45] Martin Lüscher. "Properties and uses of the Wilson flow in lattice QCD." In: *JHEP* 08 (2010). [Erratum: JHEP 03, 092 (2014)], p. 071. DOI: 10.1007/JHEP08(2010)071. arXiv: 1006.4518 [hep-lat].

[46] Patrick Fritzsch and Alberto Ramos. "The gradient flow coupling in the Schrödinger Functional." In: *JHEP* 10 (2013), p. 008. DOI: 10.1007/JHEP10(2013)008. arXiv: 1301.4388 [hep-lat].

[47] I. Campos, R. Kirchner, I. Montvay, J. Westphalen, A. Feo, S. Luckmann, G. Munster, and K. Spanderen. "Monte Carlo simulation of SU(2) Yang-Mills theory with light gluinos." In: *Eur. Phys. J. C* 11 (1999), pp. 507–527. DOI: 10.1007/s100520050651. arXiv: hep-lat/9903014.

[48] Daniel Mohler and Stefan Schaefer. "Remarks on strange-quark simulations with Wilson fermions." In: *Phys. Rev. D* 102.7 (2020), p. 074506. DOI: 10.1103/PhysRevD.102.074506. arXiv: 2003.13359 [hep-lat].

[49] Isabel Campos, Patrick Fritzsch, Martin Hansen, Marina Krstic Marinkovic, Agostino Patella, Alberto Ramos, and Nazario Tantalo. "openQ*D code: a versatile tool for QCD+QED simulations." In: *Eur. Phys. J. C* 80.3 (2020), p. 195. DOI: 10.1140/epjc/s10052-020-7617-3. arXiv: 1908.11673 [hep-lat].

[50] Martin Luscher and Stefan Schaefer. "Lattice QCD with open boundary conditions and twisted-mass reweighting." In: *Comput. Phys. Commun.* 184 (2013), pp. 519–528. DOI: 10.1016/j.cpc.2012.10.003. arXiv: 1206.2809 [hep-lat].

[51] Isabel Campos, Patrick Fritzsch, Martin Hansen, Marina Krstić Marinković, Agostino Patella, Alberto Ramos, and Nazario Tantalo. "openQ*D simulation code for QCD+QED." In: *EPJ Web Conf.* 175 (2018). Ed. by M. Della Morte, P. Fritzsch, E. Gámiz Sánchez, and C. Pena Ruano, p. 09005. DOI: 10.1051/epjconf/201817509005. arXiv: 1710.08839 [hep-lat].

[52] G. G. Batrouni, G. R. Katz, Andreas S. Kronfeld, G. P. Lepage, B. Svetitsky, and K. G. Wilson. "Langevin Simulations of Lattice Field Theories." In: *Phys. Rev. D* 32 (1985), p. 2736. DOI: 10.1103/PhysRevD.32.2736.

[53] Simon Duane and Brian J. Pendleton. "GAUGE INVARIANT FOURIER ACCELERATION." In: *Phys. Lett. B* 206 (1988), pp. 101–106. DOI: 10.1016/0370-2693(88)91270-1.

[54] J. C. Sexton and D. H. Weingarten. "Hamiltonian evolution for the hybrid Monte Carlo algorithm." In: *Nucl. Phys. B* 380 (1992), pp. 665–677. DOI: 10.1016/0550-3213(92)90263-B.

[55] I.P. Omelyan, Ihor Mryglod, and R. Folk. "Symplectic analytically integrable decomposition algorithms: Classification, derivation, and application to molecular dynamics, quantum and celestial mechanics simulations." In: *Computer Physics Communications* 151 (Apr. 2003), pp. 272–314. DOI: 10.1016/S0010-4655(02)00754-3.

[56] M. Albanese et al. "Glueball Masses and String Tension in Lattice QCD." In: *Phys. Lett. B* 192 (1987), pp. 163–169. DOI: 10.1016/0370-2693(87)91160-9.

[57] Thomas A. DeGrand and Richard D. Loft. "Wave-function tests for lattice QCD spectroscopy." In: *Computer Physics Communications* 65.1 (1991), pp. 84–91. ISSN: 0010-4655. DOI: https://doi.org/10.1016/0010-4655(91)90158-H. URL: https://www.sciencedirect.com/science/article/pii/001046559190158H.

[58] R.H. Dalitz and F. Von Hippel. "Electromagnetic Λ-Σo mixing and charge symmetry for the Λ-Hyperon." In: *Physics Letters* 10.1 (1964), pp. 153–157. ISSN: 0031-9163. DOI: https://doi.org/10.1016/0031-9163(64)90617-1. URL: https://www.sciencedirect.com/science/article/pii/0031916364906171.

[59] Avraham Gal. "Comment on "Lattice determination of Σ-Λ mixing"." In: *Phys. Rev. D* 92.1 (2015), p. 018501. DOI: 10.1103/PhysRevD.92.018501. arXiv: 1506.01143 [nucl-th].

[60] Kostas Orginos and David Richards. "Improved methods for the study of hadronic physics from lattice QCD." In: *Journal of Physics G: Nuclear and Particle Physics* 42.3 (Feb. 2015), p. 034011. DOI: 10.1088/0954-3899/42/3/034011. URL: https://doi.org/10.1088/0954-3899/42/3/034011.

[61] George Backus and Freeman Gilbert. "The Resolving Power of Gross Earth Data." In: *Geophysical Journal International* 16.2 (Oct. 1968), pp. 169–205. ISSN: 0956-540X. DOI: 10.1111/j.1365-246X.1968.tb00216.x. eprint: https://academic.oup.com/gji/article-pdf/16/2/169/5891044/16-2-169.pdf. URL: https://doi.org/10.1111/j.1365-246X.1968.tb00216.x.

[62] Maxwell T. Hansen, Harvey B. Meyer, and Daniel Robaina. "From deep inelastic scattering to heavy-flavor semileptonic decays: Total rates into multihadron final states from lattice QCD." In: *Phys. Rev. D* 96.9 (2017), p. 094513. DOI: 10.1103/PhysRevD.96.094513. arXiv: 1704.08993 [hep-lat].

[63] William H. Press, Saul A. Teukolsky, William T. Vetterling, and Brian P. Flannery. *Numerical Recipes in C (2nd Ed.): The Art of Scientific Computing.* USA: Cambridge University Press, 1992. ISBN: 0521431085.

[64] C. Q. Geng, Chia-Wei Liu, and Tien-Hsueh Tsai. "Mixing effects of $\Sigma^0 - \Lambda^0$ in Λ_c^+ decays." In: *Phys. Rev. D* 101.5 (2020), p. 054005. DOI: 10.1103/PhysRevD.101.054005. arXiv: 2002.09583 [hep-ph].

[65] Tosio Kato. *Perturbation theory for linear operators; 2nd ed.* Grundlehren der mathematischen Wissenschaften : a series of comprehensive studies in mathematics. Berlin: Springer, 1976. URL: https://cds.cern.ch/record/101545.

[66] Ulli Wolff. "Monte Carlo errors with less errors." In: *Comput. Phys. Commun.* 156 (2004). [Erratum: Comput.Phys.Commun. 176, 383 (2007)], pp. 143–153. DOI: 10.1016/S0010-4655(03)00467-3. arXiv: hep-lat/0306017.

[67] Stefan Schaefer, Rainer Sommer, and Francesco Virotta. "Critical slowing down and error analysis in lattice QCD simulations." In: *Nucl. Phys. B* 845 (2011), pp. 93–119. DOI: 10.1016/j.nuclphysb.2010.11.020. arXiv: 1009.5228 [hep-lat].

C-EVEN CORRELATORS

In this section, we explain how our desired correlators can be expressed in two different bases, in the orbifold construction and in the periodic/anti-periodic basis, and to show that the global sum of the correlator in the orbifold construction is equivalent to taking the sum over only C-even correlators in the periodic/anti-periodic basis.

A.1 CONVENTIONS

In this calculation, we are using the representation of the charge conjugation matrix C given by

$$C = i\gamma_0\gamma_2; \tag{A.1a}$$

$$C = C^{-1} = C^\dagger = -C^T, \tag{A.1b}$$

where γ_μ are the Euclidean Dirac matrices.

A fermion field ψ with a period of $2L$ can be decomposed into L-periodic and L-anti-periodic components, $\psi_P(x) = \psi_P(x + L)$ and $\psi_A(x) = -\psi_A(x + L)$ respectively. These components have the following properties:

$$\psi_P(x) = C\overline{\psi}_P^T(x); \tag{A.2a}$$

$$\psi_A(x) = -C\overline{\psi}_A^T(x); \tag{A.2b}$$

$$\overline{\psi}_P(x) = -\psi_P^T(x)C; \tag{A.2c}$$

$$\overline{\psi}_A(x) = \psi_A^T(x)C. \tag{A.2d}$$

Fermions transform under charge conjugation as:

$$\psi \to \psi^C(x) = C\overline{\psi}^T(x); \tag{A.3a}$$

$$\overline{\psi} \to \overline{\psi}^C(x) = -\psi^T(x)C. \tag{A.3b}$$

A.2 CORRELATOR EXPRESSION IN TERMS OF C* PROPAGATORS

Under C* boundary conditions, momentum eigenstates are automatically eigenstates of the charge conjugation operator. Hence, C-even fields are periodic and C-odd fields are anti-periodic. This makes equivalent two descriptions of the C* boundary conditions:

- Periodic/anti-periodic basis: The lattice is entirely 'physical' with dimensions $L_T \times L \times L \times L$. The fermion ψ and its Dirac adjoint $\overline{\psi}$ are independent variables and thus it is valid to describe the correlator in terms of these. The fermion and its adjoint can then be split into L-periodic and L-anti-periodic components and the correlator may be written in terms of periodic and anti-periodic propagators.

- Orbifold construction: The extended lattice of dimensions $L_T \times 2L \times L \times L$ is formed from the usual physical lattice and its mirror image. The orbifold constraints describing the C* boundary conditions between the physical and the mirror lattice mean that the

Dirac adjoint of the fermion is dependent on the fermion, and the correlator must be treated in a different fashion. When referring to the different sections of the lattice, we will denote the extended lattice of dimensions $L_T \times 2L \times L \times L$ as Λ, the physical sublattice as $\widetilde{\Lambda}$ and the mirror sublattice as $\Lambda / \widetilde{\Lambda}$. In the following calculation, when operating within the orbifold construction we will assume that there are C* boundary conditions in at least one spatial direction, with any remaining spatial directions subject to periodic boundary conditions. The direction corresponding to the unit vector $\hat{1}$ is the direction that always has C* boundary conditions and which corresponds to direction 1 in Fig. 2 of [49]. The choice of temporal boundary conditions is arbitrary.

In the rest of the section, we relate the global sum over correlators in the orbifold construction to correlators expressed in terms of the C-symmetry properties of the interpolating operators from which they are formed. In this way the equivalence of the two methods for obtaining C-even correlators is shown. This is followed later by another derivation of the same correlators starting from the generating functional in the periodic-anti-periodic basis, which is then used to check our C-even correlators in our implementation of the C* formulation.

Let $\mathbf{x}$ denote a position in the lattice. In the orbifold construction, if $\mathbf{x}$ lies on the physical lattice, then the position of its corresponding adjoint fermion on the mirror lattice is given by $\overline{\mathbf{x}} = \mathbf{x} + \hat{1}L$. We define a translation operator T by its operation on a fermion: $T\psi(\mathbf{x}) \equiv \psi(\overline{\mathbf{x}})$, i.e. T translates a fermion from position $\mathbf{x}$ to its corresponding position $\overline{\mathbf{x}}$ on the mirror lattice. This operator acts in an equivalent way to that of matrix K defined in Sec. 4.8, but is defined here as acting only on one fermion at a time.

The right hand side of Eq. (A.3) is the same as the action of the translation of fermions due to the C* boundary conditions given in Eq. (3.3a), meaning that $\psi^C(x) = \psi(\overline{x})$.

Taking $\mathbf{x}$ to lie in the physical lattice, $\mathbf{x} \in \widetilde{\Lambda}$, we can provide a relation between fermions Ψ on the ordinary physical lattice of the periodic/anti-periodic basis and the fermions ψ of the orbifold construction:

$$\Psi(\mathbf{x}) = \psi(\mathbf{x});$$
$$\overline{\Psi}(\mathbf{x}) = \overline{\psi}^C(\overline{\mathbf{x}}) = -\psi^T(\overline{\mathbf{x}})C = -\psi(\mathbf{x})^T CT. \tag{A.4}$$

The free action of the fermion is given by

$$S_F = \sum_{\mathbf{x} \in \widetilde{\Lambda}} \overline{\Psi}(\mathbf{x}) D_\psi \Psi(\mathbf{x}) = -\frac{1}{2} \sum_{\mathbf{x} \in \Lambda} \psi(\mathbf{x})^T CT D_\psi \psi(\mathbf{x}), \tag{A.5}$$

where the factor of $\frac{1}{2}$ comes from double counting due to summing over the extended lattice, and D_ψ is the Dirac operator for the fermion ψ.

A.2.1 *Physical lattice*

Still taking $\mathbf{x} \in \widetilde{\Lambda}$, we can relate the correlator of the physical basis to that of the orbifold construction:

$$C(t, \mathbf{x}) = \langle \overline{U}(\mathbf{0}) \Gamma V(\mathbf{0}) \overline{V}(\mathbf{x}) \Gamma U(\mathbf{x}) \rangle, \tag{A.6}$$
$$= \text{Tr} \left[\overline{u}(\mathbf{0}) \Gamma v(\mathbf{0}) \overline{v}(\mathbf{x}) \Gamma u(\mathbf{x}) \right], \tag{A.7}$$

where the source is positioned at $\mathbf{0}$ on the physical lattice and where Γ is some interpolating operator formed from one or more Dirac matrices. Using the Grassmann algebra of the fermions we get the standard expression for the a meson correlator:

$$C(t, \mathbf{x}) = \mathrm{Tr}\left[\overline{u}(\mathbf{0})\Gamma v(\mathbf{0})\overline{v}(\mathbf{x})\Gamma u(\mathbf{x})\right], \tag{A.8}$$
$$= \mathrm{Tr}\left[\Gamma \langle \overline{v}(\mathbf{x})v(\mathbf{0})\rangle \Gamma \langle \overline{u}(\mathbf{0})u(\mathbf{x})\rangle\right],$$
$$= \mathrm{Tr}\left[\Gamma D_v^{-1}(\mathbf{x}, \mathbf{0})\Gamma D_u^{-1}(\mathbf{0}, \mathbf{x})\right]. \tag{A.9}$$

A.2.2 *Mirror lattice*

If the correlator between the source at position $\mathbf{0}$ on the physical lattice with the sink at position $\mathbf{x}$ on the physical lattice ($\mathbf{x} \in \widetilde{\Lambda}$) is given by $C(t, \mathbf{x}) = \langle \overline{U}(\mathbf{0})\Gamma V(\mathbf{0})\overline{V}(\mathbf{x})\Gamma U(\mathbf{x})\rangle$, then the correlator between the source at position $\mathbf{0}$ on the physical lattice with the sink at position $\overline{\mathbf{x}}$ on the mirror lattice is given by $C(t, \overline{\mathbf{x}}) = \langle \overline{U}(\mathbf{0})\Gamma V(\mathbf{0})\overline{v}(\overline{\mathbf{x}})\Gamma u(\overline{\mathbf{x}})\rangle$. Here the fermions on the mirror lattice have been expressed in the orbifold basis in order to be valid for $\overline{x} \in \Lambda/\widetilde{\Lambda}$. Note that the representation of the source is unchanged as its position is unchanged and it remains on the physical lattice.

Using the definition of the C* boundary conditions, we infer that $\psi^C(x) = \psi(\overline{x})$, and similarly $\overline{\psi}^C(x) = \overline{\psi}(\overline{x})$, giving

$$C(t, \overline{\mathbf{x}}) = \langle \overline{\mathcal{O}}(\mathbf{0})\overline{v}(\overline{\mathbf{x}})\Gamma u(\overline{\mathbf{x}}))\rangle,$$
$$= \langle \overline{\mathcal{O}}(\mathbf{0})\overline{v}^C(\mathbf{x})\Gamma u^C(\mathbf{x}))\rangle,$$
$$= \langle \overline{\mathcal{O}}(\mathbf{0})\mathcal{O}^C(\mathbf{x})\rangle. \tag{A.10}$$

We therefore find that

$$C(t, \mathbf{x}) + C(t, \overline{\mathbf{x}}) = \langle \overline{\mathcal{O}}(\mathbf{0})\mathcal{O}(\mathbf{x})\rangle + \langle \overline{\mathcal{O}}(\mathbf{0})\mathcal{O}^C(\mathbf{x})\rangle. \tag{A.11}$$

From the definition of the C* formulation, it may be seen that taking the spatial sum over both the physical and mirror lattices on one end of the correlator corresponds to making the corresponding interpolating operator C-even. It is in fact only necessary to make one of the interpolating operators of the correlator C-even, as the C-odd components of the remaining interpolating operator will vanish in combination with the C-even interpolating operator due to the nature of the C* boundary conditions.

As for the case above, we derive an explicit expression for the correlator with the sink on the mirror lattice:

$$C(t, \overline{x}) = \langle \overline{U}(\mathbf{0})\Gamma V(\mathbf{0})\overline{v}(\overline{\mathbf{x}})\Gamma u(\overline{\mathbf{x}})\rangle, \tag{A.12}$$
$$= \langle \overline{u}(\mathbf{0})\Gamma v(\mathbf{0})\overline{v}(\overline{\mathbf{x}})\Gamma u(\overline{\mathbf{x}})\rangle,$$
$$= \langle \overline{u}(\mathbf{0})\Gamma v(\mathbf{0})T(x \to \overline{x})\overline{v}(\mathbf{x})\Gamma T(x \to \overline{x})u(\mathbf{x})\rangle,$$
$$= \mathrm{Tr}\left[u(\mathbf{x})\overline{u}(\mathbf{0})\Gamma v(\mathbf{0})\overline{v}(\mathbf{x})\Gamma\right] T(x \to \overline{x})T(x \to \overline{x}),$$
$$= \mathrm{Tr}\left[\langle \overline{u}(\mathbf{0})u(\mathbf{x})\rangle \Gamma \langle \overline{v}(\mathbf{x})v(\mathbf{0})\rangle \Gamma\right] T(x \to \overline{x})T(x \to \overline{x}),$$
$$= \mathrm{Tr}\left[D_u^{-1}(\mathbf{0}, \mathbf{x})\Gamma D_v^{-1}(\mathbf{x}, \mathbf{0})\Gamma\right] T(x \to \overline{x})T(x \to \overline{x}),$$
$$= \mathrm{Tr}\left[D_u^{-1}(\mathbf{0}, \overline{\mathbf{x}})\Gamma D_v^{-1}(\overline{\mathbf{x}}, \mathbf{0})\Gamma\right], \tag{A.13}$$

where we have taken the trace in Dirac space. We therefore see that, in the orbifold construction, we can treat the correlators the same irrespective of whether the sink lies on the physical or mirror lattice. The logic presented above also applies to the baryons.

112

C-even interpolating operators are necessary for the construction of zero-momentum fields in the C* formulation. A correlator $C(t)$ can be constructed as the trace of the product of an interpolating operator $\mathcal{O}_{\text{even}}$ and its Dirac adjoint $\overline{\mathcal{O}}_{\text{even}}$. In order to construct a C-even correlator, we require these interpolating operators to be either both C-even or both C-odd. For now, we will consider the case where they are both C-even. This is because we are considering the effective mass, so C-odd components are selected against by taking the momenta to be zero. These C-even operators can be formed by taking the sum of the usual interpolating operator with its charge-conjugate:

$$
\begin{aligned}
C(t) &= \left\langle \overline{\mathcal{O}}_{\text{even}} \mathcal{O}_{\text{even}} \right\rangle, \\
&= \left\langle \frac{1}{2} \left(\overline{\mathcal{O}} + \overline{\mathcal{O}}^C \right) \frac{1}{2} \left(\mathcal{O} + \mathcal{O}^C \right) \right\rangle, \\
&= \frac{1}{4} \left(\left\langle \overline{\mathcal{O}} \mathcal{O} \right\rangle + \left\langle \overline{\mathcal{O}}^C \mathcal{O} \right\rangle + \left\langle \overline{\mathcal{O}} \mathcal{O}^C \right\rangle + \left\langle \overline{\mathcal{O}}^C \mathcal{O}^C \right\rangle \right).
\end{aligned}
\tag{A.14}
$$

We therefore see that the C-even or, indeed, the C-odd correlator can be found by evaluating four different correlation functions and taking the appropriate sum.

Charge-conjugated interpolating operators $\mathcal{O}^C$ and $\overline{\mathcal{O}}^C$ can be constructed by applying the charge conjugation operation given in Eqns. (A.3) to each fermion field in $\mathcal{O}$ and $\overline{\mathcal{O}}$ respectively.

Defining our meson interpolating operators as

$$
\mathcal{O}(x) = \overline{d}(x)_\alpha \Gamma_{\alpha\beta} u(x)_\beta;
\tag{A.15a}
$$

$$
\overline{\mathcal{O}}(x) = \overline{u}(x)_\alpha \Gamma_{\alpha\beta} d(x)_\beta,
\tag{A.15b}
$$

leads to the charge-conjugated interpolating operators

$$
\mathcal{O}^C(x) = -d(x)_\omega C_{\omega\alpha} \Gamma_{\alpha\beta} C_{\beta\kappa} \overline{u}(x)_\kappa;
\tag{A.16a}
$$

$$
\overline{\mathcal{O}}^C(x) = -u(x)_\omega C_{\omega\alpha} \Gamma_{\alpha\beta} C_{\beta\kappa} \overline{d}(x)_\kappa.
\tag{A.16b}
$$

A final expression for the meson C-even correlator is given in Sec. 4.5, while the baryon C-even interpolating operators and correlators are given in Sec. 5.2.3.

C-EVEN CORRELATOR FROM THE GENERATING FUNCTIONAL

Starting from the generating functional in the periodic/anti-periodic basis, we hereby derive the expression for the C-even meson correlator on a purely physical lattice. This is intended both as a demonstration and to be used later in this appendix as a check on our calculation of the correlators inside our implementation of the C* formulation.

The generating functional W for two flavours of fermion u and d can be written in terms of the action S as

$$
W[S] = \int \mathcal{D}u \mathcal{D}\overline{u} \mathcal{D}d \mathcal{D}\overline{d} e^{-S}
\tag{A.17}
$$

or, treating the periodic and anti-periodic components of the fermions independently, as

$$
W[S] = \int \mathcal{D}u_P \mathcal{D}u_A \mathcal{D}d_P \mathcal{D}d_A e^{-S}.
\tag{A.18}
$$

When Eqs. (A.2) are applied to the fermion fields, the free action may be written

$$
\begin{aligned}
S_{\text{free}} &= \int_{L^3 T} d^4 x \Big(\overline{u}_P(x) D_{uP}(x, x') u_P(x') + \overline{u}_A(x) D_{uA}(x, x') u_A(x') \\
&\qquad + \overline{d}_P(x) D_{dP}(x, x') d_P(x') + \overline{d}_A(x) D_{dA}(x, x') u_A(x') \Big), \\
&= \int_{L^3 T} d^4 x \Big(- u_P^T(x) C D_{uP}(x, x') u_P(x') + u_A^T(x) C D_{uA}(x, x') u_A(x') \\
&\qquad - d_P^T(x) C D_{dP}(x, x') d_P(x') + d_A^T(x) C D_{dA}(x, x') d_A(x') \Big),
\end{aligned}
\tag{A.19}
$$

where $D_\psi(x, x')$ is the Dirac operator for the fermion ψ. The label on the Dirac operator does not imply any symmetry properties of the Dirac operator.

Introducing arbitrary source fields for each fermion field component gives us the generating functional

$$
\begin{aligned}
&W\left[j_{u_P}, j_{u_A}, j_{d_P}, j_{d_A} \right] \\
&= B_1 \int \mathcal{D}u \mathcal{D}\overline{u} \mathcal{D}d \mathcal{D}\overline{d} \\
&\quad \cdot \exp\Big(- S_{\text{free}} + \int_{L^3 T} d^4 x \big[j_{u_P}^T u_P + j_{u_A}^T u_A + j_{d_P}^T d_P + j_{d_A}^T d_A \big](x) \Big),
\end{aligned}
\tag{A.20}
$$

where B_1 is some constant.

Using the standard integral

$$
\int_\infty^\infty d\vec{p}\, e^{-\frac{1}{2}\vec{p}\cdot A \cdot \vec{p} + \vec{j}\vec{p}} = B_2 e^{\frac{1}{2}\vec{j}\cdot A^{-1}\cdot \vec{j}},
\tag{A.21}
$$

where B_2 is a constant, the generating functional can be written

$$
\begin{aligned}
W[j] = \exp\Big(\frac{1}{4}\big(&-j_{u_P \alpha}(x')(S_{u_P}C)(x', x'')_{\alpha\beta} j_{u_P \beta}(x'') \\
&+ j_{u_A \alpha}(x')(S_{u_A}C)(x', x'')_{\alpha\beta} j_{u_A \beta}(x'') \\
&- j_{d_P \alpha}(x')(S_{d_P}C)(x', x'')_{\alpha\beta} j_{d_P \beta}(x'') \\
&+ j_{d_A \alpha}(x')(S_{d_A}C)(x', x'')_{\alpha\beta} j_{d_A \beta}(x'') \big) \Big),
\end{aligned}
\tag{A.22}
$$

where we have neglected a constant which cancels later.

Correlator $\langle \mathcal{O}(x)\overline{\mathcal{O}}(y) \rangle$

It is simple to show that the correlator

$$
\langle \mathcal{O}(x)\overline{\mathcal{O}}(y) \rangle = \Big\langle \overline{d}(x)_\alpha \Gamma_{\alpha\beta} u(x)_\beta \overline{u}(y)_\gamma \Gamma_{\gamma\sigma} d(y)_\sigma \Big\rangle
\tag{A.23}
$$

can be expressed in the form

$$
\begin{aligned}
&\frac{1}{W[0]} \Gamma_{\alpha\beta} \Gamma_{\gamma\sigma} C_{\epsilon\alpha} C_{\omega\gamma} \left(-\frac{\delta}{\delta j_{d_P \epsilon}(x)} + \frac{\delta}{\delta j_{d_A \epsilon}(x)} \right) \left(\frac{\delta}{\delta j_{u_P \beta}(x)} + \frac{\delta}{\delta j_{u_A \beta}(x)} \right) \\
&\left(-\frac{\delta}{\delta j_{u_P \omega}(y)} + \frac{\delta}{\delta j_{u_A \omega}(y)} \right) \left(\frac{\delta}{\delta j_{d_P \sigma}(y)} + \frac{\delta}{\delta j_{d_A \sigma}(y)} \right) W[j] \Big|_{j=0}.
\end{aligned}
\tag{A.24}
$$

We can therefore express the correlator in terms of the periodic and anti-periodic propagators as

$$\left\langle \mathcal{O}(x)\overline{\mathcal{O}(y)} \right\rangle = \left\langle \overline{d}(x)_\alpha \Gamma_{\alpha\beta} u(x)_\beta \overline{u}(y)_\gamma \Gamma_{\gamma\sigma} d(y)_\sigma \right\rangle,$$

$$= \frac{1}{W[0]} \left(\Gamma_{\alpha\beta} \Gamma_{\gamma\sigma} C_{\epsilon\alpha} C_{\omega\gamma} \left(-\frac{\delta}{\delta j_{d_P\epsilon}(x)} + \frac{\delta}{\delta j_{d_A\epsilon}(x)} \right) \left(\frac{\delta}{\delta j_{u_P\beta}(x)} + \frac{\delta}{\delta j_{u_A\beta}(x)} \right) \right.$$

$$\left(-\frac{\delta}{\delta j_{u_P\omega}(y)} + \frac{\delta}{\delta j_{u_A\omega}(y)} \right) \left(\frac{\delta}{\delta j_{d_P\sigma}(y)} + \frac{\delta}{\delta j_{d_A\sigma}(y)} \right)$$

$$\exp\left(\frac{1}{4} \left(-j_{u_P\kappa}(x')(S_{u_P}C)(x',x'')_{\kappa\zeta} j_{u_P\zeta}(x'') \right.\right.$$

$$+ j_{u_A\kappa}(x')(S_{u_A}C)(x',x'')_{\kappa\zeta} j_{u_A\zeta}(x'')$$

$$- j_{d_P\kappa}(x')(S_{d_P}C)(x',x'')_{\kappa\zeta} j_{d_P\zeta}(x'')$$

$$\left.\left.\left.+ j_{d_A\kappa}(x')(S_{d_A}C)(x',x'')_{\kappa\zeta} j_{d_A\zeta}(x'') \right) \right) \right)\Bigg|_{j=0}. \tag{A.25}$$

Performing the first pair of derivatives gives

$$f_1[j,S] := \left(\frac{\delta}{\delta j_{d_P\sigma}(y)} + \frac{\delta}{\delta j_{d_A\sigma}(y)} \right) W[j],$$

$$= \frac{1}{2} \left(-(S_{d_P}C)(y,x'')_{\sigma\zeta} j_{d_P\zeta}(x'') \right.$$

$$\left. + (S_{d_A}C)(y,x'')_{\sigma\zeta} j_{d_A\zeta}(x'') \right) W[j], \tag{A.26}$$

where the skew-symmetry of SC has been used. Performing the remaining pairs of derivatives, and neglecting terms which will evaluate to zero when j = 0 is assigned, gives

$$f_2[j,S] := \left(-\frac{\delta}{\delta j_{u_P\omega}(y)} + \frac{\delta}{\delta j_{u_A\omega}(y)} \right) f_1[j,S],$$

$$= \frac{1}{2} \left(-(S_{d_P}C)(y,x_1)_{\sigma\zeta} j_{d_P\zeta}(x_1) \right.$$

$$\left. + (S_{d_A}C)(y,x_1)_{\sigma\zeta} j_{d_A\zeta}(x_1) \right)$$

$$\left(-\frac{\delta}{\delta j_{u_P\omega}(y)} + \frac{\delta}{\delta j_{u_A\omega}(y)} \right) W[j],$$

$$= \frac{1}{4} \left(-(S_{d_P}C)(y,x_1)_{\sigma\zeta} j_{d_P\zeta}(x_1) \right.$$

$$\left. + (S_{d_A}C)(y,x_1)_{\sigma\zeta} j_{d_A\zeta}(x_1) \right)$$

$$\left((S_{u_P}C)(y,x_2)_{\omega\xi} j_{u_P\xi}(x_2) \right.$$

$$\left. + (S_{u_A}C)(y,x_2)_{\omega\xi} j_{u_A\xi}(x_2) \right) W[j]; \tag{A.27}$$

$$f_3[j,S] := \left(\frac{\delta}{\delta j_{u_P\beta}(x)} + \frac{\delta}{\delta j_{u_A\beta}(x)} \right) f_2[j,S],$$

$$= \frac{1}{4} \big(-(S_{d_P}C)(y,x_1)_{\sigma\zeta} j_{d_P\zeta}(x_1)$$
$$+ (S_{d_A}C)(y,x_1)_{\sigma\zeta} j_{d_A\zeta}(x_1) \big)$$
$$\left(\frac{\delta}{\delta j_{u_P\beta}(x)} + \frac{\delta}{\delta j_{u_A\beta}(x)} \right)$$
$$\big((S_{u_P}C)(y,x_2)_{\omega\xi} j_{u_P\xi}(x_2)$$
$$+ (S_{u_A}C)(y,x_2)_{\omega\xi} j_{u_A\xi}(x_2) \big) W[j],$$

$$= \frac{1}{4} \big(-(S_{d_P}C)(y,x_1)_{\sigma\zeta} j_{d_P\zeta}(x_1)$$
$$+ (S_{d_A}C)(y,x_1)_{\sigma\zeta} j_{d_A\zeta}(x_1) \big) \tag{A.28}$$
$$\big((S_{u_P}C)(y,x)_{\omega\beta}$$
$$+ (S_{u_A}C)(y,x)_{\omega\beta} \big) W[j];$$

$$f_4[j,S] := \left(-\frac{\delta}{\delta j_{d_P\epsilon}(x)} + \frac{\delta}{\delta j_{d_A\epsilon}(x)} \right) f_3[j,S],$$

$$= \frac{1}{4} \big((S_{u_P}C)(y,x)_{\omega\beta} + (S_{u_A}C)(y,x)_{\omega\beta} \big)$$
$$\left(-\frac{\delta}{\delta j_{d_P\epsilon}(x)} + \frac{\delta}{\delta j_{d_A\epsilon}(x)} \right)$$
$$\big(-(S_{d_P}C)(y,x_1)_{\sigma\zeta} j_{d_P\zeta}(x_1)$$
$$+ (S_{d_A}C)(y,x_1)_{\sigma\zeta} j_{d_A\zeta}(x_1) \big) W[j],$$

$$= \frac{1}{4} \big((S_{d_P}C)(y,x)_{\sigma\epsilon} + (S_{d_A}C)(y,x)_{\sigma\epsilon} \big)$$
$$\big((S_{u_P}C)(y,x)_{\omega\beta} + (S_{u_A}C)(y,x)_{\omega\beta} \big) W[j],$$

$$= \frac{1}{4} C_{\nu\epsilon} C_{\tau\beta} \big(S_{d_P}(y,x)_{\sigma\nu} + S_{d_A}(y,x)_{\sigma\nu} \big) \tag{A.29}$$
$$\big(S_{u_P}(y,x)_{\omega\tau} + S_{u_A}(y,x)_{\omega\tau} \big) W[j].$$

Gathering together the Γ and C matrices and applying Eqns. (A.1) lets us simplifies the expression to

$$(C_{\nu\epsilon} C_{\epsilon\alpha} \Gamma_{\alpha\beta} C_{\tau\beta})(C_{\omega\gamma} \Gamma_{\gamma\sigma}) = (\delta_{\nu\alpha} \Gamma_{\alpha\beta} C_{\tau\beta})(C_{\omega\gamma} \Gamma_{\gamma\sigma})$$
$$= (-\Gamma_{\nu\beta} C_{\beta\tau})(C_{\omega\gamma} \Gamma_{\gamma\sigma}) = -(\Gamma C)_{\nu\tau}(C\Gamma)_{\omega\sigma}.$$

The correlator can therefore be expressed as

$$\left\langle \mathcal{O}(x)\overline{\mathcal{O}(y)} \right\rangle$$
$$= -\frac{1}{4} \Big(\frac{1}{W[0]} (\Gamma C)_{\nu\tau}(C\Gamma)_{\omega\sigma} (S_{d_P} + S_{d_A})(y,x)_{\sigma\nu}$$
$$(S_{u_P} + S_{u_A})(y,x)_{\omega\tau} W[j] \Big) \Big|_{j=0},$$
$$= -(C\Gamma)_{\omega\sigma}(\Gamma C)_{\nu\tau} S_d(y,x)_{\sigma\nu} S_u(y,x)_{\omega\tau}, \tag{A.30}$$

where $S_\psi(x,y) := \frac{1}{2}(S_{\psi_P}(x,y) + S_{\psi_A}(x,y))$.

Following the same procedure in the cases $\left\langle \mathcal{O}(x)\overline{\mathcal{O}}^C(y) \right\rangle$, $\left\langle \mathcal{O}^C(x)\overline{\mathcal{O}}(y) \right\rangle$ and $\left\langle \mathcal{O}^C(x)\overline{\mathcal{O}}^C(y) \right\rangle$ gives:

-

$$\left\langle \mathcal{O}^C(x)\overline{\mathcal{O}(y)} \right\rangle$$
$$= - \left\langle d(x)_\alpha [C\Gamma C]_{\alpha\beta}\overline{u}(x)_\beta \overline{u}(y)_\gamma \Gamma_{\gamma\sigma} d(y)_\sigma \right\rangle$$
$$= -\frac{1}{4}\Big(\frac{1}{W[0]}(C\Gamma)_{\omega\sigma}(\Gamma C)_{\nu\tau}(-S_{d_P} + S_{d_A})(y,x)_{\sigma\nu}$$
$$(-S_{u_P} + S_{u_A})(y,x)_{\omega\tau}W[j]\Big)\Big|_{j=0},$$
$$= -\frac{1}{4}(C\Gamma)_{\omega\sigma}(\Gamma C)_{\nu\tau}(-S_{d_P} + S_{d_A})(y,x)_{\sigma\nu}$$
$$(-S_{u_P} + S_{u_A})(y,x)_{\omega\tau}. \tag{A.31}$$

-

$$\left\langle \mathcal{O}(x)\overline{\mathcal{O}(y)}^C \right\rangle$$
$$= - \left\langle \overline{d}(x)_\alpha \Gamma_{\alpha\beta} u(x)_\beta u(y)_\gamma [C\Gamma C]_{\gamma\sigma}\overline{d}(y)_\sigma \right\rangle$$
$$= -\frac{1}{4}\Big(\frac{1}{W[0]}(\Gamma C)_{\nu\tau}(C\Gamma)_{\gamma\omega}(-S_{d_P} + S_{d_A})(y,x)_{\omega\nu}$$
$$(-S_{u_P} + S_{u_A})(y,x)_{\gamma\tau}W[j]\Big)\Big|_{j=0},$$
$$= -\frac{1}{4}(\Gamma C)_{\nu\tau}(C\Gamma)_{\gamma\omega}(-S_{d_P} + S_{d_A})(y,x)_{\omega\nu}$$
$$(-S_{u_P} + S_{u_A})(y,x)_{\gamma\tau},$$
$$= -\frac{1}{4}(C\Gamma)_{\omega\sigma}(\Gamma C)_{\nu\tau}(-S_{d_P} + S_{d_A})(y,x)_{\sigma\nu}$$
$$(-S_{u_P} + S_{u_A})(y,x)_{\omega\tau},$$
$$= \left\langle \mathcal{O}^C(x)\overline{\mathcal{O}(y)} \right\rangle. \tag{A.32}$$

-

$$\left\langle \mathcal{O}^C(x)\overline{\mathcal{O}^C(y)} \right\rangle$$
$$= \left\langle d(x)_\alpha [C\Gamma C]_{\alpha\beta}\overline{u}(x)_\beta u(y)_\gamma [C\Gamma C]_{\gamma\sigma}\overline{d}(y)_\sigma \right\rangle$$
$$= -\frac{1}{4}\Big(\frac{1}{W[0]}(\Gamma C)_{\nu\tau}(C\Gamma)_{\gamma\omega}(S_{d_P} + S_{d_A})(y,x)_{\omega\nu}$$
$$(S_{u_P} + S_{u_A})(y,x)_{\gamma\tau}W[j]\Big)\Big|_{j=0},$$
$$= -\frac{1}{4}(\Gamma C)_{\nu\tau}(C\Gamma)_{\gamma\omega}(S_{d_P} + S_{d_A})(y,x)_{\omega\nu}$$
$$(S_{u_P} + S_{u_A})(y,x)_{\gamma\tau},$$
$$= -(\Gamma C)_{\nu\tau}(C\Gamma)_{\gamma\omega}S_d(y,x)_{\omega\nu}S_u(y,x)_{\gamma\tau},$$
$$= -(C\Gamma)_{\omega\sigma}(\Gamma C)_{\nu\tau}S_d(y,x)_{\sigma\nu}S_u(y,x)_{\omega\tau},$$
$$= \left\langle \mathcal{O}(x)\overline{\mathcal{O}(y)} \right\rangle \tag{A.33}$$

As the correlators $\left\langle \mathcal{O}\overline{\mathcal{O}} \right\rangle$ and $\left\langle \mathcal{O}^C\overline{\mathcal{O}}^C \right\rangle$ give the same expression as each other, as do $\left\langle \mathcal{O}\overline{\mathcal{O}}^C \right\rangle$ and $\left\langle \mathcal{O}^C\overline{\mathcal{O}} \right\rangle$, we find that the sum of these correlators is consistent with Eq. (A.11), the global sum over correlators in the orbifold construction, up to a constant factor.

C-even correlator

We see that the C-even correlator can finally be evaluated as

$$
\begin{aligned}
C(t) &= \left\langle \mathcal{O}_{\text{even}} \overline{\mathcal{O}}_{\text{even}} \right\rangle, \\
&= \frac{1}{4} \left(\left\langle \mathcal{O}\overline{\mathcal{O}} \right\rangle + \left\langle \mathcal{O}^C \overline{\mathcal{O}} \right\rangle + \left\langle \mathcal{O}\overline{\mathcal{O}}^C \right\rangle + \left\langle \mathcal{O}^C \overline{\mathcal{O}}^C \right\rangle \right), \\
&= -\frac{1}{4}\frac{1}{4} \left((\Gamma C)_{\nu\tau}(C\Gamma)_{\omega\sigma} \right) \\
& \quad \left((S_{d_P}(y,x)_{\sigma\nu} + S_{d_A}(y,x)_{\sigma\nu})(S_{u_P}(y,x)_{\omega\tau} + S_{u_A}(y,x)_{\omega\tau}) \right. \\
& \quad + (-S_{d_P}(y,x)_{\sigma\nu} + S_{d_A}(y,x)_{\sigma\nu})(-S_{u_P}(y,x)_{\omega\tau} + S_{u_A}(y,x)_{\omega\tau}) \\
& \quad + (-S_{d_P}(y,x)_{\sigma\nu} + S_{d_A}(y,x)_{\sigma\nu})(-S_{u_P}(y,x)_{\omega\tau} + S_{u_A}(y,x)_{\omega\tau}) \\
& \quad \left. + (S_{d_P}(y,x)_{\sigma\nu} + S_{d_A}(y,x)_{\sigma\nu})(S_{u_P}(y,x)_{\omega\tau} + S_{u_A}(y,x)_{\omega\tau}) \right), \\
&= -\frac{1}{4}\frac{1}{4} \left((\Gamma C)_{\nu\tau}(C\Gamma)_{\omega\sigma} \right) \\
& \quad (S_{d_P}(y,x)_{\sigma\nu}S_{u_P}(y,x)_{\omega\tau} + S_{d_P}(y,x)_{\sigma\nu}S_{u_A}(y,x)_{\omega\tau} \\
& \quad + S_{d_A}(y,x)_{\sigma\nu}S_{u_P}(y,x)_{\omega\tau} + S_{d_A}(y,x)_{\sigma\nu}S_{u_A}(y,x)_{\omega\tau} \\
& \quad + S_{d_P}(y,x)_{\sigma\nu}S_{u_P}(y,x)_{\omega\tau} - S_{d_P}(y,x)_{\sigma\nu}S_{u_A}(y,x)_{\omega\tau} \\
& \quad - S_{d_A}(y,x)_{\sigma\nu}S_{u_P}(y,x)_{\omega\tau} + S_{d_A}(y,x)_{\sigma\nu}S_{u_A}(y,x)_{\omega\tau} \\
& \quad + S_{d_P}(y,x)_{\sigma\nu}S_{u_P}(y,x)_{\omega\tau} - S_{d_P}(y,x)_{\sigma\nu}S_{u_A}(y,x)_{\omega\tau} \\
& \quad - S_{d_A}(y,x)_{\sigma\nu}S_{u_P}(y,x)_{\omega\tau} + S_{d_A}(y,x)_{\sigma\nu}S_{u_A}(y,x)_{\omega\tau} \\
& \quad + S_{d_P}(y,x)_{\sigma\nu}S_{u_P}(y,x)_{\omega\tau} + S_{d_P}(y,x)_{\sigma\nu}S_{u_A}(y,x)_{\omega\tau} \\
& \quad + S_{d_A}(y,x)_{\sigma\nu}S_{u_P}(y,x)_{\omega\tau} + S_{d_A}(y,x)_{\sigma\nu}S_{u_A}(y,x)_{\omega\tau}), \\
&= -\frac{1}{4} \left((\Gamma C)_{\nu\tau}(C\Gamma)_{\omega\sigma} \right) (S_{d_P}(y,x)_{\sigma\nu}S_{u_P}(y,x)_{\omega\tau} \\
& \quad + S_{d_A}(y,x)_{\sigma\nu}S_{u_A}(y,x)_{\omega\tau}).
\end{aligned}
\tag{A.34}
$$

The expression above gives the C-even propagator defined in terms of the spatially periodic and spatially anti-periodic propagators on the entirely physical lattice construction. We carried out a check to ensure that the result of the meson correlator in our implementation of the orbifold construction, summed over both the physical and mirror lattice at the sink, was consistent with the above expression calculated on a physical lattice of length $2L$ in one spatial dimension and length L in the other spatial dimensions, which passed. This is a demonstration that our implementation of the orbifold construction may be used to give the C-even correlators necessary for the calculation of masses using C^* boundary conditions.

CLASSICAL VACUA OF COMPACT QED$_\text{C}$

This appendix proves the below proposition that is used in the discussion of minima of the Wilson action in Section 3.9.

PROPOSITION B.1.   *Let $U(x,\mu)$ be some configuration of gauge fields that minimises the Wilson action.*

1. A vector z exists such that it satisfies the conditions

$$z_3 = 1; \qquad z_\mu^2 = 1, \tag{B.1}$$

and that, under a gauge transformation $U(x,\mu)$ is equivalent to the gauge configuration

$$\overline{U}_z(x,\mu) = \begin{cases} z_\mu & \text{if } x_\mu = L_\mu - 1 \\ 1 & \text{otherwise} \end{cases}. \tag{B.2}$$

2. The above vector z is unique.

Regarding the proof of the first part of the proposition, if we define the set $\mathcal{C}$ to contain the directions μ along which C* boundary conditions are implemented on a lattice, an Abelian gauge field will obey the following conditions

$$U(x + \hat{L}_\mu, \rho) = \begin{cases} U(x,\rho), & \text{if } \mu \notin \mathcal{C} \\ U(x,\rho)^*, & \text{if } \mu \in \mathcal{C}, \end{cases} \tag{B.3}$$

where the lattice has discrete integer-valued coordinates

$$0 \leq x_\mu \leq L_\mu - 1. \tag{B.4}$$

The following working assumes that there is at least one C*-periodic boundary, with direction $\mu = 3$ being C*-periodic, and at least one periodic direction, with $\mu = 0$.

In order to explore the classical vacua of compact QED$_\text{C}$, we must explore the properties of all gauge-field configurations for which the Wilson action is minimised. This minimisation condition may be written simply in terms of the plaquette

$$P(x,\mu,\nu) \equiv U(x,\mu)U(x+\hat{\mu},\nu)U(x+\hat{\nu},\mu)^{-1}U(x,\nu)^{-1} \tag{B.5}$$

as

$$P(x,\mu,\nu) = 1. \tag{B.6}$$

If one were to transform the gauge links into axial gauge in a particular direction, this would be equivalent to setting all gauge-links to unity apart from those that lie on the hyperplane π_μ defined as

$$\pi_\mu : x_\mu = L_\mu - 1. \tag{B.7}$$

Those non-unity links on the hyperplanes will in this appendix henceforth be referred to as *active* gauge links. In fact, this is always possible along any given direction, and it may be shown through Eq. B.6 that a simultaneous gauge-transformation to axial gauge along all directions is possible.

Through imposing the above conditions on the gauge links that lie on the hyperplanes, further conditions on these gauge links may be deduced. Whereas a plaquette at an intersection between two hyperplanes will have four active-gauge links, a plaquette that exists on only one hyperplane will only have two active links, adjacent to each other. The necessity that this plaquette be equal to unity, along with noting that the boundary conditions leave unity values unchanged, leads to the conclusion that the two active links of the plaquette must be equal-valued:

$$U(x,\mu) = U(x+\hat{v},\mu), \text{ for any } x \in \pi_\mu, \ v \neq \mu. \tag{B.8}$$

When this relation is used recursively, it becomes evident that all active links along a given direction μ must be equal-valued.

For simplicity in the following discussion, we denote a hyperplane link as

$$W_\mu = U(x,\mu), \text{ for any } x \in \pi_\mu. \tag{B.9}$$

We now turn our focus to those plaquettes that lie at the intersection between two distinct hyperplanes. Considering first the plaquette that sits at a site x in the hyperplane $x \in \pi_\mu \cap \pi_3$ for those directions μ that are periodic

$$1 = P(x,\mu,3) = W_\mu W_3 W_\mu W_3^{-1}. \tag{B.10}$$

This necessarily implies that

$$W_\mu = \pm 1, \text{ if } \mu \notin \mathcal{C}. \tag{B.11}$$

Conversely, taking $\mu \neq 3$ to be a direction with $C*$ boundary conditions gives

$$1 = P(x,\mu,3) = W_\mu W_3^{-1} W_\mu W_3^{-1}, \tag{B.12}$$

from which we get

$$W_\mu = \pm W_3 \text{ if } \mu \in \mathcal{C}. \tag{B.13}$$

The final step to prove the first part of the proposition is to show that, with a gauge transformation, W_3 may be set to unity. If one defines w to be a complex number such that a hyperplane link may be written as W_3, and the gauge transformation to be

$$\Lambda(x) = w \text{ for } 0 \leq x_\mu \leq L_\mu - 1, \tag{B.14}$$

to which the following boundary conditions are applied to extend the domain above,

$$\Lambda(x+\hat{L}_\mu) = \begin{cases} \Lambda(x) & \text{if } \mu \notin \mathcal{C}; \\ \Lambda(x)^* & \text{if } \mu \in \mathcal{C}, \end{cases} \tag{B.15}$$

one may notice that both the axial gauge and the gauge-field boundary conditions are preserved under this gauge transformation. In fact, the above gauge transformation also leaves unchanged the values of all active links along periodic directions. In the case of the C^* directions $\mu \in \mathcal{C}$, the gauge transformation acts on active link variables oriented along μ as

$$W_\mu \to wW_\mu w = W_3^{-1}W_\mu = \pm 1. \tag{B.16}$$

In particular, if $\mu = 3$, then

$$W_3 \rightarrow wW_3w = W_3^{-1}W_3 = 1. \tag{B.17}$$

Hence, one sees that the first part of the above proposition is proven, as to summarise: all links outside of the above-defined hyperplanes are set to unity by the axial gauge, W_3 can be set to unity whilst preserving the axial gauge and gauge-field boundary conditions, and in all other hyperplanes $W_\mu = \pm 1$.

In order to prove the second part of the proposition, that being that z is unique, we may carry on the above argument, adding the introduction of the Wilson lines

$$W(\mu) = \prod_{s=0}^{L_\mu - 1} U(s\hat{\mu}, \mu), \tag{B.18}$$

to notice that the original gauge configuration $U(x, \mu)$ determines the vector z uniquely to be

$$z_\mu = \begin{cases} W(\mu) & \text{if } \mu \notin \mathcal{C}; \\ W(\mu)W(3)^{-1} & \text{if } \mu \in \mathcal{C}. \end{cases} \tag{B.19}$$

That $W(\mu)$ must be gauge invariant iff μ is a periodic direction, whilst the parallel transport $W(\mu)W_3^{-1}$ is gauge-invariant iff μ is a C* direction, may be shown easily through expansion of the products. Thus the second part of the proposition is proven.

C

ANATOMY OF THE SIGN PROBLEM

In order to discuss whether there is potentially a sign problem, for reasons somewhat analogous to the case of usual periodic spatial setup, we must rewrite the fermionic path integral in terms of linear algebra.

In the case of periodic boundary conditions in space, integrating the fermion fields in the path integral gives one the Dirac operator determinant. This is not possible in the case of C^* boundary conditions, as $\psi(x)$ and $\overline{\psi}$ are not independent of each other. Instead, a change of variables may be employed,

$$\psi_\pm(x) = \frac{\psi(x) \pm C^{-1}\overline{\psi}^T(x)}{\sqrt{2}}, \tag{C.1}$$

and a new field defined:

$$\eta(x) = \begin{pmatrix} \psi_+(x) \\ -i\psi_-(x) \end{pmatrix}. \tag{C.2}$$

When this change of variables is employed, the condition for C^* boundary conditions can be expressed as

$$\eta(x + \hat{L}_k) = K\eta(x), \qquad K = \begin{pmatrix} 1 & 0 \\ 0 & -1 \end{pmatrix}, \tag{C.3}$$

with matrix K acting on the two-component η. These will henceforth be referred to as K boundary conditions in this appendix.

The condition

$$C^{-1}D[V]^T C = D[V^*], \tag{C.4}$$

an identity of the Wilson-Dirac operator valid for an arbitrary non-Abelian gauge theory, may be used in order to rewrite the fermionic action as

$$S_F = \overline{\psi}D[V]\psi = -\frac{1}{2}\eta^T C D[\mathcal{J}(V)]\eta, \tag{C.5}$$

taking $D_{\mathcal{J}} \equiv D[\mathcal{J}(\mathcal{V})]$ to be the Wilson-Dirac operator where the gauge field $J(V)$ is used as an input, $J(V)$ being

$$\mathcal{J}(\mathcal{V}) = 1_2 \otimes \mathrm{Re}V + J \otimes \mathrm{Im}V, \qquad J = \begin{pmatrix} 0 & -1 \\ 1 & 0 \end{pmatrix}. \tag{C.6}$$

As with the K matrix above, 1_2 and J are 2-by-2 matrices that act upon the two components of η. The gauge group representation $J(V)$ is equivalent within a unitary transformation to the representation V.

Substituting C.5 into the fermionic action and integrating gives

$$\int_{C^* \text{ b.cś}} \mathcal{D}\overline{\psi}\mathcal{D}\psi e^{-\overline{\psi}D[V]\psi} = \int_{K \text{ b.cś}} \mathcal{D}\eta e^{\frac{1}{2}\eta^T C D_{\mathcal{J}}\eta} = \mathrm{Pf}_K C D_{\mathcal{J}}. \tag{C.7}$$

Here, $CD_{\mathcal{J}}$ is a complex and antisymmetric matrix, and the fact that the derivative that appears in the Dirac operator is defined on the space of those fields that satisfy K boundary

conditions is denoted by the subscript K. The Pfaffian of $CD_{\mathcal{J}}$ is represented as $\mathrm{Pf}_K CD_{\mathcal{J}}$ and can be related to determinant of $D_{\mathcal{J}}$ through the use of algebraic identities and using the fact that $\mathrm{Det}(C) = 1$, giving

$$(\mathrm{Pf}_K CD_{\mathcal{J}})^2 = \mathrm{Det}_K CD_{\mathcal{J}} = \mathrm{Det}_K D_{\mathcal{J}}. \tag{C.8}$$

Now that the fermionic path integral has been expressed in such a form, the matter of whether a sign problem exists in this setup may be addressed. The fact that the squared Pfaffian is real may be deduced through substitution using the γ_5-Hermiticity of the Dirac operator, $\gamma_5 D \gamma_5 = D^\dagger$, into Eq. (C.8). In order to instead demonstrate that the Pfaffian is real by itself, we may introduce an auxiliary operator $C(D_{\mathcal{J}} - s)$ where s is some complex number, expressed as a polynomial in s and the distinct roots λ_α:

$$\mathrm{Pf}_K C(D_{\mathcal{J}} - s) = \prod_\alpha (s - \lambda_\alpha)^{m_\alpha}. \tag{C.9}$$

The Pfaffian value as the limit of s is taken to infinity determines the normalisation of this expression. Using the above equation and Eq. (C.8), we may write an expression for the determinant $\mathrm{Det}_K(D_{\mathcal{J}} - s)$ using the characteristic polynomial of $D_{\mathcal{J}}$

$$\mathrm{Det}_K(D_{\mathcal{J}} - s) = [\mathrm{Pf}_K C(D_{\mathcal{J}} - s)]^2 = \prod_\alpha (s - \lambda_\alpha)^{2m_\alpha}. \tag{C.10}$$

We see that, as λ_α are the roots of the characteristic polynomial for $D_{\mathcal{J}}$, they may be identified as the eigenvalues of $D_{\mathcal{J}}$. We may declare that all of these eigenvalues are either real or appear only in pairs of complex conjugates, as a consequence of the γ_5-Hermiticity of $D_{\mathcal{J}}$. As the algebraic multiplicity of λ_α is $2m_\alpha$, we see that, if one requires that s be real, $\mathrm{Det}_K(D_{\mathcal{J}} - s)$ is necessarily positive, and therefore the Pfaffian is real. To return to the original problem, $s = 0$ may be enforced. In this case, we get

$$\mathrm{Pf}_K CD_{\mathcal{J}} = \prod_{\alpha | Im\lambda_\alpha = 0} \lambda_\alpha^{m_\alpha} \prod_{\alpha | Im\lambda_\alpha > 0} |\lambda_\alpha^{m_\alpha}|^2. \tag{C.11}$$

We therefore see that the fermionic Pfaffian is real is the case of C* boundary conditions.

Finally, a note must be made about a mild sign problem at finite lattice spacing in the case of C* boundary conditions, that is totally analogous to the case of periodic boundary conditions with a single flavour; the possibility for Wilson fermions to be negative allows the Pfaffian to be negative, as shown by Eq. (C.11). This possibility however disappears when the continuum limit is taken, as the eigenvalues of the Dirac operator tend towards $m > 0$.

D

PROPERTIES OF THE PFAFFIAN

In the following discussion of the properties of the Dirac operator and of its Pfaffian, we hereby set $a = 1$.

The quark-antiquark doublet, on which the Dirac operator acts, may be written as

$$\chi = \begin{pmatrix} \psi \\ \psi^C \end{pmatrix} = \begin{pmatrix} \psi \\ C^{-1}\overline{\psi}^t \end{pmatrix} . \tag{D.1}$$

The Dirac operator itself is formed of a sum of terms,

$$D = m + D_{\mathrm{w}} + \delta D_{\mathrm{sw}}, \tag{D.2}$$

where D_{w} is the Wilson-Dirac operator and δD_{sw} is the Sheikholeslami-Wohlert (SW) term, a term used in the Symanzik improvement program to correct for $\mathcal{O}(a)$ systematic error due to the lattice discretisation.

The Wilson-Dirac operator can be written as

$$D_{\mathrm{w}} = \frac{1}{2} \sum_{\mu} \left\{ \gamma_{\mu}(\nabla_{\mu} - \nabla_{\mu}^{\dagger}) - \nabla_{\mu}^{\dagger}\nabla_{\mu} \right\} . \tag{D.3}$$

In our implementation, however, attention has been paid in order to ensure that the forward covariant derivative ∇_{μ} be constructed such that the quark and antiquark fields transform respectively under representations of the gauge group that are complex conjugates of each other,

$$\nabla_{\mu}\chi(x) = \begin{pmatrix} z^{\hat{q}}(x,\mu)U(x,\mu) & 0 \\ 0 & z^{-\hat{q}}(x,\mu)U^*(x,\mu) \end{pmatrix} \chi(x+\hat{\mu}) - \chi(x). \tag{D.4}$$

Here the SU(3) gauge link variable is denoted as $U(x,\mu)$ while the U(1) gauge link variable is denoted as $z(x,\mu)$, while the electric charge of the given quark flavour is given by $\hat{q}q_{\mathrm{el}}$ as in Eq. (3.62), which, for our choice $q_{\mathrm{el}} = 1/6$, gives the up-type quarks $\hat{q} = 4$ and the down-type quarks $\hat{q} = -2$. The following temporal and spatial boundary conditions are applied to the quark-antiquark doublet,

$$\chi(x + \tfrac{T}{a}\hat{0}) = \chi(x), \tag{D.5a}$$

$$\chi(x + \tfrac{L}{a}\hat{k}) = K\chi(x), \tag{D.5b}$$

for spatial directions labelled $k = 1, 2, 3$, where K is a matrix that exchanges the quark and antiquark, thus enforcing the C* boundary conditions that characterise the QCD+QED$_{\mathrm{C}}$ formalism, and whose explicit form is given by

$$K = \begin{pmatrix} 0 & 1 \\ 1 & 0 \end{pmatrix} . \tag{D.6}$$

The SW term is given by

$$\delta D_{\text{sw}} = -\frac{1}{4} \sum_{\mu,\nu} \sigma_{\mu\nu} \left\{ c_{\text{sw}}^{\text{SU(3)}} \begin{pmatrix} \hat{G}_{\mu\nu} & 0 \\ 0 & -\hat{G}_{\mu\nu}^* \end{pmatrix} + \hat{q}\, c_{\text{sw}}^{\text{U(1)}} \begin{pmatrix} \hat{F}_{\mu\nu} & 0 \\ 0 & -\hat{F}_{\mu\nu}^* \end{pmatrix} \right\}, \qquad \text{(D.7)}$$

where $\sigma_{\mu\nu} = \frac{i}{2}[\gamma_\mu, \gamma_\nu]$, and, as for the Wilson-Dirac term, the SW term is constructed taking into account the different gauge group representations under which the SU(3) and U(1) fields transform respectively. In the above expression, the Hermitian SU(3) and U(1) field tensors have the respective clover discretisations $\hat{G}_{\mu\nu}$ and $\hat{F}_{\mu\nu}$.

With these properties in mind, three propositions will now be presented that are used in Sec. 4.8 in order to explain the strategy by which the sign of the Pfaffian is calculated.

Proposition 1. *The matrix CKD is antisymmetric.*

Proof. For reference, we work in the chiral basis of Euclidean Dirac matrices, where γ_5 is diagonal, $\gamma_{0,2} \in \mathbf{R}$ and $\gamma_{1,3} \in \mathbf{I}$. We operate using the chosen representation for the charge-conjugation matrix of

$$C = i\gamma_0\gamma_2, \qquad \text{(D.8)}$$

which satisfies the properties of antisymmetry, being its own inverse $C^2 = 1$ and being imaginary. The Euclidean Dirac algebra and properties of the gamma matrices give the identities

$$\gamma_5 C \gamma_\mu C \gamma_5 = \gamma_\mu^* , \qquad \text{(D.9a)}$$

$$\gamma_5 C \sigma_{\mu\nu} C \gamma_5 = -\sigma_{\mu\nu}^* , \qquad \text{(D.9b)}$$

while we have the following identities for the K matrix,

$$K \begin{pmatrix} z^{\hat{q}} U & 0 \\ 0 & z^{-\hat{q}} U^* \end{pmatrix} K = \begin{pmatrix} z^{\hat{q}} U & 0 \\ 0 & z^{-\hat{q}} U^* \end{pmatrix} K = \begin{pmatrix} z^{\hat{q}} U & 0 \\ 0 & z^{-\hat{q}} U^* \end{pmatrix}^* , \qquad \text{(D.10a)}$$

$$K \begin{pmatrix} \hat{G}_{\mu\nu} & 0 \\ 0 & -\hat{G}_{\mu\nu}^* \end{pmatrix} K = - \begin{pmatrix} \hat{G}_{\mu\nu} & 0 \\ 0 & -\hat{G}_{\mu\nu}^* \end{pmatrix}^* , \qquad \text{(D.10b)}$$

$$K \begin{pmatrix} \hat{F}_{\mu\nu} & 0 \\ 0 & -\hat{F}_{\mu\nu}^* \end{pmatrix} K = - \begin{pmatrix} \hat{F}_{\mu\nu} & 0 \\ 0 & -\hat{F}_{\mu\nu}^* \end{pmatrix}^* . \qquad \text{(D.10c)}$$

Using these two sets of identities, one may prove

$$\gamma_5 CKDKC\gamma_5 = D^* . \qquad \text{(D.11)}$$

This is equivalent to

$$CKD = \gamma_5 D^* \gamma_5 CK = D^t CK = -(CKD)^t, \qquad \text{(D.12)}$$

where the γ_5-Hermiticity of the Dirac operator has been used, as well as the transposition properties of the C and K matrices, $C^t = -C$ and $K^t = K$. $\qquad\qquad \square$

Proposition 2. *The operator $Q = \gamma_5 D$ has a doubly degenerate spectrum.*

Proof. If we define the matrix $U = CK\gamma_5$, it can be shown easily to have the following properties:

$$U = U^\dagger = U^{-1} = -U^t = U^* . \qquad \text{(D.13)}$$

Using the property of anti-symmetry of the matrix CKD, we have that

$$UQ^* = CKD^* = -(CKD)^* = (CKD)^\dagger = \gamma_5 D \gamma_5 CK = QU \,. \tag{D.14}$$

This result may be used to derive the following properties:

1. Given that Q has an eigenvector v with eigenvalue λ, Uv^* is also an eigenvector of Q with the same eigenvector λ:

$$QUv^* = UQ^*v^* = U(\lambda v)^* = \lambda Uv^* \,. \tag{D.15}$$

2. Uv^* is orthogonal to v:

$$(Uv^*, v) = v^t U^\dagger v = v^t U v = 0 \,. \tag{D.16}$$

3. If w is orthogonal to both v and Uv^*, then it follows that Uw^* is also orthogonal to v and Uv^*:

$$(Uw^*, v) = w^t U v = -v^t U w$$
$$= -(v^*, Uw) = -(Uv^*, w) = 0; \tag{D.17a}$$
$$(Uw^*, Uv^*) = w^t U^2 v^* = v^\dagger w = (v, w) = 0. \tag{D.17b}$$

These properties allow one to use a modified form of the Gram-Schmidt algorithm, alternating between an orthogonalisation step and the construction of eigenvectors Uv_i^*, to prove the even degeneracy d of any eigenvector. As v and Uv^* share the same eigenvalue but are orthogonal, an orthonormal basis for the eigenspace can be chosen as

$$v_1, \; Uv_1^*, \; v_2, \; Uv_2^*, \; \dots \,, \; v_{d/2}, \; Uv_{d/2}^* \,, \tag{D.18}$$

where the corresponding eigenvectors will be repeated once each. $\qquad\square$

Proposition 3. *If we denote the list of eigenvalues of Q as $\lambda_{n=1,\dots,12V} \in \mathbb{R}$, with each eigenvalue appearing $d/2$ times, where d is the eigenvalue's degeneracy, then the following equation holds:*

$$Pf(CKD) = \prod_{n=1}^{12V} \lambda_n \,. \tag{D.19}$$

Proof. Considering that the Pfaffian of a matrix is a polynomial of its entries, then we define

$$f(m) = \mathrm{Pf}\,[CTD(m)] \tag{D.20}$$

to be a polynomial function in the bare mass m, as the Dirac operator D depends linearly on m. The eigenvalues λ_n of the Hermitian Dirac operator Q, that also depends linearly on m, are analytic functions of m even at points where they cross zero [65]. We may therefore define a function

$$g(m) = \prod_{n=1}^{12V} \lambda_n(m), \tag{D.21}$$

where $m \in \mathbb{R}$.

If we take the limit $m \to +\infty$, we see that the approximation $D \simeq mI_{24V}$ may be made. This implies

$$\lim_{m \to +\infty} f(m) = \lim_{m \to +\infty} m^{12V} \mathrm{Pf}(C \otimes K \otimes I_{3V}) = \lim_{m \to +\infty} m^{12V} = +\infty \,. \tag{D.22}$$

126

Applying the same limit $m \to +\infty$ to the Q matrix, we may approximate $Q \simeq m I_{6V} \otimes \gamma_5$. This limit sends half of the eigenvalues asymptotically to $+m$ and the other half asymptotically towards $-m$, giving

$$\lim_{m \to +\infty} g(m) = \lim_{m \to +\infty} \prod_{n=1}^{12V} \lambda_n = \lim_{m \to +\infty} m^{6V}(-m)^{6V} = +\infty \ . \tag{D.23}$$

Therefore, both $f(m)$ and $g(m)$ must be positive for every $m > M$ for some value M. One may show that, through the properties of the determinant and of the Pfaffian,

$$\begin{aligned} f(m)^2 &= \mathrm{Pf}\,[CTD(m)]^2 = \det\,[D(m)] \\ &= \det\,[Q(m)] = \prod_{n=1}^{12V} \lambda_n^2(m) = g(m)^2, \end{aligned} \tag{D.24}$$

for every m. As elucidated above, both $f(m)$ and $g(m)$ are positive for $m > M$, therefore Eq. (D.24) implies that $f(m)$ and $g(m)$ are equal. As they are equal for every $m > M$, and they are analytic functions of m, they must therefore be equal everywhere, as otherwise there would be a discontinuity in the determinant of either of the two functions. $\qquad\square$

ERROR ANALYSIS

In this appendix, we discuss the two different methods of error analysis that we have used in this work, jackknife bootstrapping, which was used in the optimisation phase and is therefore used in the GEVP results, and the Gamma method, which, unlike the Jackknife method, gives an accurate quantification of the autocorrelation of the data series, and is therefore used in the analysis of our final mass results.

E.1 PRELIMINARIES

The non-linear methods of analysis, through which we obtain physical observables from the results of simulation, lead to difficulties in accurate error estimation of the final observables. Myriad different approaches exist, including bootstrapping techniques in which samples are created from a statistical ensemble and are independently operated on, with errors calculated at the end through assessing the spread of the samples around the mean of the samples, and techniques such as the Gamma method, in which a more thorough analysis of MC autocorrelation is carried out, with errors that account for autocorrelation being calculated through piecemeal error propagation. The aim of this section is to develop a mathematical vocabulary for later discussing the properties of different techniques for error analysis.

E.1.1 *Configuration series and correlation functions*

The primary observables calculated in Lattice QCD are n-point correlation functions. From the expectation values of these, physical quantities are derived. For example, masses are obtained from two-point correlation functions with the momentum set to zero. If we denote by A_r a real-valued primary observable, then we may write the n-point correlation functions of these primary observables as $\langle A_{r_1} \dots A_{r_n} \rangle$, where $\langle O \rangle$ is the expectation value of the observable O. The fermion-connected parts of these correlators, $\langle A_{r_1} \dots A_{r_n} \rangle_c$, may be defined in the conventional way and thereby satisfy the properties

$$\langle A_r \rangle_c = \langle A_r \rangle, \tag{E.1a}$$

$$\langle A_r A_s \rangle_c = \langle A_r A_s \rangle - \langle A_r, \rangle \langle A_s \rangle. \tag{E.1b}$$

The measurement of primary observable A_r on a representative series, or ensemble, of N gauge configurations that are each statistically independent of each other gives a series which may be said to be the observable measured on the ensemble,

$$a_{r,1}, a_{r,2}, \dots, a_{r,N}. \tag{E.2}$$

A stochastic estimate $\overline{a}_r$ of the expectation value $\langle A_r \rangle$ is then obtained by averaging over the series:

$$\overline{a}_r = \frac{1}{N} \sum_{i=1}^{N} a_{r,i}. \tag{E.3}$$

This logic may be extended to the case of n-point correlators where $n > 1$, by considering that the data series of the product of two observables A_r and A_s calculated on an ensemble with

configurations numbered $i = 1, \cdots, N$ is $a_{r,i}a_{s,i}$. Therefore, this product may be viewed as simply another primary observable, and the expectation value $\langle A_r A_s \rangle$ of this product is the average of $\langle a_{r,i}a_{s,i} \rangle$ over the ensemble. Through induction this may be extended to arbitrarily long correlation functions.

E.1.2 *Validity of simulation statistics*

In order to quantify statistically the accuracy of the measured estimate $\bar{a}_r$ against the expectation value $\langle A_r \rangle$, in principle many estimates must be taken, meaning that one must repeat the simulation numerous times. Denoting the average of a function ψ of measured primary observables over an infinite number of such simulations as $\langle\!\langle \psi \rangle\!\rangle$, the standard deviation between $\bar{a}_r$ and $\langle A_r \rangle$ is given by $\langle\!\langle (\bar{a}_r - \langle A_r \rangle)^2 \rangle\!\rangle^{1/2}$.

Two conditions must be satisfied in order for the use of simulation statistics to be valid in the estimation of physical observables, the first being that the measured primary observables are unbiased relative to the expectation values, i.e.

$$\langle\!\langle a_{r,i} \rangle\!\rangle = \langle A_r \rangle \tag{E.4}$$

for any primary observable A_r and all i. The second condition that should be satisfied is the statistical independence of the generated fields. This may be expressed as

$$\langle\!\langle a_{r,i} a_{s,j} \rangle\!\rangle = \langle\!\langle a_{r,i} \rangle\!\rangle \langle\!\langle a_{s,j} \rangle\!\rangle \quad \text{if} \quad i \neq j, \tag{E.5}$$

meaning that in the limit of infinite statistics there are no correlations between either fields at non-zero separations. This may be expressed more generally as requiring a factorisation of the correlation function $\langle\!\langle a_{r_1,i_1} \cdots a_{r_n,i_n} \rangle\!\rangle$ into a product of separate averages for each distinct value of the "configuration time" i.

Enforcing that the fields in the generated representative ensembles have vanishing auto-correlation is sufficient to satisfy the two above conditions, as discussed in Sec. 2.4.2. This is made difficult by the abundance of configurations that is require to accurately determine the autocorrelation functions and associated autocorrelation time, due to the statistical fluctuations inherent in the measurements. One way of assessing this is through the Gamma method [66], which we touch upon later.

E.1.3 *Mean value distribution*

The fact that all mean values $\bar{a_r}, \bar{a_s}$ of the primary observables calculated on a given representative ensemble indeed share the same underlying ensemble inevitably leads to correlations between the mean values that can be written as

$$\langle\!\langle \bar{a}_{r_1} \ldots \bar{a}_{r_k} \rangle\!\rangle = \frac{1}{N^k} \sum_{i_1=1}^{N} \cdots \sum_{i_k=1}^{N} \langle\!\langle \bar{a}_{r_1,i_1} \ldots \bar{a}_{r_k,i_k} \rangle\!\rangle. \tag{E.6}$$

We may seek to rewrite these in terms of the correlation functions measured $\langle A_{r_1} \cdots A_{r_n} \rangle$; if we consider, for example, two point correlators, we may use Eq. (E.4) and (E.5) to obtain the expression

$$\langle\!\langle \bar{a}_r \bar{a}_s \rangle\!\rangle = \frac{1}{N^2} \sum_{i,j=1}^{N} \langle\!\langle a_{r,i} a_{s,j} \rangle\!\rangle = \langle A_r \rangle \langle A_s \rangle + \frac{1}{N} \langle A_r A_s \rangle_c. \tag{E.7}$$

Provided that $k \geq 1$, Eq. (E.6) may be rewritten in terms of the measured correlation functions as

$$\langle\!\langle \bar{a}_{r_1} \ldots \bar{a}_{r_k} \rangle\!\rangle = \sum_{l=1}^{k} \frac{1}{N^{k-l}l!} \sum_{P \in \mathcal{P}_{k,l}} \langle A_{P_1} \rangle_c \ldots \langle A_{P_l} \rangle_c, \tag{E.8}$$

where set $\mathcal{P}_{k,l}$ is the set of all possible partitions $P = (P_1, \ldots, P_l)$ into l non-empty subsets of the set $\{1, \ldots, k\}$, where $P_1, \ldots, P_l$ are ordered. In addition,

$$A_{P_i} = \prod_{j \in P_i} A_{r_j}. \tag{E.9}$$

Taking the limit of large N gives the behaviour

$$\langle\!\langle \bar{a}_{r_1} \ldots \bar{a}_{r_k} \rangle\!\rangle = \langle A_{r_1} \rangle \ldots \langle A_{r_k} \rangle + \mathcal{O}(N^{-1}), \tag{E.10}$$

as proven in [26].

We may now turn our attention to the deviations of the mean values from the expectation values,

$$\delta \bar{a}_r = \bar{a}_r - \langle A_r \rangle, \tag{E.11}$$

and the statistical properties thereof. If we recall Eq. (E.7), we see that we can rewrite it as

$$\langle\!\langle \delta \bar{a}_r \delta \bar{a}_s \rangle\!\rangle = \frac{1}{N} \langle A_r A_s \rangle_c. \tag{E.12}$$

This shows that the deviations of the mean values from the expectation value, of the two-point correlator at least, are proportional to $\frac{1}{\sqrt{N}}$. Similarly, for an n-point correlator in general, the expression

$$\langle\!\langle \delta \bar{a}_{r_1} \ldots \delta \bar{a}_{r_k} \rangle\!\rangle = \sum_{l=1}^{k} \frac{1}{N^{k-l}l!} \sum_{P \in \tilde{\mathcal{P}}_{k,l}} \langle A_{P_1} \rangle_c \ldots \langle A_{P_l} \rangle_c \tag{E.13}$$

may be derived [26], however this is far more involved. Here $\tilde{\mathcal{P}}_{k,l} \subset \mathcal{P}_{k,l}$ represents the set of partitions of $1, \ldots, k$ into l subsets with at least two elements. This may be split into the two cases, of even and odd k. In the case of even k,

$$\langle\!\langle \delta \bar{a}_{r_1} \ldots \delta \bar{a}_{r_k} \rangle\!\rangle = \frac{1}{N^{k/2}} \left\{ \langle A_{r_1} A_{r_2} \rangle_c \ldots \langle A_{r_{k-1}} A_{r_k} \rangle_c + \text{permutations} \right\}. \tag{E.14}$$

In the case of odd k, however, deviations are more heavily suppressed, with a factor of $N^{-(k+1)/2}$ at the leading order. This is due to all possible ways in which the set may be partitioned containing at least one subset with at least three elements. If we combine this discussion with the expression for the correlation of the mean values in terms of the expectation values, Eq. (E.10), we see, scaling the deviations by $\sqrt{N}$, that we have a joint probability distribution of $\sqrt{N} \delta \bar{a}_r$, with a Gaussian form to leading order in $1/N$ that has a zero mean and a variance $\langle A_r A_s \rangle$.

E.1.4 *Physical quantities from measured observables*

It must be noted that in the following discussion, a physical quantity is taken to mean any function of expectation values that is well-defined. This may be arbitrarily complex and need not have any real-world physical significance. The prime example that we will use is the mass of a hadron for the sake of relevance to this work; however, for example, any well-defined ratio of expectation values or the limit thereof would also be admissible in this discussion. Through the averaging of primary observables measured on the lattice, correlation functions may be attained that are combined in the appropriate way to calculate physical quantities.

Using the example of the mass of a hadron, the primary observables measured are two-point correlation functions $O_\pi(x_0, y)$ measured at all lattice times x_0 and with, for the sake of simplicity, a single source at point y. The effective mass of the chosen hadron may be extracted through the function

$$m_{\text{eff}}(x_0) = -a^{-1}\ln\frac{\overline{O}_\pi(x_0 + a, y)}{\overline{O}_\pi(x_0, y)}, \tag{E.15}$$

which should produce a curve that leads into a plateau with increasing $t < T/2$ as the contribution from excited states diminishes. The signal of this plateau then typically degrades due to the statistical noise that increases with time separation for almost all hadrons. Assuming that in the body of the plateau the statistical errors are significantly larger in magnitude than the contribution from excited states, the fit of the plateau to a constant value may be taken as a stochastic estimate of the mass for that particular lattice. The results from different lattices and at different values of physical parameters are then extrapolated and/or interpolated towards the physical point to give an estimate of the theoretical value of the physical observable.

Turning now to another rather abstract concept, we call a stochastic estimator any function ϕ of the measured primary observables A_r and number of data points N that estimates a given physical quantity Q such that

$$Q = \lim_{N\to\infty} \phi \quad \text{with probability 1.} \tag{E.16}$$

While this defines the stochastic estimator, we demand in the following discussion a more strict requirement, namely that the asymptotic expansion

$$\phi \underset{N\to\infty}{\sim} \sum_{k=0}^{\infty} N^{-k}\phi^k(\bar{a}_{r_1}, \bar{a}_{r_2}, \dots) \tag{E.17}$$

is followed. Here, the expansion coefficients $\phi^{(k)}$ are smooth functions of their arguments, the number of which must be finite regardless of the k-value. An example of a stochastic estimator that we have already visited is that of the effective mass function given in Eq. (E.15), which stochastically estimates the effective mass associated with the exact hadronic propagator $g(x_0 - y_0)$.

Whilst the leading term in the expansion, which is independent of N, is a function only of the averages $\bar{a}_r$ of the measured primary observables and is therefore a valid stochastic estimator, it is necessary to define the stochastic estimator as an expansion in N as the leading term may in fact be inaccessible at large N. An example of where this may occur is when taking a fit of the averages. In this case, as we will see in the case of the Jackknife error estimation procedure, an expansion in terms of N is required.

Following on from our discussion of the requirements for the validity of simulation statistics, let us explore the statistical quantities of the bias and the covariance matrix and how they relate to the expansion of the stochastic estimators discussed above. In the following, Q_α denotes some physical quantity with index α, and ϕ_α corresponds to a stochastic estimator of this physical quantity. We denote the bias of the stochastic estimator as

$$B_\alpha = \langle\langle\delta\phi_\alpha\rangle\rangle, \qquad \delta\phi_\alpha = \phi_\alpha - Q_\alpha; \tag{E.18}$$

this measures the deviation of the estimate relative to the true value of the physical quantity. Similarly, the magnitude of the statistical fluctuations of the observables measured on the lattice, which are expected to be markedly larger than the bias of the estimator, is given by the covariance matrix

$$C_{\alpha\beta} = \langle\langle\delta\phi_\alpha\delta\phi_\beta\rangle\rangle. \tag{E.19}$$

Our task is to express the bias and covariance matrix as expansions in terms of $1/N$, the coefficients of these series being functions of the correlation functions $\langle A_{r_1} \cdots A_{r_n} \rangle$ of the primary observables. We first express the average of the measured value as

$$\bar{a}_r = \langle A_r \rangle + \delta \bar{a}_r, \tag{E.20}$$

remembering that $\delta \bar{a}_r = \mathcal{O}(N^{-1/2})$. Taylor-expanding the expression in Eq. (E.17) in terms of the deviations $\delta \bar{a}_r$, and ordering by inverse powers of N, gives

$$\begin{aligned}
\phi_\alpha &= \hat{\phi}_\alpha^{(0)} + \sum_r \delta_r \hat{\phi}_\alpha^{(0)} \delta \bar{a}_r \\
&+ \frac{1}{N} \hat{\phi}_\alpha^{(1)} + \frac{1}{2} \sum_{r,s} \delta_r \delta_s \hat{\phi}_\alpha^{(0)} \delta \bar{a}_r \delta \bar{a}_s + \mathcal{O}(N^{-3/2})
\end{aligned} \tag{E.21}$$

with coefficients $\hat{\phi}_\alpha^{(k)}$ and derivatives δ_r denoting

$$\hat{\phi}_\alpha^{(k)} = \phi_\alpha^{(k)}(\langle A_{r_1} \rangle, \langle A_{r_2} \rangle, \dots), \qquad \delta_r = \frac{\delta}{\delta \langle A_r \rangle}. \tag{E.22}$$

We identify the physical observable Q_α with the leading term $\hat{\phi}_\alpha^{(0)}$, which means that the remaining right-hand side terms of Eq. (E.21) together give the deviation $\delta \phi_\alpha$.

Using Eq. (E.12), and recognising that the deviations $\delta \bar{a}_r$ are the sole stochastic variables in the expansion, one may average the above expansions over many simulations to receive the expressions

$$B_\alpha = \frac{1}{N} \left\{ \hat{\phi}_\alpha^{(1)} + \frac{1}{2} \sum_{r,s} \delta_r \delta_s \hat{\phi}_\alpha^{(0)} \langle A_r A_s \rangle_c \right\} + \mathcal{O}(N^{-2}), \tag{E.23}$$

$$C_{\alpha\beta} = \frac{1}{N} \sum_{r,s} \delta_r \hat{\phi}_\alpha^{(0)} \delta_s \hat{\phi}_\beta^{(0)} \langle A_r A_s \rangle_c + \mathcal{O}(N^{-2}). \tag{E.24}$$

We see here that the statistical fluctuations appear at order $\mathcal{O}(N^{-1/2})$, while the bias appears at order $\mathcal{O}(N^{-1})$.

E.2 JACKKNIFE BOOTSTRAPPING

Following the reasoning presented above, we see that one may estimate the bias and covariance matrices using simulation statistics, through the calculation of expectation values and two-point correlation functions from measured primary observables. This would require the explicit knowledge of the coefficient functions $\phi^{(0)}$ and $\phi^{(1)}$, which may be complicated by, for example, fit procedures, or even inaccessible.

Jackknife resampling is a simple and effective method for error analysis, through which certain statistical properties of the observables may be determined at any stage of the calculation. As the large-N limits of NB_α and $NC_{\alpha\beta}$ are functions of the primary observable expectation values, they are, in this discussion, physical quantities. The Jackknife method is able to construct, at any point of the calculation, stochastic estimators for these statistical quantities.

In order to construct the jackknife samples from a set of N measured values $a_{r,1}, \ldots, a_{r,N}$ of primary observable A_r, for each measured value a_i out of the set, this same value is removed to give the collection

$$a_{r,1}, \ldots, a_{r,i-1}, a_{r,i+1}, \ldots, a_{r,N}, \tag{E.25}$$

and the average of the set is taken,

$$\bar{a}_{r,i}^J \equiv \frac{1}{N-1} \sum_{k \neq i}^N a_{r,k}. \tag{E.26}$$

We note that the removed value a_i is reintroduced after the corresponding average is taken. In this way we end up with N distinct jackknife samples.

If we want an expression for the stochastic estimator of the jackknife samples, we may assume that the stochastic estimator ϕ takes the value ϕ_i^J if one discards the i'th measurement and here treats the jackknife samples as a series with length $N-1$. Using Eq. (E.17) as a template, it may then be inferred that

$$\phi_i^J \underset{N \to \infty}{\sim} \sum_{k=0}^{\infty} (N-1)^{-k} \phi^{(k)}(\bar{a}_{r_1,i}^J, \bar{a}_{r_2,i}^J, \ldots), \tag{E.27}$$

with the same expansion coefficients $\phi^{(k)}$ as before the resampling.

As for the bias and covariance matrices in terms of the jackknife samples, one may derive the formulae

$$B_\alpha^J = \sum_{i=1}^N (\phi_{\alpha,i}^J - \phi_\alpha), \tag{E.28a}$$

$$C_{\alpha\beta}^J = \sum_{i=1}^N (\phi_{\alpha,i}^J - \phi_\alpha)(\phi_{\beta,i}^J - \phi_\beta). \tag{E.28b}$$

Composed as they are themselves of stochastic estimators that by definition tend to the value of the physical quantity as $N \to \infty$, the expressions NB_α^J and $NC_{\alpha\beta}^J$ act as scaled stochastic estimators of the following physical quantities respectively:

$$\lim_{N \to \infty} NB_\alpha = \hat{\phi}_\alpha^{(1)} + \frac{1}{2} \sum_{r,s} \delta_r \delta_s \hat{\phi}_\alpha^{(0)} \langle A_r A_s \rangle_c, \tag{E.29a}$$

$$\lim_{N \to \infty} NC_{\alpha\beta} = \sum_{r,s} \delta_r \hat{\phi}_\alpha^{(0)} \delta_s \hat{\phi}_\beta^{(0)} \langle A_r A_s \rangle_c. \tag{E.29b}$$

If one compares B^J and C^J with the physical B and C with regards to the orders of N at which the terms contribute, one sees that the approximation is valid to order $N^{-3/2}$, at which statistical fluctuations contribute.

Through substituting the definition of a jackknife sample,

$$\bar{a}_{r,i}^J = \bar{a}_r + \frac{1}{N-1}(\bar{a}_r - a_{r,i}), \tag{E.30}$$

into the expressions for the jackknife estimators of the bias and correlation matrices, Eq. (E.28a) and (E.28b) respectively, and expanding in terms of N^{-1}, one may arrive at the expansions

of the jackknife estimators for $N \to \infty$. For instance, one arrives at the expression for the correlation matrix,

$$C^J_{\alpha\beta} = \frac{1}{N} \sum_{r,s} \overline{\delta}_r \phi^{(0)}_\alpha(\overline{a}_{r_1}, \dots) \overline{\delta}_s \phi^{(0)}_\beta(\overline{a}_{r_1}, \dots)(\overline{a}_{rs} - \overline{a}_r \overline{a}_s) + \mathcal{O}(N^{-2}) \tag{E.31}$$

where

$$\overline{a}_{rs} = \frac{1}{N} \sum_{i=1}^N a_{r,i} a_{s,i}, \qquad \overline{\delta}_r = \frac{\delta}{\delta \overline{a}_r}. \tag{E.32}$$

We see that the structure of Eq. (E.31) follows that of the physical quantity that it estimates, shown in Eq. (E.29b), the higher order terms of Eq. (E.31) being of the same structure as the first term apart from the products of the measured primary observables $a_{r,i}$ growing in length.

It is important to note here that, in the calculation of the estimators for the statistical properties such as the bias and the correlation matrix, the derivatives of the coefficient function $\phi^{(0)}$ does not require explicit calculation; the jackknife procedure performs numerical differentiation of $\phi^{(0)}$ through the use of the jackknife samples running through the calculation. As the jackknife samples deviate relative to the average of the measured primary observables $\overline{a}_r$ on the scale of $\mathcal{O}(N^{-1})$, the estimators are also assumed to vary smoothly on this scale.

E.2.2 *Propagating errors*

An important property of the jackknife method is, for a function Φ of stochastic estimators $\psi_1, \cdots, \psi_m$, that $\phi^J_i = \phi(\psi^J_1, \cdots, \psi^J_m)$. This allows one to pass jackknife samples through an arbitrarily long sequence of operations that produce a valid stochastic estimator at each stage, with nothing more needed than the jackknife samples of the measured primary observables and the evaluation of said stochastic estimators.

Focusing on the relevant case of hadron masses, the jackknife procedure for the extraction of the mass starts with the jackknife averages $\overline{O}(x_0, y)^J_i$ of the primary observables $O(x_0, y)^J$, which are the correlation functions with interpolating operators chosen to select the appropriate state, calculated on each gauge-field configuration, with appropriate projection operators and folding applied. As before, the operator has a source at time x_0 and is measured at lattice time y. The jackknife effective mass is given by the formula

$$m^J_{\text{eff}}(x_0)_i = -a^{-1} \ln \frac{\overline{O}(x_0 + a, y)^J_i}{\overline{O}(x_0, y)^J_i}, \tag{E.33}$$

while the covariance matrix is given by

$$C^J_{x_0 x'_0} = \sum_{i=1}^N \{m^J_{\text{eff}}(x_0)_i - m_{\text{eff}}(x_0)\} \{m^J_{\text{eff}}(x'_0)_i - m_{\text{eff}}(x'_0)\}, \tag{E.34}$$

where $m_{\text{eff}}(x_0)$ may be calculated from the average of the jackknife samples themselves. One may extract the statistical error of $m_{\text{eff}}(x_0)$ at this point from $(C^J_{x_0 x_0})^{1/2}$.

In order to perform a fit to extract a final value for the mass, the χ^2-statistic

$$\chi^2 = \sum_{x_0=t_0}^{t_1} \sum_{x'_0=t_0}^{t_1} \{m_h - m_{\text{eff}}(x_0)\} [(C^J)^{-1}]_{x_0 x'_0} \{m_h - m_{\text{eff}}(x'_0)\}, \tag{E.35}$$

is minimised over the range of effective mass values that form the plateau, falling in the range $[t_0, t_1]$,

$$m_h = \frac{\sum_{x_0, x'_0 = t_0}^{t_1} [(C^J)^{-1}]_{x_0 x'_0} m_{\text{eff}}(x'_0)}{\sum_{x_0, x'_0 = t_0}^{t_1} [(C^J)^{-1}]_{x_0 x'_0}}. \tag{E.36}$$

Note that the jackknife estimator of the correlation matrix weights the contributions at each time-point; this gives precedence to the time-points with smaller errors. As the mass is a function of stochastic estimators, its statistical error may also be computed through the jackknife method, through the calculation of the plateau for each jackknife sample, from which the standard deviation is calculated.

As the above-described method requires the correlation matrix to be calculated for each jackknife sample, this would require the jackknife samples of jackknife samples to be calculated. This turns the problem into an $\mathcal{O}(N^2)$ problem, which may be impractical for large data sets. A simpler procedure is therefore often used, in which the error of the correlation matrix is disregarded and the correlation matrix is calculated for the whole sample space, the value remaining constant during the plateau fit and the associated jackknife error propagation. In our jackknife analysis, we chose to use this simplification. Strictly speaking, the correctness of this simplification requires that the statistical error is much larger in magnitude than any systematic slope in the effective mass with time; also, asymptotically large values of N are required to show the correctness. Lastly, the formula for the bias given by Eq. (E.28a) is no longer valid when the simplication is used.

In order to perform a naive exploration of the autocorrelation length, one may separate the original data into bins, that are averaged within themselves and form the new data set. The jackknife procedure may then carry on as normal. Autocorrelation is then assessed by checking at which bin-size the results start to diverge from the results at larger bin-sizes. The autocorrelation length should be roughly equal to this bin-size. This binning procedure, it must be said, is not as efficient with regards to controlling autocorrelation as other techniques such as the Gamma method discussed later in this thesis, and is limited steeply by the size of the ensemble.

e.3 gamma method for error estimation

When resampling methods such as the jackknife or bootstrap methods are used, the autocorrelation may be naively quantified and adjusted for through the use of binning, in which the data series is split into bins of equal size, which are each averaged and then replace the old data as the new primary observables. These may then be resampled according to the chosen method and the rest of the analysis may proceed as usual, although with a reduced number of primary observables with respect to the un-binned calculation.

This binning is supposed to reduce the autocorrelation between sequential primary observables, and indeed it does. There is however a flaw in the capacity of the binning technique to quantify the autocorrelation; when a data series is split into bins, there will always be adjacent values that are separated into different bins, regardless of the chosen size of the bins. These values enter into the mean of the bins, causing some amount of residual autocorrelation between the bins. The integrated autocorrelation time for binned data is shown in [66] to behave at the leading order as $\mathcal{O}(1/N_B)$ for a large bin size N_B. This means that these values that are close in MC time become problematic when binning, as they force a power law in the autocorrelation function measured through binning, when the autocorrelation function is expected from theory to take the form of an exponential decay. This is disadvantageous because it is difficult to reduce the effect of autocorrelation to the desired level, as data sets are limited in length and it may be impossible to have bins with a size much larger than the exponential autocorrelation time. This means that errors will be underestimated significantly

in this regime far from the region of asymptotic $\mathcal{O}(1/N_B)$ scaling of the autocorrelation function.

In the Gamma method of error analysis, the explicit form of the autocorrelation function is calculated, as opposed to the jackknife method where the autocorrelation is estimated indirectly. This leads us to two benefits of the Gamma method with respect to binning techniques, the first being that the Gamma method has truncation errors that are exponential rather than power-like. Secondly, the Gamma method is able to offer an improved method of estimation when the data series is not much longer than the exponential autocorrelation time, through including an estimate of the slowest decaying modes of the autocorrelation function in its form; no equivalent method is available for the binning methods.

E.3.1 *Method*

In our analysis, our objective is to best exploit the finite number N_α of measurements on an ensemble α for a given primary observable A_i^α,

$$a_i^\alpha(t), \qquad t = 1, \cdots, N_\alpha, \tag{E.37}$$

in order to reduce the error on the estimation of the observable to the greatest possible extent whilst remaining accurate within that error. In the above, t gives the computer time i.e. the index of the configuration that the primary observable is being measured upon. It is assumed that each observable is measured successfully on each of the configurations of the ensemble. The average of the observable over the thermalised ensemble then gives an estimate for the expectation value $\langle A_i^\alpha \rangle$ of the observable at values of the physical parameters at which the ensemble is generated,

$$\overline{a}_i^\alpha = \frac{1}{N_\alpha} \sum_{t=1}^{N_\alpha} a_i^\alpha(t). \tag{E.38}$$

The fluctuations of the values of the primary observable with respect to the mean may then be written as

$$\delta_i^\alpha(t) = a_i^\alpha(t) - \overline{a}_i^\alpha. \tag{E.39}$$

This is calculated for each observable and on each ensemble.

Defining a derived observable as some function of the measured primary observables,

$$F \equiv f(\langle A_i^\alpha \rangle), \tag{E.40}$$

the estimate of this derived observable is given as before using a mean of the function values over the ensemble,

$$\overline{F} = f(\overline{a}_i^\alpha). \tag{E.41}$$

Linear error propagation may be used to investigate the error associated with this function. Consider a Taylor expansion of f around $\langle A_i^\alpha \rangle$,

$$f(\langle A_i^\alpha \rangle + \epsilon_i^\alpha) = F + f_i^\alpha \epsilon_i^\alpha + (\epsilon_i^2), \tag{E.42}$$

where the shorthands

$$f_i^\alpha = \partial_i^\alpha f|_{\langle A_i^\alpha \rangle} = f \frac{\partial f}{\partial \langle A_i^\alpha \rangle} \bigg|_{\langle A_i^\alpha \rangle} \tag{E.43}$$

have been used. In reality, one does not have access to the expectation values of A_i^α, so the mean values $\overline{a}_i^\alpha$ are used:

$$\overline{f}_i^\alpha = \partial_i^\alpha f|_{\overline{a}_i^\alpha}. \tag{E.44}$$

Recalling Eq. (2.45), in order to help us express the error associated with the function f, we may define the autocorrelation function projected onto f as

$$\Gamma_F^\alpha(t) + \sum_{ij} \overline{f}_i^\alpha \overline{f}_j^\alpha \Gamma_{ij}^{\alpha\alpha}(t). \tag{E.45}$$

This may then be used to define both the variance and the integrated autocorrelation time specific to derived observable F and ensemble α,

$$(\sigma_F^\alpha)^2 = \Gamma_F^\alpha(0), \qquad \tau_{\mathrm{int}}^\alpha(F) = \frac{1}{2} + \sum_{t=1}^{\infty} \frac{\Gamma_F^\alpha(t)}{\Gamma_F^\alpha(0)}. \tag{E.46}$$

Given that there may be different ensembles with the same physical parameters but with different algorithmic parameters or initial seed values, that are at the same time statistically uncorrelated with each other, the total error on observable F in this case may be calculated through the summation in quadrature of the σ_F^α from all ensembles calculated,

$$(\delta \overline{F})^2 = \sum_\alpha \frac{(\sigma_F^\alpha)^2}{N_\alpha} 2\tau_{\mathrm{int}}^\alpha(F). \tag{E.47}$$

The fraction that each ensemble in this scenario would contribute is given by

$$R_\alpha(F) = \frac{(\sigma_F^\alpha)^2 2\tau_{\mathrm{int}}^\alpha(F)}{N_\alpha (\delta \overline{F})^2}, \tag{E.48}$$

where we note that this is possible through the Gamma method because each ensemble is analysed independently.

A distinguishing feature of the Gamma method is the estimation of the integrated auto-correlation time through the truncation of the infinite sum with an upper limit W_F^α that is chosen for each observable of each ensemble using an automatised procedure,

$$\tau_{\mathrm{int}}^\alpha(F) = \frac{1}{2} + \sum_{t=1}^{W_F^\alpha} \frac{\Gamma_F^\alpha(t)}{\Gamma_F^\alpha(0)}. \tag{E.49}$$

If we neglect for a moment the issue of statistical error, it would be preferable to have a W_F^α that is significantly larger than the characteristic decay time of the slowest mode of the Markov operator, the exponential autocorrelation time $\tau_{\mathrm{exp}}^\alpha$. If this condition is satisfied, then the autocorrelation function is well-represented by a single exponential and the systematic error due to truncation is given by $\mathcal{O}(e^{-W^\alpha/\tau_{\mathrm{exp}}^\alpha})$.

However, when statistical error is brought into consideration, it is evident that a W_F^α that is too large will cause the signal-to-noise ratio to diminish. This is because the signal from $\Gamma_F^\alpha(t)$ exponentially decays with time, whereas the statistical error of $\Gamma_F^\alpha(t)$ is roughly constant in time. Increasing unduly the length of the summation window therefore decreases the quality of the signal without much gain in estimation accuracy. In practice, this is mitigated against by minimising the combined error, which is a sum of the statistical error and the systematic error due to the truncation. This relies on the assumption that $\tau_{\mathrm{exp}}^\alpha \approx S_\tau \tau_{\mathrm{int}}^\alpha$, where S_τ is optimised through inspection of the characteristics of the ensemble(s), and usually has values in the range 2 - 5. In our analysis, the value $S_\tau = 1$ was used.

Although the above assumption is made in order to define the size of the summation window, in many LQCD contexts one finds that the values of $\tau_{\mathrm{int}}^\alpha$ and $\tau_{\mathrm{exp}}^\alpha$ differ by a large factor, as noted in [67]. This may lead to the underestimation of the error, as, due to the above-mentioned statistical errors, it is unsatisfactory to take the summation window to be much greater than $\tau_{\mathrm{exp}}^\alpha$.

Fortunately, this is simple to address, through the addition to the formula for $\tau_{\text{int}}^{\alpha}$ of another term. Through ensuring that the summation window size W_F^{α} is large but that $\rho_F^{\alpha}(W_F^{\alpha})$ is distinguishable statistically from zero, the remaining section of $\tau_{\text{int}}^{\alpha}$ in the region $t > W_F^{\alpha}$ is assumed to be well-described by the exponential tail that is given by the slowest mode of the Markov operator, $\rho_F^{\alpha} \sim \exp(-|t|/\tau_{\text{exp}}^{\alpha})$, where $\rho_F^{\alpha} = \frac{\Gamma_F^{\alpha}(t)}{\Gamma_F^{\alpha}(0)}$. When this term is integrated and added on to the sum, the expression for $\tau_{\text{int}}^{\alpha}$ becomes

$$\tau_{\text{int}}^{\alpha}(F) = \frac{1}{2} + \sum_{t=1}^{W_F^{\alpha}} \rho_F^{\alpha}(t) + \tau_{\text{exp}}^{\alpha} \rho_F^{\alpha}(W_F^{\alpha}+1). \tag{E.50}$$

With the addition of this third term in mind, there are two common approaches to choosing where to add the tail to the function, or equivalently how to select W_F^{α}. The first is the original proposed in [66], in which the tail is added to the autocorrelation function starting at the point where $\rho_F(t)$ is different from zero by three standard deviations. In this procedure, Eq. (E.50) becomes the error upper bound. The second approach, used by the ALPHA collaboration [67], is to attach the tail at the point where one is about to lose the signal in $\rho_F(t)$, which should be approximately 1-2 standard deviations away from zero. Using this treatment, Eq. (E.50) is treated as simply the estimate of the error. The ALPHA approach for the incorporation of the integrated autocorrelation time into the error of observables is used for all ensembles on which we have measured baryon masses, with the tail being added when $\rho_F(t)$ is different from zero by two standard deviations. This point is found through checking the condition iteratively along the data series.

Finally, we shall end with a note about the implementation of the Gamma method with respect to the construction of derived observables through the sequential application of different functions. This will lead on to the discussion below of automatic differentiation. When using the Gamma method, it is pragmatic to store for each derived observable both the mean and the projected fluctuations per ensemble,

$$\overline{F} \equiv f(\overline{a}_i^{\alpha}), \qquad \delta_F^{\alpha}(t) = \sum_i \overline{f}_i^{\alpha} \delta_i^{\alpha}(t). \tag{E.51}$$

If we define the successive function G as

$$G = g(f(\langle A_i^{\alpha}\rangle)), \tag{E.52}$$

that being a function of the function $f(\langle A_i^{\alpha}\rangle)$, then, if we first compute the values given in Eq. (E.51), the error associated with G only requires the further calculation of the derivative $\overline{g}_F = \partial^F g|_{\overline{F}}$,

$$\overline{G} = g(\overline{F}) = g(f(\overline{a}_i^{\alpha})), \tag{E.53a}$$

$$\delta_G^{\alpha}(t) = \overline{g}_F \delta_F^{\alpha}(t) = \sum_i \overline{g}_F \overline{f}_i^{\alpha} \delta_i^{\alpha}(t) = \sum_i \overline{g}_i^{\alpha} \delta_i^{\alpha}(t), \tag{E.53b}$$

where $\overline{g}_i^{\alpha} = \partial_i^{\alpha} g|_{\overline{a}_i^{\alpha}}$. Thus, the only objects that require passing through the calculation in order to be able to calculate the error propagation are the mean and the fluctuations. It is also self-evident that any primary observable may also be treated in the same fashion, if one identifies the function with the identity.

E.3.2 *Automatic differentiation*

Various approaches exists for the analysis of errors of a derived observable. For example, the jackknife method computes the error of a derived observable through calculating the function

value for each jackknife sample and then measuring the standard deviation of the collection of such function values. Aside from the above-mentioned problems with the treatment of autocorrelation, there may exist with the jackknife method the problem that fits over some samples do not converge. Linear error propagation may also be used to derive analytically the expression for the error of a derived function; this, however, becomes more difficult as the function becomes more complex. For a method as complicated as the Gamma method, analytical linear error propagation is unfeasible. Finite difference methods, also known as numerical differentiation, are usually used instead inside the Gamma method. This numerical differentiation has the drawback that all finite difference formulae are ill-conditioned, and care must also be taken to determine the optimal step size to use for the differentiation.

Auto-differentiation is an approach in which the derivative of an arbitrarily complicated function is determined exactly, at least to machine precision. This is achieved through the overloading of simple functions, inside which the function derivative is hard-coded and calculated using the input data provided through the function call, to automatically calculate the error of a derived observable at the same time as the function value is calculated. Through the use of the chain rule, a complicated function may be split into its smallest operations, reducing the analytical complexity and thereby the chance of a miscalculation of the error propagation, whilst preserving the exactness of the differentiation which would be lost were numerical differentiation used. Not only does auto-differentiation provide a remedy to the problems discussed in the above paragraph, but it also allows one to assess the error of a function of MC observables with potentially different run parameters or from different ensembles. This could be useful in the context of a fit during the interpolation/extrapolation to the physical point.

E.3.3 *Application example: fit parameters*

A fitting procedure is an example of a procedure that is often used in LQCD and whose error would be very difficult to express through analytical error propagation. When we perform a least-squares fit, we are in fact calculating for the parameter values $p_i(i = 1, \cdots, N_{\text{parm}})$ at which the function

$$\chi^2(p_i; d_a), \qquad p_i(i = 1, \cdots, N_{\text{parm}}), \qquad d_a(a = 1, \cdots, N_{\text{data}}) \tag{E.54}$$

is minimised when the data d_a are fitted. Generally, χ^2 may be expressed as

$$\chi^2 = \sum_{a=1}^{N_{\text{data}}} \left(\frac{f(x_a; p_i) - d_a}{\sigma(d_a)} \right)^2, \tag{E.55}$$

where $f(x_a; p_i)$ is a function of the parameters p_i that is constrained to have a given form a priori. The fitting procedure returns a set of parameters $\overline{p}_i$ that minimise the function $\chi^2(\overline{p}_i; \overline{d}_a)$ when the fixed data set $\overline{d}_a$ is provided.

In order to ascertain the error associated with the fitting procedure, we must consider how a small shift in the input data affects the parameters returned. When shifting the data as $d_a \to \overline{d}_a + \delta d_a$, to leading order the χ^2 function will change as

$$\chi^2(p_i; \overline{d}_a + \delta d_a) = \chi^2(p_i; \overline{d}_a) + \partial_a \chi^2\big|_{(p_i; \overline{d}_a)} \delta d_a, \qquad (\partial_a \equiv \partial/\partial d_a). \tag{E.56}$$

This shift in χ^2 will then cause a shift by δp_i in the parameter values at which χ^2 is minimised. The above equation is differentiated with respect to p_i and then set to zero, in order to find

the new minimum. Expanding the resulting expression at $p_i = \overline{p}_i$ gives at leading order the condition

$$\partial_j \partial_i \chi^2\big|_{(\overline{p}_i; \overline{d}_a)} \delta p_j + \partial_i \partial_a \chi^2\big|_{(\overline{p}_i; \overline{d}_a)} \delta d_a = 0, \qquad (\partial_i \equiv \partial/\partial p_i). \tag{E.57}$$

For convenience, we define the χ^2 Hessian

$$H_{ij} = \partial_j \partial_i \chi^2\big|_{(\overline{p}_i; \overline{d}_a)} \tag{E.58}$$

evaluated at the minimum of χ^2, and therefore arrive at the expression for the derivative with respect to the input data of the fit parameters

$$\frac{\delta p_i}{\delta d_a} = - \sum_{j=1}^{N_{\text{parm}}} (H^{-1})_{ij} \partial_j \partial_a \chi^2\big|_{(\overline{p}_i; \overline{d}_a)}, \tag{E.59}$$

which of course can enter as discussed above into the successive process of error analysis through the chain rule. Here, only one pass of the data through the iterative process is required, as only the fit parameter central values $\overline{p}_i; \overline{d}_a$ and the χ^2 derivatives evaluated at those central values are needed for the error analysis.